Micromechanics Based Multiscale Modeling of the Inelastic Response and Failure of Complex Architecture Composites

by

Kuang Liu

A Dissertation Presented in Partial Fulfillment
of the Requirements for the Degree
Doctor of Philosophy

Approved July 2011 by the
Graduate Supervisory Committee:

Aditi Chattopadhyay, Chair
Hanqing Jiang
Jian Li
Marc Mignolet
John Rajadas

ARIZONA STATE UNIVERSITY

December 2011

ABSTRACT

Advanced composites are being widely used in aerospace applications due to their high stiffness, strength and energy absorption capabilities. However, the assurance of structural reliability is a critical issue because a damage event will compromise the integrity of composite structures and lead to ultimate failure. In this dissertation a novel homogenization based multiscale modeling framework using semi-analytical micromechanics is presented to simulate the response of textile composites. The novelty of this approach lies in the three scale homogenization/localization framework bridging between the constituent (micro), the fiber tow scale (meso), weave scale (macro), and the global response. The multiscale framework, named Multiscale Generalized Method of Cells (MSGMC), continuously bridges between the micro to the global scale as opposed to approaches that are top-down and bottom-up. This framework is fully generalized and capable of modeling several different weave and braids without reformulation. Particular emphasis in this dissertation is placed on modeling the nonlinearity and failure of both polymer matrix and ceramic matrix composites. Results are presented for the cases of plain, twill, satin, and triaxially braided composites. Inelastic, failure, strain rate and damage effects are included at the microscale and propagated to the global scale. MSGMC was successfully used to predict the in-plane material response plain and five harness satin woven polymer composites, triaxially braided polymer composite and both the in-plane and out-of-plane response of silicon carbide ceramic matrix composites.

This dissertation is dedicated to my wife and child, my parents, my uncle, and my sister for their support in pursuing my doctoral degree.

ACKNOWLEDGMENTS

I would first like to thank my advisor and mentor, Prof. Aditi Chattopadhyay, for the confidence and support she has given me. I would also like to acknowledge Dr. Steven M. Arnold for mentoring me during my time at NASA Glenn Research Center. I want to give a special thanks to Dr. Robert Goldberg and Dr. Brett Bednarcyk from NASA Glenn Research Center for their time spent on advice for my research. Lastly, I would like to thank Prof. Jacob Aboudi from Tel Aviv University for teaching me the fundamental concepts of micromechanics that allowed me to complete my research.

I would also like to thank other members of my Supervisory Committee, Prof. Marc Mignolet, Dr. Hangqing Jiang, Dr. Jian Li, and Dr. John Rajadas for their support and advice. I am also grateful to all of my fellow graduate students and colleagues at NASA Glenn who have made my graduate study enjoyable. I would like to thank NASA Glenn Research Center for supporting me through the Graduate Student Researchers Program during the completion of my doctoral studies through grant number NNX08AZ11H, technical monitor Dr. Steven M. Arnold.

TABLE OF CONTENTS

Page

Page

Page

LIST OF TABLES

LIST OF FIGURES

Figure Page

Chapter 1

1. INTRODUCTION

1.1. Motivation

Advanced composites are being widely used in aerospace applications due to their high stiffness, strength and energy absorption capabilities. However, the assurance of structural reliability is a critical issue because a damage event will compromise the integrity of a composite structures and lead to ultimate failure. Composites are often employed in impact damage susceptible locations. The associated dynamic response with an impact event is complex due to complicated stress wave patterns, material nonlinearity and the inherent nonlinearity associated with continuously evolving geometry. A particular problem of interest is the impact response of composite fan containment system. Current and next generation fan casings are being manufactured not from metals or traditional laminated composites, but braided and woven fabric composites. A concern for manufacturers is the ability of the fan containment system to meet Federal Aviation Agency (FAA) standards for blade-out containment. Current testing methods and design procedures are expensive and time consuming; a modeling approach is necessary to take full advantage of the composite material's capabilities.

Traditional analysis methods and material characterization for composites typically considers only the macroscale or structural level response. Many methods are based on lamination theories or anistropic elasticity analysis. These methods are inadequate when applied to a complex structure, such as the fan

casing, with a complex material such as a triaxially braided composite. Research in multiscale modeling, especially applied to composite materials, is an emerging topic and is particularly well suited for this problem. Multiscale modeling allows for the analysis of composites at multiple length scales and can track stress, damage, and other state variables throughout critical stages. Multiscale modeling is essential to capturing the most important damage events in a complex structure, where damage can exist at the fiber level, tow level, and braid level.

1.2. Background

Textile and braided composites are both architecturally and mechanically complex composite materials. In the aerospace industry, there are several mainstream weaves and braids; Fig. 1.1 illustrates the most common of those. Textile and braided composites differ from traditional laminated composites, in that each lamina contains fibers in more than one direction, achieved through weaving or braiding. This produces desirable effects, such as reduce propensity for delamination, thicker lamina, quasi-isotropic fabrics. However, often maximum volume fraction and subsequently strength are sacrificed. In contrast to traditional unidirectional laminated composites, textile and braided composites often have varying orientations due to undulation, warp, weft, and braid tows. Damage mechanisms in these composites contain all those of traditional laminated composites plus additional modes that arise due to their geometric features. Typically the relevant physical mechanisms that need to be considered, in no particular order, are matrix nonlinearity, matrix and fiber failure, tow splitting/first matrix cracking, fiber/matrix debonding, tow/matrix debonding, and

fiber buckling/kinking. From this list, it is apparent that these mechanisms occur at various length scales occurring on the order of <10 microns to >1cm. Development of a high fidelity model should contain the most relevant damage mechanisms and formulation of a multiscale modeling is the most practical method to implement those although various techniques have been developed.

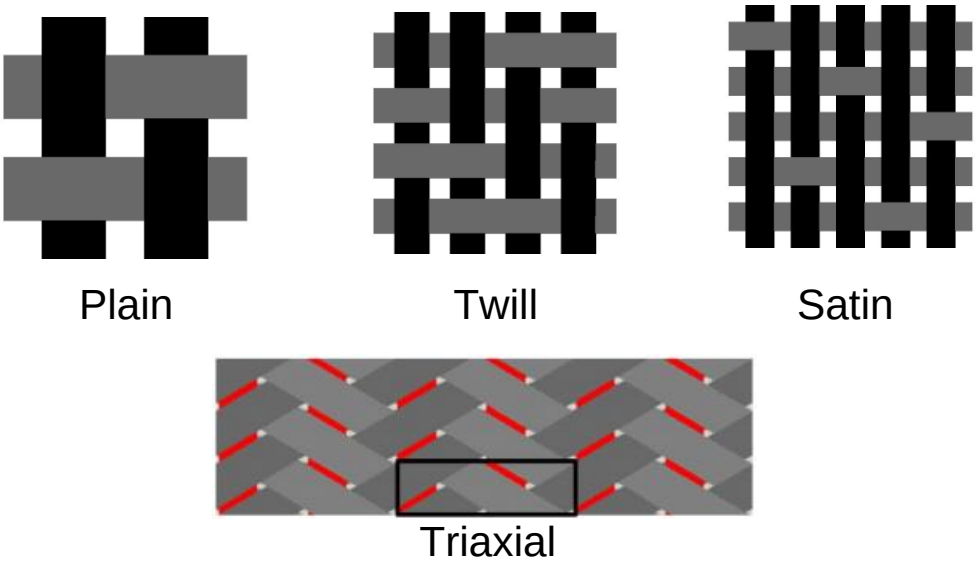

Fig. 1.1 Commonly Used Weave Patterns

There are four primary methods used for modeling textile and braided composites and are illustrated in Fig. 1.2. The first approach shown is referred to as a fully homogenized weave model. In this type of modeling, the architecture of the weave is not explicitly represented and a “smeared” (homogenized) approach, where the material is considered completely homogeneous, is used. These are typically orthotropic, transversely isotropic or anisotropic constitutive models carefully formulated to match the macroscopic or overall global response of a plain weave laminate. Most often these models focus on capturing the highly

nonlinear shear response and the hydrostatic effects, typically employing damage or progressive damage mechanics techniques to achieve this. The advantage of this type of approach is the simplicity of use and low computational effort. The disadvantages are a lack of fidelity and possibility of disregarding or overestimating damage mechanisms that are architecturally dependent, i.e. when the architecture changes phenomenon such as first matrix cracking will change and will not be reflected in this type of approach. A typical application of this approach is structural component level modeling. Due to the fast computation time and the widespread use of stiffness driven models, this approach is particularly well adapted for modeling low stress level composites, particularly outside hot spots. An exhaustive literature review is not presented here because the goals of this approach differ from the work presented in this dissertation.

The second approach shown in Fig. 1.2 is typically referred to as micromechanics modeling. In this approaches the architecture is specifically modeled and usually discretized into critical subvolumes, with each subvolume containing either resin or a homogenized fiber tow. A discerning feature of this approach is modeling the fiber tow homogeneously, as opposed to explicitly modeling the individual fibers as in the third approach. The benefits and disadvantages are discussed further on. Once the material has been discretized into subvolumes, iso-strain, iso-stress, or mixed boundary conditions are then assumed and a macro-micro relationship is derived. These are referred to as analytical methods or analytical micromechanics. However, a second set of approaches using finite element techniques to model the architecture have also

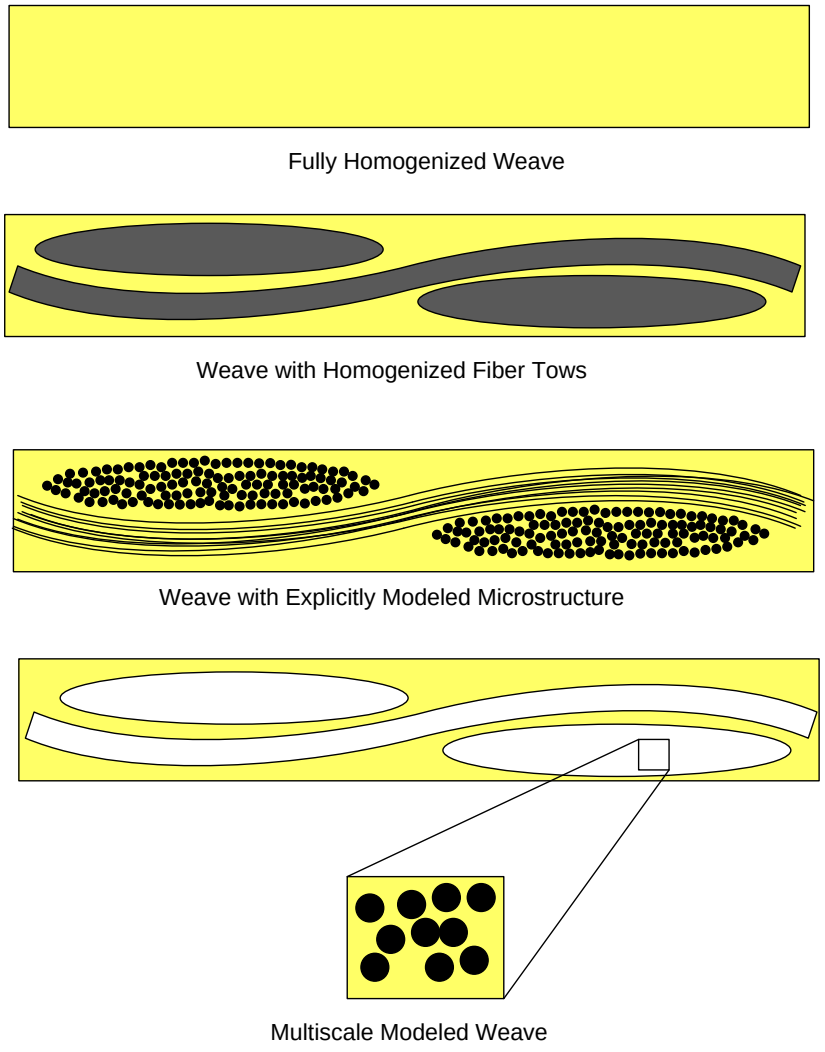

Fig. 1.2 Various Modeling Techniques for Textile Composites

been developed, known is numerical techniques or finite element based micromechanics. Furthermore, there two approaches to ascertain the geometric microstructure. The most common type is an approach based on idealized repeating unit cells, i.e. a material without imperfections. In contrast to the fully homogenized models, these analytical models are often generalized and are equipped to handle changes in features such as fiber volume fraction, tow spacing,

thickness, and etc. These methods are mostly associated with analytical micromechanics; however, there are a few finite element based approaches in this realm. The second most common type is based on the actual microstructure obtained from optical image or computed tomography scan. These are almost exclusively associated with finite element based approaches. More often than not, these approaches formulate a representative volume element of the composite for their analysis. These techniques are computationally intensive are used to study a specific material.

One of the first significant reported publications in analytical micromechanics modeling was the works of Halpin 1971. This work envisioned fabric composites (both 2D and 3D) as a laminate analysis of the "crimped" and "non-crimped" portions of the fabric. This allowed for the modeling and prediction of the in-plane elastic constants and thermal expansion coefficients. This approach and variations are commonly used today in industry and other applications requiring only elastic response. Ishikawa and Chou (1982) presented three analytical models, the "mosaic model", "fibre undulation model", and "briding model". Through use of all three models, the in-plane mechanical elastic constants and "knee behaviour" for plain, twill and satin composite could be predicted. The "mosaic model", remains a very popular model in literature for elastic analysis and has been extended by other authors. Ishikawa and Chou (1982) also used their "mosaic model" to examine hybrid fabric composites, defined as fabric composites with different fiber tow sizes. After these publications, there was a lull in research and interest in fabric composites until a

resurgence occurred in the late 1980s. At this point, two main methods for analysis began emerging: analytical and finite element approaches. In addition, the use of braided composites became popular and subsequently research in the modeling these materials also began emerging. The works of Naik and his colleagues (Naik 1994, Naik 1995) extended the use of analytical methods for modeling the elastic constants, nonlinear shear behavior, nonlinear geometric effects (crimping and straightening of tows), and overall failure. Naik applied his model to both woven and braided composites with success. Other researchers (Stanton and Kipp, Jortner, Ko and Pastore, Ko, Dow and Ramnath, Masters and Fedro and Ifju, Dadkah, Swanson, Cox and Flanagan, Tabiei and Ivanov) have also developed In contrast to the approximation techniques used in the analytical techniques, which provide computationally efficient results that sacrifice on accuracy, finite element methods can provide a high fidelity geometric model and highly accurate local stress fields at the cost of computational efficiency in both analysis and preprocessing. Finite element methods are also less generalized then equivalent analytical methods. Whitcomb and his colleagues (Whitcomb 2000, Whitcomb 2004) expanded finite element techniques to model textile composites. This approaches typically involves generating a finite element mesh of a weave repeating unit cell and applying carefully formulated boundary conditions to determine the response of the composite. Other authors (Kriz, Binienda, Quek Waas) have also taken similar approaches to modeling textiles and fabrics for various applications.

In all previously cited works, a common fundamental assumption regarding the behavior of the fiber tow bundles is applied: the fiber tow bundles can be represented as a homogeneous transversely isotropic material. This assumption is valid under certain conditions, such as low stress, strongly bonded (fiber/matrix) systems, and static loading. Determination of tow elastic properties is a critical issue with this approach. Many authors estimate or apply rudimentary micromechanics, such as strength of materials or rule of mixtures, to determine the properties. Another issue of this approach is the assumption of linear elastic behavior when, in fact, the fiber tow response is high nonlinear and inelastic, much like a unidirectional laminate.

The third approach shown in Fig. 1.2, explicitly models each constituent in the composite. While this approach would provide the highest geometric fidelity and possibly highest accuracy, it is currently impractical to implement. Development of a 3D model and explicitly modeling each fiber, (on the order of 10,000-100,000 fibers for a typical RUC) would require an extraordinary amount of time in experimental characterization and model simulation. In contrast, simulations of explicit microstructure in metallic materials often consider less than 1000 grains, 1 to 2 orders of magnitude less than the requirement for composites. This type of approach would also be “tied” to a specific microstructure at a point for a given sample or component.

The fourth approach is known as a multiscale modeling, wherein the goal is to encompass the accuracy of explicitly modeling the microstructure, while retaining computational efficiency. There are two primary subsets of multiscale

models developed with different purposes. One subset focuses on a high fidelity modeling of the architecture, similar to the finite element micromechanics mentioned previously, in order to study the nuances of damage initiation and evolution. These models are rarely used to model large structures or components as they require a significant amount of computational time and may not have been derived in a proper constitutive model framework for implementation within a commercial software, such as an Abaqus user subroutine. Examples of these include the work of Kollegal and Ernst et al. The second subset focuses on the development of multiscale models within a constitutive framework for implementation within commercial software. These models are typically analytical or semi-analytical, computationally efficient and applicable to a variety of weaves. The works of Tabiei, as well as the work presented in this dissertation, fall into this category.

In this dissertation a novel homogenization based multiscale modeling framework using semi-analytical micromechanics is presented. The novelty of this approach lies in the three scale homogenization/localization framework bridging between the constituent (micro), the fiber tow scale (meso), weave scale (macro), and the global response. The multiscale framework, named Multiscale Generalized Method of Cells (MSGMC), continuously bridges between the micro to the global scale as opposed to approaches that are top-down and button-up. In addition, this framework is fully generalized and capable of modeling several different weave and braids without reformulation. Particular emphasis in this

dissertation is placed on modeling the nonlinearity and failure of both polymer matrix and ceramic matrix composites.

1.3. Objectives of the work

This research aims at the following principal objectives:

- Develop a generalized multiscale modeling methodology for complex composite materials considering nonlinear constitutive effects including damage and failure.
- Characterize various complex composites (weaves and braids) and apply those within the multiscale modeling methodology to predict their response.
- Analyze materials and determine the relevant length scales necessary for efficient analysis and the necessary detail for accurate modeling.
- Experimentally validate and verify the methodology at multiple length scales.

1.4. Outline of the report

The report is structured as follows:

Chapter 2 introduces the weave architecture, characterization, and experimental observations for use in the multiscale modeling theory. This chapter covers two types of architectures: woven and braided fabrics. It covers the geometric constraints of the weave architecture as well as assumptions made for the analysis.

Chapter 3 discusses the background and theory of the multiscale modeling methodology used to model the complex composites. The chapter begins with the background and need for multiscale modeling, particularly in composite

applications. Next an overview of the various micromechanics formulations is presented and how they are applied to the new methodology, a Multiscale Generalized Method of Cells (MSGMC).

Chapter 4 focuses on the applying MSGMC to modeling triaxially braided composites with carbon fiber and polymer constituents. Results are presented for elastic, plastic, and viscoplastic for two types of triaxial braids. Results are compared to experimental, lamination theory and finite element techniques.

Chapter 5 applies MSGMC to modeling woven composites with carbon fiber and polymer constituents. Results are presented for elastic, plastic, and viscoplastic for plain and five harness satin weaves. These are compared to other micromechanical (and multiscale), experimental, and finite element techniques. In addition, an exhaustive parametric study was performed to assess the sensitivity of the model parameters.

Chapter 6 applies MSGMC to modeling woven composites with ceramic/ceramic constituents. Particular research effort was focused on modeling the voids at the weave and tow scales, the fiber interface and the damage mechanics of the matrix. Results are compared to experimental studies and a parametric study was performed to assess sensitivity.

Chapter 7 focuses on the future directions of the current research. There are four main topics for future research: 1) Further development of MSGMC, 2) Implementation of material constitutive modeling, 3) Detailed material characterization and analysis, 4) Coupled implementation with finite element analysis.

Chapter 2

2. WOVEN AND BRAIDED COMPOSITE CHARACTERIZATION

2.1 Introduction

Traditional laminated composites with unidirectional aligned fibers have simple idealized representative architectures. Woven and braided composites have more complex architectures and require a more detail analysis to characterize the parameters necessary to capture the most important geometric effects. Typically, parameters need to be characterized at multiple length scales and can be either dependent or independent on parameters at other length scales. Woven fabric composites are generally orthogonal, but this is not necessarily always the case. When the weaves are at an angle less than perpendicular they are often called "biaxial" weave or braid. Woven fabrics typically consist of two perpendicular tows or yarns of fabric, whereas braided fabrics consists of three or more. This research focuses on orthogonal/perpendicular woven fabrics as well as triaxially braided fabrics.

2.2 Orthogonal Weaves

There are several types of orthogonal weaves, but not all are commonly used in the aerospace industry as a composite constituent. Many types of fabrics are products of the textile industry and are still unexplored in the area of aerospace composite structures. Some common weaves include: plain, twill, satin, basket, and crows foot. These are illustrated in Fig. 2.1. Characterization will be presented for plain, twill and satin weaves. In the following characterization, the following assumptions/approximations are made:

1. The fiber tows are assumed to have rectangular cross section.
2. The undulation is discontinuous and occurs only between tows.
3. The twist of the tows is negligible.
4. Tow fiber volume fraction is uniform throughout the RUC.

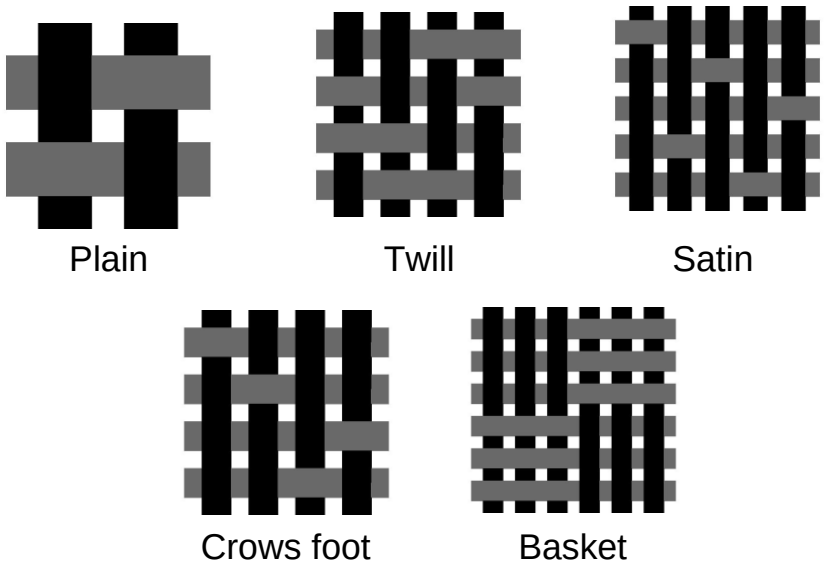

Fig. 2.1 Orthogonal Textile Weave Patterns

2.2.1 Plain Weave

Using the previously discussed assumptions, the plain weave RUC can be dimensioned as shown in Fig. 2.2. The plain weave has a one-over-one-under fabric pattern. This is one of the more commonly used fabrics for aerospace applications. As will be explained further in detail, the weave will need to be discretized into orthogonal three dimensional parallel piped subvolumes, known as subcells. The plain weave will be discretized into $5x5x4$ subcells. The RUC is discretized into subcells by using key geometric features as boundaries, i.e. the tow boundaries, and can be seen in Fig. 2.3. In this figure, the blank subcells

represent the matrix material and the subcells with a hatch pattern represent the tow subcells. The orientation angle is represented by the angle of the fibers, i.e. orientation of the hatch pattern.

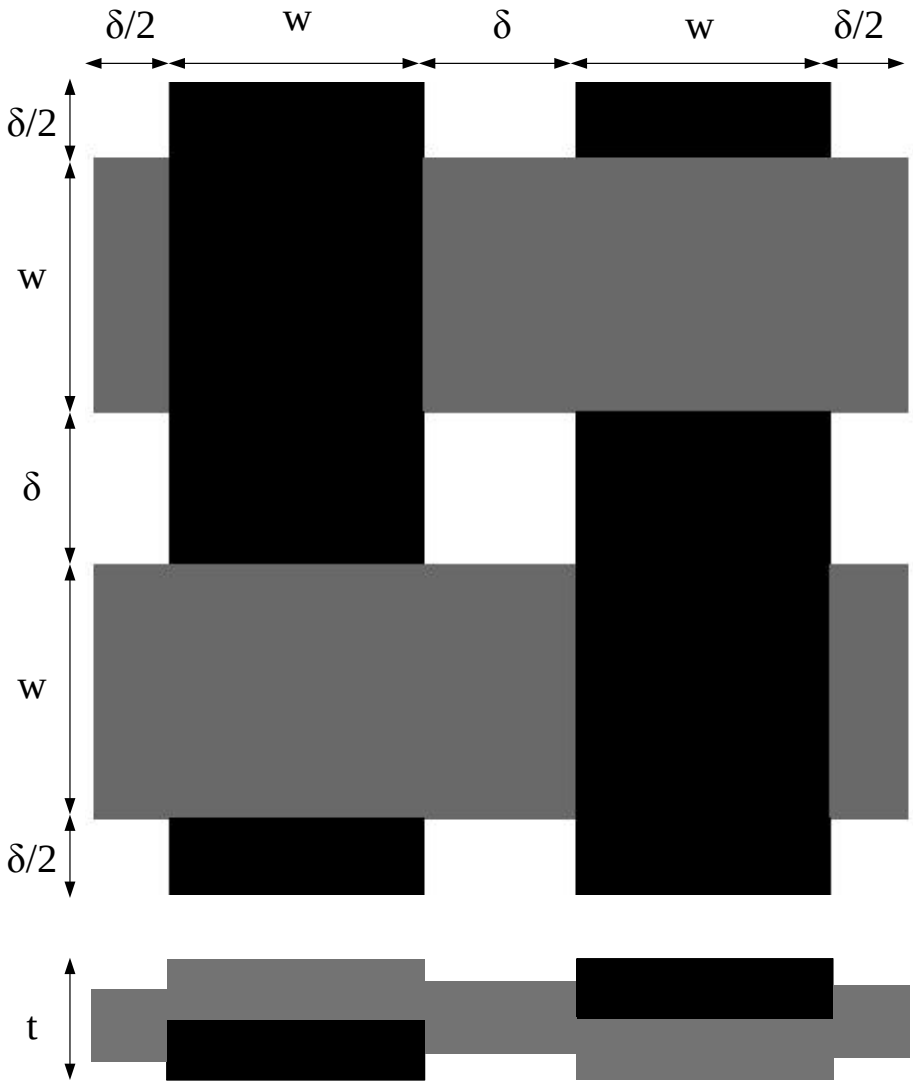

Fig. 2.2 Discretized Plain Weave Architecture

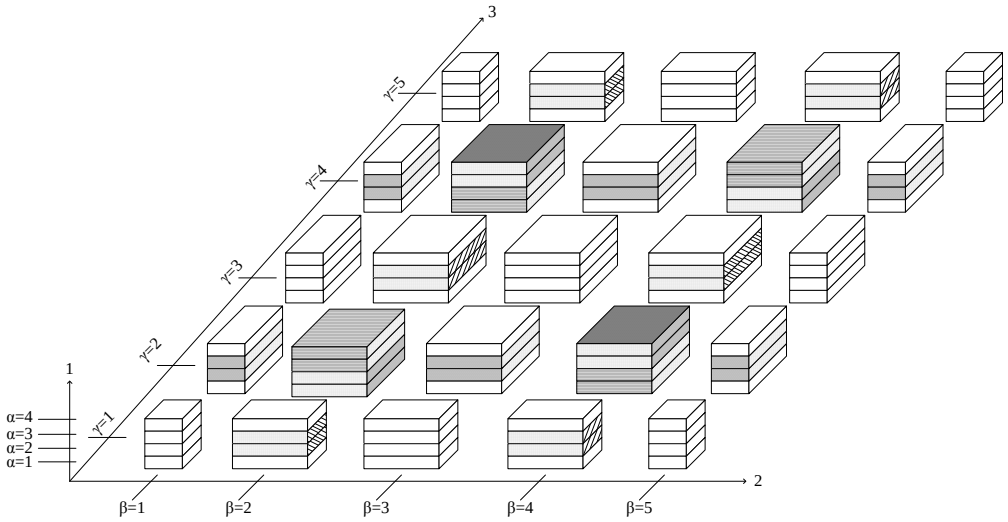

Fig. 2.3 3D Subcell Discretization of Plain Weave Composite

Due to the assumptions previously stated, it is important to ensure that the overall fiber volume fraction, V_f, is correctly represented, which depends on the tow fiber volume fraction, $V_{f_{tow}}$, fiber tow width, w, tow spacing, δ, and the ply thickness, t. The total volume fraction of the RUC can be expressed by summing the fiber volumes over all the subcells and dividing by the RUC volume.

$$V_f = \frac{8\left(\frac{w\delta t}{2}\right)+4\left(w^2 t\right)}{\left(2w+2\delta\right)\left(2w+2\delta\right)t} V_{f_{tow}} \tag{2.1}$$

This can be further simplified to

$$V_f = \frac{w}{\left(w+\delta\right)} V_{f_{tow}} \tag{2.2}$$

From Eq. (2.2) it can be seen that thickness is not directly present. In application, thickness and $V_{f_{tow}}$ are typically inversely proportional, but this is not always true. The geometry of the RUC can be constrained based on any three of the four

variables, shown in Eq. (2.2). Specifying all four variables will violate the geometric constraints. The last parameter needed to calculate is the undulation angle for the subcells containing tows that are undulating. Using the assumption that the undulation is uniform across one subcell and discontinuous, the undulation angle can be approximated by,

$$\theta = \arctan\left(\frac{t}{2\delta}\right) \tag{2.3}$$

The undulation angle is present in the following subcells for the (α,β,γ) coordinate system depicted in Fig. 2.3: (2-3,2,1), (2-3,4,1), (2-3,1,2), (2-3,3,2), (2 3,5,2), (2-3,2,3), (2-3,4,3), (2-3,1,4), (2-3,3,4), (2 3,5,4), (2-3,2,5), and (2-3,4,5). The dimensions for each subcell are represented by the variables *D* ,*H,* and *L*, representing the dimensions in the 1-, 2-, and 3-direction, respectively. For the plain weave the dimensions are shown in (2.3).

$$\begin{aligned} D &= \{t/4, t/4, t/4, t/4\} \\ H &= \{\delta, w, \delta, w, \delta\} \\ L &= \{\delta, w, \delta, w, \delta\} \end{aligned} \tag{2.4}$$

2.2.2 Twill, Harness Satin, and Other Weaves

Two other common weaves are the twill and 5 harness satins (Figs. 2.4 and 2.5). A twill weave is characterized by its distinctive diagonal pattern seen in bulk. The twill pattern can be woven in many different configurations, but the most common is the 2x2 which will be analyzed in this study. This means that each tow goes over-two-under-two. The adjacent tows are offset by one tow to

produce the diagonal effect. Fig. 2.4 demonstrates the key features of a twill pattern.

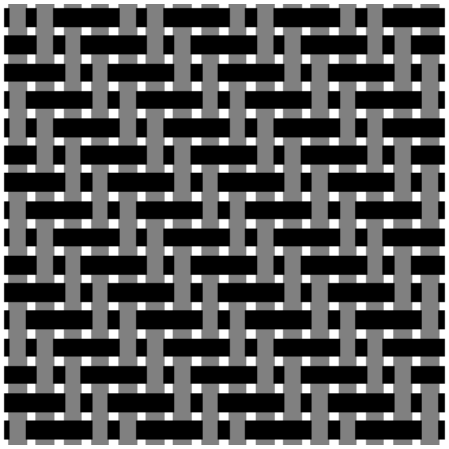

Fig. 2.4 Twill Weave Diagonal Pattern

Harness satin weaves are unique because no adjacent tows undulate at the same point. Typically, harness satin weaves are denoted with a numerical character prefacing the word “harness satin”, i.e. “5-harness satin”. This denotes a 4x1 pattern, where a tow goes over four and under one. Another common pattern is the 8-harness satin where this is a 7x1 pattern. Fig. 2.5 shows the key features of a 5-harness satin weave.

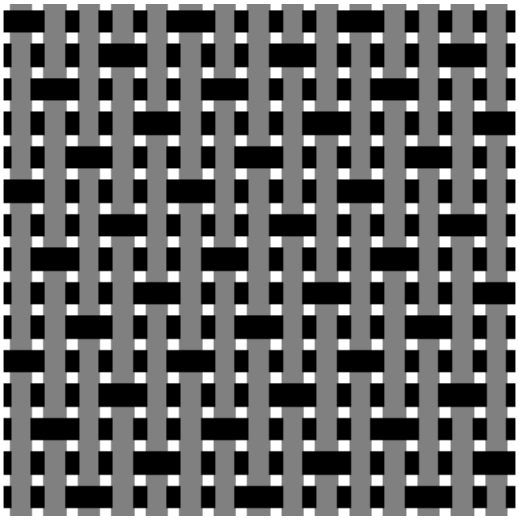

Fig. 2.5 5 Harness Satin Weave Pattern

The geometry of these fabrics will need to be constrained in the same manner as that of the plain weave, and both the twill and 5-harness satin are constrained by Eq. (2.2). It can also be shown that any other orthogonal weave can be constrained by this relationship. The undulation angle is also approximated in the same manner as that of the plain weave. Subcell stacks 2-5 are the ones containing the undulating tows, this is explained further on. To discretize the twill and 5-harness satin weaves, the same methodology used on the plain fabric is employed. For easier visualization, the discretization will be described in terms of subcell stacks, where these stacks correspond to through thickness groups of subcells (similar to the subcells shown in Fig. 2.3). A total of 11 unique stacks can be assembled together to form each weave pattern, like a mosaic, as shown in Fig. 2.6. For both the twill and 5-harness satin, the configuration is shown in Figs. 2.7 and 2.8, respectively. Any other orthogonal weave can be assembled using these subcell stacks. Each stack has the same thickness dimensions as specified in *D* of Eq. 2.4. The dimensions of both weaves are shown below. If any refinement of

the geometry or subcell changes are made, these dimensions are invalid. For a twill weave, the subcell dimensions are

$$D = \{t/4, t/4, t/4, t/4\}$$
$$H = \{\delta, w, \delta, w, \delta, w, \delta, w, \delta\} \tag{2.5}$$
$$L = \{\delta, w, \delta, w, \delta, w, \delta, w, \delta\}$$

and for a 5 harness satin the subcell dimensions are

$$D = \{t/4, t/4, t/4, t/4\}$$
$$H = \{\delta, w, \delta, w, \delta, w, \delta, w, \delta, w, \delta\} \tag{2.6}$$
$$L = \{\delta, w, \delta, w, \delta, w, \delta, w, \delta, w, \delta\}.$$

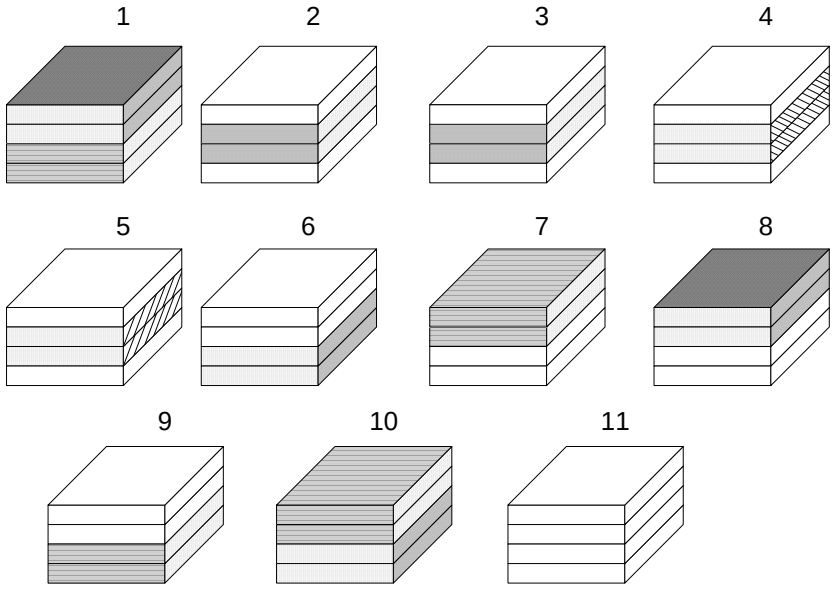

Fig. 2.6 Subcell Stacks for Orthogonal Weaves

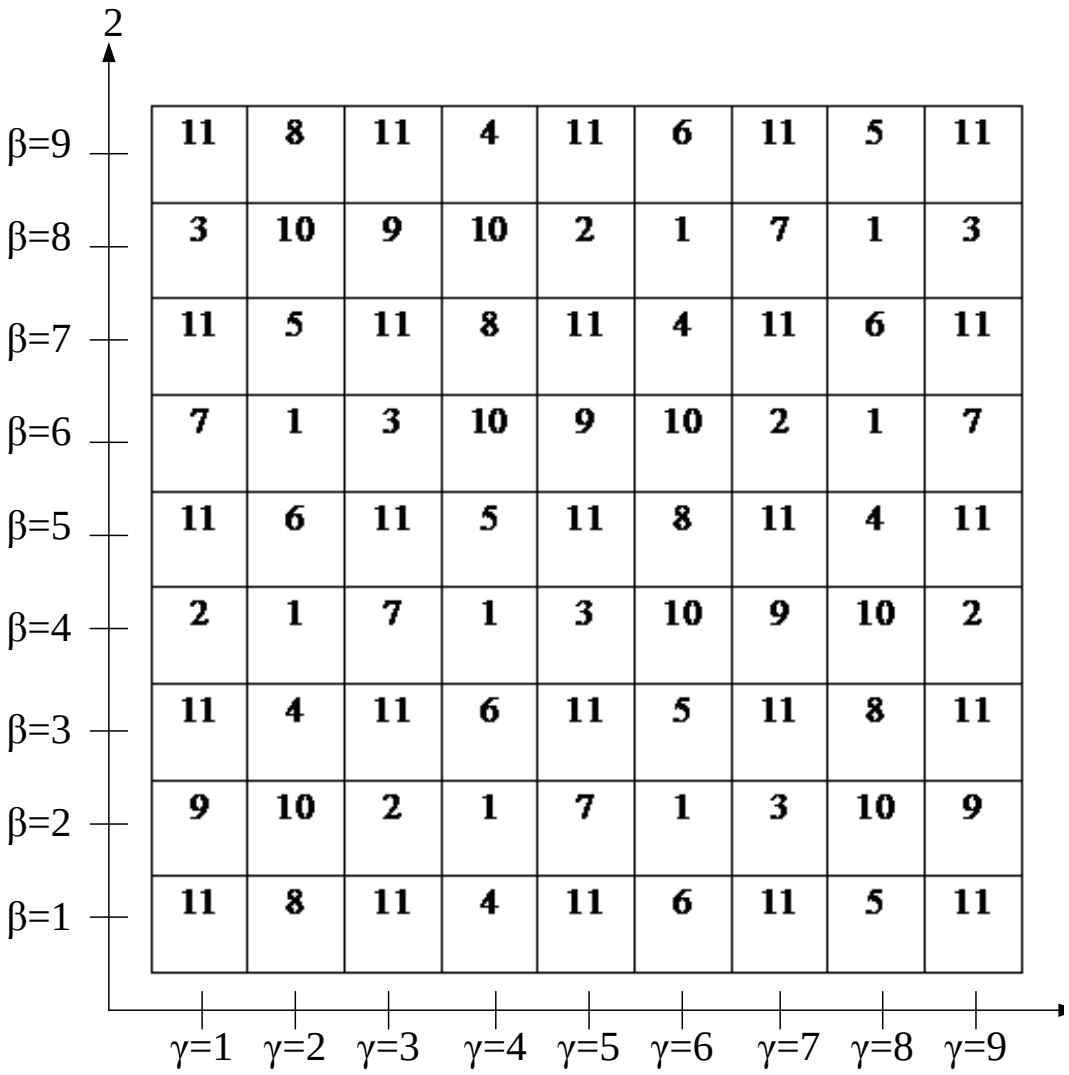

Fig. 2.7 2x2 Twill Subcell Stack Configuration

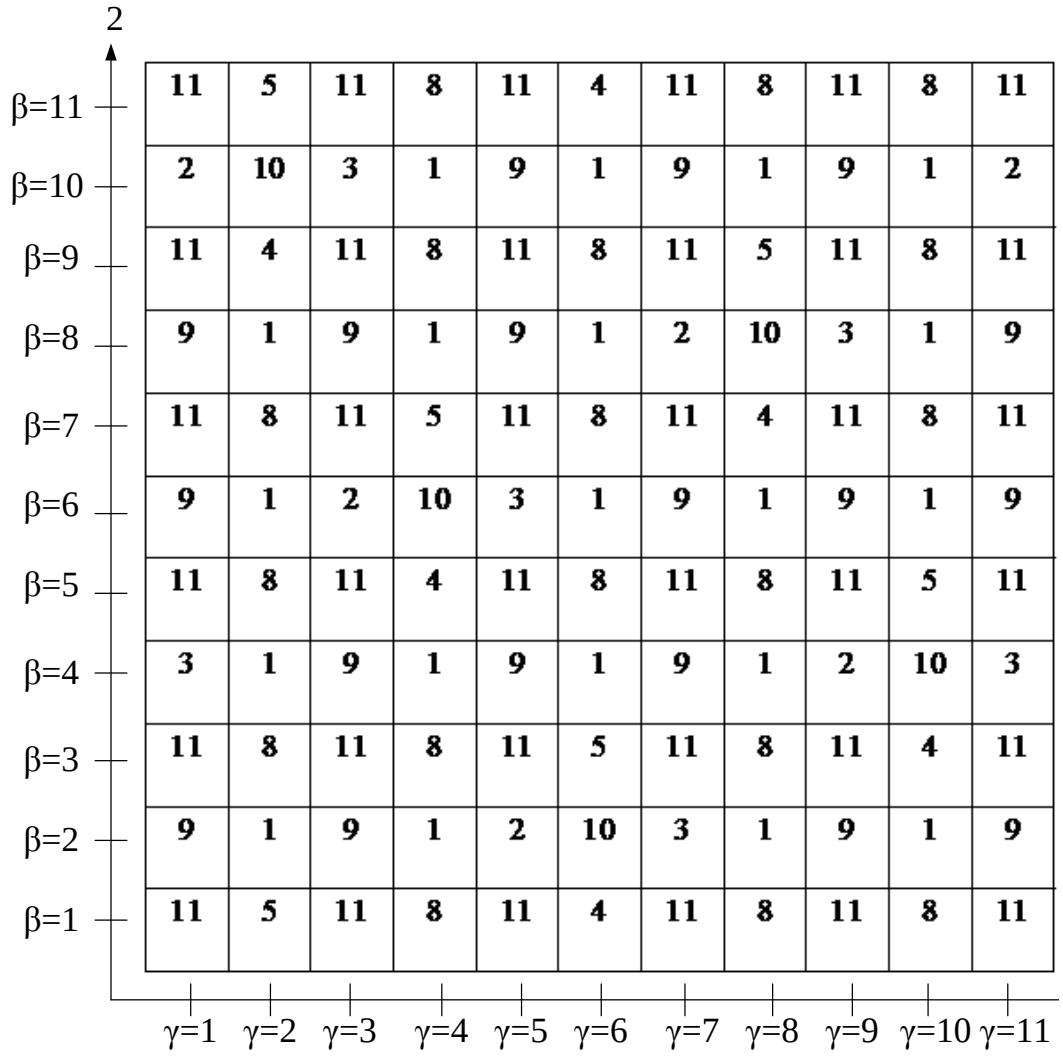

Fig. 2.8 5 Harness Satin Subcell Stack Configuration

2.3 Triaxial Braids

Triaxial braids can be split into two categories: a) traditional triaxial braid, the more commonly used fabric, and b) true triaxial braid. Fig. 2.9 shows the typical components of a triaxial weave composite. The traditional triaxial braid differs from the true triaxial in several aspects, and a comparison between them is shown in Fig. 2.10 and Fig. 2.11.

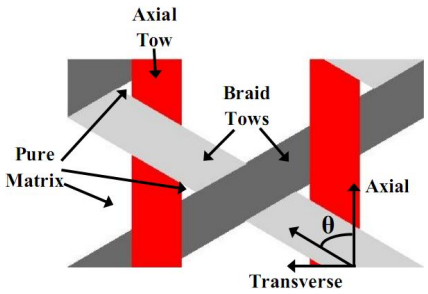

Fig. 2.9 Typical Triaxial Braid Components

First, in the true triaxial, all tows have the same cross sectional area. On the other hand, the traditional triaxial has an axial tow with twice the cross sectional area as the braided tows. To maintain triaxiality, there is twice the number of braided tows as compared to axial tows. Second, in the traditional braid, the axial tow does not undulate, while the true triaxial has all tows undulating evenly and uniformly. Characterizing the geometry of a triaxial braid is more involved than of the orthogonal weaves. A detailed derivation and characterization of all the parameters is shown in the following sections.

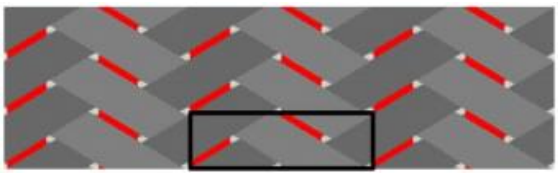

Fig. 2.10 Traditional Triaxial Braid

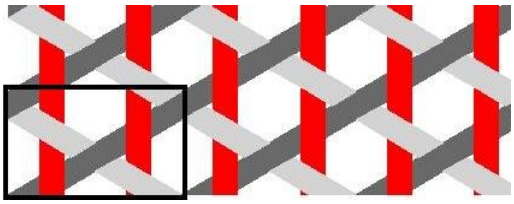

Fig. 2.11 True Triaxial Braid

2.3.1 Tradiational Triaxial Braids

A typical architecture of a traditional triaxial braided composite is shown in Fig. 2.10 with the repeating unit cell indicated by the black box. The triaxial braid RUC consists of straight axial fiber tows and braided fiber tows oriented at an angle θ. It is assumed for this analysis that the architecture being analyzed can be

represented by an idealized homogenized RUC, thus imperfections in the architecture are not considered.

The traditional triaxial braided composite is composed of three significant volumes: pure matrix, axial tows, and braided tows. The braided tows are offset from the axial tows at an angle θ, known as the braid angle. The total volume of the RUC is the summation of each individual volume as denoted in the following equation, where subscripts 0° denotes the axial tow, ±θ denotes the braided tows, and *m* denotes the pure matrix.

$$V = V_{0^o} + V_{\pm\theta} + V_m \tag{2.7}$$

The overall volume fraction of fibers (filaments, as opposed to tows) can be computed by identifying the fiber volume fractions in both the axial and braided tows and then determining the total volume of fibers in the RUC. Subscript *f* in the following equations denotes the fiber (as opposed to the tow).

$$V_f = \frac{V_{f_{0^o}} V_{0^o} + V_{f_{\pm\theta}} V_{\pm\theta}}{V} \tag{2.8}$$

The volume of the RUC in Equations (2.7) and (2.8) was previously expressed in terms of the volumes of the tows and matrix, but it is also useful to express this in terms of physical parameters that are typically specified during manufacturing processes or can be identified in micrographs, such as the tow width, spacing and thickness. The RUC volume can be described as a parallelepiped consisting of length (*L*), height (*H*) and depth (*D*). To generalize the traditional triaxial braided composite architecture, it is assumed that the axial and braided tows have

independent geometries. The RUC volume is only dependent on the width and spacing of the braided tows and the thickness of both the axial and braided tows. It has no direct dependence on the axial tow width, but this does not imply that it is arbitrary, as will be shown later. In the following, *t* denotes the thickness and *w* denotes the width of a tow or RUC, while *w'* denotes the spacing between tows.

$$V = DHL \tag{2.9}$$

$$L = \frac{1}{\sin\theta}\left(w_{\pm\theta} + w'_{\pm\theta}\right)$$

$$H = \frac{2}{\cos\theta}\left(w_{\pm\theta} + w'_{\pm\theta}\right)$$

$$D = t_{0^\circ} + 2t_{\pm\theta}$$

Since the axial tows do not undulate, their volume can be directly computed based on the cross-sectional area of each tow, *A*, and the length of the RUC. It must be noted that the coefficient 2 in (2.10) comes from the presence of two axial tows in the RUC.

$$V_{0^\circ} = 2A_{0^\circ}L = \frac{2A_{0^\circ}}{\sin\theta}\left(w_{\pm\theta} + w'_{\pm\theta}\right) \tag{2.10}$$

The volume of the braided tows is more difficult to determine directly, but can be conveniently written as a proportion to the volume of the axial tows expressed as a scalar *m*. This scalar *m* can be approximated for small undulations as shown,

$$\frac{V_{0^\circ}}{V_{\pm\theta}} = m = \frac{A_{0^\circ}}{2A_{\pm\theta}}\cos\theta \tag{2.11}$$

For the simple case where the cross sectional areas of the axial tow is twice that of the braided tow, with a braid angle of 60 degrees, this results in m= 0.5. Substitution of Equations (2.9), (2.10), and (2.11) into Equation (2.8) yields,

$$V_f = \frac{A_{0^o}\left(V_{f_{0^o}} + \frac{V_{f_{\pm\theta}}}{m}\right)}{\left(\frac{1}{\cos\theta}\right)\left(w_{\pm\theta} + w'_{\pm\theta}\right)\left(t_{0^o} + 2t_{\pm\theta}\right)} \tag{2.12}$$

Typically, fiber volume fraction is thought of as a specified property in which the braided tow spacing is not specified. Therefore it is beneficial to rewrite Equation (2.12) as,

$$w'_{\pm\theta} = \frac{A_{0^o}\frac{1}{V_f}\left(V_{f_{0^o}} + \frac{V_{f_{\pm\theta}}}{m}\right)}{\left(\frac{1}{\cos\theta}\right)\left(t_{0^o} + 2t_{\pm\theta}\right)} - w_{\pm\theta} \tag{2.13}$$

At this point, the architecture is constrained in terms of several parameters, but the tow cross-sectional area is still not defined. Therefore an assumption is made regarding the cross-sectional area of the tows. For simplicity of integration with the generalized method of cells, the present analysis considers tows to be of a rectangular cross section of width w and thickness t. This yields a final equation providing the braided tow spacing expressed as follows.

$$w'_{\pm\theta} = \frac{\left(w_{0^\circ}t_{0^\circ}\right)\frac{1}{V_f}\left(V_{f_{0^o}} + \frac{V_{f_{\pm\theta}}}{m}\right)}{\left(\frac{1}{\cos\theta}\right)\left(t_{0^o} + 2t_{\pm\theta}\right)} - w_{\pm\theta} \tag{2.14}$$

The rectangular approximation of tows is acceptable since the overall fiber volume fraction and local fiber volume fractions are accurately represented. The effective elastic moduli and first failure modes are considered in this study, thus the representation rectangular cross section of the tows provides acceptable results. If nonlinear damage progression and failure is to be considered, a more refined cross section may be necessary. The axial tow spacing is not arbitrary, as mentioned previously, and can be determined using Equations (2.9) and (2.13) expressed as follows,

$$w'_{0^o} = \frac{1}{\cos\theta}\left(w_{\pm\theta} + w'_{\pm\theta}\right) - w_{0^o} \tag{2.15}$$

Lastly, the undulation angle of the braided tows can be defined in terms of the thickness and the braided tow spacing as follows,

$$\varphi = \arctan\left(\frac{t_{0^o} + t_{\pm\theta}}{\frac{w'_{\pm\theta}}{\sin\theta}}\right) \tag{2.16}$$

The resulting characterization of the traditional triaxial braided composite architecture is dependent on ten parameters. Table 2.1 lists all the parameters with additional suggestions as to how they may be determined. Typically, in an idealized problem, it is assumed that the tow fiber volume fractions $V_{f_{0^o}}$ and $V_{f_{\pm\theta}}$ are equivalent and uniform. If the cross-sectional areas are assumed to be rectangular, it is simplified to only seven parameters being needed. The two parameters defining tow spacing are constrained based on the parameters listed in Table 2.1.

Table 2.1 Triaxial Braided Composite Parameters Determination Methods

Parameter	Determination Method
V_f	ASTM D3171
$V_{f_{0^o}}, V_{f_{\pm\theta}}$	Assume 80% for PMC
$w_{0^o}, w_{\pm\theta}, \theta, t_{0^\circ}, t_{\pm\theta}$	Optical microscope measurement
$A_{0^o}, A_{\pm\theta}$	Shape function or approximation

Two unique types of triple periodic repeating unit cells, of size $D \times H \times L$ and matching the dimension given by the microstructural parameters, were discretized into $n_{\mathrm{A}} \times n_{\mathrm{B}} \times n_{\Gamma}$ parallelepiped subcells, with each subcell having dimensions $d^{\mathrm{A}} \times h^{\mathrm{B}} \times l^{\Gamma}$. A simplified RUC was developed for the purpose of reducing computation effort and for eventual implementation in finite element analysis and optimization algorithms. A refined RUC has also been developed for detailed material characterization purposes and provides more detailed local stress/strain states (Fig. 2.12).

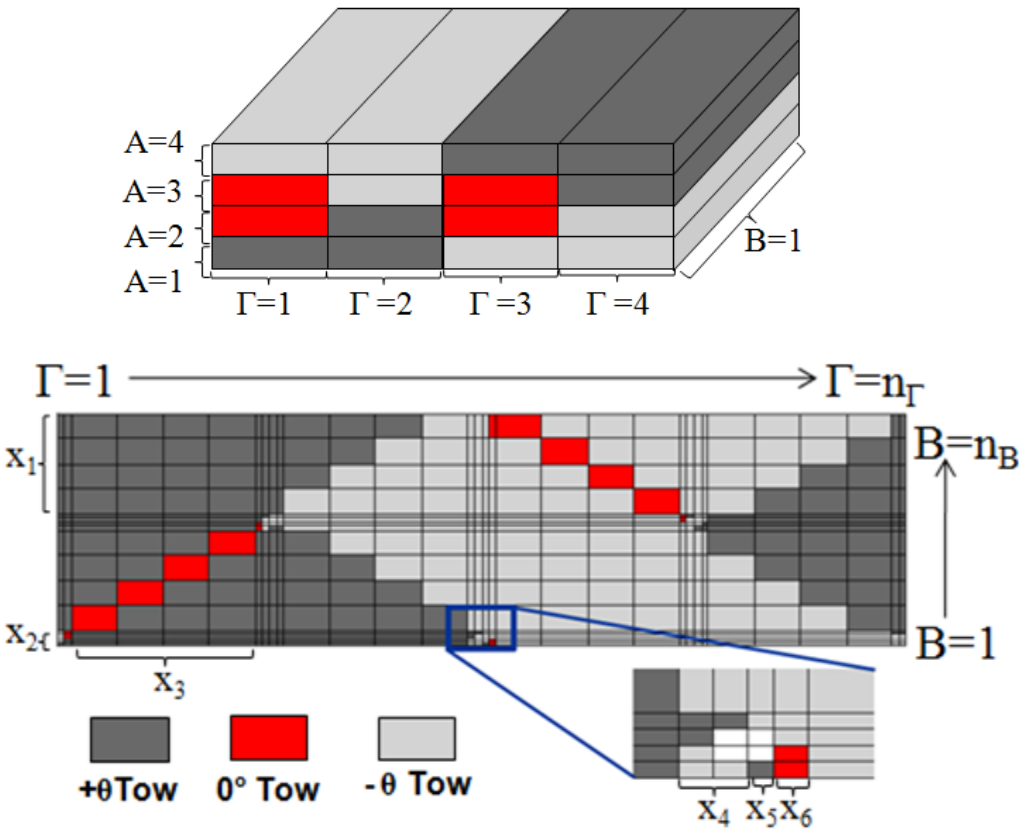

Fig. 2.12 Traditional Triaxial Braid Discretized RUCs (top simplified, bottom refined)

The simplified model discretizes the traditional triaxial braided composite RUC into four architecturally governed sections through the width and four through the thickness as shown in Fig. 2.12. The through-width subcells are separated into sections containing axial tows (Γ=1 and Γ=3) and those that do not (Γ=2 and Γ=4). The through-width subcells are separated into sections of either axial or braided tows. For subcells with A=1 and A=4, the properties from the mesoscale are rotated by an angle θ to represent the braid; subcells Γ=2 and Γ=4 are rotated

once more by angle φ to represent the undulation. The end result is that each subcell contains only a single tow material, either axial or braided, with correct orientation. No pure matrix regions are explicitly represented. To maintain a true representation of the previously described architectural parameters, the geometric dimensions and fiber volume fraction of each subcell are analytically determined and expressed in terms of the architectural parameters by,

$$
\begin{aligned}
d^1 &= \frac{1}{\sin\theta}\left(w_{\pm\theta} + w'_{\pm\theta}\right) \\
h^1 &= h^4 = t_{\pm\theta} \\
h^2 &= h^3 = t_{0^\circ} \\
l^1 &= l^3 = w_{0^\circ} \\
l^2 &= l^4 = w_{0^\circ} - \frac{1}{\cos\theta}\left(w_{\pm\theta} + w'_{\pm\theta}\right)
\end{aligned}
\tag{2.17}
$$

With the exception of subcells containing axial tows, all subcells have an effective volume fraction that encompasses the resin rich sections which are not directly represented. As can be seen from Equation (2.14), as the fiber volume fraction increases, $w'_{\pm\theta}$ decreases along with the volume of resin rich sections. This indicates that at high volume fractions, the simplified model is not an accurate approximation. The subcell effective volume fractions are determined by enforcing the correct overall volume fraction as well as the correct volume fraction per column and per row of the subcells. The overall fiber volume fraction in the simplified RUC is matched analytically to that of the true RUC, with the final expression.

Table 2.2 Simplified RUC Effective Fiber Volume Fraction by Subcell

Subcell {A,B,Γ}	Fiber volume fraction
{2,1,1},{2,1,3},{3,1,1},{3,1,3}	$V_{f_{0^o}}$
{1,1,1},{1,1,3},{4,1,1},{4,1,3}	$\left(1-\frac{w'_{\pm\theta}}{w_{0^o}\left(w_{\pm\theta}+w'_{\pm\theta}\right)}\right)V_{f_{\pm\theta}}$
{1-4,1,2},{1-4,1,4}	$\frac{l^1+l^2}{l^2}V_f-\frac{l^1}{l^2}\left(1-\frac{w'_{\pm\theta}}{w_{0^o}\left(w_{\pm\theta}+w'_{\pm\theta}\right)}\right)V_{f_{\pm\theta}}$

$$V_f=\left(V_{f_{0^o}}\frac{t_{0^\circ}}{t_{0^\circ}+t_{\pm\theta}}+\left(1-\frac{w'_{\pm\theta}}{w_{0^o}\left(w_{\pm\theta}+w'_{\pm\theta}\right)}\right)V_{f_{\pm\theta}}\frac{t_{\pm\theta}}{t_{0^\circ}+t_{\pm\theta}}\right)\frac{\gamma_1}{\gamma_1+\gamma_2}$$
$$+\left(\frac{\gamma_1+\gamma_2}{\gamma_2}V_f-\frac{\gamma_1}{\gamma_2}\left(1-\frac{w'_{\pm\theta}}{w_{0^o}\left(w_{\pm\theta}+w'_{\pm\theta}\right)}\right)V_{f_{\pm\theta}}\right)\frac{\gamma_2}{\gamma_1+\gamma_2} \quad (2.18)$$

The expressions for the fiber volume fractions of each subcell are given in Table 2.2 and have been determined through the use of Equations (2.7)-(2.16). It is important to note that undulation is represented in the Γ_2 and Γ_4 subcell columns through rotation of the effective microscale properties of the braided tow by angle φ.

A refined RUC that further discretizes the traditional triaxial braided composite RUC into subcells that explicitly include the resin rich regions is shown in Fig. 2.12. Note that a top view of the RUC is shown in this case. This RUC takes into consideration the braided tow spacing, which was only effectively represented in the simplified model. The through-thickness discretization is

identical to that of the simplified model, separating the axial and braided tows. The in-plane discretization also follows a similar methodology to the simplified RUC, where subcell dimensions are governed by geometrical parameters. This is in sharp contrast to a typical finite element mesh, in which element shape and dimensions lack physical meaning. In Fig. 2.12, key dimensions are shown and defined in Table 2.3. These dimensions are derived from the architectural parameters previously mentioned. The refined traditional triaxial braided composite RUC contains a total of 572 subcells.

2.3.2 True Triaxial Braid

Unlike the traditional triaxial braid architecture, whose axial tows are merely laid straight between the biased (±θ°) tows, the true triaxial braid architecture offers the unique property of having the axial fiber tows interweaved with the biased tows. Fig. 2.13 shows a more detailed view of the RUC for the true triaxial braid. Since the axial tows are braided through the biased tows in a manner such that the axial tow always lies on top of the +θ tows and below the –θ tows, while the +θ tows always lie on top of the –θ tows, not only are the axial tows interleaved through the biased tows, but also the biased tows are undulated in the ±θ material directions. Therefore, this true triaxial braid architecture presents a unique microstructure that has yet to be fully developed with applications as opposed to traditional triaxial braided composites.

Table 2.3 Refined RUC Subcell Dimension Parameters

Parameter	Value
x_1	$\frac{1}{2\sin\theta}\left(w_{\pm\theta} - w'_{\pm\theta}\right)$
x_2	$\frac{w'_{\pm\theta}}{\sin\theta}$
x_3	$\frac{1}{2\cos\theta}\left(w_{\pm\theta} - w'_{\pm\theta}\right)$
x_4	$\frac{w'_{\pm\theta}}{2\cos\theta}$
x_5	$\frac{1}{2}\left(\frac{w'_{\pm\theta} + w_{\pm\theta}}{2\cos\theta} - w_{0^o}\right)$
x_6	$\frac{w'_{\pm\theta}}{4\cos\theta} - \frac{1}{2}\left(\frac{w_{\pm\theta}}{2\cos\theta} - w_{0^o}\right)$

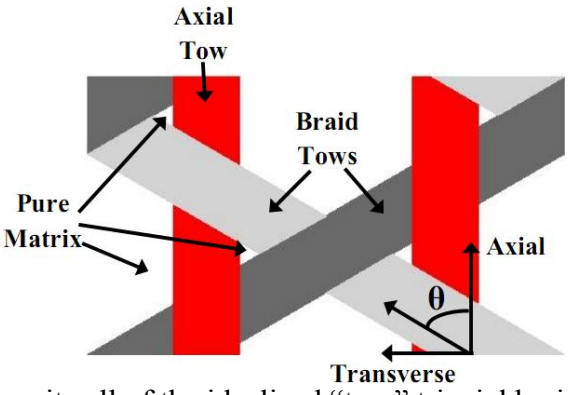

Fig. 2.13 Repeating unit cell of the idealized "true" triaxial braid architecture

With the geometric microstructural differences in the two triaxial braid patterns clearly identified, it is necessary to constrain the microstructure (i.e., define the biased tow spacing, axial tow spacing, and maximum producible volume fraction) as a function of the braid angle, volume fraction, and tow geometries. In the following section, w, t, s, and A_0 are used to denote the tow

width, thickness, spacing, and cross sectional area, respectively, while V_f and V_{f_t} are the overall fiber volume fraction and the tow volume fraction, respectively. The braid angle, θ, denotes the angle between the biased tows and the axial tows. The subscript, *a*, is used to denote properties of the axial tows, and the subscript, *b*, denotes the biased tow properties. Capital variables with no subscript, L, W, D, and V, are used to denote RUC scale properties of length, width, thickness, and volume, respectively.

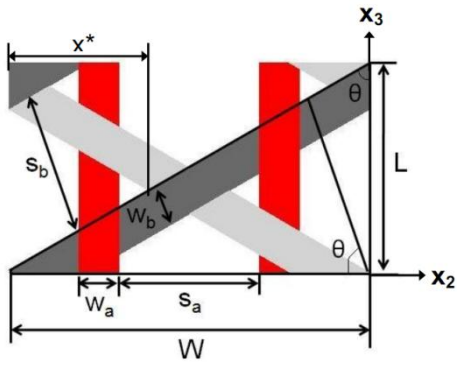

Fig. 2.14 Idealized RUC architecture of the "true" triaxial braid with variable labels

The geometry of the traditional triaxial braid by introducing a parameter, *m*, which represented the ratio of the volume of the axial tows to the volume of the biased tows. This process allowed the volume of the biased tows to be expressed analytically without ignoring the undulations in the biased direction. Therefore, assuming the axial tows and the biased tows have the same tow volume fraction, V_{f_t}, and assuming the tow cross section can be represented as rectangular, the biased tow spacing for the "traditional" triaxial braid architecture is constrained via the following equation,

$$s_b = \frac{w_a t_a V_{f_t}(1 + m^{-1})}{\frac{V_f}{\cos\theta}(t_a + 2t_b)} - w_b \tag{2.19}$$

However, since the tow thickness is small in comparison to the tow width, the undulations in all tows are ignored for the purpose of calculating the tow volumes in the true triaxial braid architecture. This simplification allows the microstructure to be constrained in terms of the braid angle, volume fraction, and tow geometries without introducing any additional parameters. Furthermore, the tow cross section is represented via a rectangular approximation, and it is assumed that analysis of the idealized microstructure provides an accurate representation of the effective composite scale elastic properties without accounting for any imperfections within the microstructure. This idealized microstructure is shown in Fig. 2.14 with all of its variables labeled, and its subsequent GMC discretization via subcell stacks is shown in Fig. 2.15.

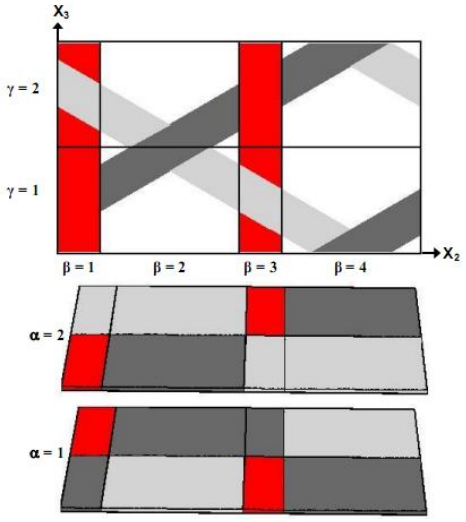

Fig. 2.15 GMC subcell stack discretization of the idealized "true" triaxial braid RUC

For the true triaxial braid, the total RUC volume may be written as

$$V = LWD \tag{2.20}$$

where the RUC length, *L*, and the RUC width, *W*, are given by

$$L = \frac{s_b + w_b}{\sin\theta} \tag{2.21}$$

$$W = \frac{s_b + w_b}{\cos\theta} \tag{2.22}$$

Furthermore, since no more than two tows are stacked together through the thickness within the braided lamina, the total RUC thickness, *D*, can be expressed as follows.

$$D = t_a + t_b \tag{2.23}$$

Therefore, the overall volume fraction may be written as

$$V_f = \frac{V_{ft}(V_a + V_b)}{V} \tag{2.24}$$

where V_a and V_b are the volumes of the axial and braid tows, respectively, within the RUC. Using a rectangular cross section for the tows, V_a and V_b can be written directly in terms of the tow dimensions and the braid angle.

$$V_a = 2A_{0_a}L \tag{2.25}$$

$$= 2w_a t_a \frac{s_b + w_b}{\sin\theta}$$

$$V_b = 2A_{0_b}\frac{L}{\cos\theta} \tag{2.26}$$

$$= 2w_b t_b \frac{s_b + w_b}{\sin\theta\cos\theta}$$

Substituting (2.20) – (2.23) and (2.25) – (2.26) into (2.24) yields,

$$V_f = \frac{2V_{f_t}(w_a t_a \cos\theta + w_b t_b)}{(s_b + w_b)(t_a + t_b)} \tag{2.27}$$

However, the volume fraction is desired to be an input parameter and the biased tow spacing, s_b, is often a variable difficult to measure experimentally. Therefore, the biased tow spacing is fully constrained by rearranging (2.27) in terms of the braid angle, volume fraction, and tow geometries.

$$s_b = \frac{2V_{f_t}(w_a t_a \cos\theta + w_b t_b)}{V_f(t_a + t_b)} - w_b \tag{2.28}$$

With the biased tow spacing constrained, the axial tow spacing can be derived from the overall RUC width. As shown in Eq. 2.22, the RUC width, *W*, can be expressed either as shown in Eq.2.29 or as follows,

$$W = 2(w_a + s_a) \tag{2.29}$$

Therefore, equating Eq. 2.29 and Eq. 2.22 constrains the axial tow spacing as follows,

$$s_a = \frac{V_{f_t}(w_a t_a \cos\theta + w_b t_b)}{V_f \cos\theta\,(t_a + t_b)} - w_a \tag{2.30}$$

Furthermore, in addition to constraining the geometry, it is also necessary to limit the maximum volume fraction to be physically feasible within context of the

true triaxial braid pattern. Therefore, the dimension *x** must satisfy the following relationship in order to ensure that the axial tows will fit between the bias tows.

$$x^* \geq 0.5s_a + w_a \tag{2.31}$$

Meanwhile, the x* term can be expressed as follows,

$$x^* = s_b \frac{\cos(90° - \theta)}{\cos(2\theta - 90°)} \tag{2.32}$$

Therefore, the lower bound of the biased tow spacing is expressed as follows,

$$s_b \geq \frac{2w_a \cos\theta + w_b}{4\cos\theta \dfrac{\cos(90° - \theta)}{\cos(2\theta - 90°)} - 1} \tag{2.33}$$

Substituting (2.33) into (2.27) constrains the upper bound of the volume fraction for the true triaxial braid.

$$V_f \leq \frac{2V_{f_t}(w_a t_a \cos\theta + w_b t_b)}{\left(\dfrac{2w_a \cos\theta + w_b}{4\cos\theta \dfrac{\cos(90° - \theta)}{\cos(2\theta - 90°)} - 1} + w_b\right)(t_a + t_b)} \tag{2.34}$$

If the axial tows and biased tows have identical geometries, (2.34) proves to be independent of braid angle and simplifies conveniently to the following form,

$$V_f \leq \frac{V_{f_t}}{2} \tag{2.35}$$

Optical micrographs have shown the tow volume fraction to be approximately 60%, therefore the maximum physically feasible volume fraction of the true triaxial braid is 30%. However, by modifying the arrangement of the biased tows, such that every other +θ tow lies flat along the bottom of the lamina with no undulations at all while the remainder of the +θ biased tows remain undulated as

they are shown, the minimum biased tow spacing is significantly reduced. Furthermore, by increasing the number of flat biased tows between each undulated biased tow in the previously described modification of the true triaxial braid, the biased tow spacing can be reduced to zero allowing significantly higher volume fractions to be produced. The extension of this microstructural characterization and the subsequent RUC definition for the three-step homogenization procedure to account for modifications with an arbitrary number of flat biased tows between each undulated biased tow is outside the scope of the present study. Future work will consider these implementations.

Once the microstructural geometry is fully constrained, the idealized microstructure of the RUC must be discretized into a series of subcell rows and columns consisting of through-the-thickness subcell stacks, which are homogenized in the 2nd homogenization step prior to the final in-plane homogenization step. A coarse subcell representation of the true triaxial braid microstructure consistent with the coarse discretization of the traditional triaxial braid is employed for this comparison of the two triaxial braid architectures. The volume fraction of the axial tow subcells is assumed to have a tow volume fraction of 60%. However, since a portion of the volume of the biased tow subcells shown in Fig. 2.15 is actually occupied by pure matrix, an equivalent effective volume fraction $\left(V_{f_\beta}^{*}\right)$ must be imposed for each of the biased tow subcells, where the index β denotes the subcell column number. Since the volume of the biased tows in subcell column 1 (β=1) is equal to that of the third subcell column (β=3) and likewise for the 2nd and 4th subcell columns, the

effective volume fraction for the biased tow subcells can be derived by only considering the first two columns of subcells. Due to symmetry between the subcell rows (denoted by the index γ), all biased tow subcells in a given subcell column have the same effective volume fraction. Therefore, let $V_{f_\beta}^*$ denote the equivalent effective volume fraction for the biased tow subcells in subcell column β. Then the volume fraction can be written as follows,

$$V_f = \frac{V_{f_t} w_a t_a + {V_{f_1}}^* w_a t_b + 2{V_{f_2}}^* s_a t_b}{(w_a + s_a)(t_a + t_b)} \tag{2.36}$$

Furthermore, the effective volume fraction of the first subcell column can easily be expressed in closed form,

$$V_{f_1}^* = V_{f_3}^* = \frac{2{w_b}^2 V_{f_t}}{w_a(w_b + s_b)} \tag{2.37}$$

Therefore, (2.36) is rearranged to yield the effective volume fraction of the second subcell column.

$$V_{f_2}^* = V_{f_4}^* \tag{2.38}$$

$$= \frac{V_f(w_a + s_a)(t_a + t_b) - V_{f_t} w_a t_a - \frac{2{w_b}^2 t_b V_{f_t}}{w_b + s_b}}{2 s_a t_b}$$

With the geometry fully constrained and the effective volume fraction of the biased tow subcells defined analytically, the final step of the microstructural characterization is the definition of the Euler rotation angles used to describe the undulations of the tows. Therefore, let the Euler rotation angle, ϕ, denote the angle of undulation of the tows along their respective axes. The angle

representing the tow twist was shown to be insignificant to the degree of machine precision for elastic property predictions and is, therefore, neglected for this study.

Therefore, let the undulation angles for the biased tow subcells be denoted as $\phi_{\pm\theta}^{(\alpha,\beta,\gamma)}$, where the index α denotes the order of the subcell layers within the subcell stacks in the through-thickness direction corresponding to the X_1 material coordinate direction, such that α =1 corresponds to the bottom surface of the lamina, and α =2 corresponds to the top surface of the lamina, while the indices β and γ denote the subcell columns and rows, respectively. Furthermore, it is recognized that the biased tows do not undulate as they cross over the axial tows. Therefore, the undulation angles for the biased tows in the first and third subcell columns are set to zero $\left(\phi_{+\theta}^{(1,1,1)} = \phi_{+\theta}^{(1,3,2)} = \phi_{-\theta}^{(2,1,2)} = \phi_{-\theta}^{(2,3,1)} = 0\right)$, and the undulation angles for the biased tows in the second and fourth subcell columns are defined as follows,

$$\phi_{+\theta}^{(2,2,1)} = \phi_{-\theta}^{(1,2,1)} = \phi_{+\theta}^{(2,4,2)} = \phi_{-\theta}^{(1,4,2)} = \tan^{-1}\left(2\frac{t_b}{s_a}\sin\theta\right) \tag{2.39}$$

$$\phi_{+\theta}^{(1,2,2)} = \phi_{-\theta}^{(2,2,2)} = \phi_{+\theta}^{(1,4,1)} = \phi_{-\theta}^{(2,4,1)} = -\tan^{-1}\left(2\frac{t_b}{s_a}\sin\theta\right) \tag{2.40}$$

Likewise, the undulations of all axial tows can be derived from considering only axial tow subcell (2, 1, 1).

$$\phi_a^{(2,1,1)} = \phi_a^{(2,3,2)} = \tan^{-1}\left(\frac{2t_b}{L}\right) \tag{2.41}$$

$$\phi_a^{(1,1,2)} = \phi_a^{(1,3,1)} = -\tan^{-1}\left(\frac{2t_b}{L}\right) \tag{2.42}$$

Therefore, this microstructural characterization of the true triaxial braid architecture constrains the microstructural geometry of the idealized RUC, derives the equivalent effective volume fractions for the biased tows subcells that account for the pure matrix regions within the coarse subcell discretization, and defines the undulation angles of all subcells within the RUC.

2.4 Fiber Tow Architecture

For all previous mentioned weaves and braids, the architecture of the fiber tows was not yet discussed and needs to be considered. For the following analysis, two types of fiber tows are considered: square and hexagonal packed. Each of these architectures can have various levels of refinement. These analyses only consider the simplest formulation of discretized subcells for both architectures. Fig. 2.16 shows a comparison between the two architecture configurations. These are both double periodic RUC. This RUC is assumed to be

infinitely long in the thickness direction. These are defined in terms of the tow volume fraction, $V_{f_{tow}}$, and their dimensions are shown below.

Square Packing:

$$H = \left\{ \sqrt{V_{f_{tow}}}, 1 - \sqrt{V_{f_{tow}}} \right\}$$
$$L = \left\{ \sqrt{V_{f_{tow}}}, 1 - \sqrt{V_{f_{tow}}} \right\} \tag{2.43}$$

Hexagonal Packing:

$$H = \left\{ \sqrt{\frac{\sqrt{3}V_{f_{tow}}}{2}}, \frac{1}{2} - \sqrt{\frac{\sqrt{3}V_{f_{tow}}}{2}}, \sqrt{\frac{\sqrt{3}V_{f_{tow}}}{2}}, \frac{1}{2} - \sqrt{\frac{\sqrt{3}V_{f_{tow}}}{2}}, \right\}$$
$$L = \left\{ \sqrt{\frac{\sqrt{3}V_{f_{tow}}}{2}}, \sqrt{\frac{3}{4}} - \sqrt{\frac{\sqrt{3}V_{f_{tow}}}{2}}, \sqrt{\frac{\sqrt{3}V_{f_{tow}}}{2}}, \sqrt{\frac{3}{4}} - \sqrt{\frac{\sqrt{3}V_{f_{tow}}}{2}} \right\} \tag{2.44}$$

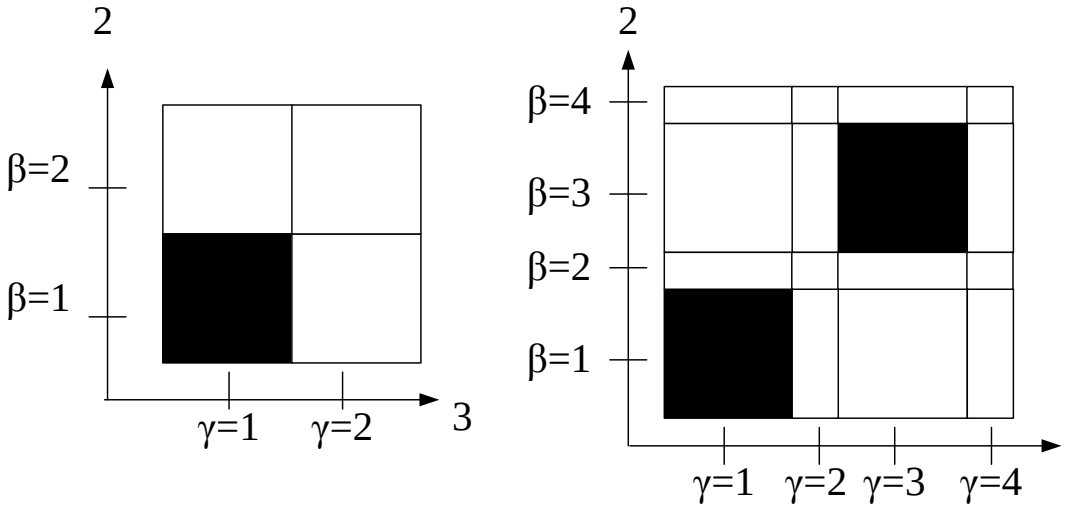

Fig. 2.16 Fiber Tow Architectures: Left is square packing, Right is hexagonal packing

2.5 Future Work

The research presented previously focused on simplistic and idealized architectures. Two possible paths of future research can originate from improving these limitations. Firstly, the assumptions of a rectangular tow and square fiber are suitable for first order approximations and served well for analysis (see Chapters 4-6). However, improving the architecture can result in higher fidelity analysis of local fields and possibly higher fidelity. For example, a fiber tow bundle is typically elliptical in cross-section shape and a higher order model could discretized as shown in Fig. 2.17. Improving the undulation assumptions will also help improve the out of plane predictions. Both of these improvements will cost computational efficiency and analysis time, therefore an optimal compromise is necessary.

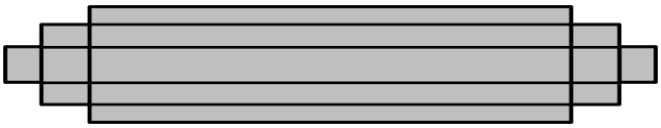

Fig. 2.17 Possible Elliptical Tow Discretization

Investigation the actual microstructure of a weave or braid reveals that there is significant variation in the actual microstructure. In addition, laminates can have ply level nesting in which successive plies are not planar and interact with each other (see Fig. 2.18). Developing a representative volume element to model the weave variations as well as the variations in the fiber tow architecture will improve the stochastic modeling capabilities for modeling woven and braided composites.

a) 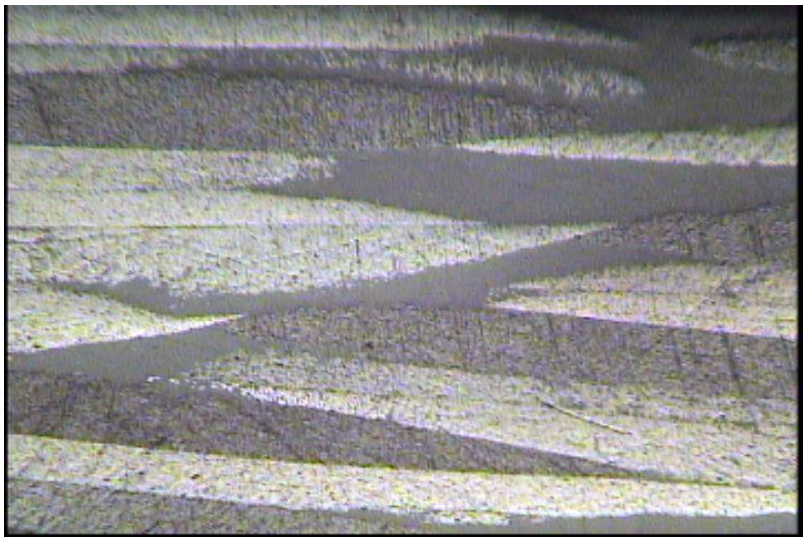

b) 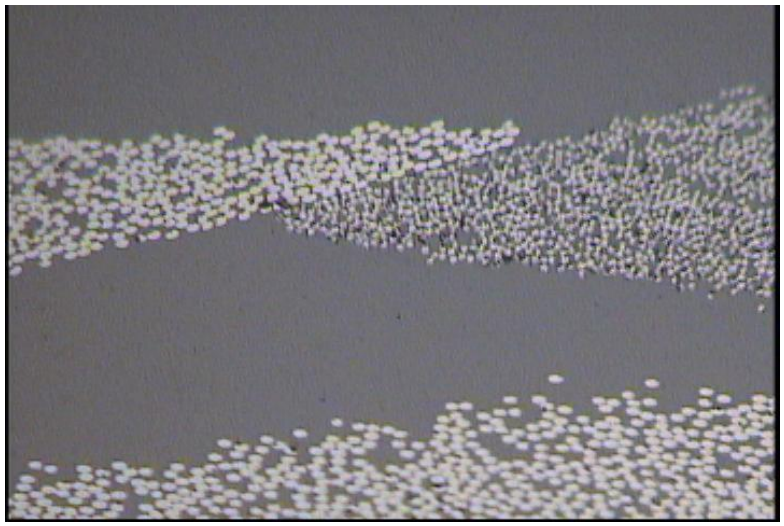

Fig. 2.18 Triaxial Braided Composites Microstructure From Optical Microscopy: a) 32x b) 200x

Chapter 3

3. MULTISCALE GENERALIZED METHOD OF CELLS

3.1 Background and Introduction

Multiscale modeling is in an effective technique used to capture effects of both geometry and material that spans several length scales. Multiscale modeling has been particularly useful for understanding the microstructure on the global or structural level response. In the past, it has been applied to both metals investigating crystalline microstructures and composites understanding constituent response and effects. Although nomenclature in the literature varies, typically a multiscale modeling analysis will follow contain at the very least a micro and global response. For example, in the case of woven composites, there are several relevant length scales for continuum mechanics. These scales, progressing from left to right in Fig. 3.1, are the microscale (constituent level; fiber, matrix, interface), the mesoscale (tow), the macroscale (repeating woven unit cell), and the global/structural scale. Traditionally, one traverses (transcends (moves right) or descends (moves left)) these scales via homogenization and localization techniques, respectively (Fig. 3.1 and 3.2a); where a homogenization technique provides the properties or response of a "structure" (higher level) given the properties or response of the structure's "constituents" (lower scale). Conversely, localization techniques provide the response of the constituents given the response of the structure. Fig. 3.2b illustrates the interaction of homogenization and localization techniques, in that during a multiscale analysis, a particular stage in the analysis procedure can function on both levels

simultaneously. For example, during the process of homogenizing the stages represented by X and Y to obtain properties for the stage represented by V, X and Y should be viewed as the constituent level while V is on the structure level. However, during the process of homogenizing V and W to obtain properties for U, V is now on the constituent level (as is W). Obviously, the ability to homogenize and localize accurately requires a sophisticated theory that relates the geometric and material characteristics of structure and constituent.

The Generalized Method of Cells (GMC) (Paley and Aboudi, Aboudi) is a micromechanics theory that allows for localization and homogenization between the micro and global length scales of a repeating unit cell. This theory is well suited for analyzed such things was a fiber embedded in matrix repeating unit cell of a laminated composite. GMC can be applied to any material composed of repeating unit cell architecture. GMC descretizes the materials periodic repeating unit cell in subcells and applies period boundary conditions at the edges and displacement/traction boundary conditions at the interface. Through the boundary conditions, a concentration matrix A, allows the determination of subcell strains in terms of globally applied strains. The concentration matrix effectively localizes global strains to local subcell strains. The global stress can then be determined by homogenizing the subcell stresses.

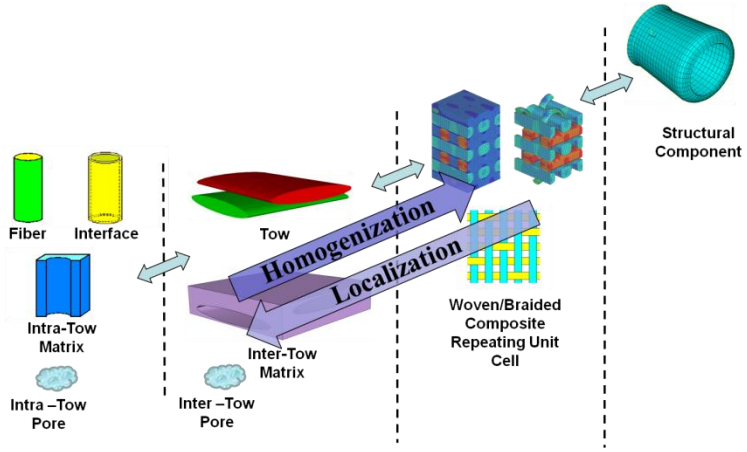

Fig. 3.1 Illustration of associated levels scales for woven/braided composite analysis.

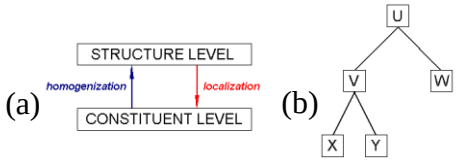

Fig. 3.2 (a) Homogenization provides the ability to determine structure level properties from constituent level properties while localization provides the ability to determine constituent level responses from structure level results. (b) Example tree diagram.

3.2 Reformulated Triply Periodic Generalized Method of Cells Theory

Typically micromechanics rely on empirical assumptions for the stress strain relationships between subcells. However, Generalized Method of Cells uses kinematic formulations to derive the stress strain conditions as opposed to empirical assumptions. For the generalized multiscale framework, both a doubly periodic and triply periodic formulation of GMC will be applied, the details of

these formulations can be found in [Aboudi] and Fig. 3.3 shows the typical discretized unit cell. A reformulation of the triply periodic Generalized Method of Cells micromechanics similar to that of [Bednarcyk] is shown here.

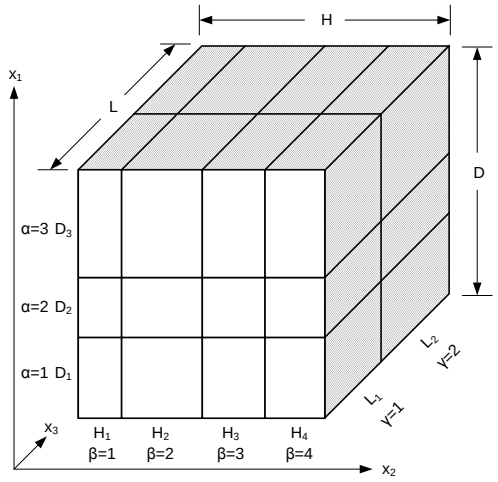

Fig. 3.3 Example of GMC Repeating Unit Cell consisting of $N_\alpha = 3, N_\beta = 4$ and $N_\gamma = 2$

The following kinematics are repeated from [Aboudi] as reference and critical to the understanding of multiscale model. As in the nature of GMC, a first order expansion of the displacement field about the distances from the center of each subcell, i.e. $\bar{x}_1^{(\alpha)}$, $\bar{x}_2^{(\beta)}$, and $\bar{x}_3^{(\gamma)}$, is assumed.

$$u_i^{(\alpha\beta\gamma)} = w_i^{(\alpha\beta\gamma)}(\boldsymbol{x}) + \bar{x}_1^{(\alpha)}\phi_i^{(\alpha\beta\gamma)} + \bar{x}_2^{(\beta)}\chi_i^{(\alpha\beta\gamma)} + \bar{x}_3^{(\gamma)}\psi_i^{(\alpha\beta\gamma)} \quad i = 1,2,3 \qquad (3.1)$$

Here, $w_i^{(\alpha\beta\gamma)}$ are the displacements at the center of the subcell and the variables $\phi_i^{(\alpha\beta\gamma)}$, $\chi_i^{(\alpha\beta\gamma)}$, and $\psi_i^{(\alpha\beta\gamma)}$ are microvariables for the first order expansion about the local coordinates $\bar{x}_1^{(\alpha)}$, $\bar{x}_2^{(\beta)}$, and $\bar{x}_3^{(\gamma)}$. The variable,

$\boldsymbol{x} = (x_1, x_2, x_3)$, is the center location of a subcell with respect to the fixed global coordinate system. By applying infinitesimal strain theory, the small strain tensor in a subcell can be related to the displacement field by

$$\varepsilon_{ij}^{(\alpha\beta\gamma)} = \frac{1}{2}\left(u_{i,j}^{(\alpha\beta\gamma)} + u_{j,i}^{(\alpha\beta\gamma)}\right) \quad i, j = 1,2,3 \tag{3. 2}$$

where $,_1^{(\alpha\beta\gamma)} = \frac{\partial}{\partial \overline{x}_1^{(\alpha)}}$, $,_2^{(\alpha\beta\gamma)} = \frac{\partial}{\partial \overline{x}_2^{(\beta)}}$, and $,_3^{(\alpha\beta\gamma)} = \frac{\partial}{\partial \overline{x}_3^{(\gamma)}}$.

Therefore, each strain component can then be computed in terms of the microvariables. Due to the first order expansion of the displacement field, this results in constant strains within the subcell, which are referred to as average strains.

$$\begin{aligned}
\overline{\varepsilon}_{11}^{(\alpha\beta\gamma)} &= \phi_1^{(\alpha\beta\gamma)} \\
\overline{\varepsilon}_{22}^{(\alpha\beta\gamma)} &= \chi_2^{(\alpha\beta\gamma)} \\
\overline{\varepsilon}_{33}^{(\alpha\beta\gamma)} &= \psi_3^{(\alpha\beta\gamma)} \\
\overline{\gamma}_{23}^{(\alpha\beta\gamma)} &= 2\overline{\varepsilon}_{23}^{(\alpha\beta\gamma)} = \chi_3^{(\alpha\beta\gamma)} + \psi_2^{(\alpha\beta\gamma)} \\
\overline{\gamma}_{13}^{(\alpha\beta\gamma)} &= 2\overline{\varepsilon}_{13}^{(\alpha\beta\gamma)} = \phi_3^{(\alpha\beta\gamma)} + \psi_1^{(\alpha\beta\gamma)} \\
\overline{\gamma}_{12}^{(\alpha\beta\gamma)} &= 2\overline{\varepsilon}_{12}^{(\alpha\beta\gamma)} = \phi_2^{(\alpha\beta\gamma)} + \chi_1^{(\alpha\beta\gamma)}
\end{aligned} \tag{3. 3}$$

Therefore the average strains in the composite RUC can be written as

$$\overline{\varepsilon}_{ij} = \frac{1}{d}\frac{1}{h}\frac{1}{l}\sum_{\alpha=1}^{n_\alpha}\sum_{\beta=1}^{n_\beta}\sum_{\gamma=1}^{n_\gamma}\overline{\varepsilon}_{ij}^{(\alpha\beta\gamma)} d_\alpha h_\beta l_\gamma \,. \tag{3. 4}$$

Assuming an elasto-plastic temperature dependent constitutive model, the stress-strain constitutive relationship can be used to determine the average subcell stresses, i.e.

$$\bar{\sigma}_{ij}^{(\alpha\beta\gamma)} = C_{ijkl}^{(\alpha\beta\gamma)}\left(\bar{\varepsilon}_{kl}^{(\alpha\beta\gamma)} - \bar{\varepsilon}_{kl}^{I(\alpha\beta\gamma)} - \bar{\varepsilon}_{kl}^{T(\alpha\beta\gamma)}\right) \tag{3. 5}$$

where $\bar{\sigma}_{ij}^{(\alpha\beta\gamma)}$ is the average stress tensor, $C_{ijkl}^{(\alpha\beta\gamma)}$ is the elastic stiffness tensor, $\bar{\varepsilon}_{kl}^{I(\alpha\beta\gamma)}$ is the inelastic strains, and $\bar{\varepsilon}_{kl}^{T(\alpha\beta\gamma)}$ is the thermal strains. The global average stress can be defined in the same manner as the strains by

$$\bar{\sigma}_{ij} = \frac{1}{d}\frac{1}{h}\frac{1}{l}\sum_{\alpha=1}^{n_\alpha}\sum_{\beta=1}^{n_\beta}\sum_{\gamma=1}^{n_\gamma}\bar{\sigma}_{ij}^{(\alpha\beta\gamma)} d_\alpha h_\beta l_\gamma \ . \tag{3. 6}$$

In order to solve for the microvariables, a set of interfacial boundary conditions for continuity of traction and displacement must be established. For each subcell, the neighboring subcell must have an equivalent set of displacement components at the interface. This leads to the following set of conditions,

$$\begin{aligned} u_i^{(\alpha\beta\gamma)}\Big|_{\bar{x}_1^\alpha = d_\alpha/2} &= u_i^{(\hat{\alpha}\beta\gamma)}\Big|_{\bar{x}_1^{\hat{\alpha}} = -d_{\hat{\alpha}}/2} \\ u_i^{(\alpha\beta\gamma)}\Big|_{\bar{x}_2^\beta = h_\beta/2} &= u_i^{(\alpha\hat{\beta}\gamma)}\Big|_{\bar{x}_2^{\hat{\beta}} = -h_{\hat{\beta}}/2} \\ u_i^{(\alpha\beta\gamma)}\Big|_{\bar{x}_3^\gamma = l_\gamma/2} &= u_i^{(\alpha\beta\hat{\gamma})}\Big|_{\bar{x}_3^{\hat{\gamma}} = -l_{\hat{\gamma}}/2} \end{aligned} \ . \tag{3. 7}$$

applied for $\alpha = 1,...,n_\alpha$, $\beta = 1,...,n_\beta$, and $\gamma = 1,...,n_\gamma$. In the GMC framework, these continuity conditions are applied in an average sense across the boundary yielding the following conditions.

$$\int_{-l_\gamma/2}^{l_\gamma/2}\int_{-h_\beta/2}^{h_\beta/2} u_i^{(\alpha\beta\gamma)}\Big|_{\bar{x}_1^\alpha = d_\alpha/2} d\bar{x}_2^\beta d\bar{x}_3^\gamma = \int_{-l_\gamma/2}^{l_\gamma/2}\int_{-h_\beta/2}^{h_\beta/2} u_i^{(\hat{\alpha}\beta\gamma)}\Big|_{\bar{x}_1^{\hat{\alpha}} = -d_{\hat{\alpha}}/2} d\bar{x}_2^\beta d\bar{x}_3^\gamma$$

$$\int_{-l_\gamma/2}^{l_\gamma/2}\int_{-d_\alpha/2}^{d_\alpha/2} u_i^{(\alpha\beta\gamma)}\Big|_{\bar{x}_2^\beta = h_\beta/2} d\bar{x}_1^\alpha d\bar{x}_3^\gamma = \int_{-l_\gamma/2}^{l_\gamma/2}\int_{-d_\alpha/2}^{d_\alpha/2} u_i^{(\alpha\hat{\beta}\gamma)}\Big|_{\bar{x}_2^{\hat{\beta}} = -h_{\hat{\beta}}/2} d\bar{x}_1^\alpha d\bar{x}_3^\gamma$$

$$\int_{-h_\beta/2}^{h_\beta/2}\int_{-d_\alpha/2}^{d_\alpha/2} u_i^{(\alpha\beta\gamma)}\Big|_{\bar{x}_3^\gamma = l_\gamma/2} d\bar{x}_1^\alpha d\bar{x}_2^\beta = \int_{-h_\beta/2}^{h_\beta/2}\int_{-d_\alpha/2}^{d_\alpha/2} u_i^{(\alpha\beta\hat{\gamma})}\Big|_{\bar{x}_3^{\hat{\gamma}} = -l_{\hat{\gamma}}/2} d\bar{x}_1^\alpha d\bar{x}_2^\beta \tag{3. 8}$$

Substitution of the displacement field expansion into the above equation yields a set of equations in terms of the microvariables.

$$w_i^{(\alpha\beta\gamma)} + \frac{d_\alpha}{2}\phi_i^{(\alpha\beta\gamma)} = w_i^{(\hat{\alpha}\beta\gamma)} - \frac{d_{\hat{\alpha}}}{2}\phi_i^{(\hat{\alpha}\beta\gamma)}$$

$$w_i^{(\alpha\beta\gamma)} + \frac{h_\beta}{2}\chi_i^{(\alpha\beta\gamma)} = w_i^{(\alpha\hat{\beta}\gamma)} - \frac{h_{\hat{\beta}}}{2}\chi_i^{(\alpha\hat{\beta}\gamma)} \tag{3. 9}$$

$$w_i^{(\alpha\beta\gamma)} + \frac{l_\gamma}{2}\psi_i^{(\alpha\beta\gamma)} = w_i^{(\alpha\beta\hat{\gamma})} - \frac{l_{\hat{\gamma}}}{2}\psi_i^{(\alpha\beta\hat{\gamma})}$$

In the above equation, all the field variables, w_i, are evaluated at the center of the subcell, however it is necessary to evaluate these at a common location, the interface. In the global coordinate system, the interface is defined as

$$x_1^I = \left(x_1^{(\alpha)} + \frac{d_\alpha}{2}, x_2, x_3\right)$$

$$x_1^I = \left(x_1^{(\hat{\alpha})} - \frac{d_{\hat{\alpha}}}{2}, x_2, x_3\right) \tag{3. 10}$$

$$x_2^I = \left(x_1, x_2^{(\beta)} + \frac{h_\beta}{2}, x_3\right)$$

$$x_2^I = \left(x_1, x_2^{(\hat{\beta})} - \frac{h_{\hat{\beta}}}{2}, x_3\right)$$

$$x_3^I = \left(x_1, x_2, x_3^{(\gamma)} + \frac{l_\gamma}{2} \right)$$
$$x_3^I = \left(x_1, x_2, x_3^{(\hat{\gamma})} - \frac{l_{\hat{\gamma}}}{2} \right)$$

To evaluate the field variables ($w_i^{(\alpha\beta\gamma)}$) at the interface, a first order Taylor expansion about the common interface is used. The continuity conditions then become,

$$\begin{aligned}
w_i^{(\alpha\beta\gamma)} - \frac{d_\alpha}{2}\left(\frac{\partial w_i^{(\alpha\beta\gamma)}}{\partial x_1} - \phi_i^{(\alpha\beta\gamma)} \right) &= w_i^{(\hat{\alpha}\beta\gamma)} + \frac{d_{\hat{\alpha}}}{2}\left(\frac{\partial w_i^{(\hat{\alpha}\beta\gamma)}}{\partial x_1} - \phi_i^{(\hat{\alpha}\beta\gamma)} \right) \\
w_i^{(\alpha\beta\gamma)} - \frac{h_\beta}{2}\left(\frac{\partial w_i^{(\alpha\beta\gamma)}}{\partial x_2} - \chi_i^{(\alpha\beta\gamma)} \right) &= w_i^{(\alpha\hat{\beta}\gamma)} + \frac{h_{\hat{\beta}}}{2}\left(\frac{\partial w_i^{(\alpha\hat{\beta}\gamma)}}{\partial x_2} - \chi_i^{(\alpha\hat{\beta}\gamma)} \right) \\
w_i^{(\alpha\beta\gamma)} - \frac{l_\gamma}{2}\left(\frac{\partial w_i^{(\alpha\beta\gamma)}}{\partial x_3} - \psi_i^{(\alpha\beta\gamma)} \right) &= w_i^{(\alpha\beta\hat{\gamma})} + \frac{l_{\hat{\gamma}}}{2}\left(\frac{\partial w_i^{(\alpha\beta\hat{\gamma})}}{\partial x_3} - \psi_i^{(\alpha\beta\hat{\gamma})} \right)
\end{aligned} \tag{3. 11}$$

where each field variable and field variable derivative is evaluated at the interface. Next, let the functions F , G , and H be defined as

$$\begin{aligned}
F_i^{(\alpha)} &= w_i^{(\alpha\beta\gamma)}\Big|_{\mathbf{x}=x_1^I} + f_i^{(\alpha)} - w_i^{(\hat{\alpha}\beta\gamma)}\Big|_{\mathbf{x}=x_1^I} - f_i^{(\hat{\alpha})} \\
G_i^{(\beta)} &= w_i^{(\alpha\beta\gamma)}\Big|_{\mathbf{x}=x_2^I} + g_i^{(\beta)} - w_i^{(\alpha\hat{\beta}\gamma)}\Big|_{\mathbf{x}=x_2^I} - g_i^{(\hat{\beta})} \\
H_i^{(\gamma)} &= w_i^{(\alpha\beta\gamma)}\Big|_{\mathbf{x}=x_3^I} + h_i^{(\hat{\gamma})} - w_i^{(\alpha\beta\hat{\gamma})}\Big|_{\mathbf{x}=x_3^I} - h_i^{(\hat{\gamma})}
\end{aligned} \tag{3. 12}$$

where,

$$f_i^{(\alpha)} = -\frac{d_\alpha}{2}\left(\left.\frac{\partial w_i^{(\alpha\beta\gamma)}}{\partial x_1}\right|_{\mathbf{x}=x_1^I} - \phi_i^{(\alpha\beta\gamma)} \right)$$
$$g_i^{(\beta)} = -\frac{h_\beta}{2}\left(\left.\frac{\partial w_i^{(\alpha\beta\gamma)}}{\partial x_2}\right|_{\mathbf{x}=x_2^I} - \chi_i^{(\alpha\beta\gamma)} \right) \qquad (3.\ 13)$$
$$h_i^{(\gamma)} = -\frac{l_\gamma}{2}\left(\left.\frac{\partial w_i^{(\alpha\beta\gamma)}}{\partial x_3}\right|_{\mathbf{x}=x_3^I} - \psi_i^{(\alpha\beta\gamma)} \right)$$

The three continuity equations can then be rewritten as

$$\begin{aligned} F_i^{(\alpha)} &= 0 \quad \alpha = 1,...,n_\alpha \\ G_i^{(\beta)} &= 0 \quad \beta = 1,...,n_\beta \\ H_i^{(\gamma)} &= 0 \quad \gamma = 1,...,n_\gamma \end{aligned} \qquad (3.\ 14)$$

and subsequently these can be written as a summation series

$$\sum_{\alpha=1}^{n_\alpha} F_i^{(\alpha)} = 0, \quad \sum_{\beta=1}^{n_\beta} G_i^{(\beta)} = 0, \quad \sum_{\gamma=1}^{n_\gamma} H_i^{(\gamma)} = 0. \qquad (3.\ 15)$$

These summations lead to the conclusion that

$$\sum_{\alpha=1}^{n_\alpha} f_i^{(\alpha)} = 0, \quad \sum_{\beta=1}^{n_\beta} g_i^{(\beta)} = 0, \quad \sum_{\gamma=1}^{n_\gamma} h_i^{(\gamma)} = 0. \qquad (3.\ 16)$$

Under first order theory, in which the second derivative of $w_i^{(\alpha\beta\gamma)}$ is zero,

$$\frac{\partial f_i^{(\alpha)}}{\partial x_1} = 0, \quad \frac{\partial g_i^{(\beta)}}{\partial x_2} = 0, \quad \frac{\partial h_i^{(\gamma)}}{\partial x_3} = 0. \qquad (3.\ 17)$$

In addition, differentiation of the continuity equations with respect to x_1, x_2, and x_3 results in

$$\frac{\partial w_i^{(\alpha\beta\gamma)}}{\partial x_1} = \frac{\partial w_i^{(\hat{\alpha}\beta\gamma)}}{\partial x_1} \qquad (3.\ 18)$$
$$\frac{\partial w_i^{(\alpha\beta\gamma)}}{\partial x_2} = \frac{\partial w_i^{(\alpha\hat{\beta}\gamma)}}{\partial x_2}$$
$$\frac{\partial w_i^{(\alpha\beta\gamma)}}{\partial x_3} = \frac{\partial w_i^{(\alpha\beta\hat{\gamma})}}{\partial x_3}$$

which can be satisfied by assuming that common displacement functions, w_i, exist such that

$$w_i^{(\alpha\beta\gamma)} = w_i \qquad (3.\ 19)$$

and therefore

$$w_i^{(\alpha\beta\gamma)}\Big|_{\mathbf{x}=x_j^I} = w_i. \qquad (3.\ 20)$$

Using this assumption and Eq. 3.16 a set of continuum relations can be derived

$$\sum_{\alpha=1}^{n_\alpha} d_\alpha \phi_i^{(\alpha\beta\gamma)} = d\,\frac{\partial w_i}{\partial x_1} \qquad (3.\ 21)$$
$$\sum_{\beta=1}^{n_\beta} h_\beta \chi_i^{(\alpha\beta\gamma)} = h\,\frac{\partial w_i}{\partial x_2}$$
$$\sum_{\gamma=1}^{n_\gamma} l_\gamma \psi_i^{(\alpha\beta\gamma)} = l\,\frac{\partial w_i}{\partial x_3}.$$

The previously defined small strain tensor can be written in terms of the common displacement functions,

$$\bar{\varepsilon}_{ij} = \frac{1}{2}\left(w_{i,j} + w_{j,i}\right). \qquad (3.\ 22)$$

Substitution of this into the set of continuum relations yields,

$$\sum_{\alpha=1}^{n_\alpha} d_\alpha \bar{\varepsilon}_{11}^{(\alpha\beta\gamma)} = d\bar{\varepsilon}_{11}, \qquad \beta = 1,...,n_\beta, \gamma = 1,...,n_\gamma$$
$$\sum_{\beta=1}^{n_\beta} h_\beta \bar{\varepsilon}_{22}^{(\alpha\beta\gamma)} = h\bar{\varepsilon}_{22}, \qquad \alpha = 1,...,n_\alpha, \gamma = 1,...,n_\gamma \tag{3. 23}$$
$$\sum_{\gamma=1}^{n_\gamma} l_\gamma \bar{\varepsilon}_{33}^{(\alpha\beta\gamma)} = l\bar{\varepsilon}_{33}, \qquad \alpha = 1,...,n_\alpha, \beta = 1,...,n_\beta.$$

Combining Eq. 3.21a multiplied by h_β and summed over β for $i = 1$ to Eq. 3.21b multiplied by d_α and summed over α for $i = 2$ yields,

$$\sum_{\alpha=1}^{n_\alpha}\sum_{\beta=1}^{n_\beta} d_\alpha h_\beta \left(\phi_2^{(\alpha\beta\gamma)} + \chi_1^{(\alpha\beta\gamma)}\right) = dh\left(\frac{\partial w_1}{\partial x_2} + \frac{\partial w_2}{\partial x_1}\right), \qquad \gamma = 1,...,n_\gamma \tag{3. 24}$$
$$\sum_{\alpha=1}^{n_\alpha}\sum_{\beta=1}^{n_\beta} d_\alpha h_\beta \bar{\varepsilon}_{12}^{(\alpha\beta\gamma)} = dh\bar{\varepsilon}_{12}, \qquad \gamma = 1,...,n_\gamma.$$

Similar operations yields,

$$\sum_{\beta=1}^{n_\beta}\sum_{\gamma=1}^{n_\gamma} h_\beta l_\gamma \bar{\varepsilon}_{23}^{(\alpha\beta\gamma)} = hl\bar{\varepsilon}_{23}, \qquad \alpha = 1,...,n_\alpha$$
$$\sum_{\alpha=1}^{n_\alpha}\sum_{\gamma=1}^{n_\gamma} d_\alpha l_\gamma \bar{\varepsilon}_{13}^{(\alpha\beta\gamma)} = dl\bar{\varepsilon}_{13}, \qquad \beta = 1,...,n_\beta \tag{3. 25}$$

These global-local strain relationships can be cast into matrix form as

$$A_G \varepsilon_s = J\bar{\varepsilon} \tag{3. 26}$$

where

$$\bar{\varepsilon} = \left(\bar{\varepsilon}_{11}, \bar{\varepsilon}_{22}, \bar{\varepsilon}_{33}, 2\bar{\varepsilon}_{23}, 2\bar{\varepsilon}_{13}, 2\bar{\varepsilon}_{12}\right) \tag{3. 27}$$

and

$$\varepsilon_s = \left(\bar{\varepsilon}^{(111)}, ..., \bar{\varepsilon}^{(n_\alpha n_\beta n_\gamma)}\right). \tag{3. 28}$$

The interfacial traction continuity conditions, like the displacement continuity conditions, are also imposed on an average sense. The conditions can be expressed as,

$$\begin{aligned}\bar{\sigma}_{1i}^{(\alpha\beta\gamma)} &= \bar{\sigma}_{1i}^{(\hat{\alpha}\beta\gamma)} \\ \bar{\sigma}_{2i}^{(\alpha\beta\gamma)} &= \bar{\sigma}_{2i}^{(\alpha\hat{\beta}\gamma)} \\ \bar{\sigma}_{3i}^{(\alpha\beta\gamma)} &= \bar{\sigma}_{3i}^{(\alpha\beta\hat{\gamma})}\end{aligned} \tag{3. 29}$$

for $i, j, k = 1, 2, 3$ and $\alpha = 1, ...n_\alpha$, $\beta = 1, ..., n_\beta$, and $\gamma = 1, ..., n_\gamma$. However, only a subset of these equations are independent and they can expressed as,

$$\begin{aligned}
&\bar{\sigma}_{11}^{(\alpha\beta\gamma)} = \bar{\sigma}_{11}^{(\hat{\alpha}\beta\gamma)} && \alpha = 1, ..., n_\alpha - 1, \beta = 1, ..., n_\beta, \gamma = 1, ..., n_\gamma \\
&\bar{\sigma}_{22}^{(\alpha\beta\gamma)} = \bar{\sigma}_{22}^{(\alpha\hat{\beta}\gamma)} && \alpha = 1, ..., n_\alpha, \beta = 1, ..., n_\beta - 1, \gamma = 1, ..., n_\gamma \\
&\bar{\sigma}_{33}^{(\alpha\beta\gamma)} = \bar{\sigma}_{33}^{(\alpha\beta\hat{\gamma})} && \alpha = 1, ..., n_\alpha, \beta = 1, ..., n_\beta, \gamma = 1, ..., n_\gamma - 1 \\
&\bar{\sigma}_{23}^{(\alpha\beta\gamma)} = \bar{\sigma}_{23}^{(\alpha\hat{\beta}\gamma)} && \alpha = 1, ..., n_\alpha, \beta = 1, ..., n_\beta - 1, \gamma = 1, ..., n_\gamma \\
&\bar{\sigma}_{32}^{(\alpha\beta\gamma)} = \bar{\sigma}_{32}^{(\alpha\beta\hat{\gamma})} && \alpha = 1, ..., n_\alpha, \beta = n_\beta, \gamma = 1, ..., n_\gamma - 1 \\
&\bar{\sigma}_{13}^{(\alpha\beta\gamma)} = \bar{\sigma}_{13}^{(\hat{\alpha}\beta\gamma)} && \alpha = 1, ..., n_\alpha - 1, \beta = 1, ..., n_\beta, \gamma = 1, ..., n_\gamma \\
&\bar{\sigma}_{31}^{(\alpha\beta\gamma)} = \bar{\sigma}_{31}^{(\alpha\beta\hat{\gamma})} && \alpha = n_\alpha, \beta = 1, ..., n_\beta, \gamma = 1, ..., n_\gamma - 1 \\
&\bar{\sigma}_{12}^{(\alpha\beta\gamma)} = \bar{\sigma}_{12}^{(\hat{\alpha}\beta\gamma)} && \alpha = 1, ..., n_\alpha - 1, \beta = 1, ..., n_\beta, \gamma = n_\gamma \\
&\bar{\sigma}_{21}^{(\alpha\beta\gamma)} = \bar{\sigma}_{21}^{(\alpha\hat{\beta}\gamma)} && \alpha = n_\alpha - 1, \beta = 1, ..., n_\beta - 1, \gamma = n_\gamma.
\end{aligned} \tag{3. 30}$$

By rewriting the subcell stresses in terms of the subcell strains and the constitutive law, these conditions can be cast into matrix form as

$$A_M \left(\varepsilon_s - \varepsilon_s^I - \varepsilon_s^T \right) = 0. \tag{3. 31}$$

Combining the interfacial displacement and traction conditions yields

$$\tilde{A}\varepsilon_s - \tilde{D}\left(\varepsilon_s^I + \varepsilon_s^T \right) = K\varepsilon \tag{3. 32}$$

where

$$\tilde{A}=\begin{bmatrix} A_M \\ A_G \end{bmatrix}, \quad \tilde{D}=\begin{bmatrix} A_M \\ 0 \end{bmatrix}, \quad K=\begin{bmatrix} 0 \\ J \end{bmatrix}. \tag{3. 33}$$

Solving for the local subcell strains results in the final micromechanical relationship,

$$\varepsilon_s = A\bar{\varepsilon} + D\left(\varepsilon_s^I + \varepsilon_s^T\right) \tag{3. 34}$$

where

$$A=\tilde{A}^{-1}K, \quad D=\tilde{A}^{-1}\tilde{D}. \tag{3. 35}$$

These concentration matrices can be further decomposed into submatrices resulting in

$$A=\begin{bmatrix} A^{(111)} \\ \vdots \\ A^{(n_\alpha n_\beta n_\gamma)} \end{bmatrix}, \quad D=\begin{bmatrix} D^{(111)} \\ \vdots \\ D^{(n_\alpha n_\beta n_\gamma)} \end{bmatrix}. \tag{3. 36}$$

and leading to a relationship between the local subcell strains and globally applied strains,

$$\varepsilon^{(\alpha\beta\gamma)} = A^{(\alpha\beta\gamma)}\bar{\varepsilon} + D^{(\alpha\beta\gamma)}\left(\varepsilon_s^I + \varepsilon_s^T\right). \tag{3. 37}$$

Lastly, the local stress in a subcell can be computed by

$$\sigma^{(\alpha\beta\gamma)} = C^{(\alpha\beta\gamma)}\left(A^{(\alpha\beta\gamma)}\bar{\varepsilon} + D^{(\alpha\beta\gamma)}\left(\varepsilon_s^I + \varepsilon_s^T\right) - \left(\varepsilon^{(\alpha\beta\gamma)I} + \varepsilon^{(\alpha\beta\gamma)T}\right)\right) \tag{3. 38}$$

and the effective composite stress can be computed as

$$\bar{\sigma} = C^*\left(\bar{\varepsilon} - \bar{\varepsilon}^I\right) \tag{3. 39}$$

where

$$C^{*} = \frac{1}{dhl} \sum_{\alpha=1}^{n_\alpha} \sum_{\beta=1}^{n_\beta} \sum_{\gamma=1}^{n_\gamma} d_\alpha h_\beta l_\gamma C^{(\alpha\beta\gamma)} A^{(\alpha\beta\gamma)} \tag{3. 40}$$

and

$$\bar{\varepsilon}^{I} = -\frac{C^{*-1}}{dhl} \sum_{\alpha=1}^{n_\alpha} \sum_{\beta=1}^{n_\beta} \sum_{\gamma=1}^{n_\gamma} d_\alpha h_\beta l_\gamma C^{(\alpha\beta\gamma)} \left(D^{(\alpha\beta\gamma)} \varepsilon_s^I - \bar{\varepsilon}^{I(\alpha\beta\gamma)} \right). \tag{3. 41}$$

The total unknowns using the traditional solution type is $6n_\alpha n_\beta n_\gamma$, however Bednarcyk proposed a reformulated methodology to reduce the number of unknowns to $n_\alpha n_\beta + n_\beta n_\gamma + n_\alpha n_\gamma + n_\alpha + n_\beta + n_\gamma$. The author has derived variation of Bednarcyk's reformulation more akin to the original style of GMC and useful for the multiscale framework, it is shown here.

The key fundament concept in the reformulation is that the interfacial traction conditions results in reduced number of local subcell stress unknowns. These are expressed in the following equations:

$$
\begin{aligned}
&\sigma_{11}^{(1\beta\gamma)} = \sigma_{11}^{(2\beta\gamma)} = \ldots = \sigma_{11}^{(N_\alpha\beta\gamma)} = T_1^{(\beta\gamma)} \\
&\sigma_{22}^{(\alpha 1\gamma)} = \sigma_{22}^{(\alpha 2\gamma)} = \ldots = \sigma_{22}^{(\alpha N_\beta\gamma)} = T_2^{(\alpha\gamma)} \\
&\sigma_{33}^{(\alpha\beta\gamma)} = \sigma_{33}^{(\alpha\beta 2)} = \ldots = \sigma_{33}^{(\alpha\beta N_\gamma)} = T_3^{(\alpha\beta)} \\
&\sigma_{23}^{(\alpha 1\gamma)} = \sigma_{23}^{(\alpha 2\gamma)} = \ldots = \sigma_{23}^{(\alpha N_\beta\gamma)} = T_{23}^{(\alpha\gamma)} \\
&\sigma_{32}^{(\alpha\beta 1)} = \sigma_{32}^{(\alpha\beta 2)} = \ldots = \sigma_{32}^{(\alpha\beta N_\gamma)} = T_{32}^{(\alpha\beta)} \\
&\sigma_{23}^{(\alpha\beta\gamma)} = \sigma_{32}^{(\alpha\beta\gamma)} \therefore T_{23}^{(\alpha\beta)} = T_{32}^{(\alpha\gamma)} = T_4^{(\alpha)} = \sigma_{23}^{(\alpha\beta\gamma)} \\
&\sigma_{13}^{(1\beta\gamma)} = \sigma_{13}^{(2\beta\gamma)} = \ldots = \sigma_{13}^{(N_\alpha\beta\gamma)} = T_{13}^{(\beta\gamma)} \\
&\sigma_{31}^{(\alpha\beta 1)} = \sigma_{31}^{(\alpha\beta 2)} = \ldots = \sigma_{31}^{(\alpha\beta N_\gamma)} = T_{31}^{(\alpha\beta)} \\
&\sigma_{13}^{(\alpha\beta\gamma)} = \sigma_{31}^{(\alpha\beta\gamma)} \therefore T_{13}^{(\beta\gamma)} = T_{31}^{(\alpha\beta)} = T_5^{(\beta)} = \sigma_{13}^{(\alpha\beta\gamma)} \\
&\sigma_{12}^{(1\beta\gamma)} = \sigma_{12}^{(2\beta\gamma)} = \ldots = \sigma_{12}^{(N_\alpha\beta\gamma)} = T_{12}^{(\beta\gamma)} \\
&\sigma_{21}^{(\alpha 1\gamma)} = \sigma_{21}^{(\alpha 2\gamma)} = \ldots = \sigma_{21}^{(\alpha N_\beta\gamma)} = T_{21}^{(\alpha\gamma)} \\
&\sigma_{12}^{(\alpha\beta\gamma)} = \sigma_{21}^{(\alpha\beta\gamma)} \therefore T_{12}^{(\beta\gamma)} = T_{21}^{(\alpha\gamma)} = T_6^{(\gamma)} = \sigma_{12}^{(\alpha\beta\gamma)}
\end{aligned}
\tag{3. 42}
$$

To take advantage of this inherent simplification, the interfacial displacement continuities are rewritten using the compliance form of the constitutive relationship. The compliance form of the stress-strain relationship in a given subcell can be written as,

$$
\bar{\varepsilon}_{ij}^{(\alpha\beta\gamma)} = S_{ijkl}\bar{\sigma}_{kl} + \bar{\varepsilon}_{ij}^{I(\alpha\beta\gamma)}. \tag{3. 43}
$$

Therefore, the modified displacement continuity equations become

$$\sum_{\alpha=1}^{n_\alpha} d_\alpha \left(S_{11\,jk}\sigma_{jk}^{(\alpha\beta\gamma)} + \varepsilon_{11}^{I(\alpha\beta\gamma)} \right) = d\varepsilon_{11}, \qquad \beta = 1,...,N_\beta, \gamma = 1,...,N_\gamma$$

$$\sum_{\beta=1}^{n_\beta} h_\beta \left(S_{22\,jk}\sigma_{jk}^{(\alpha\beta\gamma)} + \varepsilon_{22}^{I(\alpha\beta\gamma)} \right) = h\varepsilon_{22}, \qquad \alpha = 1,...,N_\alpha, \gamma = 1,...,N_\gamma$$

$$\sum_{\gamma=1}^{n_\gamma} l_\gamma \left(S_{33\,jk}\sigma_{jk}^{(\alpha\beta\gamma)} + \varepsilon_{33}^{I(\alpha\beta\gamma)} \right) = l\varepsilon_{33}, \qquad \alpha = 1,...,N_\alpha, \beta = 1,...,N_\beta$$

$$\sum_{\beta=1}^{n_\beta}\sum_{\gamma=1}^{n_\gamma} h_\beta l_\gamma \left(S_{23\,jk}\sigma_{jk}^{(\alpha\beta\gamma)} + \varepsilon_{23}^{I(\alpha\beta\gamma)} \right) = hl\varepsilon_{23}, \qquad \alpha = 1,...,N_\alpha$$

$$\sum_{\alpha=1}^{n_\alpha}\sum_{\gamma=1}^{n_\gamma} d_\alpha l_\gamma \left(S_{13\,jk}\sigma_{jk}^{(\alpha\beta\gamma)} + \varepsilon_{13}^{I(\alpha\beta\gamma)} \right) = dl\varepsilon_{13}, \qquad \beta = 1,...,N_\beta$$

$$\sum_{\alpha=1}^{n_\alpha}\sum_{\beta=1}^{n_\beta} d_\alpha h_\beta \left(S_{12\,jk}\sigma_{jk}^{(\alpha\beta\gamma)} + \varepsilon_{12}^{I(\alpha\beta\gamma)} \right) = dh\varepsilon_{12}, \qquad \gamma = 1,...,N_\gamma$$

(3. 44)

where S_{ijkl} is the 4th order compliance tensor and summation is implied for $i, j = 1,2,3$. Substitution of Eq. 3.42 into the above results in

$$\sum_{\alpha=1}^{n_\alpha} d_\alpha S_{1k}^{(\alpha\beta\gamma)} T_k^{(\alpha\beta\gamma)} = d\varepsilon_{11} - \sum_{\alpha=1}^{n_\alpha} d_\alpha \varepsilon_{11}^{I(\alpha\beta\gamma)}, \qquad \beta = 1,...,n_\beta, \gamma = 1,...,n_\gamma$$

$$\sum_{\beta=1}^{n_\beta} h_\beta S_{2k}^{(\alpha\beta\gamma)} T_k^{(\alpha\beta\gamma)} = h\varepsilon_{22} - \sum_{\beta=1}^{n_\beta} h_\beta \varepsilon_{22}^{I(\alpha\beta\gamma)}, \qquad \alpha = 1,...,n_\alpha, \gamma = 1,...,n_\gamma$$

$$\sum_{\gamma=1}^{n_\gamma} l_\gamma S_{3k}^{(\alpha\beta\gamma)} T_k^{(\alpha\beta\gamma)} = l\varepsilon_{33} - \sum_{\gamma=1}^{n_\gamma} l_\gamma \varepsilon_{33}^{I(\alpha\beta\gamma)}, \qquad \alpha = 1,...,n_\alpha, \beta = 1,...,n_\beta$$

$$\sum_{\beta=1}^{n_\beta}\sum_{\gamma=1}^{n_\gamma} h_\beta l_\gamma S_{4k}^{(\alpha\beta\gamma)} T_k^{(\alpha\beta\gamma)} = hl\varepsilon_{23} - \sum_{\beta=1}^{n_\beta}\sum_{\gamma=1}^{n_\gamma} h_\beta l_\gamma \varepsilon_{23}^{I(\alpha\beta\gamma)}, \qquad \alpha = 1,...,n_\alpha$$

$$\sum_{\alpha=1}^{n_\alpha}\sum_{\gamma=1}^{n_\gamma} d_\alpha l_\gamma S_{5k}^{(\alpha\beta\gamma)} T_k^{(\alpha\beta\gamma)} = dl\varepsilon_{13} - \sum_{\alpha=1}^{n_\alpha}\sum_{\gamma=1}^{n_\gamma} d_\alpha l_\gamma \varepsilon_{13}^{I(\alpha\beta\gamma)}, \qquad \beta = 1,...,n_\beta$$

$$\sum_{\alpha=1}^{n_\alpha}\sum_{\beta=1}^{n_\beta} d_\alpha h_\beta S_{6k}^{(\alpha\beta\gamma)} T_k^{(\alpha\beta\gamma)} = dh\varepsilon_{12} - \sum_{\alpha=1}^{n_\alpha}\sum_{\beta=1}^{n_\beta} d_\alpha h_\beta \varepsilon_{12}^{I(\alpha\beta\gamma)}, \qquad \gamma = 1,...,n_\gamma$$

(3. 45)

where $S_{ij}^{(\alpha\beta\gamma)}$ is the compliance matrix in Voigt notation and $T_k^{(\alpha\beta\gamma)} = \left(T_1^{(\beta\gamma)}, T_2^{(\alpha\gamma)}, T_3^{(\alpha\beta)}, T_4^{(\alpha)}, T_5^{(\beta)}, T_6^{(\gamma)} \right)$ and summation is implied over

$k = 1, 2, 3, 4, 5, 6$. This set of equations contains both the continuity of traction and displacement eliminating the need for two sets of continuity equations. In matrix form the reformulated relationship is,

$$\tilde{A}\bar{T}_s = J\bar{\varepsilon} + \tilde{D}\bar{\varepsilon}_s^I \tag{3. 46}$$

where,

$$\bar{T}_s = \left\{ T_1^{(\beta\gamma)}, ..., T_1^{(n_\beta n_\gamma)}, T_2^{(\alpha\gamma)}, ..., T_2^{(n_\alpha n_\gamma)}, T_3^{(\alpha\beta)}, ..., T_3^{(n_\alpha n_\beta)}, \right. \\ \left. T_4^{(\alpha)}, ..., T_4^{(n_\alpha)}, T_5^{(\beta)}, ..., T_5^{(n_\beta)}, T_6^{(\gamma)}, ..., T_6^{(n_\gamma)} \right\}. \tag{3. 47}$$

It is important to note that the matrices $\tilde{A}$, $\tilde{D}$, and J are not equivalent to the previously derived matrices, but the nomenclature is return because their symbolic meaning is equivalent. The final relationship between subcell stresses and global stress is

$$\bar{T}_s = \bar{A}J\bar{\varepsilon} + \bar{A}\tilde{D}\bar{\varepsilon}_s^I \tag{3. 48}$$

where,

$$\bar{A} = \tilde{A}^{-1}. \tag{3. 49}$$

The compliance constitutive law at the subcell level can be written in terms of the independent unknown subcell stress components which is of the form

$$
\begin{aligned}
\varepsilon_{11}^{(\alpha\beta\gamma)} &= S_{11}^{(\alpha\beta\gamma)}T_1^{(\beta\gamma)} + S_{12}^{(\alpha\beta\gamma)}T_2^{(\alpha\gamma)} + S_{13}^{(\alpha\beta\gamma)}T_3^{(\alpha\beta)} + \\
&\qquad S_{14}^{(\alpha\beta\gamma)}T_4^{(\alpha)} + S_{15}^{(\alpha\beta\gamma)}T_5^{(\beta)} + S_{16}^{(\alpha\beta\gamma)}T_6^{(\gamma)} - \varepsilon_{11}^{I(\alpha\beta\gamma)} \\
\varepsilon_{22}^{(\alpha\beta\gamma)} &= S_{21}^{(\alpha\beta\gamma)}T_1^{(\beta\gamma)} + S_{22}^{(\alpha\beta\gamma)}T_2^{(\alpha\gamma)} + S_{23}^{(\alpha\beta\gamma)}T_3^{(\alpha\beta)} + \\
&\qquad S_{24}^{(\alpha\beta\gamma)}T_4^{(\alpha)} + S_{25}^{(\alpha\beta\gamma)}T_5^{(\beta)} + S_{26}^{(\alpha\beta\gamma)}T_6^{(\gamma)} - \varepsilon_{22}^{I(\alpha\beta\gamma)} \\
\varepsilon_{33}^{(\alpha\beta\gamma)} &= S_{31}^{(\alpha\beta\gamma)}T_1^{(\beta\gamma)} + S_{32}^{(\alpha\beta\gamma)}T_2^{(\alpha\gamma)} + S_{33}^{(\alpha\beta\gamma)}T_3^{(\alpha\beta)} + \\
&\qquad S_{34}^{(\alpha\beta\gamma)}T_4^{(\alpha)} + S_{35}^{(\alpha\beta\gamma)}T_5^{(\beta)} + S_{36}^{(\alpha\beta\gamma)}T_6^{(\gamma)} - \varepsilon_{33}^{I(\alpha\beta\gamma)} \\
\varepsilon_{23}^{(\alpha\beta\gamma)} &= S_{41}^{(\alpha\beta\gamma)}T_1^{(\beta\gamma)} + S_{42}^{(\alpha\beta\gamma)}T_2^{(\alpha\gamma)} + S_{43}^{(\alpha\beta\gamma)}T_3^{(\alpha\beta)} + \\
&\qquad S_{44}^{(\alpha\beta\gamma)}T_4^{(\alpha)} + S_{45}^{(\alpha\beta\gamma)}T_5^{(\beta)} + S_{46}^{(\alpha\beta\gamma)}T_6^{(\gamma)} - \varepsilon_{23}^{I(\alpha\beta\gamma)} \\
\varepsilon_{13}^{(\alpha\beta\gamma)} &= S_{51}^{(\alpha\beta\gamma)}T_1^{(\beta\gamma)} + S_{52}^{(\alpha\beta\gamma)}T_2^{(\alpha\gamma)} + S_{53}^{(\alpha\beta\gamma)}T_3^{(\alpha\beta)} + \\
&\qquad S_{54}^{(\alpha\beta\gamma)}T_4^{(\alpha)} + S_{55}^{(\alpha\beta\gamma)}T_5^{(\beta)} + S_{56}^{(\alpha\beta\gamma)}T_6^{(\gamma)} - \varepsilon_{13}^{I(\alpha\beta\gamma)} \\
\varepsilon_{12}^{(\alpha\beta\gamma)} &= S_{61}^{(\alpha\beta\gamma)}T_1^{(\beta\gamma)} + S_{62}^{(\alpha\beta\gamma)}T_2^{(\alpha\gamma)} + S_{63}^{(\alpha\beta\gamma)}T_3^{(\alpha\beta)} + \\
&\qquad S_{64}^{(\alpha\beta\gamma)}T_4^{(\alpha)} + S_{65}^{(\alpha\beta\gamma)}T_5^{(\beta)} + S_{66}^{(\alpha\beta\gamma)}T_6^{(\gamma)} - \varepsilon_{12}^{I(\alpha\beta\gamma)}.
\end{aligned}
\tag{3. 50}
$$

or simply written as

$$
\varepsilon_s = \tilde{B}\bar{T}_s - \varepsilon_s^I \tag{3. 51}
$$

The complimentary stiffness constitutive law is

$$
\bar{T}_s = B\left(\varepsilon_s + \varepsilon_s^I\right) \tag{3. 52}
$$

where

$$
B = \tilde{B}^{-1}. \tag{3. 53}
$$

This can be substituted into the local stress/global strain relationship to form

$$
B\left(\varepsilon_s + \varepsilon_s^I\right) = \bar{A}J\bar{\varepsilon} + \bar{A}\tilde{D}\bar{\varepsilon}_s^I. \tag{3. 54}
$$

Solving for the local subcell strains yields

$$
\varepsilon_s = \tilde{B}\bar{A}J\bar{\varepsilon} + \left(\tilde{B}\bar{A}\tilde{D} - I\right)\bar{\varepsilon}_s^I. \tag{3. 55}
$$

Finally, comparing this to the original formulation of Aboudi (Eq. whatever), a relationship between the original and reformulated concentration matrices can be established as

$$A = \tilde{B}\bar{A}J = \begin{bmatrix} A_M \\ A_G \end{bmatrix}^{-1} \begin{bmatrix} 0 \\ J \end{bmatrix}, \qquad (3.\ 56)$$
$$D = \tilde{B}\bar{A}\tilde{D} - I = \begin{bmatrix} A_M \\ A_G \end{bmatrix}^{-1} \begin{bmatrix} A_M \\ 0 \end{bmatrix}.$$

The local stresses, global stresses, global stiffness, and global inelastic strains can be computed in the same manner as previous. The result is an equivalent formulation with significantly reduced computational effort.

3.3 Through Thickness Homogenized Generalized Method of Cells Theory

Inherent to GMC is a lack of shear coupling due to the first order displacement field assumptions. Tabiei [2004] first established that homogenization through thickness prior to in plane homogenization results in improved shear coupling for problems similar to textile composites. To take advantage of this, the original kinematic framework of GMC has to be altered to accommodate for these new assumptions. Previously, the interfacial continuity of displacements was applied on an average sense over a subcell's face. However, this now remains true only for interfaces between α to $\hat{\alpha}$. For the remaining interfaces, β to $\hat{\beta}$ and γ to $\hat{\gamma}$ the continuity of displacements are imposed as an average over the entire through thickness "stack", i.e. for $\alpha = 1 \rightarrow n_\alpha$. This is reflected in the new set of displacement continuity conditions

$$u_i^{(\alpha\beta\gamma)}\Big|_{\bar{x}_1^{\alpha}=d_\alpha/2} = u_i^{(\hat{\alpha}\beta\gamma)}\Big|_{\bar{x}_1^{\hat{\alpha}}=-d_{\hat{\alpha}}/2}$$
$$\frac{1}{d}\int_0^d u_i^{(\alpha\beta\gamma)}\Big|_{\bar{x}_2^{\beta}=h_\beta/2} dx_1 = \frac{1}{d}\int_0^d u_i^{(\alpha\hat{\beta}\gamma)}\Big|_{\bar{x}_2^{\hat{\beta}}=-h_{\hat{\beta}}/2} dx_1$$
$$\frac{1}{d}\int_0^d u_i^{(\alpha\beta\gamma)}\Big|_{\bar{x}_3^{\gamma}=l_\gamma/2} dx_1 = \frac{1}{d}\int_0^d u_i^{(\alpha\beta\hat{\gamma})}\Big|_{\bar{x}_3^{\hat{\gamma}}=-l_{\hat{\gamma}}/2} dx_1 \qquad (3.\ 57)$$

and in an averaging sense

$$\int_{-l_\gamma/2}^{l_\gamma/2}\int_{-h_\beta/2}^{h_\beta/2} u_i^{(\alpha\beta\gamma)}\Big|_{\bar{x}_1^{\alpha}=d_\alpha/2} d\bar{x}_2^{\beta} d\bar{x}_3^{\gamma} = \int_{-l_\gamma/2}^{l_\gamma/2}\int_{-h_\beta/2}^{h_\beta/2} u_i^{(\hat{\alpha}\beta\gamma)}\Big|_{\bar{x}_1^{\hat{\alpha}}=-d_{\hat{\alpha}}/2} d\bar{x}_2^{\beta} d\bar{x}_3^{\gamma}$$
$$\frac{1}{d}\int_0^d \int_{-l_\gamma/2}^{l_\gamma/2}\int_{-d_\alpha/2}^{d_\alpha/2} u_i^{(\alpha\beta\gamma)}\Big|_{\bar{x}_2^{\beta}=h_\beta/2} d\bar{x}_1^{\alpha} d\bar{x}_3^{\gamma} dx_1 =$$
$$\frac{1}{d}\int_0^d \int_{-l_\gamma/2}^{l_\gamma/2}\int_{-d_{\hat{\alpha}}/2}^{d_\alpha/2} u_i^{(\alpha\hat{\beta}\gamma)}\Big|_{\bar{x}_2^{\hat{\beta}}=-h_{\hat{\beta}}/2} d\bar{x}_1^{\alpha} d\bar{x}_3^{\gamma} dx_1$$
$$\frac{1}{d}\int_0^d \int_{-h_\beta/2}^{h_\beta/2}\int_{-d_\alpha/2}^{d_\alpha/2} u_i^{(\alpha\beta\gamma)}\Big|_{\bar{x}_3^{\gamma}=l_\gamma/2} d\bar{x}_1^{\alpha} d\bar{x}_2^{\beta} dx_1 =$$
$$\frac{1}{d}\int_0^d \int_{-h_\beta/2}^{h_\beta/2}\int_{-d_\alpha/2}^{d_\alpha/2} u_i^{(\alpha\beta\hat{\gamma})}\Big|_{\bar{x}_3^{\hat{\gamma}}=-l_{\hat{\gamma}}/2} d\bar{x}_1^{\alpha} d\bar{x}_2^{\beta} dx_1. \qquad (3.\ 58)$$

Substitution of displacement field expansion and conversion from integral to summation in the x_1 direction results in

$$w_i^{(\alpha\beta\gamma)} + \frac{d_\alpha}{2}\phi_i^{(\alpha\beta\gamma)} = w_i^{(\hat{\alpha}\beta\gamma)} - \frac{d_{\hat{\alpha}}}{2}\phi_i^{(\hat{\alpha}\beta\gamma)}$$
$$\frac{1}{d}\sum_{\alpha=1}^{n_\alpha} d_\alpha\left(w_i^{(\alpha\beta\gamma)} + \frac{h_\beta}{2}\chi_i^{(\alpha\beta\gamma)}\right) = \frac{1}{d}\sum_{\alpha=1}^{n_\alpha} d_\alpha\left(w_i^{(\alpha\hat{\beta}\gamma)} - \frac{h_{\hat{\beta}}}{2}\chi_i^{(\alpha\hat{\beta}\gamma)}\right)$$
$$\frac{1}{d}\sum_{\alpha=1}^{n_\alpha} d_\alpha\left(w_i^{(\alpha\beta\gamma)} + \frac{l_\gamma}{2}\psi_i^{(\alpha\beta\gamma)}\right) = \frac{1}{d}\sum_{\alpha=1}^{n_\alpha} d_\alpha\left(w_i^{(\alpha\beta\hat{\gamma})} - \frac{l_{\hat{\gamma}}}{2}\psi_i^{(\alpha\beta\hat{\gamma})}\right). \qquad (3.\ 59)$$

The expansion of the field variable is performed in the same manner as in GMC which yields

$$
\begin{aligned}
&w_i^{(\alpha\beta\gamma)} - \frac{d_\alpha}{2}\left(\frac{\partial w_i^{(\alpha\beta\gamma)}}{\partial x_1} - \phi_i^{(\alpha\beta\gamma)}\right) = \\
&\qquad w_i^{(\hat{\alpha}\beta\gamma)} + \frac{d_{\hat{\alpha}}}{2}\left(\frac{\partial w_i^{(\hat{\alpha}\beta\gamma)}}{\partial x_1} - \phi_i^{(\hat{\alpha}\beta\gamma)}\right) \\
&\frac{1}{d}\sum_{\alpha=1}^{n_\alpha} d_\alpha\left(w_i^{(\alpha\beta\gamma)} - \frac{h_\beta}{2}\left(\frac{\partial w_i^{(\alpha\beta\gamma)}}{\partial x_2} - \chi_i^{(\alpha\beta\gamma)}\right)\right) = \\
&\qquad \frac{1}{d}\sum_{\alpha=1}^{n_\alpha} d_\alpha\left(w_i^{(\alpha\hat{\beta}\gamma)} + \frac{h_{\hat{\beta}}}{2}\left(\frac{\partial w_i^{(\alpha\hat{\beta}\gamma)}}{\partial x_2} - \chi_i^{(\alpha\hat{\beta}\gamma)}\right)\right) \\
&\frac{1}{d}\sum_{\alpha=1}^{n_\alpha} d_\alpha\left(w_i^{(\alpha\beta\gamma)} - \frac{l_\gamma}{2}\left(\frac{\partial w_i^{(\alpha\beta\gamma)}}{\partial x_3} - \psi_i^{(\alpha\beta\gamma)}\right)\right) = \\
&\qquad \frac{1}{d}\sum_{\alpha=1}^{n_\alpha} d_\alpha\left(w_i^{(\alpha\beta\hat{\gamma})} + \frac{l_{\hat{\gamma}}}{2}\left(\frac{\partial w_i^{(\alpha\beta\hat{\gamma})}}{\partial x_3} - \psi_i^{(\alpha\beta\hat{\gamma})}\right)\right).
\end{aligned}
\tag{3. 60}
$$

The same functions F, G, and H from Equations (find) are used, however the continuity conditions are now written in the following form due to the through thickness averaging.

$$
\begin{aligned}
F_i^{(\alpha)} &= 0 \qquad \alpha = 1,\ldots,n_\alpha \\
\sum_{\alpha=1}^{n_\alpha} d_\alpha G_i^{(\beta)} &= 0 \quad \beta = 1,\ldots,n_\beta \\
\sum_{\alpha=1}^{n_\alpha} d_\alpha H_i^{(\gamma)} &= 0 \quad \gamma = 1,\ldots,n_\gamma
\end{aligned}
\tag{3. 61}
$$

Summing each function over the appropriate subcell direction yields

$$
\sum_{\alpha=1}^{n_\alpha} F_i^{(\alpha)} = 0, \quad \sum_{\beta=1}^{n_\beta}\sum_{\alpha=1}^{n_\alpha} d_\alpha G_i^{(\beta)} = 0, \quad \sum_{\gamma=1}^{n_\gamma}\sum_{\alpha=1}^{n_\alpha} d_\alpha H_i^{(\gamma)} = 0
\tag{3. 62}
$$

and the following set of conditions can be deduced

$$\sum_{\alpha=1}^{n_\alpha} f_i^{(\alpha)} = 0, \quad \sum_{\beta=1}^{n_\beta}\sum_{\alpha=1}^{n_\alpha} d_\alpha g_i^{(\beta)} = 0, \quad \sum_{\gamma=1}^{n_\gamma}\sum_{\alpha=1}^{n_\alpha} d_\alpha h_i^{(\gamma)} = 0. \tag{3. 63}$$

After manipulation the following constraints are derived.

$$\begin{aligned}
&\sum_{\alpha=1}^{n_\alpha} d_\alpha \phi_i^{(\alpha\beta\gamma)} = d\,\frac{\partial w_i}{\partial x_1} \\
&\sum_{\alpha=1}^{n_\alpha}\sum_{\beta=1}^{n_\beta} d_\alpha h_\beta \chi_i^{(\alpha\beta\gamma)} = dh\,\frac{\partial w_i}{\partial x_2} \\
&\sum_{\alpha=1}^{n_\alpha}\sum_{\gamma=1}^{n_\gamma} d_\alpha l_\gamma \psi_i^{(\alpha\beta\gamma)} = dl\,\frac{\partial w_i}{\partial x_3}.
\end{aligned} \tag{3. 64}$$

Applying the defined relationship between the subcell strains to the microvariables leads to

$$\begin{aligned}
&\sum_{\alpha=1}^{n_\alpha} d_\alpha \bar{\varepsilon}_{11}^{(\alpha\beta\gamma)} = d\bar{\varepsilon}_{11}, \qquad \beta = 1,...,n_\beta, \gamma = 1,...,n_\gamma \\
&\sum_{\alpha=1}^{n_\alpha}\sum_{\beta=1}^{n_\beta} d_\alpha h_\beta \bar{\varepsilon}_{22}^{(\alpha\beta\gamma)} = dh\bar{\varepsilon}_{22}, \qquad \gamma = 1,...,n_\gamma \\
&\sum_{\alpha=1}^{n_\alpha}\sum_{\gamma=1}^{n_\gamma} d_\alpha l_\gamma \bar{\varepsilon}_{33}^{(\alpha\beta\gamma)} = dl\bar{\varepsilon}_{33}, \qquad \beta = 1,...,n_\beta.
\end{aligned} \tag{3. 65}$$

which clear shows the through thickness averaging in the 2 and 3 directions. At this stage, it can be realized that the strains $\bar{\varepsilon}_{22}^{(\alpha\beta\gamma)}$ and $\bar{\varepsilon}_{33}^{(\alpha\beta\gamma)}$ are not entirely unique. In fact to satisfy the above continuity conditions with a reduced set of equations due to the through thickness average, two more sets of conditions on the local subcell strains need to be imposed.

$$\begin{aligned}
&\bar{\varepsilon}_{22}^{(\alpha\beta\gamma)} = \bar{\varepsilon}_{22}^{(\hat{\alpha}\beta\gamma)} = \bar{\mathrm{E}}_{22}^{(\beta\gamma)} \\
&\bar{\varepsilon}_{33}^{(\alpha\beta\gamma)} = \bar{\varepsilon}_{33}^{(\hat{\alpha}\beta\gamma)} = \bar{\mathrm{E}}_{33}^{(\beta\gamma)}
\end{aligned} \tag{3. 66}$$

This shows that each stack, i.e. for each through thickness group, the strains in the 2 and 3 direction are equivalent. The normal continuity conditions can be rewritten,

$$\begin{aligned}
&\sum_{\alpha=1}^{n_\alpha} d_\alpha \bar{\varepsilon}_{11}^{(\alpha\beta\gamma)} = d\bar{\varepsilon}_{11}, \qquad \beta = 1,...,n_\beta, \gamma = 1,...,n_\gamma \\
&\sum_{\beta=1}^{n_\beta} h_\beta \bar{\mathrm{E}}_{22}^{(\beta\gamma)} = h\bar{\varepsilon}_{22}, \qquad \gamma = 1,...,n_\gamma \\
&\sum_{\gamma=1}^{n_\gamma} l_\gamma \bar{\mathrm{E}}_{33}^{(\beta\gamma)} = l\bar{\varepsilon}_{33}, \qquad \beta = 1,...,n_\beta.
\end{aligned} \tag{3. 67}$$

The shear continuity conditions are derived to be

$$\begin{aligned}
&\sum_{\alpha=1}^{n_\alpha}\sum_{\beta=1}^{n_\beta} d_\alpha h_\beta \bar{\varepsilon}_{12}^{(\alpha\beta\gamma)} = dh\bar{\varepsilon}_{12}, \qquad \gamma = 1,...,n_\gamma. \\
&\sum_{\alpha=1}^{n_\alpha}\sum_{\beta=1}^{n_\beta}\sum_{\gamma=1}^{n_\gamma} d_\alpha h_\beta l_\gamma \bar{\varepsilon}_{23}^{(\alpha\beta\gamma)} = dhl\bar{\varepsilon}_{23}, \\
&\sum_{\alpha=1}^{n_\alpha}\sum_{\gamma=1}^{n_\gamma} d_\alpha l_\gamma \bar{\varepsilon}_{13}^{(\alpha\beta\gamma)} = dl\bar{\varepsilon}_{13}, \qquad \beta = 1,...,n_\beta
\end{aligned} \tag{3. 68}$$

and a similar conclusion can be regarding the independence of the 23-dir shear strains. Therefore,

$$\bar{\varepsilon}_{23}^{(\alpha\beta\gamma)} = \bar{\varepsilon}_{23}^{(\hat{\alpha}\beta\gamma)} = \bar{\mathrm{E}}_{23}^{(\beta\gamma)} \tag{3. 69}$$

and the continuity conditions become

$$\sum_{\alpha=1}^{n_\alpha}\sum_{\beta=1}^{n_\beta} d_\alpha h_\beta \bar{\varepsilon}_{12}^{(\alpha\beta\gamma)} = dh\bar{\varepsilon}_{12}, \qquad \gamma = 1,...,n_\gamma.$$
$$\sum_{\beta=1}^{n_\beta}\sum_{\gamma=1}^{n_\gamma} h_\beta l_\gamma \bar{\mathrm{E}}_{23}^{(\alpha\beta\gamma)} = hl\bar{\varepsilon}_{23},$$
$$\sum_{\alpha=1}^{n_\alpha}\sum_{\gamma=1}^{n_\gamma} d_\alpha l_\gamma \bar{\varepsilon}_{13}^{(\alpha\beta\gamma)} = dl\bar{\varepsilon}_{13}, \qquad \beta = 1,...,n_\beta. \tag{3. 70}$$

This yields a $N_\beta N_\gamma + 2\left(N_\beta + N_\gamma\right) + 1 \times 3N_\alpha N_\beta N_\gamma + 3N_\beta N_\gamma$ set of equations and can be cast into matrix form as follows

$$A_{\mathrm{G}}\tilde{\varepsilon}_s = J\bar{\varepsilon} \tag{3. 71}$$

where

$$\bar{\varepsilon} = \left(\bar{\varepsilon}_{11}, \bar{\varepsilon}_{22}, \bar{\varepsilon}_{33}, 2\bar{\varepsilon}_{23}, 2\bar{\varepsilon}_{13}, 2\bar{\varepsilon}_{12}\right) \tag{3. 72}$$

and

$$\tilde{\varepsilon}_s = (\varepsilon_{11}^{(\alpha\beta\gamma)}, \varepsilon_{13}^{(\alpha\beta\gamma)}, \varepsilon_{12}^{(\alpha\beta\gamma)}, ..., \varepsilon_{11}^{\left(N_\alpha N_\beta N_\gamma\right)}, \varepsilon_{13}^{\left(N_\alpha N_\beta N_\gamma\right)}, \varepsilon_{12}^{\left(N_\alpha N_\beta N_\gamma\right)},$$
$$\mathrm{E}_{22}^{(\beta\gamma)}, \mathrm{E}_{33}^{(\beta\gamma)}, \mathrm{E}_{23}^{(\beta\gamma)}, ..., \mathrm{E}_{22}^{\left(N_\beta N_\gamma\right)}, \mathrm{E}_{33}^{\left(N_\beta N_\gamma\right)}, \mathrm{E}_{23}^{\left(N_\beta N_\gamma\right)}) \tag{3. 73}$$

Furthermore it can be shown, that the traction boundary conditions are a satisfied in a through tickness average sense averaging over the 1 direction also. The modified set of

$$\bar{\sigma}_{1i}^{(\alpha\beta\gamma)} = \bar{\sigma}_{1i}^{(\hat{\alpha}\beta\gamma)}$$
$$\frac{1}{d}\sum_{\alpha=1}^{n_\alpha} d_\alpha \bar{\sigma}_{2i}^{(\alpha\beta\gamma)} = \frac{1}{d}\sum_{\alpha=1}^{n_\alpha} d_\alpha \bar{\sigma}_{2i}^{\left(\alpha\hat{\beta}\gamma\right)} \qquad i \neq 1$$
$$\frac{1}{d}\sum_{\alpha=1}^{n_\alpha} d_\alpha \bar{\sigma}_{3i}^{(\alpha\beta\gamma)} = \frac{1}{d}\sum_{\alpha=1}^{n_\alpha} d_\alpha \bar{\sigma}_{3i}^{(\alpha\beta\hat{\gamma})} \qquad i \neq 1$$
$$\bar{\sigma}_{2i}^{(\alpha\beta\gamma)} = \bar{\sigma}_{2i}^{\left(\alpha\hat{\beta}\gamma\right)} \qquad i \neq 2,3$$
$$\bar{\sigma}_{3i}^{(\alpha\beta\gamma)} = \bar{\sigma}_{3i}^{(\alpha\beta\hat{\gamma})} \qquad i \neq 2,3 \tag{3. 74}$$

The set of independent traction continuity conditions are listed below.

$$\bar{\sigma}_{11}^{(\alpha\beta\gamma)} = \bar{\sigma}_{11}^{(\hat{\alpha}\beta\gamma)} \qquad \alpha = 1,...,n_\alpha - 1, \beta = 1,...,n_\beta, \gamma = 1,...,n_\gamma \tag{3. 75}$$

$$\frac{1}{d}\sum_{\alpha=1}^{n_\alpha} d_\alpha \bar{\sigma}_{22}^{(\alpha\beta\gamma)} = \frac{1}{d}\sum_{\alpha=1}^{n_\alpha} d_\alpha \bar{\sigma}_{22}^{(\alpha\hat{\beta}\gamma)} \qquad \beta = 1,...,n_\beta - 1, \gamma = 1,...,n_\gamma$$

$$\frac{1}{d}\sum_{\alpha=1}^{n_\alpha} d_\alpha \bar{\sigma}_{33}^{(\alpha\beta\gamma)} = \frac{1}{d_\alpha}\sum_{\alpha=1}^{n_\alpha} \bar{\sigma}_{33}^{(\alpha\beta\hat{\gamma})} \qquad \beta = 1,...,n_\beta, \gamma = 1,...,n_\gamma - 1$$

$$\frac{1}{d}\sum_{\alpha=1}^{n_\alpha} \bar{\sigma}_{23}^{(\alpha\beta\gamma)} = \frac{1}{d}\sum_{\alpha=1}^{n_\alpha} \bar{\sigma}_{23}^{(\alpha\hat{\beta}\gamma)} \qquad \beta = 1,...,N_\beta - 1, \gamma = 1,...,n_\gamma$$

$$\frac{1}{d}\sum_{\alpha=1}^{n_\alpha} \bar{\sigma}_{32}^{(\alpha\beta\gamma)} = \frac{1}{d}\sum_{\alpha=1}^{n_\alpha} \bar{\sigma}_{32}^{(\alpha\beta\hat{\gamma})} \qquad \beta = n_\beta, \gamma = 1,...,n_\gamma - 1$$

$$\bar{\sigma}_{13}^{(\alpha\beta\gamma)} = \bar{\sigma}_{13}^{(\hat{\alpha}\beta\gamma)} \qquad \alpha = 1,...,n_\alpha - 1, \beta = 1,...,n_\beta, \gamma = 1,...,n_\gamma$$

$$\bar{\sigma}_{31}^{(\alpha\beta\gamma)} = \bar{\sigma}_{31}^{(\alpha\beta\hat{\gamma})} \qquad \alpha = n_\alpha, \beta = 1,...,n_\beta, \gamma = 1,...,n_\gamma - 1$$

$$\bar{\sigma}_{12}^{(\alpha\beta\gamma)} = \bar{\sigma}_{12}^{(\hat{\alpha}\beta\gamma)} \qquad \alpha = 1,...,n_\alpha - 1, \beta = 1,...,n_\beta, \gamma = n_\gamma$$

$$\bar{\sigma}_{21}^{(\alpha\beta\gamma)} = \bar{\sigma}_{21}^{(\alpha\hat{\beta}\gamma)} \qquad \alpha = n_\alpha - 1, \beta = 1,...,n_\beta - 1, \gamma = n_\gamma$$

This now gives a second set of equations on the order of

$3N_\alpha N_\beta N_\gamma + 2N_\beta N_\gamma - 2\left(N_\beta + N_\gamma\right) - 1 \times 3N_\alpha N_\beta N_\gamma + 3N_\beta N_\gamma$ and can be cast into matrix form as follows

$$A_m\left(\tilde{\varepsilon}_s - \tilde{\varepsilon}_s^I - \tilde{\varepsilon}_s^T\right) = 0 \tag{3. 76}$$

Combining the traction and displacement continuity we get a system of equations

$$\tilde{A}\tilde{\varepsilon}_s - \tilde{D}\left(\tilde{\varepsilon}_s^I + \tilde{\varepsilon}_s^T\right) = K\bar{\varepsilon} \tag{3. 77}$$

where

$$\tilde{A}=\begin{bmatrix} A_M \\ A_G \end{bmatrix}, \tilde{D}=\begin{bmatrix} A_M \\ 0 \end{bmatrix}, K=\begin{bmatrix} 0 \\ J \end{bmatrix}. \tag{3. 78}$$

Now we can determine the subcell strains

$$\tilde{\varepsilon}_s = A^* \varepsilon + D^* \left(\tilde{\varepsilon}_s^I + \tilde{\varepsilon}_s^I \right) \tag{3. 79}$$

where

$$A^* = \tilde{A}^{-1} K \, , D^* = \tilde{A}^{-1} \tilde{D} \, . \tag{3. 80}$$

Since $\tilde{\varepsilon}_s$ is not meaningful, it is of interest to express the local strains in the form of the global strains, i.e. $\bar{\varepsilon} = \left(\bar{\varepsilon}_{11}, \bar{\varepsilon}_{22}, \bar{\varepsilon}_{33}, \bar{\varepsilon}_{23}, \bar{\varepsilon}_{13}, \bar{\varepsilon}_{12} \right)$. To accomplish this another matrix is introduced, a modified identity matrix.

$$\varepsilon_s = B \tilde{\varepsilon}_s \, , \varepsilon_s^I = B \tilde{\varepsilon}_s^I \, . \tag{3. 81}$$

This purpose of this matrix is to associate the local subcell strains with the solution strains, for example

$$\begin{aligned} \varepsilon_{11}^{(\alpha\beta\gamma)} &= \varepsilon_{11}^{(\alpha\beta\gamma)} \\ \varepsilon_{22}^{(\alpha\beta\gamma)} &= \mathrm{E}_{22}^{(\beta\gamma)} \\ \varepsilon_{33}^{(\alpha\beta\gamma)} &= \mathrm{E}_{33}^{(\beta\gamma)} \\ \varepsilon_{23}^{(\alpha\beta\gamma)} &= \mathrm{E}_{23}^{(\beta\gamma)} \\ \varepsilon_{13}^{(\alpha\beta\gamma)} &= \varepsilon_{13}^{(\alpha\beta\gamma)} \\ \varepsilon_{12}^{(\alpha\beta\gamma)} &= \varepsilon_{12}^{(\alpha\beta\gamma)}. \end{aligned} \tag{3. 82}$$

Note, the B matrix contains only 1s and 0s. Substituting this into the subcell strain results

$$\varepsilon_s = B A^* \bar{\varepsilon} + B D B^T \left(\varepsilon_s^I + \varepsilon_s^T \right) \tag{3. 83}$$

Simplifying yields

$$\varepsilon_s = A\bar{\varepsilon} + D\left(\varepsilon_s^I + \varepsilon_s^T\right) \tag{3. 84}$$

where

$$A = BA^*, D = BD^*B^T. \tag{3. 85}$$

Lastly, the concentration matrices A and D can be decomposed into submatrices, as before, and the final localization equation is.

$$\varepsilon^{(\alpha\beta\gamma)} = A^{(\alpha\beta\gamma)}\bar{\varepsilon} + D^{(\alpha\beta\gamma)}\left(\varepsilon_s^I + \varepsilon_s^T\right) \tag{3. 86}$$

3.4 Reformulated Through Thickness Homogenized Generalized Method of Cells Theory

The prior formulation solves for the unknown local strain fields, three of which are independent of α. Further computational efficiency can be achieve through formulation the unknowns as a mixed set of local strain and stress fields, all of which are independent of α. This can be accomplished because of the zeroth order strain fields leads to zeroth order stress fields and as a result of the traction continuity conditions, all stress components in the 1-dir are independent of α.

This reduces the number of unknowns to $4N_\beta N_\gamma + \beta + \gamma$, which is not a function of α. The α independent local stress fields are listed below

$$\sigma_{11}^{(\alpha\beta\gamma)} = \sigma_{11}^{(\hat{\alpha}\beta\gamma)} = T_1^{(\beta\gamma)}$$
$$\sigma_{13}^{(\alpha\beta\gamma)} = \sigma_{13}^{(\hat{\alpha}\beta\gamma)} = T_5^{(\beta)}$$
$$\sigma_{31}^{(\alpha\beta\gamma)} = \sigma_{31}^{(\alpha\beta\hat{\gamma})} = T_5^{(\beta)}$$
$$\sigma_{12}^{(\alpha\beta\gamma)} = \sigma_{12}^{(\hat{\alpha}\beta\gamma)} = T_6^{(\gamma)}$$
$$\sigma_{21}^{(\alpha\beta\gamma)} = \sigma_{21}^{(\alpha\hat{\beta}\gamma)} = T_6^{(\gamma)}. \qquad (3.\ 87)$$

Substitution of these into the traction continuity conditions yields

$$\sigma_{11}^{(\alpha\beta\gamma)} = \sigma_{11}^{(\hat{\alpha}\beta\gamma)} = T_1^{(\beta\gamma)} \qquad \alpha = 1,...,n_\alpha - 1, \beta = 1,...,n_\beta, \gamma = 1,...,n_\gamma \qquad (3.\ 88)$$
$$\frac{1}{d}\sum_{\alpha=1}^{n_\alpha} d_\alpha \sigma_{22}^{(\alpha\beta\gamma)} = \frac{1}{d}\sum_{\alpha=1}^{n_\alpha} d_\alpha \sigma_{22}^{(\alpha\hat{\beta}\gamma)} \qquad \beta = 1,...,n_\beta - 1, \gamma = 1,...,n_\gamma$$
$$\frac{1}{d}\sum_{\alpha=1}^{n_\alpha} d_\alpha \sigma_{33}^{(\alpha\beta\gamma)} = \frac{1}{d}\sum_{\alpha=1}^{n_\alpha} d_\alpha \sigma_{33}^{(\alpha\beta\hat{\gamma})} \qquad \beta = 1,...,n_\beta, \gamma = 1,...,n_\gamma - 1$$
$$\frac{1}{d}\sum_{\alpha=1}^{n_\alpha} d_\alpha \sigma_{23}^{(\alpha\beta\gamma)} = \frac{1}{d}\sum_{\alpha=1}^{n_\alpha} d_\alpha \sigma_{23}^{(\alpha\hat{\beta}\gamma)} \qquad \beta = 1,...,n_\beta - 1, \gamma = 1,...,n_\gamma$$
$$\frac{1}{d}\sum_{\alpha=1}^{n_\alpha} d_\alpha \sigma_{32}^{(\alpha\beta\gamma)} = \frac{1}{d}\sum_{\alpha=1}^{n_\alpha} d_\alpha \sigma_{32}^{(\alpha\beta\hat{\gamma})} \qquad \beta = n_\beta, \gamma = 1,...,N_\gamma - 1$$
$$\sigma_{13}^{(\alpha\beta\gamma)} = \sigma_{13}^{(\hat{\alpha}\beta\gamma)} = T_5^{(\beta)} \qquad \alpha = 1,...,n_\alpha - 1, \beta = 1,...,n_\beta, \gamma = 1,...,n_\gamma$$
$$\sigma_{31}^{(\alpha\beta\gamma)} = \sigma_{31}^{(\alpha\beta\hat{\gamma})} = T_5^{(\beta)} \qquad \alpha = n_\alpha, \beta = 1,...,n_\beta, \gamma = 1,...,n_\gamma - 1$$
$$\sigma_{12}^{(\alpha\beta\gamma)} = \sigma_{12}^{(\hat{\alpha}\beta\gamma)} = T_6^{(\gamma)} \qquad \alpha = 1,...,n_\alpha - 1, \beta = 1,...,n_\beta, \gamma = n_\gamma$$
$$\sigma_{21}^{(\alpha\beta\gamma)} = \sigma_{21}^{(\alpha\hat{\beta}\gamma)} = T_6^{(\gamma)} \qquad \alpha = n_\alpha - 1, \beta = 1,...,n_\beta - 1, \gamma = n_\gamma$$

However, only the average continuity conditions are independent and thus used in the solution. The minimum required variables to define a stress/strain state of a subcell are $T_1^{(\beta\gamma)}, \mathrm{E}_2^{(\beta\gamma)}, \mathrm{E}_3^{(\beta\gamma)}, \mathrm{E}_4^{(\beta\gamma)}, T_5^{(\beta)}$, and $T_6^{(\gamma)}$, ($\mathrm{E}_2^{(\beta\gamma)} = \mathrm{E}_{22}^{(\beta\gamma)}, \mathrm{E}_3^{(\beta\gamma)} = \mathrm{E}_{33}^{(\beta\gamma)}, \mathrm{E}_4^{(\beta\gamma)} = \mathrm{E}_{23}^{(\beta\gamma)}$ using previous definitions). This is mixed set unknowns, i.e. containing both stresses and strains, and requires that the displacement and traction continuity conditions be written in terms of these

unknowns. To accomplish this, the constitutive law is rearranged such that the state at a local subcell is given by

$$
\begin{aligned}
\varepsilon_{11}^{(\alpha\beta\gamma)} &= R_{11}^{(\alpha\beta\gamma)}T_1^{(\beta\gamma)} + R_{12}^{(\alpha\beta\gamma)}\mathrm{E}_2^{(\beta\gamma)} + R_{13}^{(\alpha\beta\gamma)}\mathrm{E}_3^{(\beta\gamma)} + \\
&\quad R_{14}^{(\alpha\beta\gamma)}\mathrm{E}_4^{(\beta\gamma)} + R_{15}^{(\alpha\beta\gamma)}T_5^{(\beta\gamma)} + R_{16}^{(\alpha\beta\gamma)}T_6^{(\beta\gamma)} + \\
&\quad -Q_{11}^{(\alpha\beta\gamma)}\varepsilon_{11}^{I(\alpha\beta\gamma)} - Q_{12}^{(\alpha\beta\gamma)}\varepsilon_{22}^{I(\alpha\beta\gamma)} - Q_{13}^{(\alpha\beta\gamma)}\varepsilon_{33}^{I(\alpha\beta\gamma)} + \\
&\quad -Q_{14}^{(\alpha\beta\gamma)}\varepsilon_{23}^{I(\alpha\beta\gamma)} - Q_{15}^{(\alpha\beta\gamma)}\varepsilon_{13}^{I(\alpha\beta\gamma)} - Q_{16}^{(\alpha\beta\gamma)}\varepsilon_{12}^{I(\alpha\beta\gamma)} \\
\sigma_{22}^{(\alpha\beta\gamma)} &= R_{21}^{(\alpha\beta\gamma)}T_1^{(\beta\gamma)} + R_{22}^{(\alpha\beta\gamma)}\mathrm{E}_2^{(\beta\gamma)} + R_{23}^{(\alpha\beta\gamma)}\mathrm{E}_3^{(\beta\gamma)} + \\
&\quad R_{24}^{(\alpha\beta\gamma)}\mathrm{E}_4^{(\beta\gamma)} + R_{25}^{(\alpha\beta\gamma)}T_5^{(\beta\gamma)} + R_{26}^{(\alpha\beta\gamma)}T_6^{(\beta\gamma)} + \\
&\quad -Q_{21}^{(\alpha\beta\gamma)}\varepsilon_{11}^{I(\alpha\beta\gamma)} - Q_{22}^{(\alpha\beta\gamma)}\varepsilon_{22}^{I(\alpha\beta\gamma)} - Q_{23}^{(\alpha\beta\gamma)}\varepsilon_{33}^{I(\alpha\beta\gamma)} + \\
&\quad -Q_{24}^{(\alpha\beta\gamma)}\varepsilon_{23}^{I(\alpha\beta\gamma)} - Q_{25}^{(\alpha\beta\gamma)}\varepsilon_{13}^{I(\alpha\beta\gamma)} - Q_{26}^{(\alpha\beta\gamma)}\varepsilon_{12}^{I(\alpha\beta\gamma)} \\
\sigma_{33}^{(\alpha\beta\gamma)} &= R_{31}^{(\alpha\beta\gamma)}T_1^{(\beta\gamma)} + R_{32}^{(\alpha\beta\gamma)}\mathrm{E}_2^{(\beta\gamma)} + R_{33}^{(\alpha\beta\gamma)}\mathrm{E}_3^{(\beta\gamma)} + \\
&\quad R_{34}^{(\alpha\beta\gamma)}\mathrm{E}_4^{(\beta\gamma)} + R_{35}^{(\alpha\beta\gamma)}T_5^{(\beta\gamma)} + R_{36}^{(\alpha\beta\gamma)}T_6^{(\beta\gamma)} + \\
&\quad -Q_{31}^{(\alpha\beta\gamma)}\varepsilon_{11}^{I(\alpha\beta\gamma)} - Q_{32}^{(\alpha\beta\gamma)}\varepsilon_{22}^{I(\alpha\beta\gamma)} - Q_{33}^{(\alpha\beta\gamma)}\varepsilon_{33}^{I(\alpha\beta\gamma)} + \\
&\quad -Q_{34}^{(\alpha\beta\gamma)}\varepsilon_{23}^{I(\alpha\beta\gamma)} - Q_{35}^{(\alpha\beta\gamma)}\varepsilon_{13}^{I(\alpha\beta\gamma)} - Q_{36}^{(\alpha\beta\gamma)}\varepsilon_{12}^{I(\alpha\beta\gamma)} \\
\sigma_{23}^{(\alpha\beta\gamma)} &= R_{41}^{(\alpha\beta\gamma)}T_1^{(\beta\gamma)} + R_{42}^{(\alpha\beta\gamma)}\mathrm{E}_2^{(\beta\gamma)} + R_{43}^{(\alpha\beta\gamma)}\mathrm{E}_3^{(\beta\gamma)} + \\
&\quad R_{44}^{(\alpha\beta\gamma)}\mathrm{E}_4^{(\beta\gamma)} + R_{45}^{(\alpha\beta\gamma)}T_5^{(\beta\gamma)} + R_{46}^{(\alpha\beta\gamma)}T_6^{(\beta\gamma)} + \\
&\quad -Q_{41}^{(\alpha\beta\gamma)}\varepsilon_{11}^{I(\alpha\beta\gamma)} - Q_{42}^{(\alpha\beta\gamma)}\varepsilon_{22}^{I(\alpha\beta\gamma)} - Q_{43}^{(\alpha\beta\gamma)}\varepsilon_{33}^{I(\alpha\beta\gamma)} + \\
&\quad -Q_{44}^{(\alpha\beta\gamma)}\varepsilon_{23}^{I(\alpha\beta\gamma)} - Q_{45}^{(\alpha\beta\gamma)}\varepsilon_{13}^{I(\alpha\beta\gamma)} - Q_{46}^{(\alpha\beta\gamma)}\varepsilon_{12}^{I(\alpha\beta\gamma)} \\
\varepsilon_{13}^{(\alpha\beta\gamma)} &= R_{51}^{(\alpha\beta\gamma)}T_1^{(\beta\gamma)} + R_{52}^{(\alpha\beta\gamma)}\mathrm{E}_2^{(\beta\gamma)} + R_{53}^{(\alpha\beta\gamma)}\mathrm{E}_3^{(\beta\gamma)} + \\
&\quad R_{54}^{(\alpha\beta\gamma)}\mathrm{E}_4^{(\beta\gamma)} + R_{55}^{(\alpha\beta\gamma)}T_5^{(\beta\gamma)} + R_{56}^{(\alpha\beta\gamma)}T_6^{(\beta\gamma)} + \\
&\quad -Q_{51}^{(\alpha\beta\gamma)}\varepsilon_{11}^{I(\alpha\beta\gamma)} - Q_{52}^{(\alpha\beta\gamma)}\varepsilon_{22}^{I(\alpha\beta\gamma)} - Q_{53}^{(\alpha\beta\gamma)}\varepsilon_{33}^{I(\alpha\beta\gamma)} + \\
&\quad -Q_{54}^{(\alpha\beta\gamma)}\varepsilon_{23}^{I(\alpha\beta\gamma)} - Q_{55}^{(\alpha\beta\gamma)}\varepsilon_{13}^{I(\alpha\beta\gamma)} - Q_{56}^{(\alpha\beta\gamma)}\varepsilon_{12}^{I(\alpha\beta\gamma)} \\
\varepsilon_{12}^{(\alpha\beta\gamma)} &= R_{61}^{(\alpha\beta\gamma)}T_1^{(\beta\gamma)} + R_{62}^{(\alpha\beta\gamma)}\mathrm{E}_2^{(\beta\gamma)} + R_{63}^{(\alpha\beta\gamma)}\mathrm{E}_3^{(\beta\gamma)} + \\
&\quad R_{64}^{(\alpha\beta\gamma)}\mathrm{E}_4^{(\beta\gamma)} + R_{65}^{(\alpha\beta\gamma)}T_5^{(\beta\gamma)} + R_{66}^{(\alpha\beta\gamma)}T_6^{(\beta\gamma)} + \\
&\quad -Q_{61}^{(\alpha\beta\gamma)}\varepsilon_{11}^{I(\alpha\beta\gamma)} - Q_{62}^{(\alpha\beta\gamma)}\varepsilon_{22}^{I(\alpha\beta\gamma)} - Q_{63}^{(\alpha\beta\gamma)}\varepsilon_{33}^{I(\alpha\beta\gamma)} + \\
&\quad -Q_{64}^{(\alpha\beta\gamma)}\varepsilon_{23}^{I(\alpha\beta\gamma)} - Q_{65}^{(\alpha\beta\gamma)}\varepsilon_{13}^{I(\alpha\beta\gamma)} - Q_{66}^{(\alpha\beta\gamma)}\varepsilon_{12}^{I(\alpha\beta\gamma)}
\end{aligned}
\tag{3. 89}
$$

or more conveniently in matrix form

$$F^{(\alpha\beta\gamma)} = R^{(\alpha\beta\gamma)} U^{(\beta\gamma)} - Q^{(\alpha\beta\gamma)} \varepsilon^{I(\alpha\beta\gamma)} \tag{3. 90}$$

where

$$F^{(\alpha\beta\gamma)} = \left\{ \varepsilon_{11}^{(\alpha\beta\gamma)}, \sigma_{22}^{(\alpha\beta\gamma)}, \sigma_{33}^{(\alpha\beta\gamma)}, \sigma_{23}^{(\alpha\beta\gamma)}, \varepsilon_{13}^{(\alpha\beta\gamma)}, \varepsilon_{12}^{(\alpha\beta\gamma)} \right\} \tag{3. 91}$$

$$U^{(\beta\gamma)} = \left\{ T_1^{(\beta\gamma)}, \mathrm{E}_2^{(\beta\gamma)}, \mathrm{E}_3^{(\beta\gamma)}, \mathrm{E}_4^{(\beta\gamma)}, T_5^{(\beta)}, T_6^{(\gamma)} \right\}.$$

There is no symmetry to either R or Q in contrast to a typical stiffness or compliance matrix. The full details on these matrices are given in the appendix. By applying this new constitutive law the displacement and traction continuities, respectively, are cast into a matrix form below.

$$A_g U_s + D_g \varepsilon_s^I = J\bar{\varepsilon} \tag{3. 92}$$

$$A_m U_s + D_m \varepsilon_s^I = 0$$

and combining both of these yields

$$\tilde{A} U_s + \tilde{D} \varepsilon_s^I = K\bar{\varepsilon} \tag{3. 93}$$

where

$$\tilde{A} = \begin{bmatrix} A_M \\ A_G \end{bmatrix}, \tilde{D} = \begin{bmatrix} A_M \\ 0 \end{bmatrix}, K = \begin{bmatrix} 0 \\ J \end{bmatrix}. \tag{3. 94}$$

Solving for the unknown local fields U yields

$$U_s = \tilde{A}^{-1} K\bar{\varepsilon} - \tilde{A}^{-1} \tilde{D} \varepsilon_s^I \tag{3. 95}$$

Next, it is useful to convert U_s to the well known ε_s. This can be established through use of the constitutive law and modified identity matrices.

$$\varepsilon_s = B_F F_s + B_U U_s \tag{3. 96}$$

where

$$F_s = R_s U_s - Q_s \varepsilon_s^I \tag{3. 97}$$

B_F and B_U are matrices containing only 1s and 0s and serve the purpose of collecting the appropriate terms from each matrix F_s and U_s. Substitution of the above yields

$$\varepsilon_s = \left(B_F R_s \tilde{A}^{-1} K + B_U \tilde{A}^{-1} K\right)\bar{\varepsilon} - \left(B_F R_s \tilde{A}^{-1} \tilde{D} + B_F Q_s + B_U \tilde{A}^{-1} \tilde{D}\right)\varepsilon_s^I \tag{3. 98}$$

or

$$\varepsilon_s = A\bar{\varepsilon} + D\varepsilon_s^I \tag{3. 99}$$

where

$$\begin{aligned} A &= B_F R_s \tilde{A}^{-1} K + B_U \tilde{A}^{-1} K \\ D &= -\left(B_F R_s \tilde{A}^{-1} \tilde{D} + B_F Q_s + B_U \tilde{A}^{-1} \tilde{D}\right). \end{aligned} \tag{3. 100}$$

As previously, the A and D can be decomposed into square submatrices resulting in the final solution

$$\varepsilon^{(\alpha\beta\gamma)} = A^{(\alpha\beta\gamma)}\bar{\varepsilon} + D^{(\alpha\beta\gamma)}\varepsilon_s^I \tag{3. 101}$$

3.5 Multiscale Generalized Method of Cells Theory

Multiscae Generalized Method of Cells (MSGMC) is a multiscale framework that takes the existing methodology prescribed by the Generalized Method of Cells and implements further than the typical macro-micro or global/local framework. The multiscale framework allows for the analysis of innumerate

length scales, as physically relevant. An example would be textile composites where there are three distinct length scales: the weave RUC, the tow RUC, and the constituents. GMC is only capable of bridging between the weave RUC and tow RUC or the tow RUC and constituents, not all three. Another example is a fiber reinforced composite with a particle reinforced matrix. Here the three length scales would be the composite RUC, the RUC of the reinforced matrix, and the constituents. The power of MSGMC lies in the ability to fully integrate micromechanics analysis for RUCs at various length scales.

An important step is to character the RUC geometry at each length scale of analysis. For a material of interest, the dimensions of every subcell (D_α, H_β, and L_γ) for every multiphase material must be known. This is required to formulate the global/local relationship. In addition, each constituent must obey an elasto-plastic constitutive model. Fig. 3.4 shows a typical discretization and link between two periodic microstructures. Since there can exist multiple length scales, a nomenclature system has been establish to avoid ambiguity for variables. $\{\alpha\beta\gamma\}$ refers to a specific subcell at a single length scale. To correctly refer to a subcell at a lower length scale, an index needs to precede it. For example, $\{\alpha\beta\gamma\}^1\{\alpha\beta\gamma\}^2$ refers to a unique subcell where subscript 1 denotes the first localized scale and subscript 2 denotes the second localized scale. Since at any scale, each subcell can contain multiple smaller length scales, a subcell at any length scale can only by identified with the higher length scale indices preceding it (see Table 3.1).

Table 3.1 Nomenclature and Variables for MSGMC

Global/Local Fields, where $[\ ]$ denotes field such as $\sigma, \varepsilon, \varepsilon_p, C$

$[\ ]$ denotes global field

$[\ ]^{\{\alpha\beta\gamma\}^1}$ denotes local field (down one length scale)

$[\ ]^{\{\alpha\beta\gamma\}^1\{\alpha\beta\gamma\}^2}$ denotes local field (down two length scales)

$[\ ]^{\{\alpha\beta\gamma\}^1\{\alpha\beta\gamma\}^2\ldots\{\alpha\beta\gamma\}^n}$ denotes local field (down *n* number of length scales)

$[\ ]^{\{\alpha\beta\gamma\}\{\alpha\beta\gamma\}}$ refers to the local field of subcell $\{\alpha\beta\gamma\}\{\alpha\beta\gamma\}$ at the second length scale, superscripts dropped due to redundancy

Geometric Properties, where _ denotes a single index for a subcell, i.e. $\alpha, \beta, or \gamma$

$N_{\_}$ denotes number of subcells in _ direction

$D_{\_}, H_{\_}, L_{\_}$ denotes dimensions of a subcell in 1,2 and 3 direction (respectively)

$N_{\{\alpha\beta\gamma\}\_}$ denotes number of subcells in _ direction in one level down from subcell $\{\alpha\beta\gamma\}$

$N_{\{\alpha\beta\gamma\}\{\alpha\beta\gamma\}\ldots\{\alpha\beta\gamma\}\_}$ denotes number of subcells in _ direction in n levels down from subcell

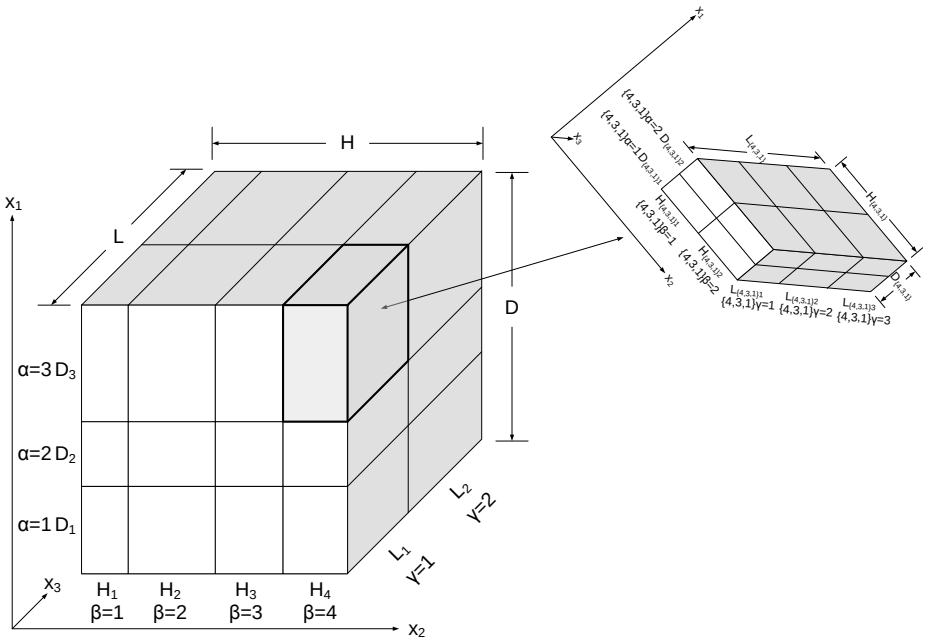

Fig. 3.4 Example of MSGMC Repeating Unit Cell consisting of $N_\alpha = 3$, $N_\beta = 4$ and $N_\gamma = 2$ with subcell $\{3,4,1\}$ as a multiphase material in an arbitrary coordinate system

To generalize MSGMC, a three length scale analysis is presented (macro,meso, and micro). The macroscale is a multiphase composite that can be described as an RUC of dimensions $D_\alpha \text{ x } H_\beta \text{ ,x } L_\gamma$. Each subcell within the macroscale, otherwise known as a mesoscale subcell, can either be a multiphase material (i.e. composite material) or a single phase material (constituent). If it is a multiphase material, it has an RUC of dimensions $D_{\{\alpha\beta\gamma\}\alpha} \text{ x } H_{\{\alpha\beta\gamma\}\beta} \text{ ,x } L_{\{\alpha\beta\gamma\}\gamma}$. If it is a single phase material, it is represented by a constitutive model. Each subcell within a mesoscale RUC is a constituent material. The relationship between all length scales will be described below.

The macro and mesoscales both contain RUCs and the microscale only contains constituents. Assuming an elasto-plastic relationship, the governing constitutive law at the macroscale can be written:

$$\sigma = C\left(\varepsilon - \varepsilon^{I}\right) \tag{3. 102}$$

Where σ is the stress tensor, C is the stiffness matrix, ε is the engineering strain tensors, and ε^{p} is the plastic engineering strain tensor. The stress at the macroscale can also be determined through volume homogenization of the stresses at the mesoscale

$$\sigma = \frac{1}{DHL}\sum_{\alpha=1}^{N_\alpha}\sum_{\beta=1}^{N_\beta}\sum_{\gamma=1}^{N_\gamma}\sigma^{\{\alpha\beta\gamma\}}D_\alpha H_\beta L_\gamma \tag{3. 103}$$

Similarly, the stiffness can be written in terms of the local mesoscale subcell stiffnesses and concentration matrices.

$$C = \frac{1}{DHL}\sum_{\alpha=1}^{N_\alpha}\sum_{\beta=1}^{N_\beta}\sum_{\gamma=1}^{N_\gamma} C^{\{\alpha\beta\gamma\}}A^{\{\alpha\beta\gamma\}}D_\alpha H_\beta L_\gamma \tag{3. 104}$$

The plastic strain can written in terms of the plastic strain concentration matrix and mesoscale parameters.

$$\varepsilon^{I} = \frac{-C^{-1}}{DHL}\sum_{\alpha=1}^{N_\alpha}\sum_{\beta=1}^{N_\beta}\sum_{\gamma=1}^{N_\gamma} D_\alpha H_\beta L_\gamma C^{\{\alpha\beta\gamma\}}\left(D^{\{\alpha\beta\gamma\}}\varepsilon_s^{I\{\alpha\beta\gamma\}} - \varepsilon^{I\{\alpha\beta\gamma\}}\right) \tag{3. 105}$$

This concludes all necessary governing equations at the macroscale. The total engineering strain tensor can be localized to any subcell from the globally applied strain and local plastic strains.

$$\varepsilon^{\{\alpha\beta\gamma\}} = A^{\{\alpha\beta\gamma\}}\varepsilon + D^{\{\alpha\beta\gamma\}}\varepsilon_s{}^{I} \tag{3. 106}$$

However, computation of the terms in Equations 25-27 depends on the mesoscale subcell properties. The stress ($\sigma^{\{\alpha\beta\gamma\}}$), plastic strain ($\varepsilon^{I\{\alpha\beta\gamma\}}$), and stiffness ($C^{\{\alpha\beta\gamma\}}$) are computed differently depending if it is a multiphase or single phase subcell.

If $\{\alpha\beta\gamma\} = \text{single phase}$

$$\sigma^{\{\alpha\beta\gamma\}} = C^{\{\alpha\beta\gamma\}}\left(\varepsilon^{\{\alpha\beta\gamma\}} - \varepsilon^{I\{\alpha\beta\gamma\}}\right) \tag{3. 107}$$

$$\textit{Constituve Model} \rightarrow C^{\{\alpha\beta\gamma\}}, \varepsilon^{I\{\alpha\beta\gamma\}} \tag{3. 108}$$

Elseif $\{\alpha\beta\gamma\} = \text{multiphase}$

$$\sigma^{\{\alpha\beta\gamma\}} = \frac{1}{D_\alpha H_\beta L_\gamma}\sum_{\{\alpha\beta\gamma\}\alpha=1}^{N_{\{\alpha\beta\gamma\}\alpha}}\sum_{\{\alpha\beta\gamma\}\beta=1}^{N_{\{\alpha\beta\gamma\}\beta}}\sum_{\{\alpha\beta\gamma\}\gamma=1}^{N_{\{\alpha\beta\gamma\}\gamma}}\sigma^{\{\alpha\beta\gamma\}\{\alpha\beta\gamma\}}D_{\{\alpha\beta\gamma\}\alpha}H_{\{\alpha\beta\gamma\}\beta}L_{\{\alpha\beta\gamma\}\gamma} \tag{3. 109}$$

$$C^{\{\alpha\beta\gamma\}} = \frac{1}{D_\alpha H_\beta L_\gamma}\sum_{\{\alpha\beta\gamma\}\alpha=1}^{N_{\{\alpha\beta\gamma\}\alpha}}\sum_{\{\alpha\beta\gamma\}\beta=1}^{N_{\{\alpha\beta\gamma\}\beta}}\sum_{\{\alpha\beta\gamma\}\gamma=1}^{N_{\{\alpha\beta\gamma\}\gamma}}\cdots C^{\{\alpha\beta\gamma\}\{\alpha\beta\gamma\}}A^{\{\alpha\beta\gamma\}\{\alpha\beta\gamma\}}D_{\{\alpha\beta\gamma\}\alpha}H_{\{\alpha\beta\gamma\}\beta}L_{\{\alpha\beta\gamma\}\gamma} \tag{3. 110}$$

$$\varepsilon^{I\{\alpha\beta\gamma\}} = \frac{-C^{\{\alpha\beta\gamma\}^{-1}}}{D_\alpha H_\beta L_\gamma}\sum_{\{\alpha\beta\gamma\}\alpha=1}^{N_{\{\alpha\beta\gamma\}\alpha}}\sum_{\{\alpha\beta\gamma\}\beta=1}^{N_{\{\alpha\beta\gamma\}\beta}}\sum_{\{\alpha\beta\gamma\}\gamma=1}^{N_{\{\alpha\beta\gamma\}\gamma}}\cdots \left[D_{\{\alpha\beta\gamma\}\alpha}H_{\{\alpha\beta\gamma\}\beta}L_{\{\alpha\beta\gamma\}\gamma}C^{\{\alpha\beta\gamma\}\{\alpha\beta\gamma\}}\left(D^{\{\alpha\beta\gamma\}\{\alpha\beta\gamma\}}\varepsilon_s^{I\{\alpha\beta\gamma\}\{\alpha\beta\gamma\}} - \varepsilon^{\,I\{\alpha\beta\gamma\}\{\alpha\beta\gamma\}}\right)\right] \tag{3. 111}$$

In addition, the multiphase subcell must also obey the governing constitutive law of

$$\sigma^{\{\alpha\beta\gamma\}} = C^{\{\alpha\beta\gamma\}}\left(\varepsilon^{\{\alpha\beta\gamma\}} - \varepsilon^{I\{\alpha\beta\gamma\}}\right) \tag{3. 112}$$

Finally, the parameters at the microscale (constituents of the mesoscale RUC), can be determined. First, the localized strain is computed through:

$$\varepsilon^{\{\alpha\beta\gamma\}\{\alpha\beta\gamma\}} = A^{\{\alpha\beta\gamma\}\{\alpha\beta\gamma\}}\varepsilon^{\{\alpha\beta\gamma\}} + D^{\{\alpha\beta\gamma\}\{\alpha\beta\gamma\}}\varepsilon_s{}^{I\{\alpha\beta\gamma\}} \tag{3. 113}$$

The stress, stiffness and plastic strain at the microscale are determined as follows:

$$\sigma^{\{\alpha\beta\gamma\}\{\alpha\beta\gamma\}} = C^{\{\alpha\beta\gamma\}\{\alpha\beta\gamma\}}\left(\varepsilon^{\{\alpha\beta\gamma\}\{\alpha\beta\gamma\}} - \varepsilon^{I\{\alpha\beta\gamma\}\{\alpha\beta\gamma\}}\right) \tag{3. 114}$$

$$\textit{Constituve Model} \rightarrow C^{\{\alpha\beta\gamma\}\{\alpha\beta\gamma\}}, \varepsilon^{I\{\alpha\beta\gamma\}\{\alpha\beta\gamma\}} \tag{3. 115}$$

Through substitution, the stress for any microscale subcell can be written in terms of the globally applied strains and local plastic strains at every length scale.

$$\sigma^{\{\alpha\beta\gamma\}\{\alpha\beta g\}} = C^{\{\alpha\beta\gamma\}\{\alpha\beta g\}}\begin{pmatrix} A^{\{\alpha\beta\gamma\}\{\alpha\beta\gamma\}}A^{\{\alpha\beta\gamma\}}\varepsilon + A^{\{\alpha\beta\gamma\}\{\alpha\beta\gamma\}}D^{\{\alpha\beta\gamma\}}\varepsilon_s{}^{I} \\ +D^{\{\alpha\beta\gamma\}\{\alpha\beta\gamma\}}\varepsilon_s{}^{I\{\alpha\beta\gamma\}} - \varepsilon^{I\{\alpha\beta\gamma\}\{\alpha\beta g\}} \end{pmatrix} \tag{3. 116}$$

There are four terms in the previous equations and the meaning of each term is easily recognized. The first two terms are localization terms from pervious length scales. The first showing the effect of the globally applied strain and the second illustrating the effect of plasticity from all the mesoscale subcells. The third term reflects the effects of plasticity from all the microscale subcells of a given

mesoscale subcell. The fourth term is the local plasticity of that subcell. This shows that the stresses at the microscale are fully coupled to the strains at all length scales and in addition coupled to all the stiffness matrices through the concentration matrices A and D. Similarly the macroscale stress and stiffness can be written in terms of local fields.

$$C = \frac{1}{DHL}\sum_{\alpha=1}^{N_\alpha}\sum_{\beta=1}^{N_\beta}\sum_{\gamma=1}^{N_\gamma}\ldots \left\{\begin{array}{c} C^{\{\alpha\beta\gamma\}} \\ or \\ \dfrac{1}{D_\alpha H_\beta L_\gamma}\displaystyle\sum_{\{\alpha\beta\gamma\}\alpha=1}^{N_{\{\alpha\beta\gamma\}\alpha}}\sum_{\{\alpha\beta\gamma\}\beta=1}^{N_{\{\alpha\beta\gamma\}\beta}}\sum_{\{\alpha\beta\gamma\}\gamma=1}^{N_{\{\alpha\beta\gamma\}\gamma}}\ldots \\ C^{\{\alpha\beta\gamma\}\{\alpha\beta\gamma\}}A^{\{\alpha\beta\gamma\}\{\alpha\beta\gamma\}}D_{\{\alpha\beta\gamma\}\alpha}H_{\{\alpha\beta\gamma\}\beta}L_{\{\alpha\beta\gamma\}\gamma} \end{array}\right\} A^{\{\alpha\beta\gamma\}}D_\alpha H_\beta L_\gamma \tag{3. 117}$$

$$\sigma = \frac{1}{DHL}\sum_{\alpha=1}^{N_\alpha}\sum_{\beta=1}^{N_\beta}\sum_{\gamma=1}^{N_\gamma}\left\{\begin{array}{c} \sigma^{\{\alpha\beta\gamma\}} \\ or \\ \dfrac{1}{D_\alpha H_\beta L_\gamma}\displaystyle\sum_{\{\alpha\beta\gamma\}\alpha=1}^{N_{\{\alpha\beta\gamma\}\alpha}}\sum_{\{\alpha\beta\gamma\}\beta=1}^{N_{\{\alpha\beta\gamma\}\beta}}\sum_{\{\alpha\beta\gamma\}\gamma=1}^{N_{\{\alpha\beta\gamma\}\gamma}}\ldots \\ \sigma^{\{\alpha\beta\gamma\}\{\alpha\beta\gamma\}}D_{\{\alpha\beta\gamma\}\alpha}H_{\{\alpha\beta\gamma\}\beta}L_{\{\alpha\beta\gamma\}\gamma} \end{array}\right\} D_\alpha H_\beta L_\gamma \tag{3. 118}$$

To solve the numerical solution for the coupled set of multiscale equations a generalized forward Euler integration formulation for the MSGMC methodology is presented. MSGMC is broken down into two steps, an initialization procedure and incremental solution. The initialization procedure is

described in Fig. 3.5. This procedure involves determining the initial stiffness for each subcell (every length scale). The effective stiffness at every length scale is also determined through homogenization. The incremental solution is outlined in Fig. 3.6. The incremental procedure is a forward Euler scheme that uses the previous increments stiffness and inelastic strains to move forward. In each increment, using the previous stiffness and inelastic strains, the concentration matrices, *A* and *D*, are solved for then the local strain increments in each subcell are determined based on global applied loads. If the stiffness of the subcells remains unchanged, then the concentration matrices, *A* and *D* do not need to be recalculated, saving significant computation effort. At each length scale after homogenization, a check for convergence is critical to verify that the forward Euler step size is sufficiently small. Verification that Equations 13 and 15 and Equations 8 and 9 yield the same answer to tolerance is useful consideration. Verifying that the predicted global stress at the beginning of the increment is equivalent to the global stress at the end of the increment is also useful. Similarly, if a damage mechanics model is being employed verifying a scalar representative of the stiffness, such as the determinant, remains unchanged with tolerance at the beginning and end of the increment is also an indication of convergence.

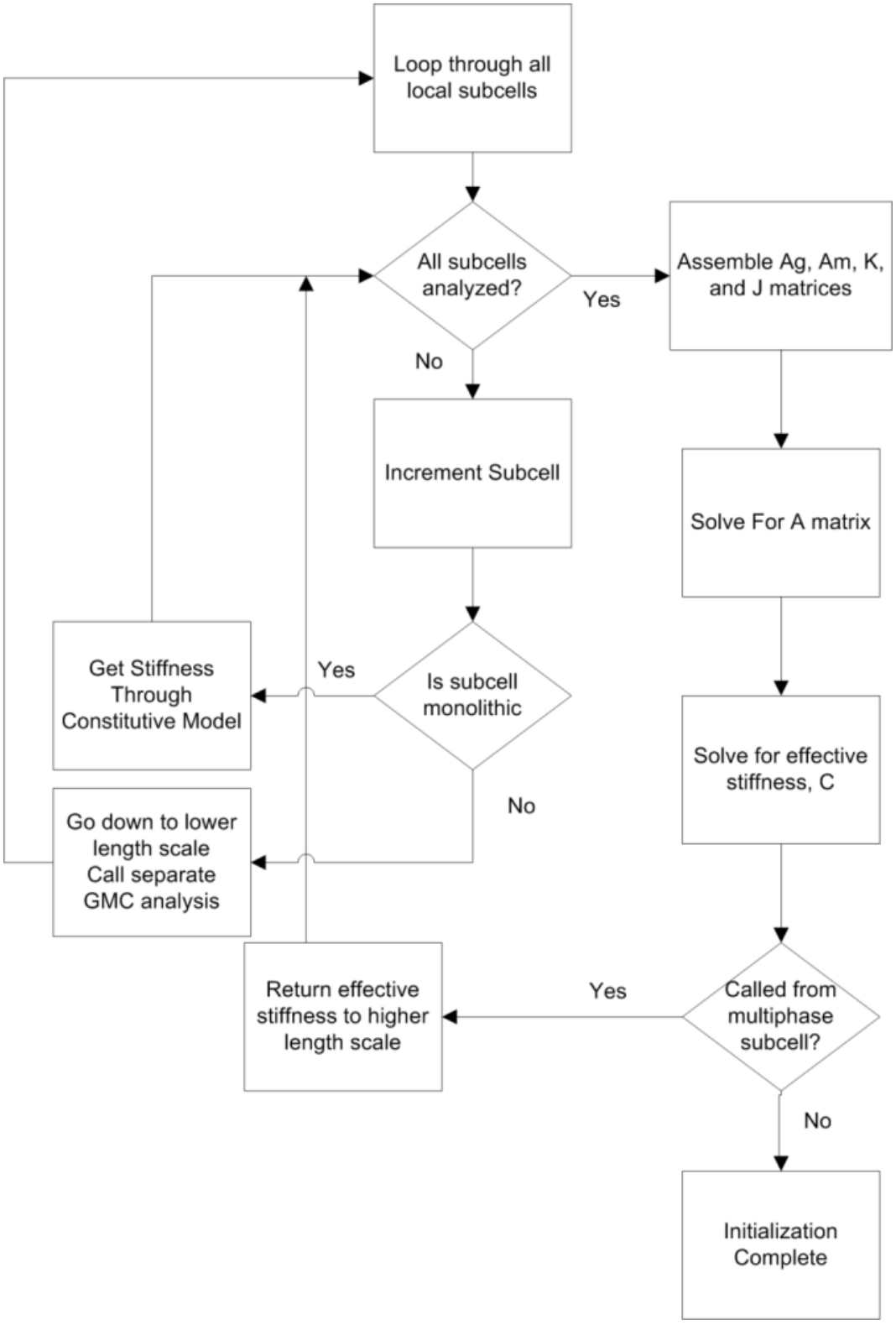

Fig. 3.5 Initialization Flow Chart for MSGMC

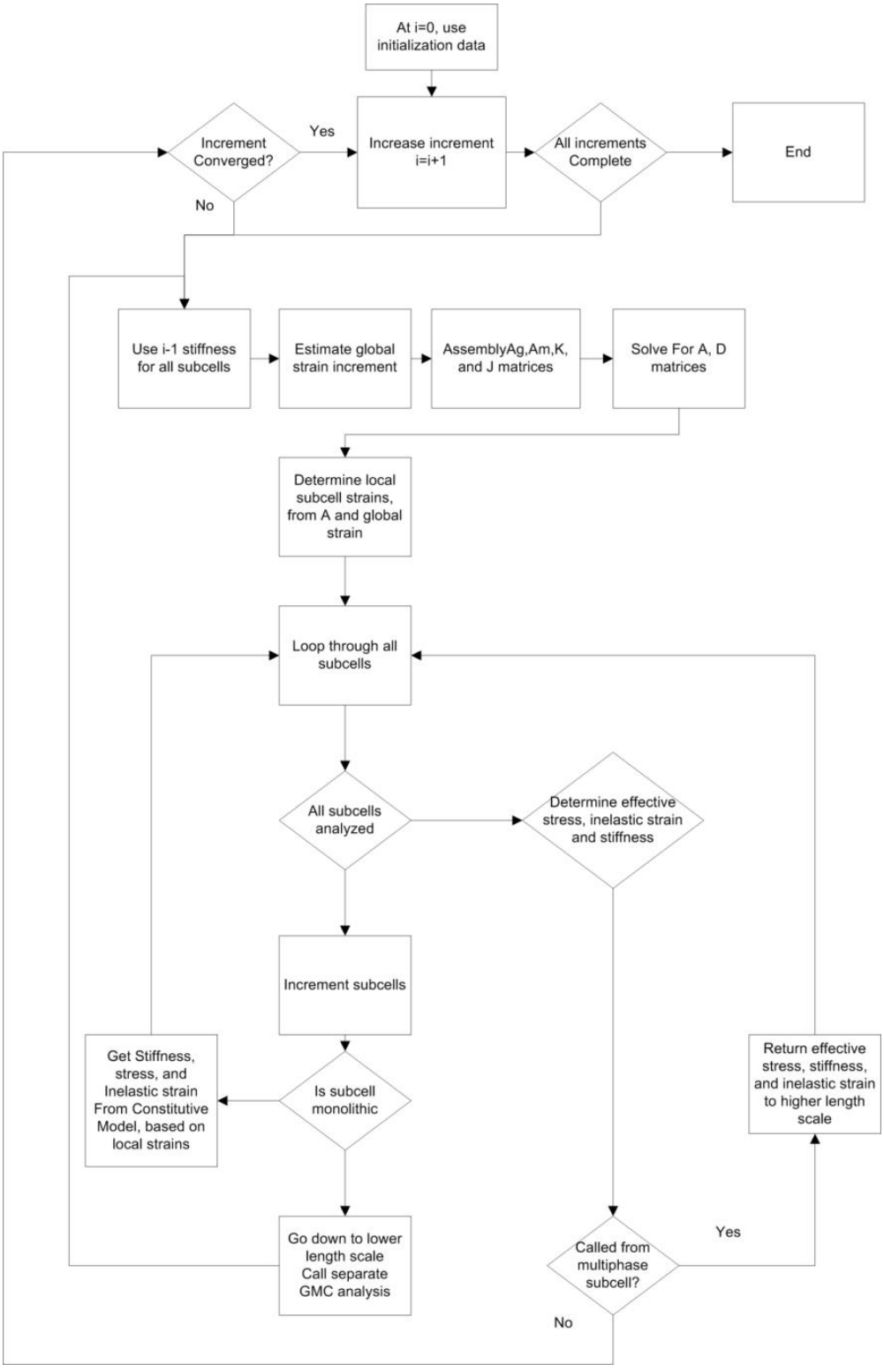

Fig. 3.6 Incremental Flow Chart for MSGMC

3.6 Application to Textile/Braided Composites

To apply MSGMC to modeling of textile and braided composites, the relevant length scales need to be identified and the material has to be characterized. The critical length scales can be seen in Fig. 3.1. These are identified as the micro, meso, and macroscales. At the microscale, the constituents namely the fiber and matrix are modeled for the constitutive response and failure. At the mesoscale, the fiber tow bundles, specifically the RUC for the fiber/matrix is modeled. Lastly at the macroscale, the weave architecture is modeled. A discretized problem for a plain weave composite is shown in Fig. 3.7.

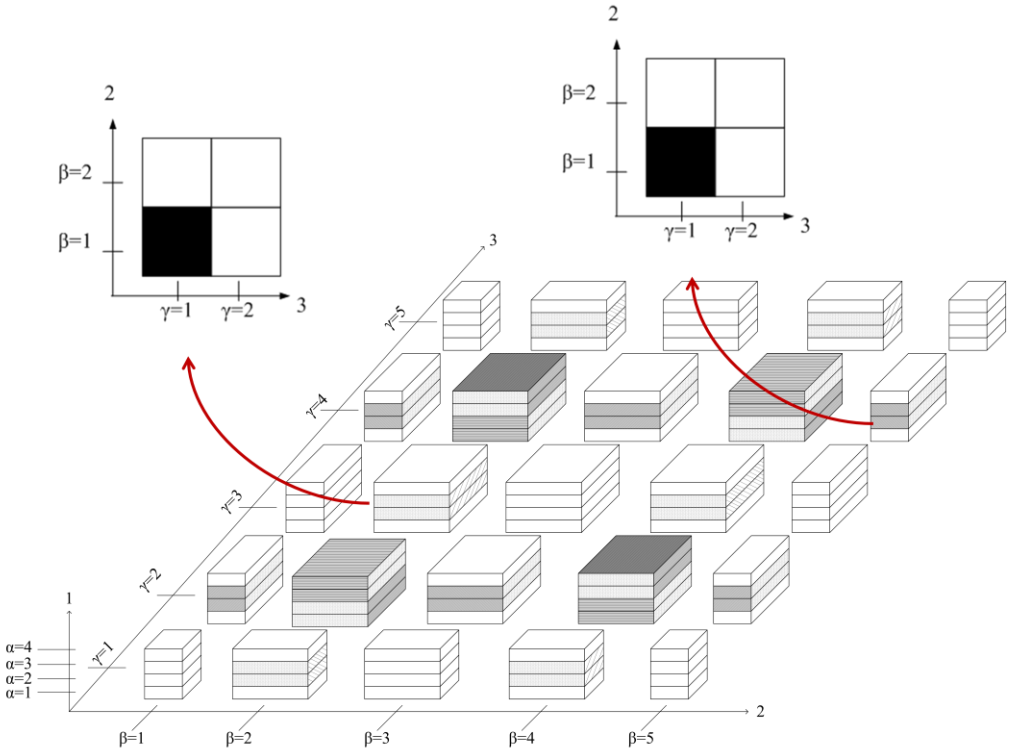

Fig. 3.7 MSGMC Applied to Textile Composites

3.6.1 Microscale

The Multiscale Generalized Method of Cells (MSGMC) is used to represents the woven fabric composite starting with its constituent materials, i.e. the fiber (monofilament) and matrix progress up the various length scales. The microscale is the only length scale where explicit constitutive models are applied to the various phases (e.g. fiber and matrix). Stress states and tangent moduli for larger length scales are determined through the Generalized Method of Cells (GMC) triply-periodic homogenization procedure developed by Aboudi[3]. The monofilament fibers are modeled using a linear elastic relationship, i.e. Hooke's Law, and the matrix material can be represented various constitutive models such as classical incremental plasticity based on a von Mises yield surface, viscoplasticity and damage mechanics..

3.6.2 Mesoscale

The mesoscale is used to represent the period structure of a fiber tow. At the mesoscale, there are two significant architectural parameters: fiber packing and tow volume fraction. Both of these parameters govern the mesoscale subcell geometries. The response of the mesoscale is subject to these parameters as well as the material variation at the microscale. The continuous fiber tows are assumed to be represented by a doubly-periodic RUC of dimensions h by l consisting of constituents from the microscale. An example of such an RUC discretized for GMC is shown in Fig. 2.16, where the inner region (shown in grey) denotes the fiber tow and the outer region (shown in white) is the matrix. The RUC is discretized in such a manner that it is composed of $N_\beta \times N_\gamma$ rectangular subcells,

with each subcell having dimensions $h_\beta \times l_\gamma$. From this point forward, superscripts with lowercase Greek letters denote a specific subcell at the microscale, superscripts of uppercase Greek letters denote a specific subcell at the macroscale and superscripts with lowercase Roman letters denotes macroscale variables. Fiber tow packing and volume fraction typically govern the architecture of the mesoscale RUC but must be in accordance with the previously described RUC microstructural parameters. The resulting stress in the fiber tow can be determined from the GMC homogenization process, where in GMC, the current stress and current tangent moduli of a particular fiber tow at a point are determined through a volume averaging integral over the repeating unit cell. This process is represented by the summation in the following equations, producing the first homogenization in the multiscale modeling framework. In these equations, σ denotes the Cauchy true stress, A denotes the strain concentration matrix, and C denotes the stiffness matrix[2,3]. The microscale subcell stresses and tangent moduli needed to complete the summation are determined through the applied constitutive models for each constituent based on their current strain state. The mesoscale strains, which are used as the boundary conditions for the GMC analysis, are determined from the through thickness (tt) homogenization at the macroscale. The subscripts tt in the concentration matrix and denote the 2nd portion of the two step homogenization process discussed later.

3.6.3 Macroscale

At the macroscale the RUC for the weave fabric is modeled. At this scale, the architecture is governed by the overall volume fraction, tow geometry (aspect

ratio, width and thickness), and overall fabric thickness, wherein the subcell "constituent" response is obviously dependent on the mesoscale and microscale responses. The weave requires a triply-periodic RUC representation, of size $D \times H \times L$ and discretized into $N_A \times N_B \times N_\Gamma$ parallelepiped subcells, with each subcell having dimensions $D_A \times H_B \times L_\Gamma$. At this length scale, a two step homogenization procedure was employed to determine the stiffness and macroscale stresses. This is to overcome the lack of shear coupling inherent to the GMC formulation[5]. The first step involves a through thickness homogenization and the second step is an in-plane homogenization, where subscripts tt and ip denote through thickness and in-plane respectively. Details for the subcell geometry and RUC information can be found in Ref. 5 and 6.

3.7 Future Work

The research presented in this chapter was based off of first order displacement field assumptions, which result in first order strain and stress fields. Applying higher order displacement fields will result in a higher fidelity analysis and improve the accuracy of the model. There is a significant amount of research necessary to derive the proper relations and bridging between length scales for higher order theories, particularly in placing the appropriate boundary conditions. Unfortunately, one disadvantage to higher order techniques is the introduction of mesh or discretization dependency that is not present with first order techniques. Secondly, with a higher order formulation allows the use of isoparametric subvolumes as opposed to parallelpiped subvolumes with appropriate mapping

(see Fig. 3.7). This will allow an even further refined tow architecture to be captured.

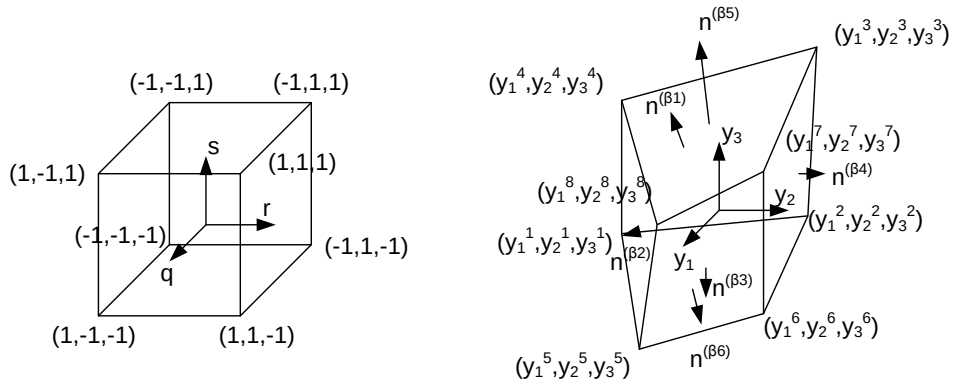

Fig. 3.7 Isoparametric Mapping

Lastly, nonlinear geometry effects, such as kinking and straightening of the fiber tow bundles are important for the accurate modeling of compression and high deformation.

Chapter 4

4. Modeling Polymeric Triaxially Braided Composites

4.1. Introduction

Triaxially braided composites (TriBCs) have been of interest for many years as replacements for metallic materials. A distinct design advantage of TriBCs is their ability to be tailored from quasi-isotropic to fully anisotropic material behavior. TriBCs have also shown a greater delamination resistance when compared to equivalent unidirectional laminates. There are numerous advantages for TriBCs, but a key disadvantage is the predictive challenge associated with the mechanical response of this material. This disadvantage initiates for two reasons: first, the repeating unit cell (RUC) microstructure is complex when considering application of traditional micromechanical methods, which tend to approximate composite microstructures; second, the microstructural length scale is often not insignificant when compared to that of the overall structure and thus the analysis is often thought of as a structural analysis, more so than a micromechanical analysis.

4.2. Effective Elastic Properties

A simple application of this multiscale methodology is the prediction of effective elastic properties at the macroscale. To validate this methodology, predictive results are compared to experimental and finite-element data for a T700/E862 material system with 56% fiber volume fraction. Using the multiscale modeling methodology, the elastic properties for the macroscale RUC are predicted for a varying volume fraction and braid angle and compared with

Table 4.1 Constituent Elastic Properties of T700/E862 Material System

	Axial Modulus (GPa)	Transverse Modulus (GPa)	Axial Poisson's Ratio	Transverse Poisson's Ratio	Shear Modulus (GPa)
T700	230	15	0.2	0.2	15
E862	2.7	2.7	0.35	0.35	1.0

limited experimental and finite-element results (Littell 2008). For the mesoscale RUC, the generalized method of cells RUC, which is a 2 × 2 RUC, was applied. The linear elastic constituent properties used for the analysis are presented in Table 4.1. The architectural properties can be found in Table 4.2. Results are also compared to classical lamination theory for reference. The predicted transverse Young's, in-plane shear, and axial Young's moduli of the 56% triaxially braided T700/E862 composite, as a function of braid angle and fiber volume fraction, are plotted in Fig. 4.1. The two RUCs bounded the predicted moduli for both axial and transverse moduli. The simplified RUC resulted in slightly stiffer properties, whereas the refined RUC presented slightly compliant properties. The coarse and refined models once again bounded the shear modulus results. Digital image correlation showed nonuniform state of shear strain in the gauge section. Due to the inherently large RUC size of the TriBC, there was difficulty in measuring the macroscale properties. Future tubular test specimens are therefore planned. Results show good correlation to both the experimental and finite-element results. In most cases, the simplified RUC and CLT followed similar trends. The CLT results are in good agreement with the multiscale GMC results for the transverse modulus for variation of braid angle, but the shear and axial moduli differ greatly. This is due in part to the limitations of using CLT directly without modification.

When using CLT, the thicknesses of equivalent laminates must be varied to enforce that the overall fiber volume fraction in each direction is enforced. For a 60° braid, the volume fractions are equal transversally and axially, so CLT works well directly. For other brand angles this is not the case and must be accounted for.

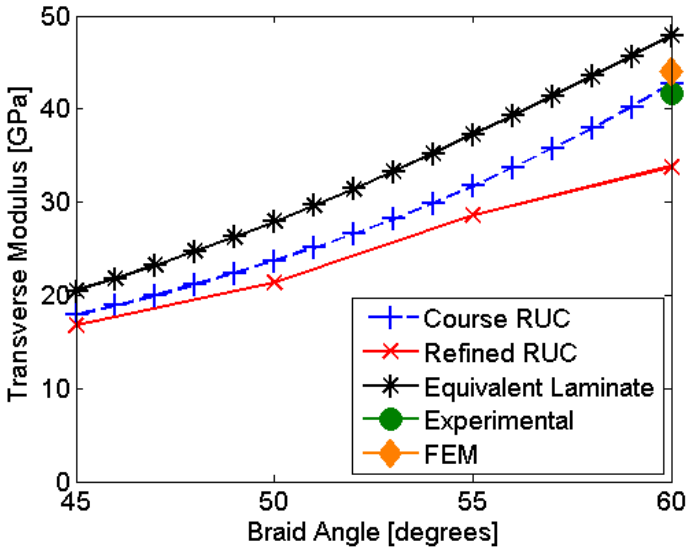

a) Transverse Modulus Versus Braid Angle

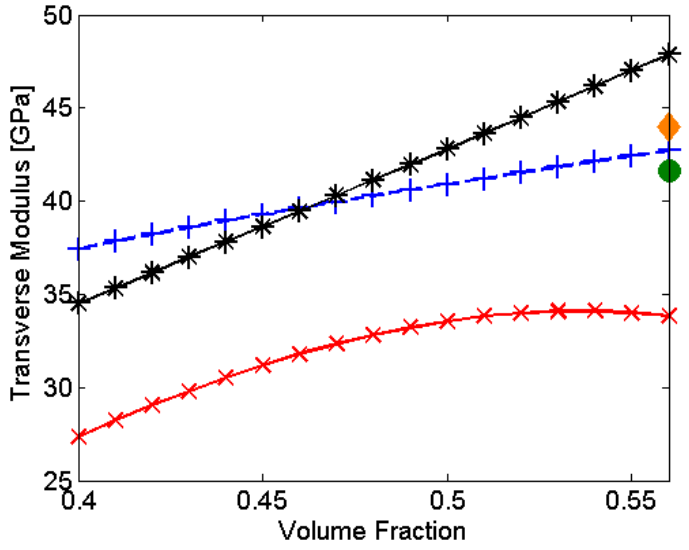

b) Transverse Modulus Volume Fraction

Fig. 4.1 Elastic properties varied with braid angle and fiber volume fraction:

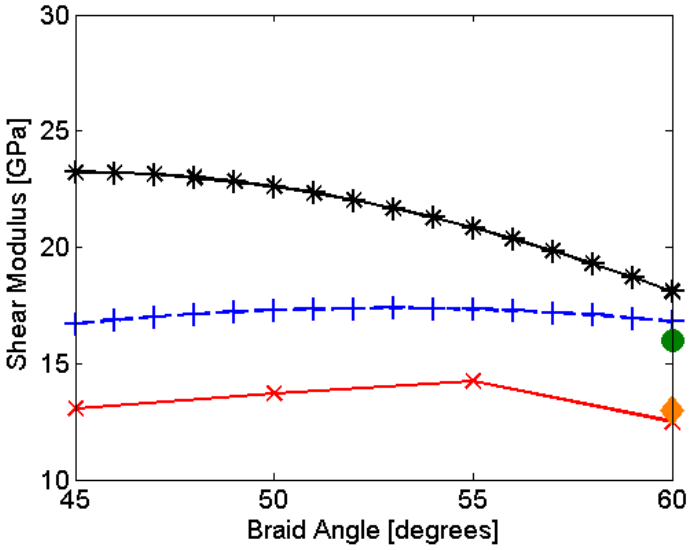

c) Shear Modulus Versus Braid Angle

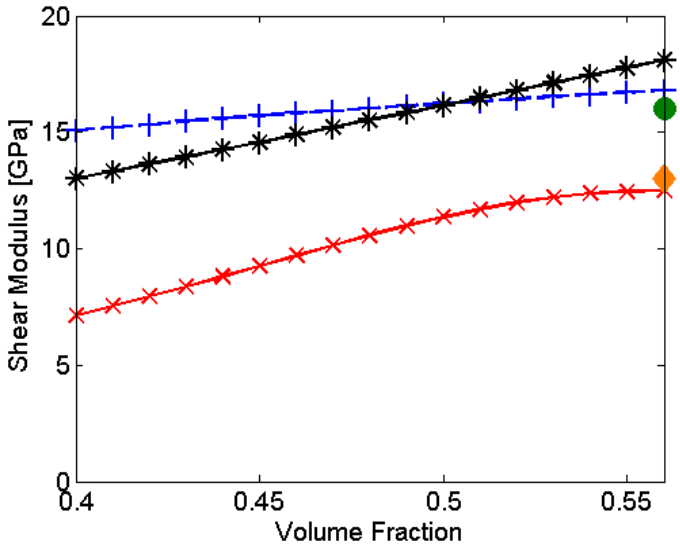

d) Shear Modulus Versus Volume Fraction

Fig. 4.1 (contd.) Elastic properties varied with braid angle and fiber volume fraction:

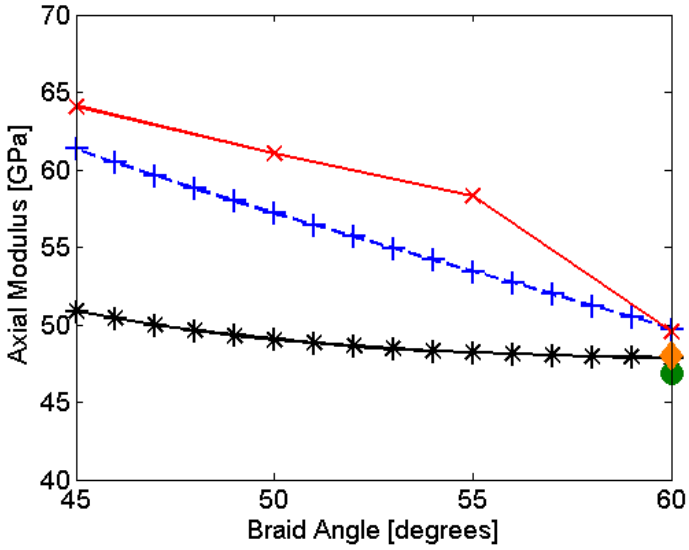

e) Axial Modulus Versus Braid Angle

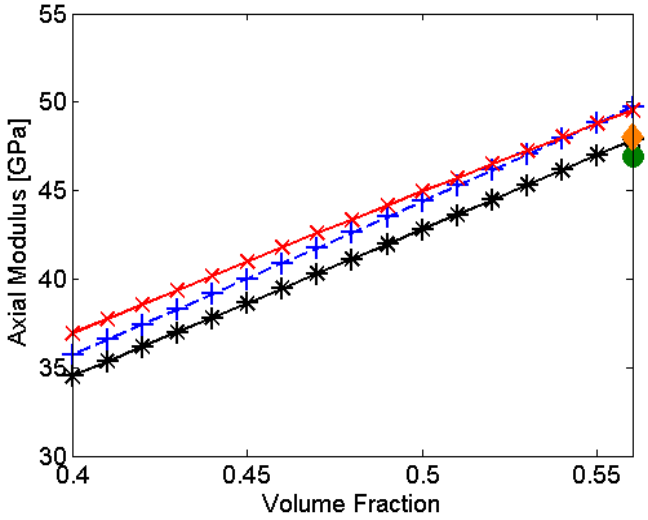

f) Axial Modulus Versus Volume Fraction

Fig. 4.1 (contd.) Elastic properties varied with braid angle and fiber volume fraction:

Lastly, the local fields for the refined RUC can be determined through MSGMC. For the case of transverse loads the homogenized through thickness strains along the loading direction are contour plotted. A reference RUC is plotted beside the strain contour plot for comparison purposes. The resin rich pocket

regions (red color in the contour plot) show high strain concentrations and similarly the resign rich regions between parallel braid tows also show a high strain concentration then the average field. This capability allows for accurate prediction of architecture dependent damage from various length scales.

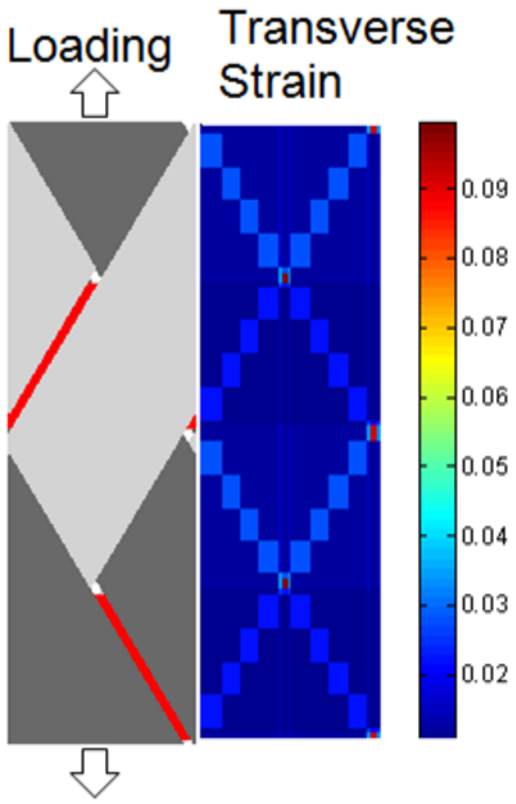

Fig. 4.2 Local Field Strain Distribution within a Refined RUC for T700/PR520 Triaxial Braided Composite

4.3. Classical Plasticity With Fiber Failure

Although predictions of elasticity constants are useful for the engineering community, it is more useful to predict the entire stress strain curve. The governing mechanism for nonlinearity is the polymer matrix. The polymer material experiences development of inelastic strain at all length scales and as

such the microscale constitutive model for the polymer should reflect that. To capture the inelastic response of the polymer, the classical J_2 incremental plasticity model with a nonlinear strain hardening law was employed. The particular formulation for this model however is derived in strain space was taken from (Bednarcyk 2004) and shown to be equivalent to the well known Radial Return technique. The yield criterion is given by

$$f = \varepsilon_{eq} - \frac{\kappa\left(\bar{\varepsilon}_p\right)}{3G} \tag{4. 1}$$

where ε_{eq} is the equivalent plastic strain defined by $\varepsilon_{eq} = \sqrt{\frac{2}{3} e'_{ij} e'_{ij}}$ and $e'_{ij} = \varepsilon_{ij} - \varepsilon_{kk} / 3$, $\kappa\left(\bar{\varepsilon}_p\right)$ is the hardening law which is a function of the equivalent plastic strain, and G is the shear modulus. The strain hardening law is given by

$$\kappa\left(\bar{\varepsilon}_p\right) = \sigma_Y + \frac{H}{A}\left(e^{-A\bar{\varepsilon}_p} - 1\right) \tag{4. 2}$$

where σ_Y is the yield stress and H and A are material parameters. The overall failure of the composite is governed by the fiber failure and a maximum strain failure criterion was used to simulate this (Eq. 4.2).

$$f = \varepsilon_{11}^f - X_A^f \tag{4. 3}$$

The strain failure of the fiber was assumed to be 2.1% based on manufacturer specification.

Table 4.2 Triaxially Braided Composite Parameters

Parameter	Value
V_f	0.56
$V_{f_{0^o}}$, $V_{f_{\pm\theta}}$	0.80
w_{0^o} , $w_{\pm\theta}$	3.5mm
θ	60 degrees
t_{0^o}	0.14mm
$t_{\pm\theta}$	0.07mm

The MSGMC analysis results are validated with experimental data for tension and shear tests. Table 4.2 lists the architectural parameters and Table 4.3 and 4.4 lists the material parameters used in the analysis. TriBCs are not truly quasi-isotropic and exhibit some orthotropy, thus it is necessary to investigate both the axial and transverse response. The predictions of the overall composite response, shown in Fig. 4.2, show very good correlation in the axial response with slight under and over predicted failure in the shear and transverse response, respectively. This result is important as it demonstrates that analyzing multiple length scales with nonlinearity and failure can provide accurate predictive

Table 4.3 Constituent Elastic Properties of T700/PR520 Material System

	Axial Modulus (GPa)	Transverse Modulus (GPa)	Axial Poisson's Ratio	Transverse Poisson's Ratio	Shear Modulus (GPa)
T700	230	15	0.2	0.2	15
PR520	3.54	3.54	0.38	0.38	1.28

responses of complex architectures. Plastic strain versus total strain is shown in Fig. 4.3. It can be seen that the shear loading produces most plastic strain followed by transverse and then axial loading. It should also be noted that under transverse loading, the rate of plastic strain is much higher than the other two loading conditions.

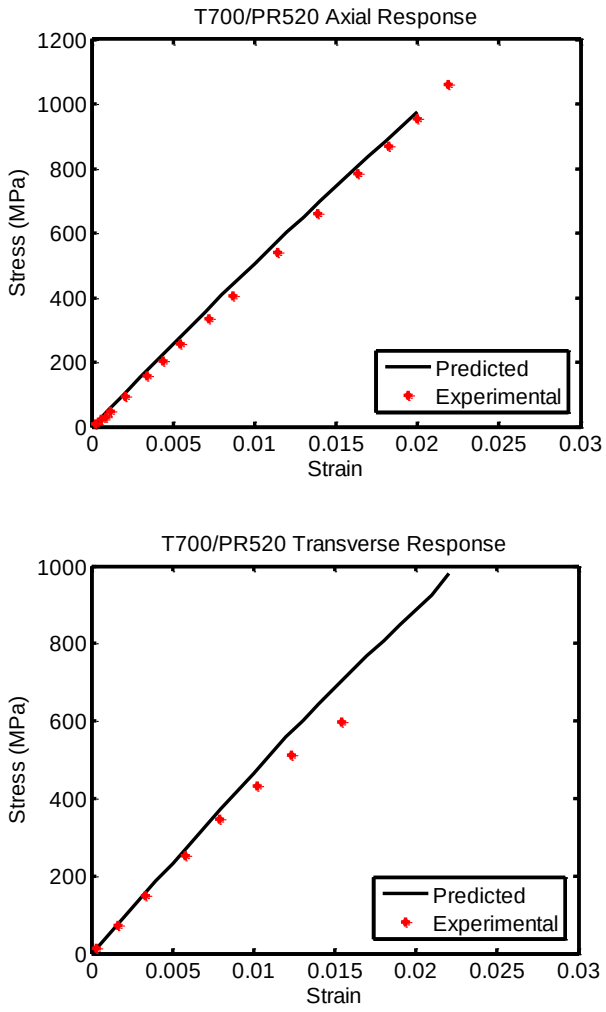

Fig. 4.3 Inelastic Triaxially Braided Composite Stress Strain Curve

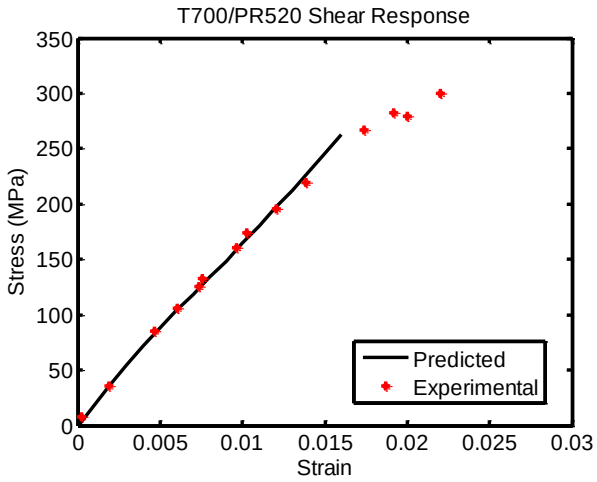

Fig. 4.3 (contd.) Inelastic Triaxially Braided Composite Stress Strain Curve

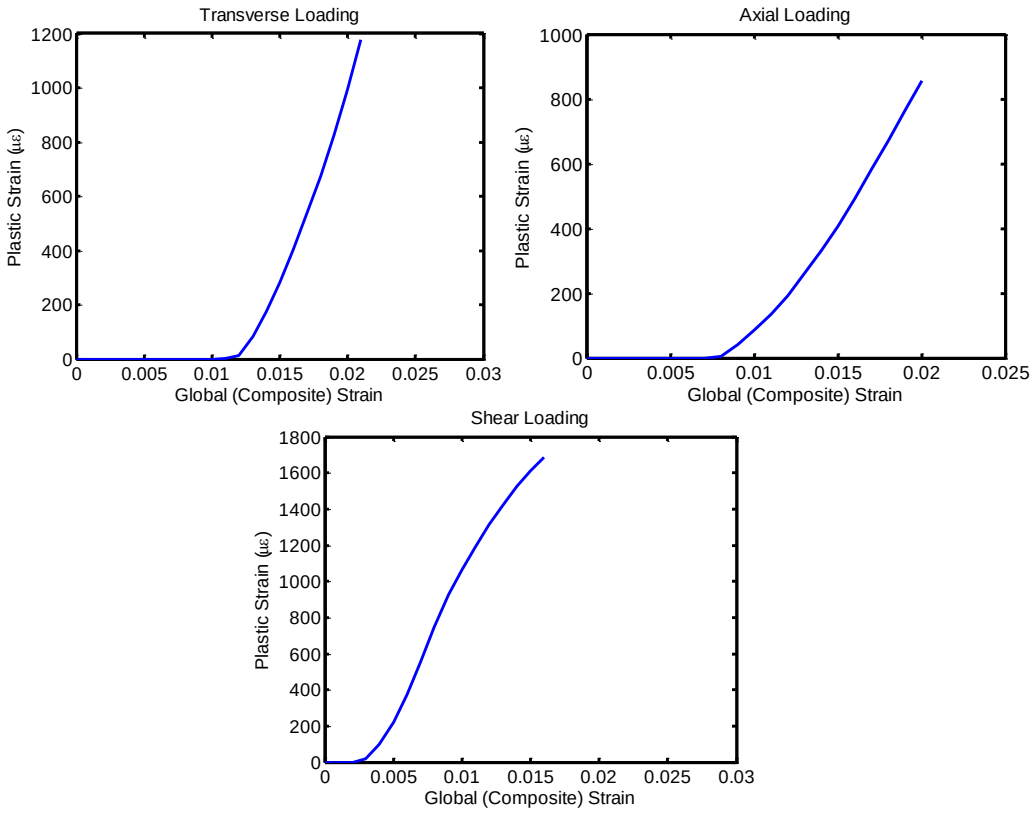

Fig. 4.4 Plastic Strain Versus Global Strain in Triaxially Braided Composite

Table 4.4 Plasticity Parameters for PR520 Material

	σ_Y (MPa)	H (MPa)	A
PR520	100	3333	0.1

One of the benefits of MSGMC is that it allows not only for the global predictive response shown previously, it provides insight to the mechanics behind the response. For example, under transverse loading, the composite stress of the RUC is shown in Fig. 4.3, but the local stresses of the tows (in local coordinates) can be computed and are shown in Fig. 4.5.

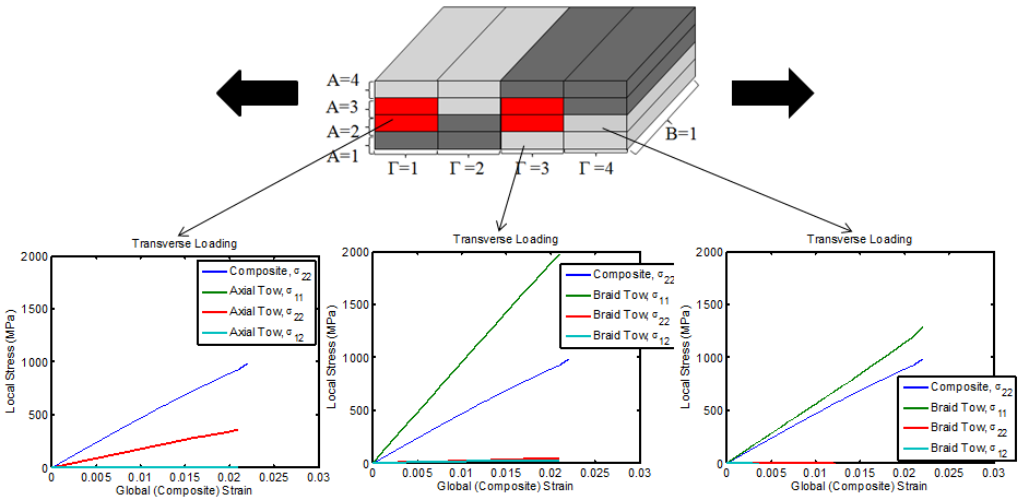

Fig. 4.5 TriBC Mesoscale Stress Distribution under Transverse Loading

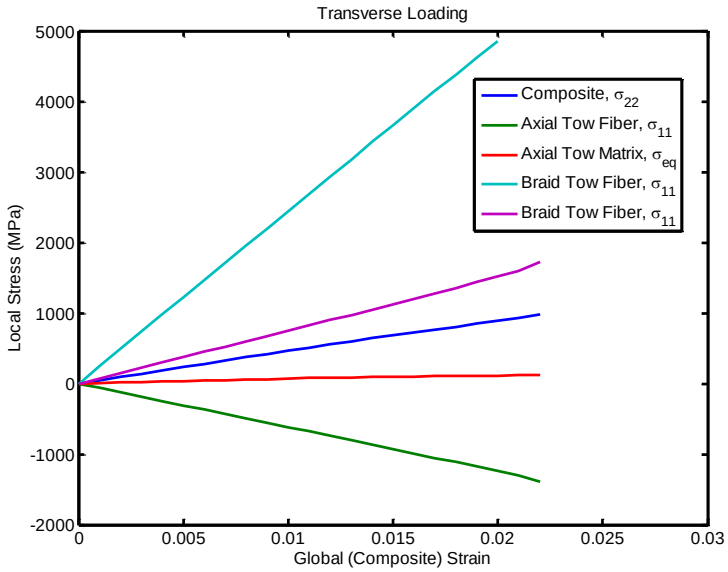

Fig. 4.6 TriBC Fiber Stresses at the Microscale under Transverse Loading

Furthermore, the axial stress in just the fiber can be plotted for each of the tows against the global strain shown in Fig. 4.6. The matrix stresses at the microscale were significantly less than those of the fiber. We can see that under transverse loading, the stresses in the braid tows far exceed that of the overall composite, however the axial tows do not carry a significant portion of the load.

Another important observation is the normalization of the stress in the tows with respect to the stress in the composite RUC, shown in Fig. 4.7. This allows an insight as to the proportion of the load being distributed internally in the composite RUC. From this plot is where the non linearity clearly becomes prevalent. In both braided tows, the axial stress begins to carry a higher percentage of the load with increasing strain. Subsequently, the stress in the axial tow must drop to maintain equilibrium. This is in an important result as it shows

that the stress distribution and load carrying response of the tows is not uniform with applied strain.

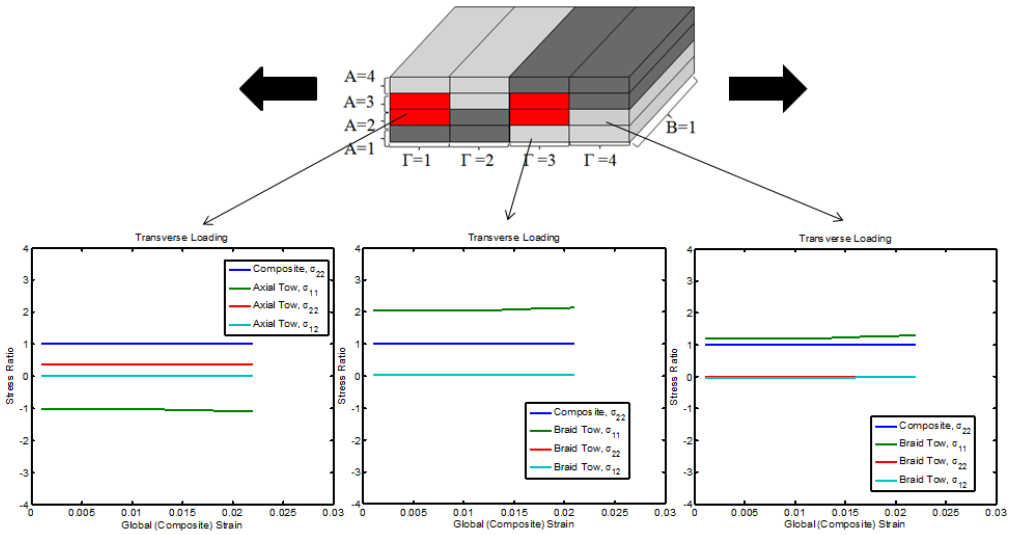

Fig. 4.7 TriBC Mesoscale Stress Ratio under Transverse Loading

The same results can be reproduced for both the axial and shear loadings as shown in Fig. 4.8 and Fig. 4.9, respectively. In the case of axial loading, it is clear that the axially aligned tows carry nearly all the load and the stress in the braided tows are close to zero. Furthermore, the axial fiber within the tows also carries the majority of this load. The opposite can be seen in the case of shear loading, where the braided tows carry the load and the axial tow is in a low stress state.

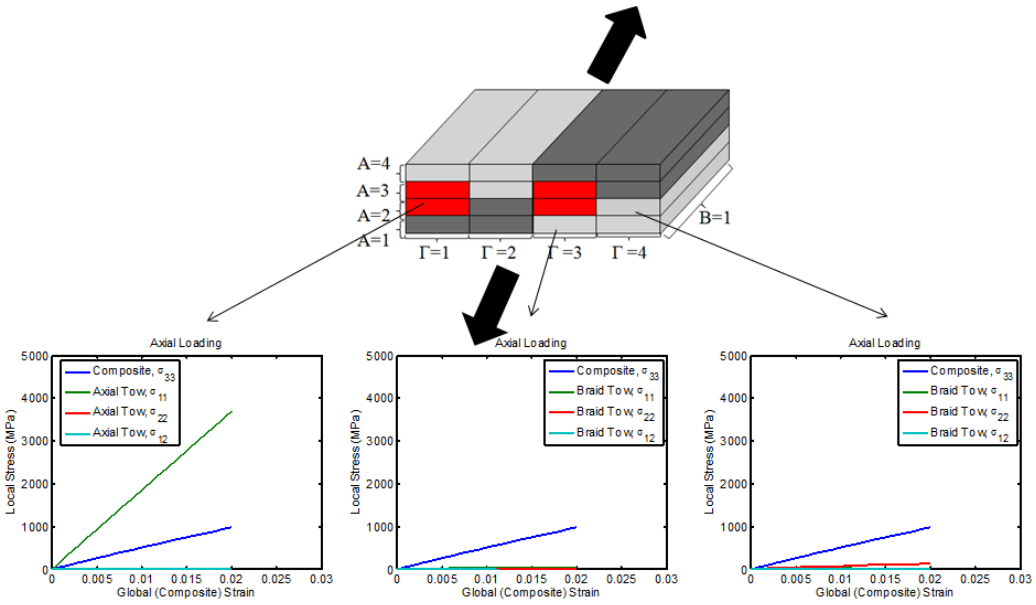

Fig. 4.8 TriBC Mesoscale Stress Distribution under Axial Loading

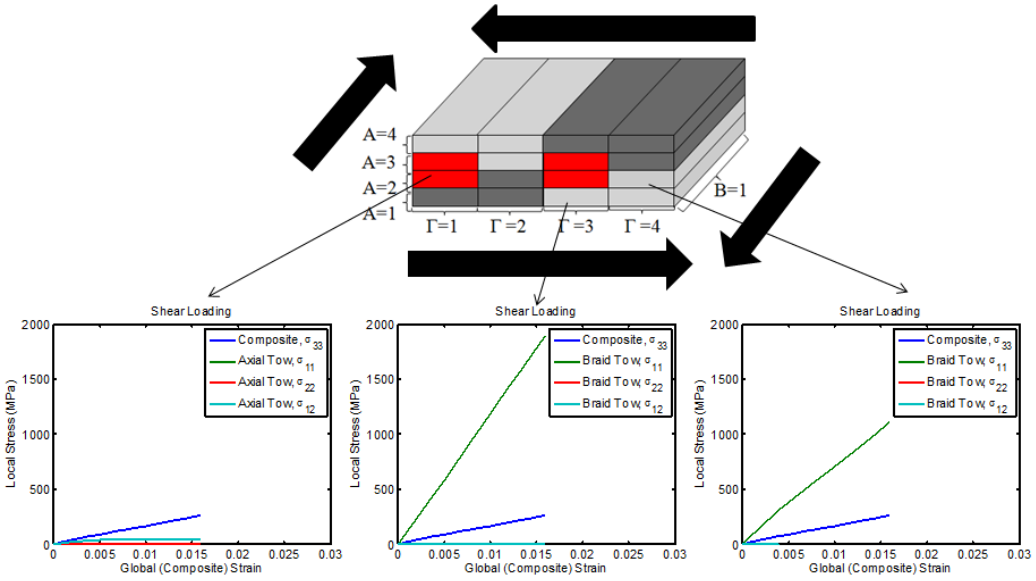

Fig. 4.9 TriBC Mesoscale Stress Distribution under Shear Loading

4.4. Viscoplastic Strain Rate Dependent Response with Constituent Failure

The viscoplasticity model developed by Goldberg, will be employed as it accurately captures the response of the polymer materials. A small modification to the model will be employed to enhance the accuracy in capturing the compressive

Table 4.5 Viscoplasticity Properties of PR520 Resin System

	D_0 (1/s)	n	Z_0 (MPa)	Z_1 (MPa)	α
PR520	$1x10^6$	0.93	396.09	753.82	0.0937

response of the material. The evolution of the state variable α, which controls the hydrostatic effects, was originally assumed to evolve in the same fashion as the Bodner Partom state variable Z, see Eqs 4.4 and 4.5. By using this evolution law it is difficult to characterize the response for tension and compression as the stress potential will always be small in compression. By keeping α constant the response can be accurately captured in compression. The modifications to the state variable evolution can be seen in the following equations.

$$\dot{\alpha} = q\left(\alpha_1 - \alpha\right)\dot{e}_e^I \tag{4. 4}$$

$$\dot{\alpha} = 0 \rightarrow \alpha = \alpha_1 \tag{4. 5}$$

The MSGMC analysis results are validated with experimental data for a T700/PR520 material system for tension and shear tests. Table 4.5 shows the key viscoplasticity parameters used in the analysis, while the architectural parameters can be found in Table 4.2 and elasticity parameters in Table 4.3. It is critical to accurately capture the nonlinear rate dependent response of the resin at the microscale, because its response governs the nonlinear response that the composite displays. The modified parameters for the PR520 resin system are shown in Table 4.5. As stated previously, the constitutive model presented by Goldberg was modified so that the state variable alpha does not evolve and then

recharactertized to better capture the compressive response of the resin. The following three figures showed the uniaxial response of the material in tension, compression, and shear. The experimental results were taken from Goldberg. The shear response is not dependent on the variable α because it acts only on the hydrostatic portion of the stress tensor, which is zero under pure shear. However, the compressive response, which was previously linear with no yielding or accumulation of plastic strain, now exhibits highly nonlinear behavior that is comparable to experimental data.

TriBCs are not truly quasi-isotropic and exhibit some orthotropy, thus it is necessary to investigate both the axial and transverse response. Experimental data was available for three strain rates for axial and transverse loading. These are labeled as high, medium and low strain rates. For the axial direction they were 5.2e-4/s, 6.4e-5/s, and 7.7e-6/s. For the transverse direction they were 5.12e-4/s, 8.00e-5/s, and 8.57e-6/s The predictions of the overall composite response, shown in Fig. 4.10 and Fig. 4.11, show very good correlation with the overlain experimental data in the axial response with slight under and over predicted failure in the shear and transverse response, respectively. This result is important as it demonstrates that analyzing multiple length scales with nonlinearity and failure can provide accurate predictive responses of complex architectures. The transverse experimental specimens show high nonlinearity, but this is due to the use of a straight sided specimen coupon. This coupon causes premature failure at the first ungripped fiber tow. This causes an artificial nonlinearity that is due to coupon structure not the material behavior, however a new specimen design has

been implemented but results are unavailable. Since the design and implementation of a test specimen that accurately captures a pure uniaxial transverse load is difficult and has not been fully implemented, the results from the multiscale model are assumed to better represent the true transverse response.

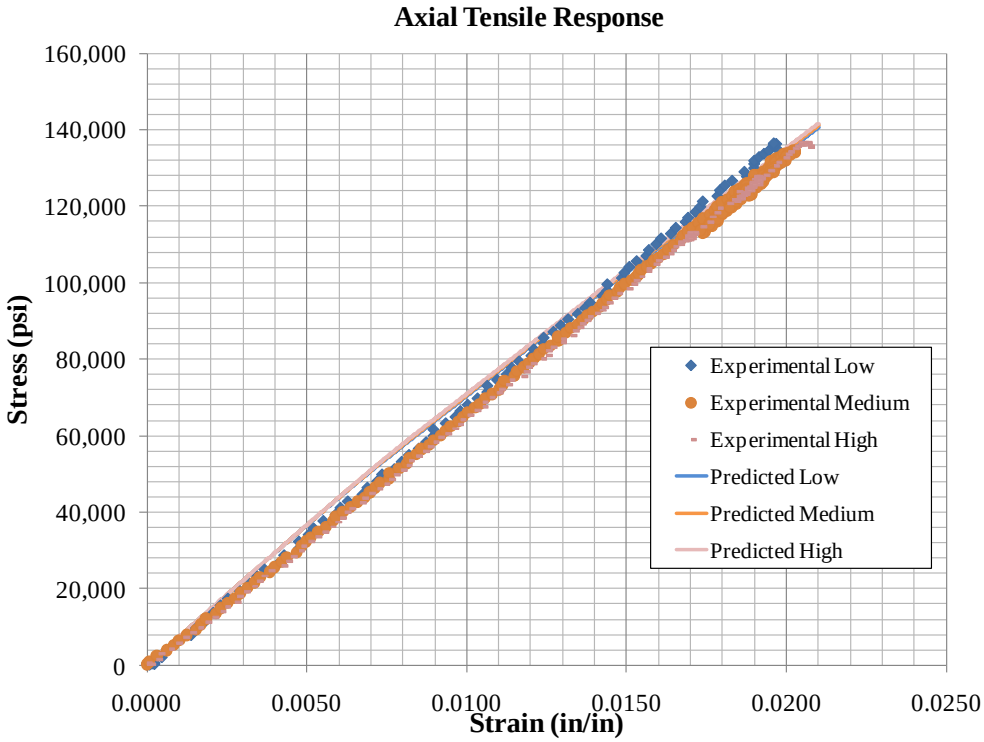

Fig. 4.10 TriBC Axial Tensile Constitutive Response Plotted Against Experimental Data

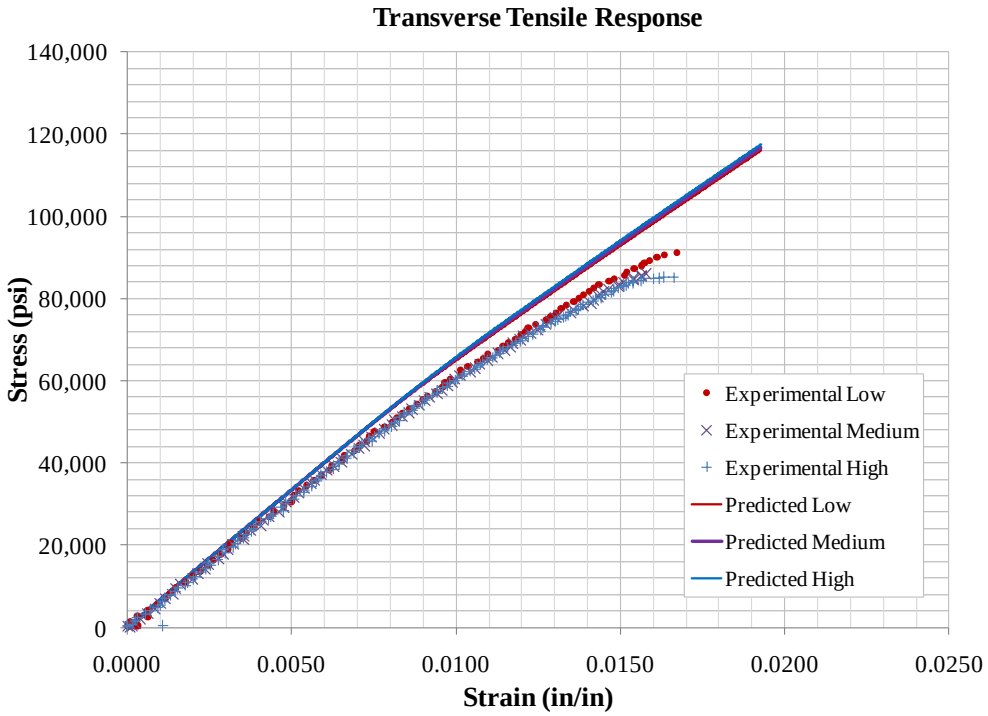

Fig. 4.11 TriBC Transverse Tensile Constitutive Response Plotted Against Experimental Data

Since the experimental data was limited to relatively low strain rates, several higher strain rate cases were carried out in order to study the rate effects. The strain rates seen in the experimental data are considered relatively slow, and at those rates, little rate dependence is seen in the resin itself. In Figs. 4.12-4.14 the strain rate dependent behavior is shown for various levels of strain rates listed in the legends. The results are presented for axial, transverse, and shear loading. Although the experimental results show little strain rate dependence, the predicted results for higher strain rates, those close to levels seen in high speed ballistic impact testing, do exhibit rate dependence. Even at the highest rates simulated, the results are still slightly nonlinear. Another important facet that has not yet

been explored is the rate dependent failure mechanisms of the polymer. Although overall failure is clearly governed by the failure of the fiber, the response in the nonloading directions can be greatly affected by the failure response of the polymer itself. Future work will be focused on implementing advanced and rate dependent failure criteria for polymers.

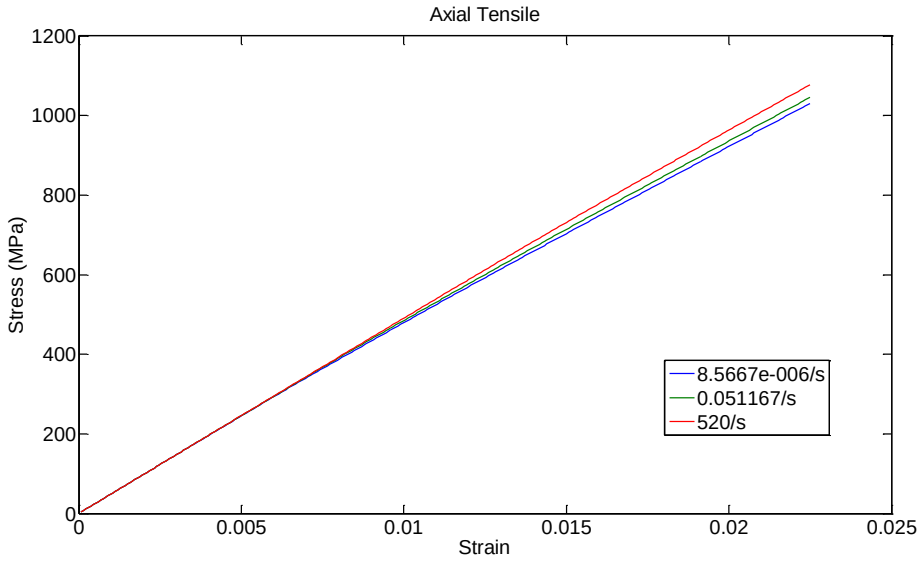

Fig. 4.12 TriBC Aixal Tensile Constitutive Predicted Response

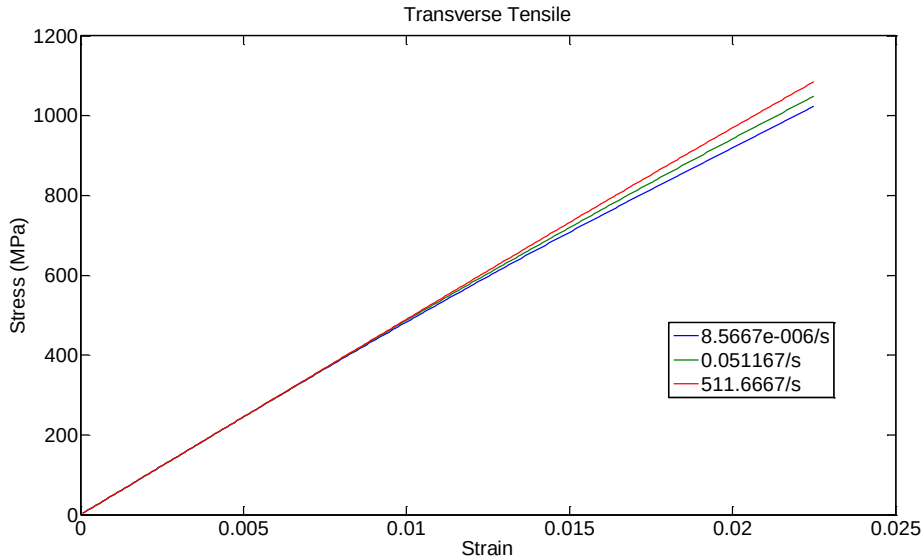

Fig. 4.13 TriBC Transverse Tensile Constitutive Predicted Response

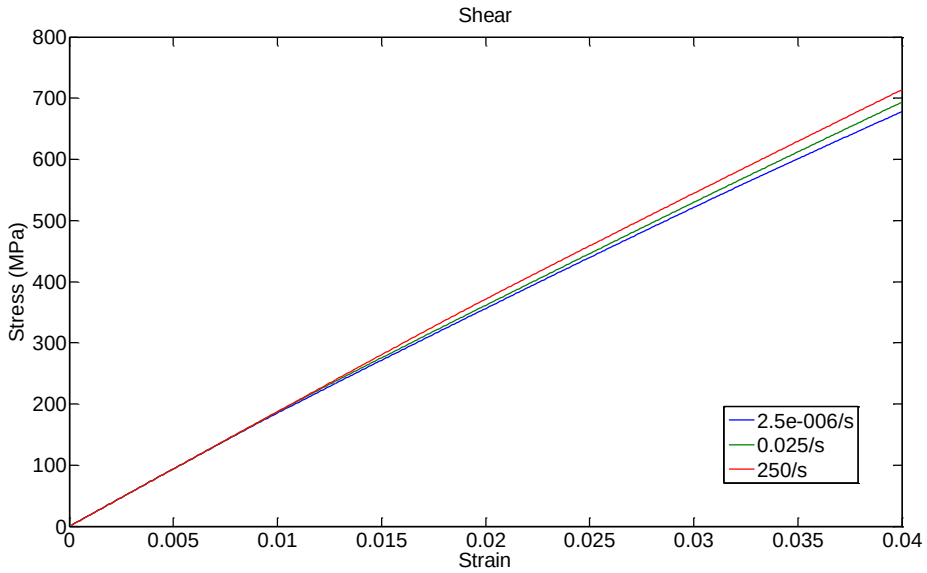

Fig. 4.14 TriBC Shear Constitutive Predicted Response

4.5. Future Work

Many important phenomenon for modeling triaxially braided composites were reported here including elasticity, plasticity, viscoplasticity, and failure. However, there are still significant mechanisms that have not been included. For example, tow delamination and fiber/matrix delamination are critical under high speed impact loadings. Additionally, modeling the failure modes and damage mechanisms of the polymer can help improve the accuracy of shear and compression loadings.

Chapter 5

5. Modeling Polymeric Woven Composites

5.1. Introduction

Woven composites are currently widely used due to their reduce delamination tendencies relative to their thickness. These materials are preferable for their direct replacement for the commonly used cross ply lamina/laminates. Even though woven composites are mainstream, commonplace analysis is limited due to the complex in-plane shear response, which is a function of both the material and geometric nonlinearity. It was previously shown that the triaxial braided composites did not exhibit severe rate dependence, however due to the high nonlinearity the strain rate dependent effects are significant in shear loading. Lastly, woven composites are readily available in a plethora of configurations controlling architectural parameters, many of which are not accounted for in traditional analysis, and the effect of changing these parameters is a critical interest in aerospace applications.

5.2. Elastic Properties

To validate MSGMC for woven polymer composites, first the elastic predictions must be valid and accurate. For the test case here is a comparison drawn between an explicitly modeled finite element technique (Kollegal 2000) and experimental results (Blackketter 1995). Here the shear modulus and Young's modulus are compared for the case of a AS-4/3501-6 60% volume fraction plain weave composite. The material properties are summarized in Table 5.2. The geometric parameters for the test case are summarized in Table 5.1. The

comparison between the two techniques and experimental data, shown in Fig. 5.1 and Fig. 5.2, shows a minute difference between them.

Table 5.2 Constituent Elastic Properties of AS-4/3501-6 Material System

	Axial Modulus (GPa)	Transverse Modulus (GPa)	Axial Poisson's Ratio	Transverse Poisson's Ratio	Shear Modulus (GPa)
AS-4	221.0	13.8	0.2	0.25	13.8
3501-6	4.4	4.4	0.34	0.34	1.62

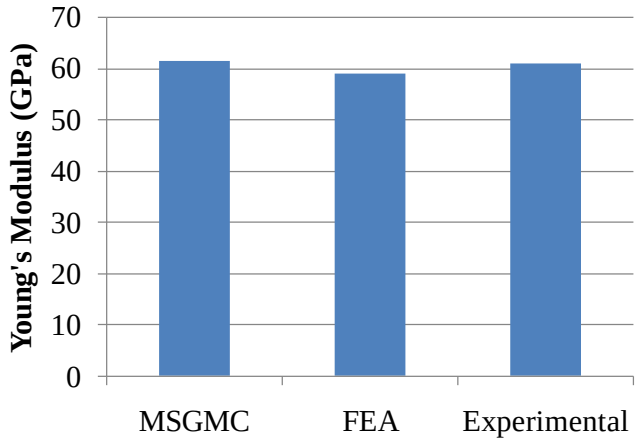

Fig. 5.1 Predict and Experiment Modulus for 60% AS-4/3501-6 Plain Weave Composite

Table 5.1 AS-4/3501-6 Plain Weave Composite Geometric Parameters

Parameter	Value
V_f	0.60
$V_{f_{tow}}$	0.70
w	1mm
t	0.5mm

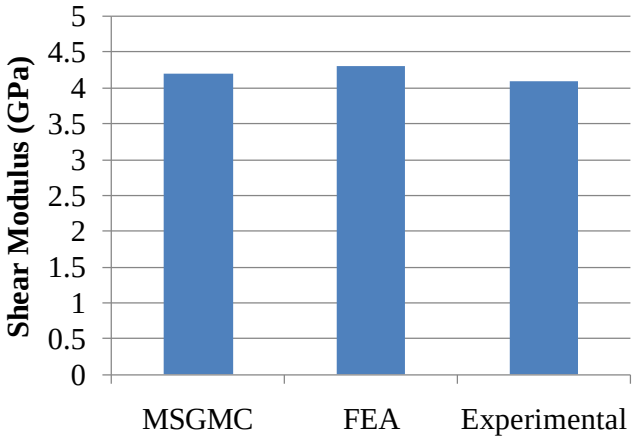

Fig. 5.2 Predict and Experiment Modulus for 60% AS-4/3501-6 Plain Weave Composite

A unique application of MSGMC, due to its high computational efficiency, is the ability to quickly vary architectural parameters and surmise their effect on modulus (coordinate system in Fig. 5.3). The quintessential modulus versus volume fraction plot for laminated is more complicated for woven composites to the coupled geometry between volume fraction and tow architecture (see Eq. 2.22). To vary the volume fraction, a relationship has to be constrained between the architectural parameters and therefore two methods result: constant thickness or constant width. In application, when volume fraction is changed neither the constant thickness nor constant width is enforced, but some

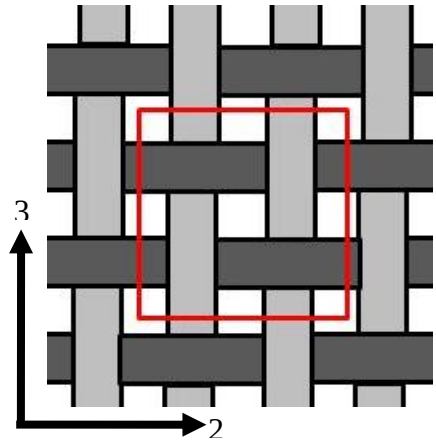

Fig. 5.3 Prescribed Coordinate System for Woven Composites

combination of both width and thickness change. For simplicity, the constant thickness or constant width assumptions are made for various volume fractions. Both plain weave and 5 harness satin weaves were simulated for volume fractions varying between 5-60%. The material parameters for this analysis are shown in Table 5.3. A tow width of 1.69 mm was used while the tow volume fraction and thickness were changed accordingly. The variation for the in-plane parameters show nonlinear trends as expected and the differences between weaves are more pronounced at higher volume fractions. This is due to the fact at lower volume fractions, the material response is more matrix dominated and less architecture dependent. An important observation is that the constant width and constant

Table 5.3 Constituent Elastic Properties of Graphite/Epoxy Material System

	Axial Modulus (GPa)	Transverse Modulus (GPa)	Axial Poisson's Ratio	Transverse Poisson's Ratio	Shear Modulus (GPa)
Graphite	230.0	15.0	0.2	0.2	15.0
Epoxy	3.1	3.1	0.38	0.38	1.12

thickness trends exhibit different convexity for the in-plane modulus variations, while the Poisson's ratio and shear modulus are similar.

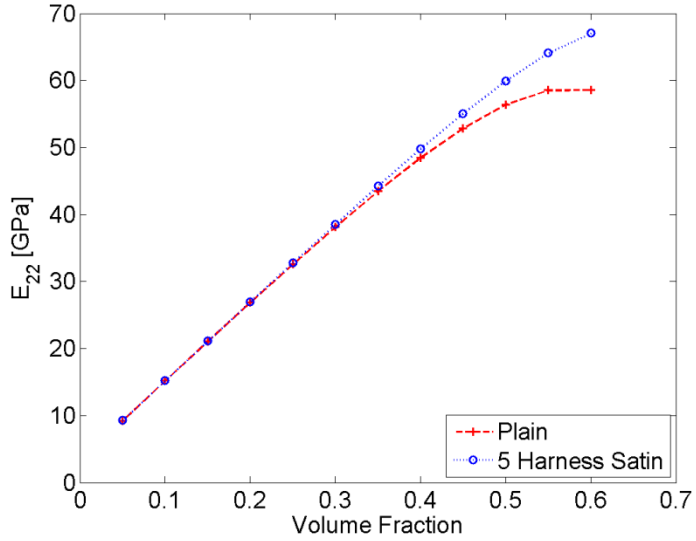

a)

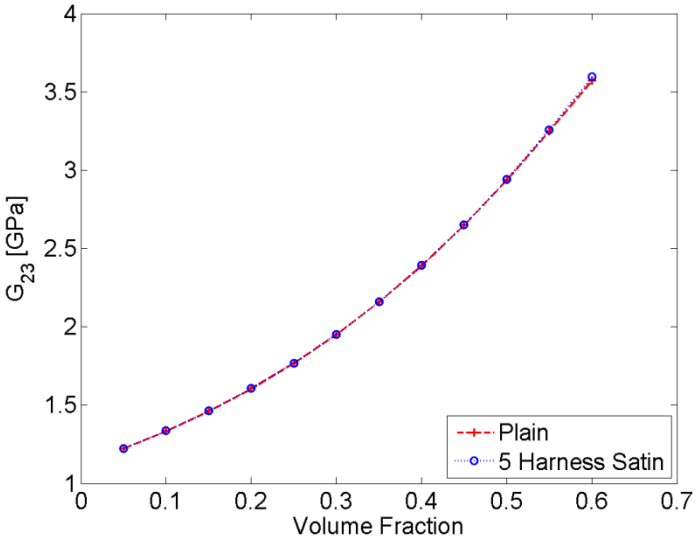

b)

Fig. 5.4 Volume Fraction Variation for Constant Thickness RUC a) In-Plane Modulus b) In-Plane Shear Modulus c) In-Plane Poisson's Ratio

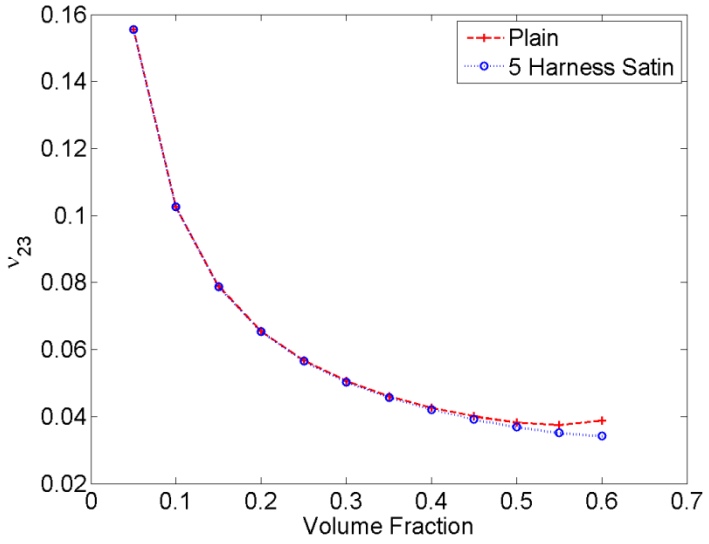

c)

Fig. 5.4 (contd.) Volume Fraction Variation for Constant Thickness RUC a) In-Plane Modulus b) In-Plane Shear Modulus c) In-Plane Poisson's Ratio

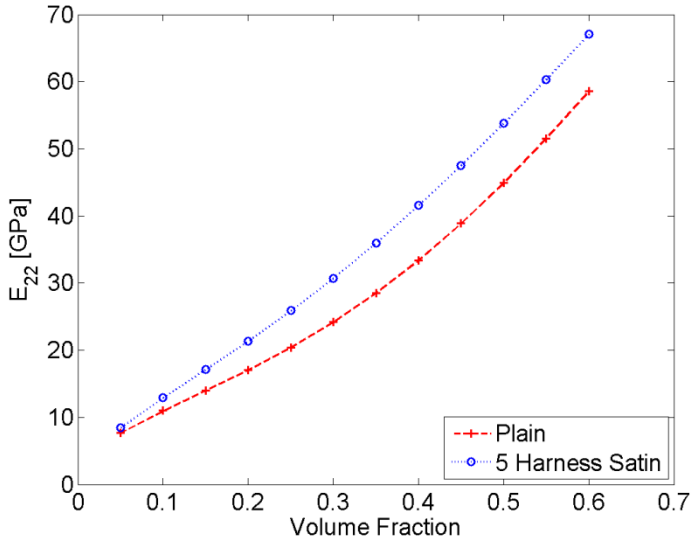

a)

Fig. 5.5 Volume Fraction Variation for Constant Width RUC a) In-Plane Modulus b) In-Plane Shear Modulus c) In-Plane Poisson's Ratio

b)

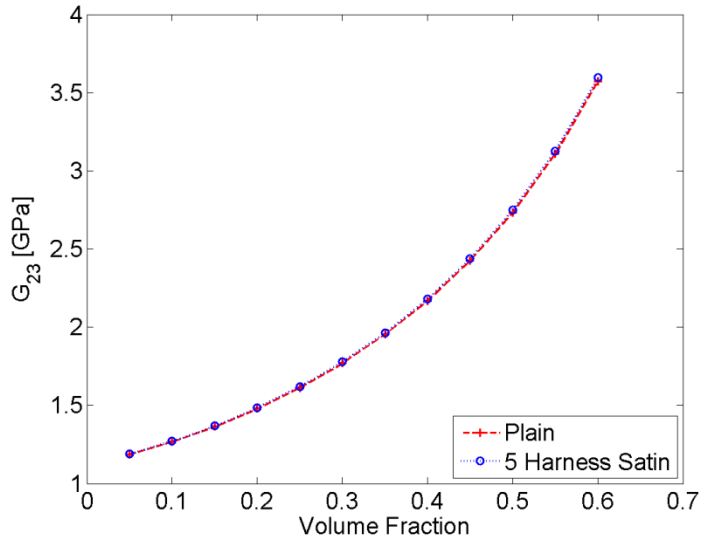

c)

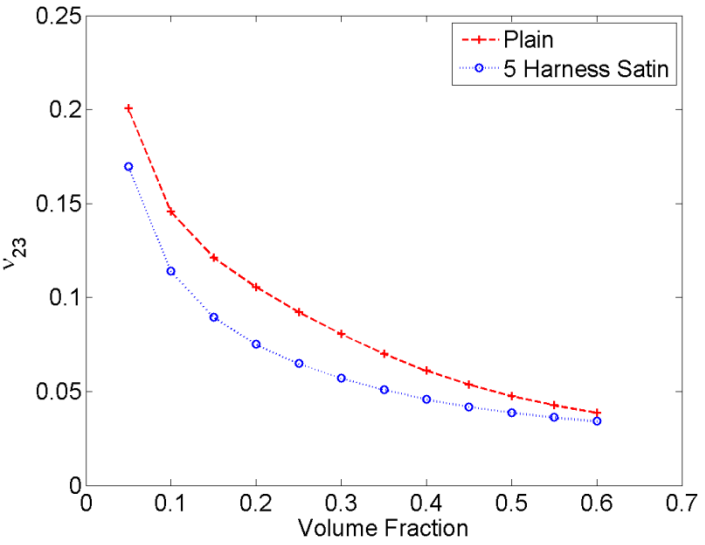

Fig. 5.5 (contd.) Volume Fraction Variation for Constant Width RUC a) In-Plane Modulus b) In-Plane Shear Modulus c) In-Plane Poisson's Ratio

5.3. Modeling Plain Weave Composites with Ramberg Osgood Deformation Plasticity

Since it has already been established that MSGMC is highly capable of predicting the components of the elastic stiffness matrix, the next step is to predict the entire stress strain curve including failure. In order to capture the nonlinear

response of the matrix material and to generate a fair comparison with other approaches, a Ramberg-Osgood type deformation plasticity model is employed. This type of model is identical the work of (Tabiei 2004), which is the most similar micromechanical approach to MSGMC. However, the particular implemented presented in the works of Tabiei is slightly unstable and its approach is more akin to a scalar damage model. Also the model is inherently unstable and requires a small time step to converge. To improve stability, the model is changed to a deformation plasticity type model with the assumption of all nonlinear being related to plastic strain. This assumption does not change the end result of the constitutive model, but allows for a simpler implementation. In Tabiei's variation of the Ramberg-Osgood model, it assumes that the shear nonlinear can be modeled by the following relationship

$$\tau(\gamma) = \frac{G_0 \gamma}{\left[1 + \left(\frac{G_0 \gamma}{S}\right)^p\right]^{1+1/p}} \tag{5. 1}$$

where τ is the shear stress, γ is the shear strain, G_0 is the initial shear modulus, S is the maximum shear strength, and p is a material constant governing the amount of curvature in the stress strain curve. A modification into a deformation plasticity can relate the plastic shear strain to the total shear strain by the following relationship

$$\gamma^p = \gamma\left(1 - \left[1 + \left(\frac{G\gamma}{S}\right)^p\right]^{-1/p}\right) \tag{5. 2}$$

.

and the shear stress can now be calculated by

$$\tau = G\left(\gamma - \gamma^{p}\right). \tag{5. 3}$$

The resulting formulation allows the elastic stiffness matrix to remain unchanged and allow for more stable convergence.

To validate the model, the overall stress strain curves for tension and shear are plotted against several other techniques and experimental data. The material system can be described by Table 5.2 and Table 5.1 along with the nonlinear properties of the matrix ($p = 2.34$ and $S = 89\,\text{MPa}$). The fiber failure strength was taken to be 2.4 GPa and the failure criteria of Eq. 4.3 was used. The overall result curves are shown in Fig. 5.6 below.

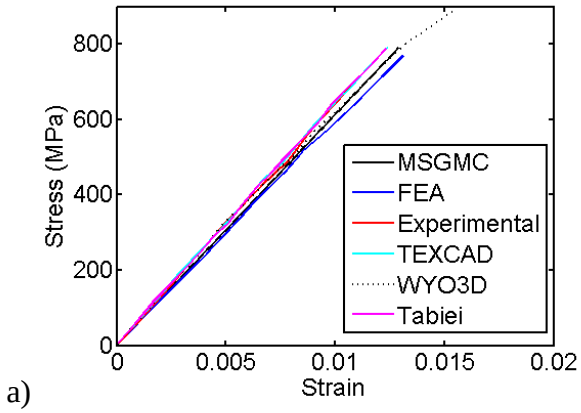

a)

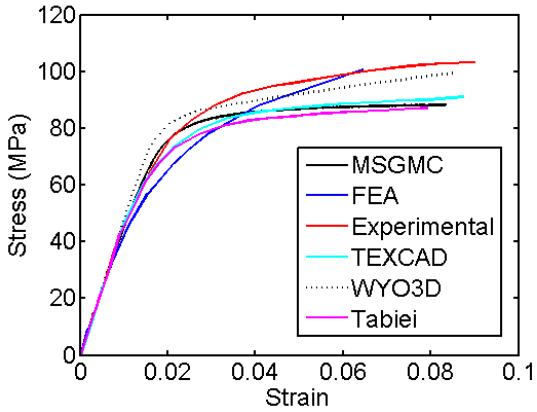

b)

Fig. 5.6 AS-4/3501 60% Volume Fraction Plain Weave Composite a) Tensile Stress-Strain Curve b) Shear Stress-Strain Curve

The global stress-strain curves are compared to experimental results (Blackketter 1995), finite element analysis (Kollegal 2000), micromechanics (Tabiei 2004), and analytical methods (Naik 1995). From the graphs, it is seen that MSGMC performs well when compared to the other methods and techniques.

5.4.Viscoplastic Strain Rate Dependent Response with Failure

Although plasticity models are useful in solving static problems, modeling the strain rate dependent response is a critical issue in dynamic problems. Orthogonal weaves show a strong rate dependent response in shear loading where the nonlinear matrix response is governing. To capture the rate-dependent response of the material parameters and governing equations in Section 4.4 were used. To demonstrate the rate dependent effects, three different strain rate cases were evaluated: 1e-5/s, 1/s and 1e3/s. These were chosen to reflect realistic loading conditions. Only shear loading was considered because other loadings did not exhibit strong rate dependent effects.

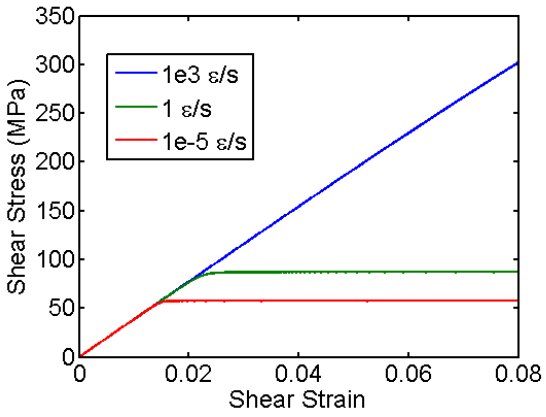

Fig. 5.7 Strain Rate Dependent Shear Response of AS-4/3501-6 60% Volume Fraction Plain weave Composite

Fig. 5.7 shows the predicted curves and it is clear that this is a critical phenomena. However, a rate dependent failure criteria for the polymer matrix is necessary to fully capture the response. This will allow the strength levels to be accurately predicted. Future research will hopefully quantify this constituent response and improve current modeling capabilities. MSGMC has the capability to compute the local field distributions at several length scales. For the case of shear loading, Fig. 5.8 shows the local shear stress (σ_{23}) distribution in the plain weave at the initial stage and at 8% shear strain, while Fig. 5.9 shows the local plastic shear strain (ε_{23}^{p}) distribution.

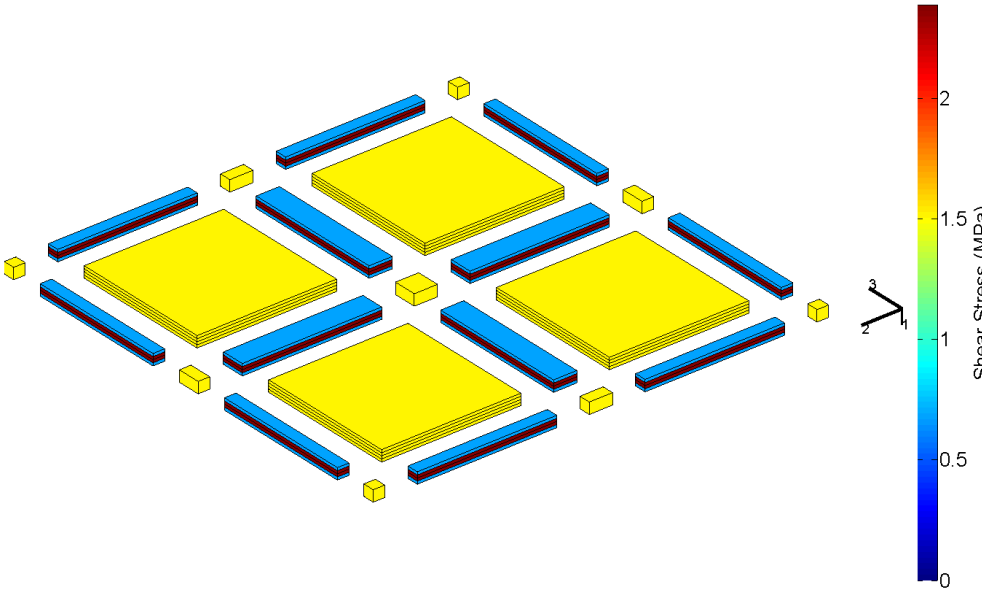

a)

Fig. 5.8 Local Shear Stress Distribution in AS-4/3501-6 60% Volume Fraction Plain Weave Composite at 1e-5/s Strain Rate a) .02% Strain b) 4% Strain

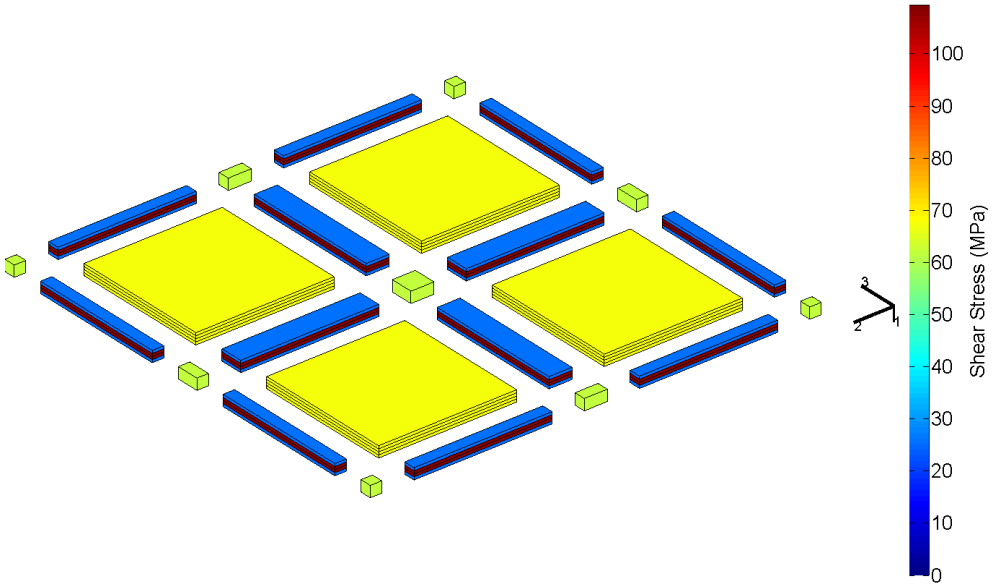

b)

Fig. 5.8 (contd.) Local Shear Stress Distribution in AS-4/3501-6 60% Volume Fraction Plain Weave Composite at 1e-5/s Strain Rate a) .02% Strain b) 4% Strain

The local stress distributions show the inherent nonlinearity in the polymer response. Load redistribution can be seen by the color changing between the two contour plots. The matrix pockets changed from a yellow to a yellow-green color, indicating loss in load carrying capability due to plasticity.

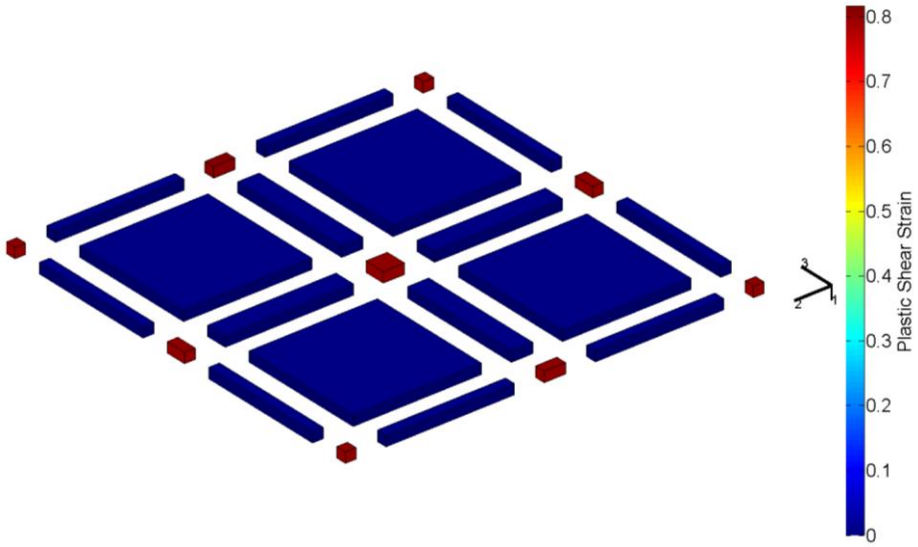

Fig. 5.9 Local Plastic Shear Strain Distribution in AS-4/3501-6 60% Volume Fraction Plain Weave Composite at 4% Global Strain

Examining these figures allows one to understand the local load carrying paths and the materials responsible for the nonlinear behavior. The undulating tows and the interweave matrix carry the majority of the shear load in the composite and thus are responsible for the overall behavior. A five harness satin variant of this weave was also simulated. The local fields for this weave exhibit similarities to that of the plain weave. The distribution is fairly consistent between the weave types.

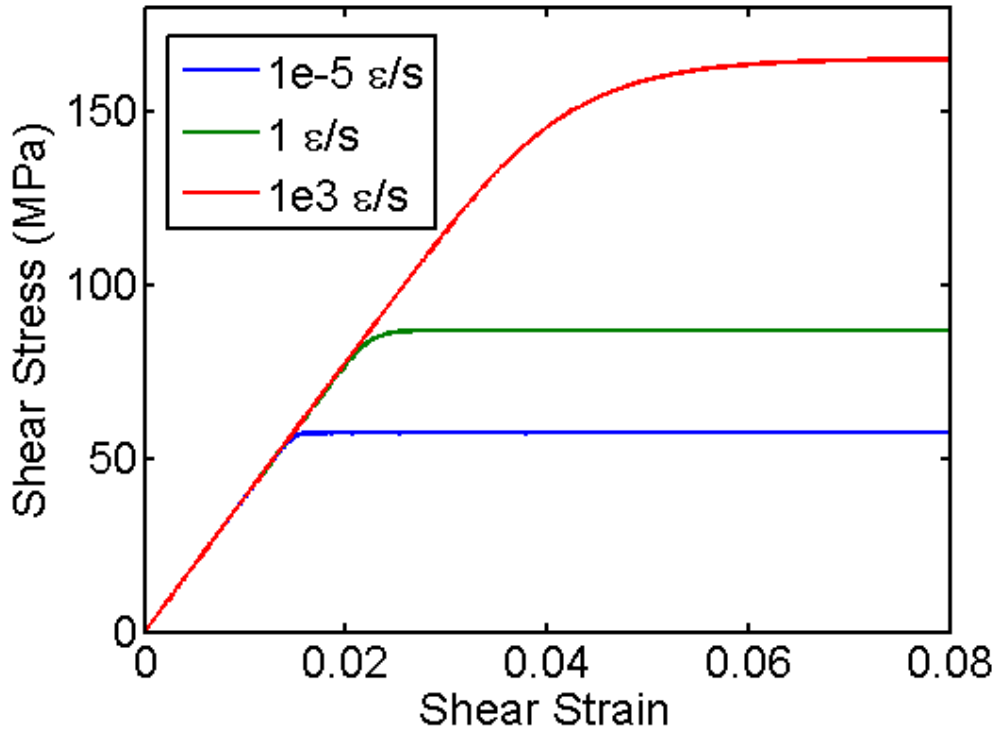

Fig. 5.10 AS-4/3501 60% Volume Fraction 5 Harness Satin Weave Composite a) Tensile Stress-Strain Curve b) Shear Stress-Strain Curve

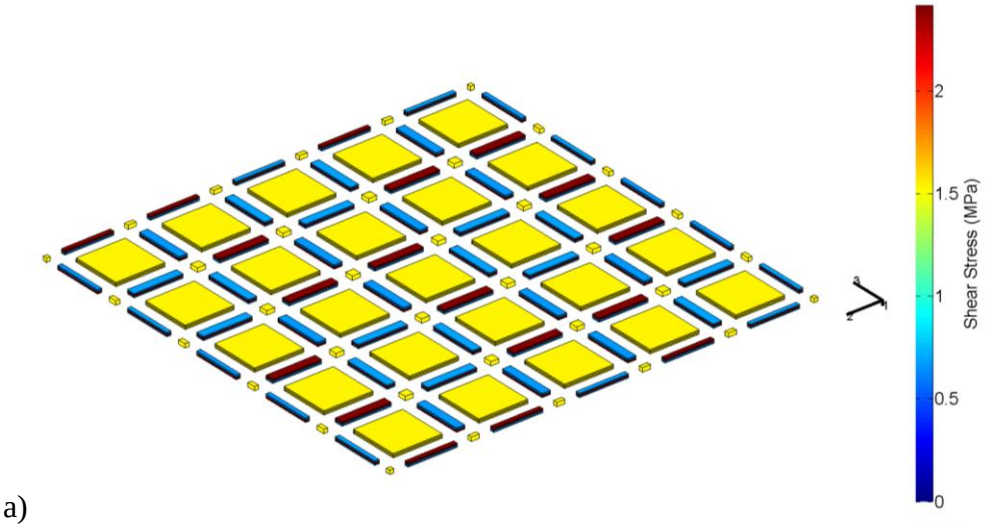

a)

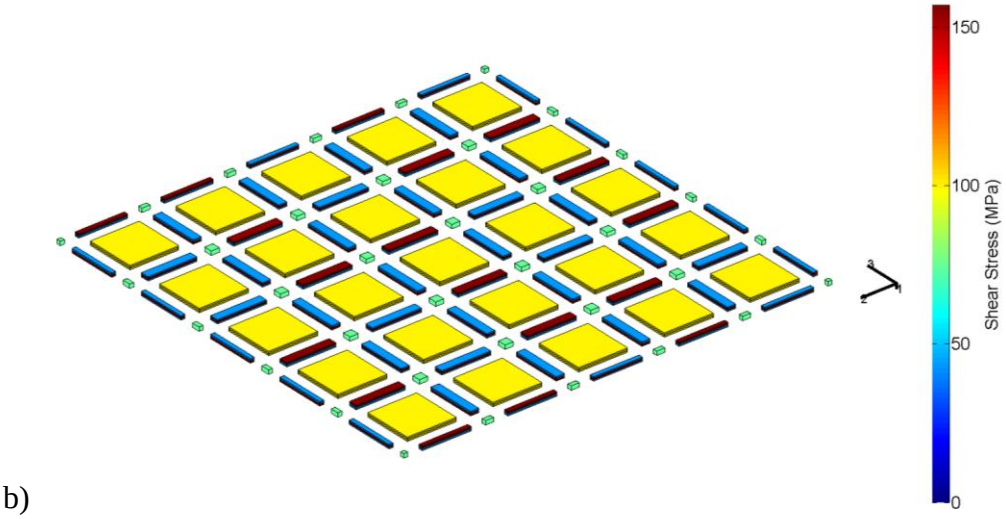

b)

Fig. 5.11 Local Shear Stress Distribution in AS-4/3501-6 60% Volume Fraction Five Harness Satin Weave Composite a) b)

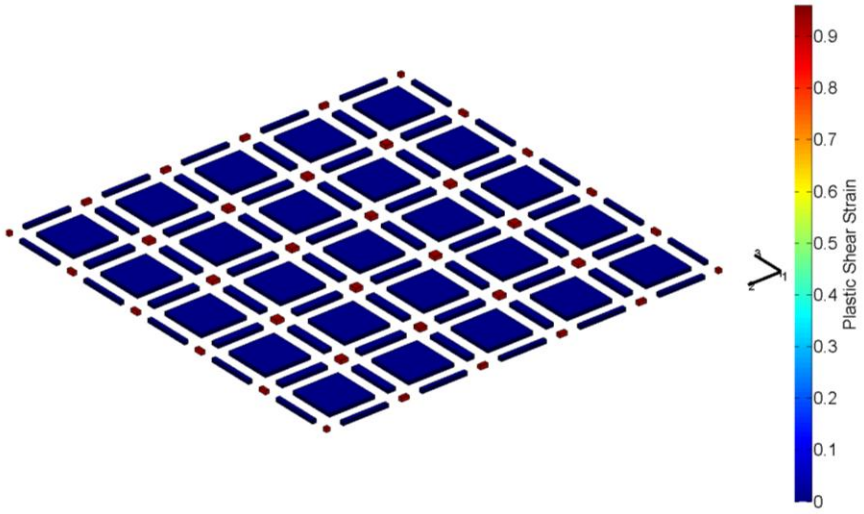

Fig. 5.12 Local Plastic Shear Strain Distribution in AS-4/3501-6 60% Volume Fraction Five Harness Satin Weave Composite

5.5. Parametric Variation

The previous sections of this report focused on modeling the macroscale response of a weave RUC. The macroscale result is dependent on several architectural and material parameters and can exhibit significant variation depending on the statistical distributions of these parameters. In a real structure, the RUC cannot be idealized to a perfect geometry due to manufacturing variations. An RVE of several RUCs is necessary to capture the response due to material variation, therefore another length scale is added, the structural scale. The structural length scale refers to the component being analyzed, i.e., an engine fan casing or in this case a region within the gage length of a typical experimental test coupon – unaffected by edge effects and thus idealized by a representative volume element (RVE) consisting of several macroscale woven repeating unit cells formed from various combinations of architectural effects. The macroscale weave refers to the RUC of the weave, for a plain and 5-harness satin fabric. The

mesoscale represents the RUC of the fiber tow, this represents a bundle of fibers (typically 3k, 6k or 12k for polymeric matrix composites). The smallest length scale is the microscale, which represents the fundamental constituent materials, such as the monofilament fiber and matrix itself.

Two scenarios were investigated at the structural scale: 1) an RUC comprised of 3x3 macroscale RUCs and 2) an RUC comprised of 6x6 macroscale RUCs. This was performed in order to investigate the influence of discretization (size) effect between the macro and structural length scales, since at the structural scale, see Fig. 5.13, macroscale RUC representing each subcell is randomly chosen. There are several "microstructural" parameters at the meso, macro, and structural level required to fully define the descritzed subcell geometries. At the mesoscale, both tow volume fraction and tow packing are required, while at the macroscale, weave architecture, weave volume fraction, tow aspect ratio and ply nesting are required. At the structural level, the spacial distribution of the macroscale RUCs are required, i.e., uniform – each subcell is associated with the same macroscale RUC or random – subcells are associated with a uniform distribution of macroscale RUCs. It has been of recent interest to study the effects of these parameters and understand what the driving factors for both elastic and inelastic response are.

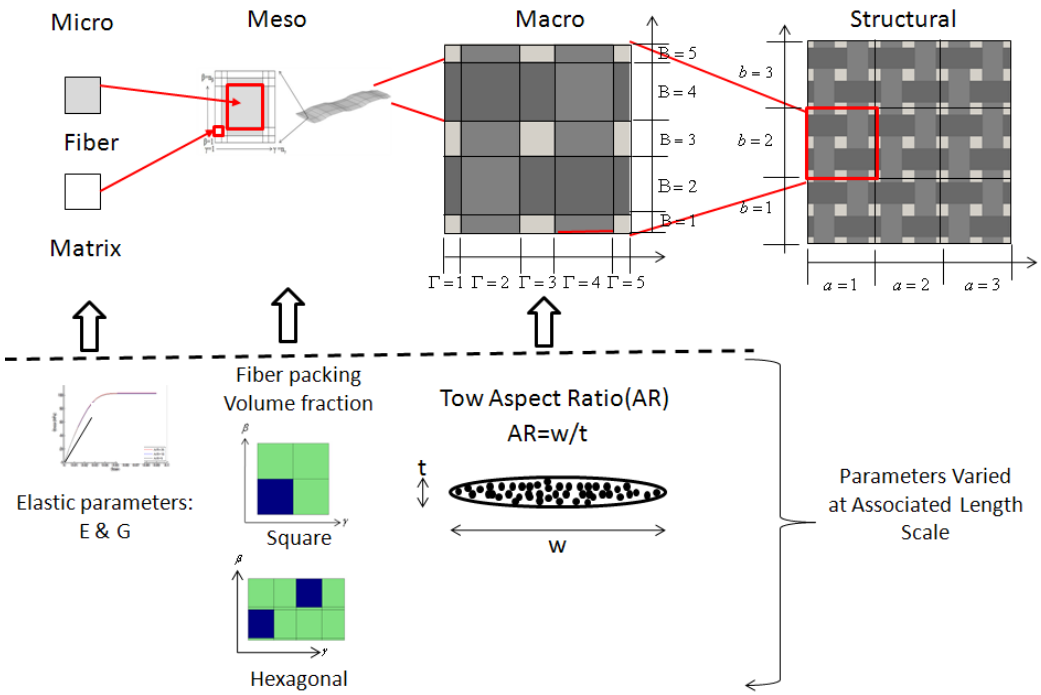

Fig. 5.13 Multiscale Framework for Parametric Variation

Table 5.4 Constituent Elastic Properties of AS-4/3501-6 Material System for Plasticity

	E_A (GPa)	E_T (GPa)	v_A	v_T	G_A (GPa)	σ_Y (MPa)	A	H (GPa)
AS-4	225.0	15.0	0.2	0.2	15.0	N/A	N/A	N/A
3501-6	4.2	4.2	0.34	0.34	1.56	71	100	1.5

To effectively study the effects of the architectural parameters, the response of the woven composite was studied at two length scales: macro and structural. For this analysis an AS-4/3501-6 material system with an overall fiber volume fraction of 60% was used. The properties of the constituent system are shown below in Table 5.3. There are three plasticity parameters σ_Y, *a*, and H. σ_Y is the yield strength of the material; a, is the exponential hardening coefficient, and H is the post yield modulus (see section 4.2). To study the effects of architectural and material variation on the macroscale response, a full factorial set of numerical simulations were conducted. The parameters varied are shown in Table 5.5 and are depicted in Fig. 5.13. The three architectural parameters varied for tow volume fraction, tow aspect ratio, and fiber packing. All other parameters in the analysis were kept constant. The tow volume fraction and fiber packing are both considered a mesoscale effect because their geometrical properties are involved in the

Table 5.5 Parameters Varied For Parametric Analysis

Microstructural Parameter	Relevant Length Scale	Values
Tow Volume Fraction (V_{tf})	Meso	0.62,0.65,0.70
Tow Packing	Meso	Hexagonal, Square
Tow Aspect Ratio (AR)	Macro	9,18,36

mesoscale concentration matrix (Eq. 2). The tow aspect ratio is considered a macroscale property because it is taken into account in the macroscale concentration matrices. The tow volume was varied over the range of 0.62, 0.65, or 0.70. These three values were chosen based of common experimental values for polymer matrix composites. Tow aspect ratio was chosen to be 9, 18 and 36. A value of 9 is typical of ceramic matrix composites, 18 is typical of polymer matrix composites, and 36 was chosen as an upper bound. Two different fiber packings were used, square and hexagonal, as both exhibit different response. Although most polymer matrix composites exhibit random packing, square and hexagonal

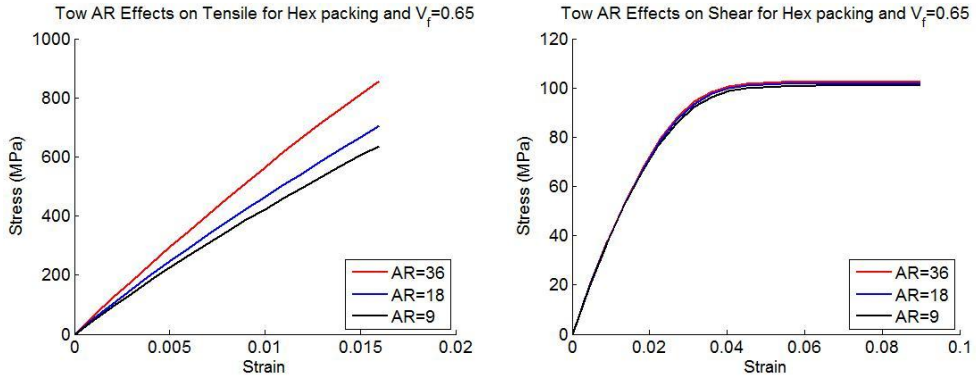

Fig. 5.14 Typical Macroscale Deformation Response, given a tow volume fraction of 65%, hexagonal fiber packing within a given tow, and varying the tow aspect ratio from 9 to 36

are both approximations of this.

The full factorial simulations were run for both the tension and shear response and was also performed for two macroscale weave RUCs; a plain and 5HS weave. The range for the parameters were chosen such that they represent the typical variation in a polymer matrix composite, future work will allow for the investigation of stochastic variables and other composite systems such as metallic and ceramic matrix composites where the properties mismatch is significantly less

than for PMCs. There were two types of fiber packing considered within the tows; square and hexagonal. The tow aspect ratio is defined as the width per thickness, as shown in Fig. 5.13. The full factorial simulations for both responses and weave types resulted in a total of 72 cases analyzed. In each of these cases, the overall volume fraction and material system was kept constant so that results are comparable. In each case, two structural features were investigated, the elastic modulus and strain energy (area under the stress-strain curve) -which enables inelasticity effects to be considered.

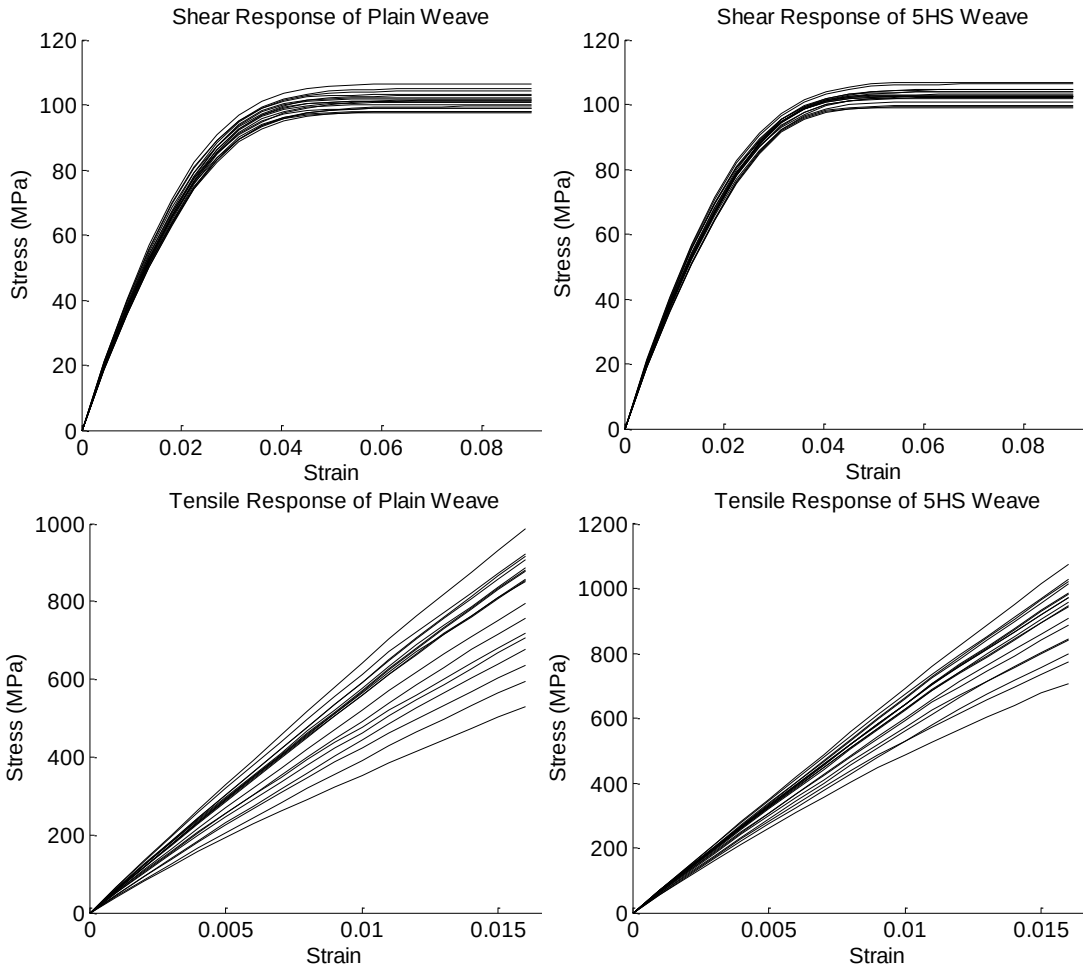

Fig. 5.15 Macroscale Tensile (bottom row) and Shear (top row), for Plain (left

row) and 5HS (right row) Response for All Architectural Variations.

The results of the macroscale analyses are presented in Table 5.6. The overall response for each case is plotted in the Appendix, with typical stress vs. strain response plots shown in Fig. 5.14 and all responses overlaid for both weave types shown in Fig. 5.15. It is apparent that there is a significant amount of variation at the macroscale. From the graphs in the Appendix some conclusions can be readily drawn. Increasing the tow aspect ratio will increase both modulus and strain energy. Decreasing tow volume fraction has the same effect as increasing tow

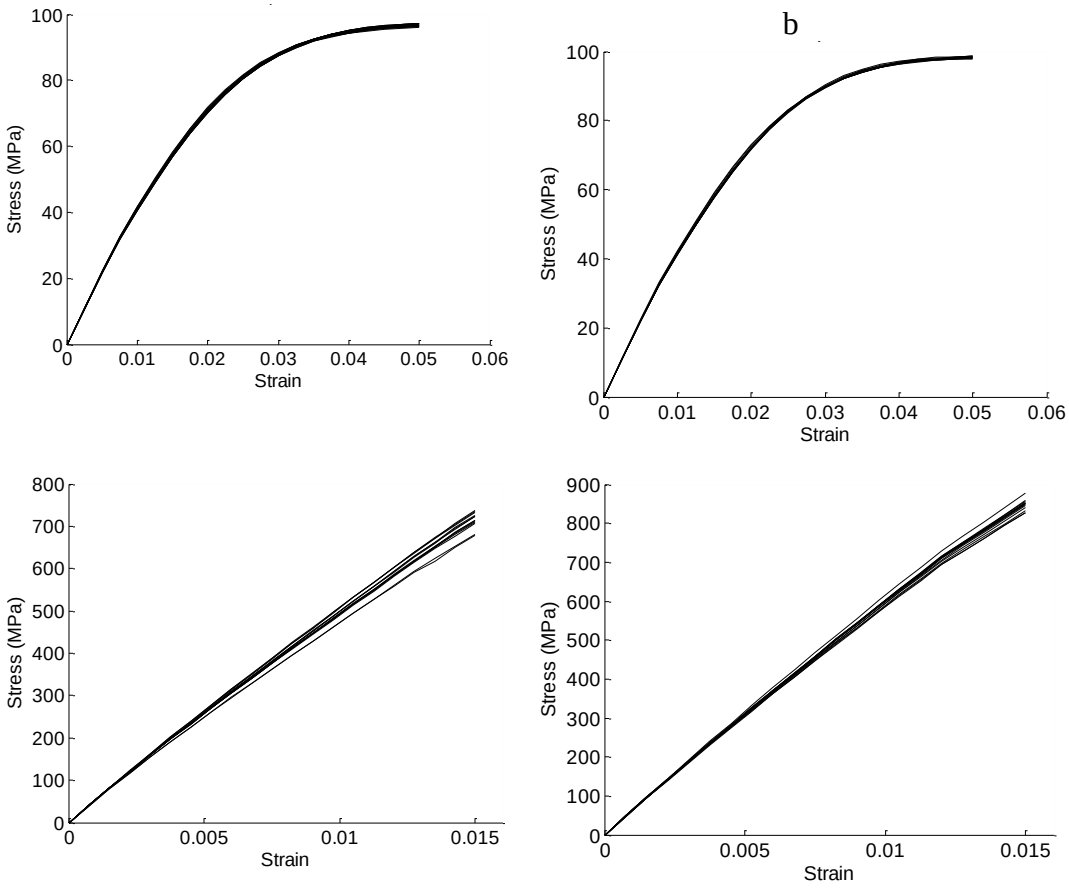

Fig. 5.16 Structural Scale Shear (top row) and Tensile (bottom row) Response Cases (for 3x3 RUC) given a Plain (left row) and 5HS (right row) weave.

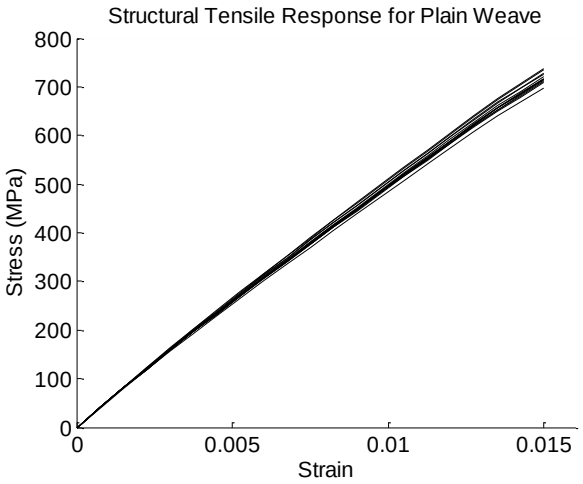

Fig. 5.17 Structural Scale Tensile Response (for 6x6 RUC).

aspect ratio, increase in modulus and strain energy. The hexagonal RUC at the mesoscale was more compliant and exhibited more plasticity than the square RUC for equivalent volume fractions. The tensile response was also more sensitive to changes than the shear response, as expected. The results show up to three times the standard deviation in tensile response when compared to shear. It is clear that there are coupling effects also present, so it was necessary investigate this further with an analysis of variance (ANOVA) was performed using Design Expert[7] software product. The p-value results are presented in Table 5.7. A p-value represents the probability that the effect determined from the ANOVA occurred due to noise. Typically a p-value of less than 0.10 indicates a significant effect, assume a 95% confidence interval. The ANOVA results show that typically these architectural effects do not influence significantly the response because of vary large p-values (much greater than 0.10). The most notable effect was seen in the interaction of the fiber packing and tow volume fraction. This was present in the plain weave tensile response cases. Clearly, the results at the macroscale indicate

that several of the meso-structural architectural effects are significant and must be considered if the macroscale is the final length scale in the analysis.

Similarly, the influence of microscale parameters were examined by holding fixed the architectural effects (square packing with a 70% tow fiber volume fraction and an aspect ratio of 18) and varying the elastic properties of the matrix and fiber by ±10%. Then inelastic properties were kept constant. Here, results for both the tensile and shear response are shown in Fig. 5.18, wherein very little variation at the macroscale is observed, which is in contrast to the previous significant influence of architectural effects. This will most likely not be the case for both ceramic matrix composites or metal matrix composites, as the mismatch between constituent materials is significantly less (by approximately a factor of ten) then in the case of a PMC material systems

Table 5.6 Macroscale Results of Parameter Study for AS-4/3501-6 Plain Weave

			Plain Weave				**5HS Weave**			
Packing	Aspect Ratio	Tow Volume Fraction	Longitudinal Modulus (GPa)	Shear Modulus (Gpa)	Long Strain Energy (MPa)	Shear Strain Energy (MPa)	Longitudinal Modulus (GPa)	Shear Modulus (Gpa)	Long Strain Energy (MPa)	Shear Strain Energy (MPa)
Hexagonal	18	0.65	55.32	4.64	9.19	7.86	42.78	4.41	7.63	7.44
Square	36	0.7	46.13	4.20	8.09	7.32	52.83	4.36	9.63	7.60
Hexagonal	36	0.65	51.65	4.30	8.98	7.51	57.86	4.12	10.73	7.32
Square	9	0.65	61.43	4.37	10.99	7.66	58.40	4.25	11.13	7.54
Square	18	0.65	66.03	4.33	12.50	7.69	58.49	4.14	10.70	7.35
Hexagonal	9	0.7	66.46	4.34	12.56	7.71	59.11	4.27	11.18	7.58
Hexagonal	18	0.7	67.35	4.21	12.45	7.49	60.95	4.18	11.18	7.42
Square	9	0.62	67.91	4.35	12.87	7.74	61.68	4.32	11.62	7.67
Hexagonal	9	0.65	62.28	4.36	10.93	7.65	62.54	4.43	11.57	7.75
Hexagonal	9	0.62	58.48	4.32	9.96	7.57	63.16	4.42	11.62	7.74
Square	36	0.65	41.15	4.50	6.86	7.58	64.17	4.70	11.41	7.99
Hexagonal	36	0.62	56.66	4.53	10.22	7.70	65.26	4.59	12.19	7.81
Hexagonal	36	0.7	65.53	4.18	12.10	7.44	65.92	4.19	12.14	7.46
Square	36	0.62	66.10	4.71	11.86	8.01	67.11	4.60	12.55	7.83
Square	9	0.7	59.30	4.38	10.80	7.66	67.85	4.39	12.43	7.71
Hexagonal	18	0.62	47.04	4.25	8.63	7.40	68.55	4.45	12.98	7.81
Square	18	0.7	54.33	4.65	9.27	7.88	70.21	4.73	13.10	8.04
Square	18	0.62	56.07	4.55	10.15	7.72	70.78	4.61	13.60	7.86

Table 5.7 Macroscale P-Value Results for Design of Experiment Study on AS-4/3501-6 Plain Weave Composite System

	P-value							
	Plain				**5HS**			
	Longitudinal Modulus	Longitudinal Strain Energy	Shear Modulus	Shear Strain Energy	Longitudinal Modulus	Longitudinal Strain Energy	Shear Modulus	Shear Strain Energy
A-Fiber Packing	0.55	0.76	0.301	0.204	0.41	0.34	0.36	0.28
B-Tow Aspect Ratio	0.08	0.16	0.743	0.624	1.00	0.97	0.82	0.99
C-Tow Volume Fraction	0.45	0.41	0.515	0.494	0.18	0.09	0.49	0.35
AB	0.29	0.34	0.832	0.721	0.42	0.27	0.56	0.51
AC	0.03	0.05	0.570	0.299	0.78	0.75	0.61	0.60
BC	0.11	0.27	0.465	0.163	0.40	0.24	0.81	0.66

Table 5.8 Structural Scale Results of Parameter Study for AS-4/3501-6 Plain Weave

	Plain (3x3)				Plain (6x6)			5HS (3x3)			
	Longitudinal Modulus (GPa)	Longitudinal Strain Energy (MPa)	Shear Modulus (GPa)	Shear Strain Energy (MPa)	Longitudinal Modulus (GPa)	Longitudinal Strain Energy (MPa)	Shear Modulus (GPa)	Longitudinal Modulus (GPa)	Longitudinal Strain Energy (MPa)	Shear Modulus (GPa)	Shear Strain Energy (MPa)
RUN 1	54.65	5.72	4.33	3.45	54.49	5.64	4.36	64.29	6.74	4.32	3.54
RUN 2	53.99	5.56	4.33	3.45	54.10	5.60	4.35	64.24	6.76	4.46	3.53
RUN 3	55.02	5.73	4.36	3.45	54.91	5.69	4.37	64.91	6.89	4.33	3.54
RUN 4	54.17	5.57	4.41	3.47	54.72	5.69	4.32	63.45	6.60	4.43	3.53
RUN 5	53.92	5.56	4.40	3.47	54.19	5.60	4.39	63.43	6.67	4.45	3.51
RUN 6	52.79	5.35	4.35	3.45	55.16	5.74	4.38	62.99	6.56	4.41	3.52
RUN 7	54.26	5.64	4.38	3.46	54.11	5.60	4.36	64.27	6.75	4.39	3.53
RUN 8	52.73	5.34	4.41	3.47	53.94	5.58	4.36	64.00	6.71	4.39	3.52
RUN 9	54.08	5.54	4.41	3.48	53.23	5.47	4.35	64.22	6.73	4.40	3.52
RUN 10	54.05	5.63	4.46	3.49	54.12	5.57	4.42	63.72	6.65	4.33	3.54
RUN 11	54.35	5.64	4.36	3.46	54.47	5.61	4.38	63.96	6.71	4.42	3.52
RUN 12	54.30	5.58	4.33	3.44	55.34	5.77	4.35	64.02	6.74	4.39	3.53
RUN 13	55.22	5.74	4.45	3.48	53.92	5.55	4.39	63.43	6.58	4.38	3.52
Average	54.12	5.59	4.38	3.46	54.36	5.62	4.37	63.92	6.70	4.39	3.53
Std. Dev	0.72	0.13	0.04	0.02	0.57	0.08	0.02	0.51	0.09	0.04	0.01
% Dev	0.01	0.02	0.01	0.00	0.01	0.01	0.01	0.01	0.01	0.01	0.00

Table 5.9 Average Results for Structural Scale Parameter Study for AS-4/3501-6 Plain Weave

		Plain (3x3)				**5HS (3x3)**			
		Longitudinal Modulus (GPa)	Longitudinal Strain Energy (MPa)	Shear Modulus (GPa)	Shear Strain Energy (MPa)	Longitudinal Modulus (GPa)	Longitudinal Strain Energy (MPa)	Shear Modulus (GPa)	Shear Strain Energy (MPa)
Average	Macro	58.29	5.23	4.40	3.82	62.09	5.76	4.40	3.83
	Structural	54.12	5.59	4.38	3.46	63.92	6.70	4.39	3.53
Percent Standard Deviation	Macro	0.14	0.17	0.04	0.02	0.11	0.12	0.04	0.03
	Structural	0.01	0.02	0.01	0.00	0.01	0.01	0.01	0.00

Table 5.10 Statistic Macroscale Results of Parameter Study for Plain Weave

	Long. Modulus (GPa)	Shear Modulus (Gpa)	Long Strain Energy (MPa)	Shear Strain Energy (MPa)
Avg.	58.29	4.40	10.47	7.64
Std. Dev	7.99	0.16	1.73	0.17
% Dev	0.14	0.04	0.17	0.02

At the structural scale, the effects of multiple macroscale RUCs are studied. For both the tension and shear response, plain and 5hs weaves were investigated for 3x3 and 6x6 structural RUC cases. The two different size RUCs at the structural scale were used to investigate the sizing effects from the macro to structural scale. Each of the RUCs composing the 3x3 or 6x6 RUC at the structural scale is comprised of a macroscale RUC with a set of randomly determined architectural parameters. For example, one RUC would have a 62% tow volume fraction with an aspect ratio of 18 and square packing and another could be completely different. Each architectural parameter was randomly selected for each RUC. Thirteen cases were run for each structural RUC in order to achieve a broad spectrum of combinations. The results of all 13 runs are shown in Fig. 5.16 for the 3x3 and Fig. 5.17 for the 6x6. Table 5.8 shows the results of

Table 5.11 Statistic Macroscale Results of Parameter Study for 5HS Weave

	Long. Modulus (GPa)	Shear Modulus (Gpa)	Long Strain Energy (MPa)	Shear Strain Energy (MPa)
Avg.	62.09	4.40	11.52	7.66
Std. Dev	6.80	0.19	1.37	0.21
% Dev	0.11	0.04	0.12	0.03

the structural cases. It is important to note that the variance is greatly reduced when compared to that of the macroscale plots. A comparison of the averages and standard deviations are shown in Table 5.9 and illustrates that the variation at the structural scale as compared to the macroscale is significantly reduced. For example, the maximum standard deviation at the macroscale showed up to a 15% while that at the structural scale was a mere 2%. Consequently, it appears that the effects of lower scale variation are diminished after one or two higher length scales of homogenization. Future work will investigate stochastic modeling of parameters as well as architectural nesting effects.

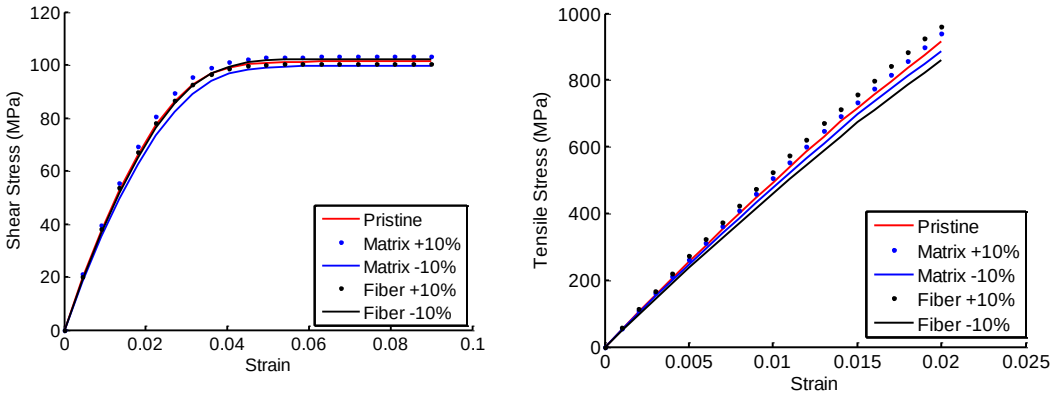

Fig. 5.18 Material Variation Results on Plain Weave Composite subjected to Shear and Tensile Loading Respectively.

5.6. Future Work

In this report it was demonstrated that MSGMC is high capable of capturing even the highly nonlinear shear response with techniques such as plasticity and viscoplasticity. This research focused on the tensile and shear response, however modeling the compressive response is a critical issue as woven composites are

commonly used in a variety of applications. Nonlinear geometric effects are a critical mechanism that partially governs the compression of woven composites. Additionally, predictive capabilities for the load/unload and fatigue response of woven composites are still rudimentary and use of MSGMC to predict these as a valuable application of the multiscale micromechanics.

Chapter 6

6. Modeling Ceramic Woven Composites

6.1. Introduction

For this particular study, a five harness satin weave is considered. In this idealization of the architecture, the repeating unit cell is assumed to be representative of the entire structure. A multiscale framework depicting the critical length scales and features for this study is shown in Fig. 6.2. A picture of the fabric with the repeating unit cell outlined in red is shown in Fig. 2.5; in this study nesting/ply shifting will be ignored. To create a RUC suitable for analysis, the weave is discretized into several sub-volume cells. There are two types of materials comprising all the subcells: fiber tows and interweave matrix. This final 3D discretization is shown in Fig. 6.1, along with example lower scale RUC representing the multiscale analyses of the interweave voids, tows and intra-tow voids. In the figure, fiber tows are indicated through the lined subcells. The lines indicate the direction of orientation. The blank subcells represent the interweave matrix. This results in a 10x10x4 sized RUC of dimensions shown in Eq. (15). In this equation w is the tow width and delta, the tow spacing, can be determined from $V_f = \frac{w}{(w+\delta)} V_{f_{tow}}$. The proper overall fiber volume fraction and tow width is enforced by back calculating the tow spacing. Due to the chemical vapor infusion process used to manufacture the woven fabric composites, there exists high levels of porosity, as shown in Fig. 6.2, that cannot be neglected.

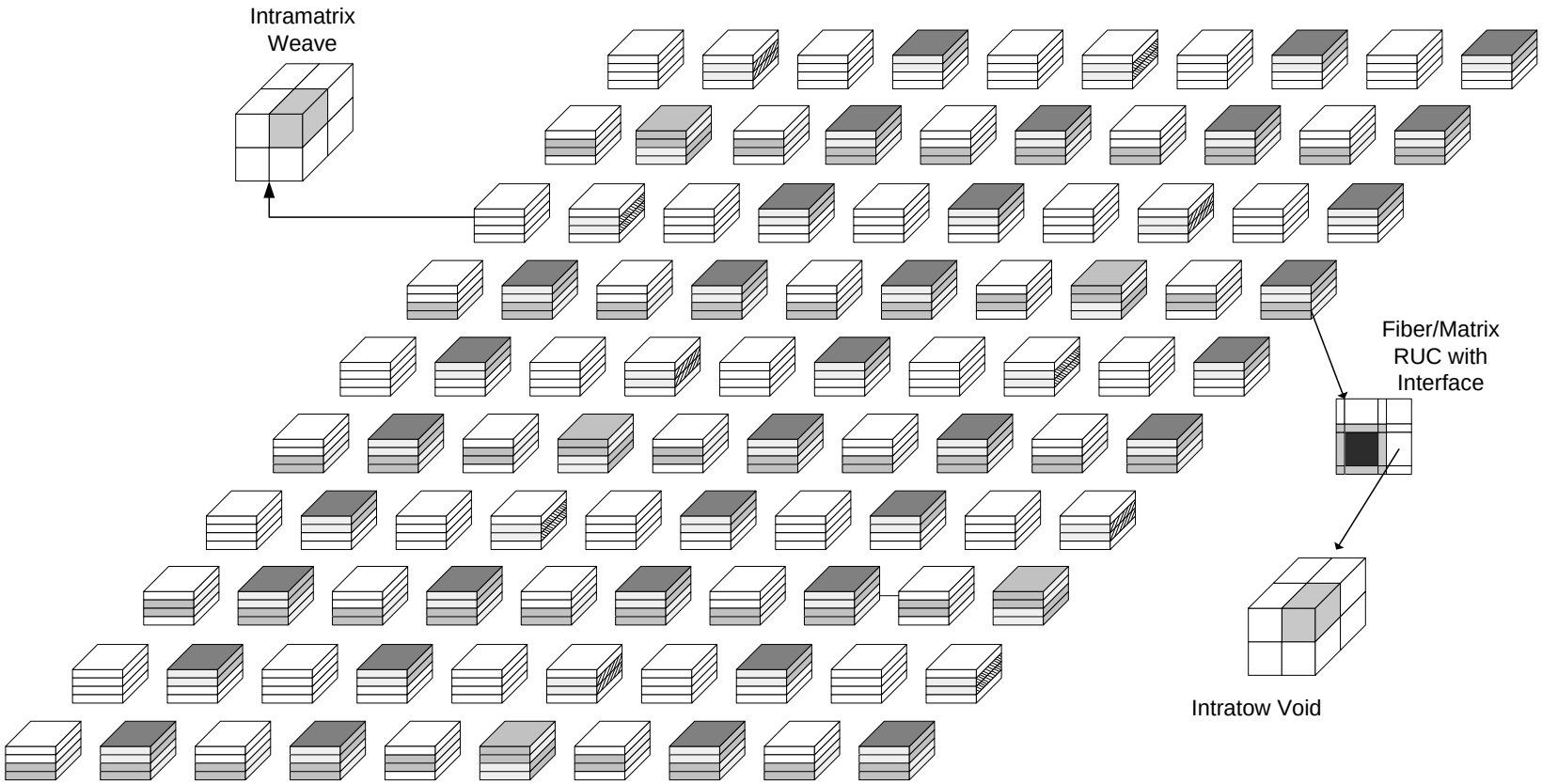

Fig. 6.1 Discretized 5-Harness Satin Subcell Configuration

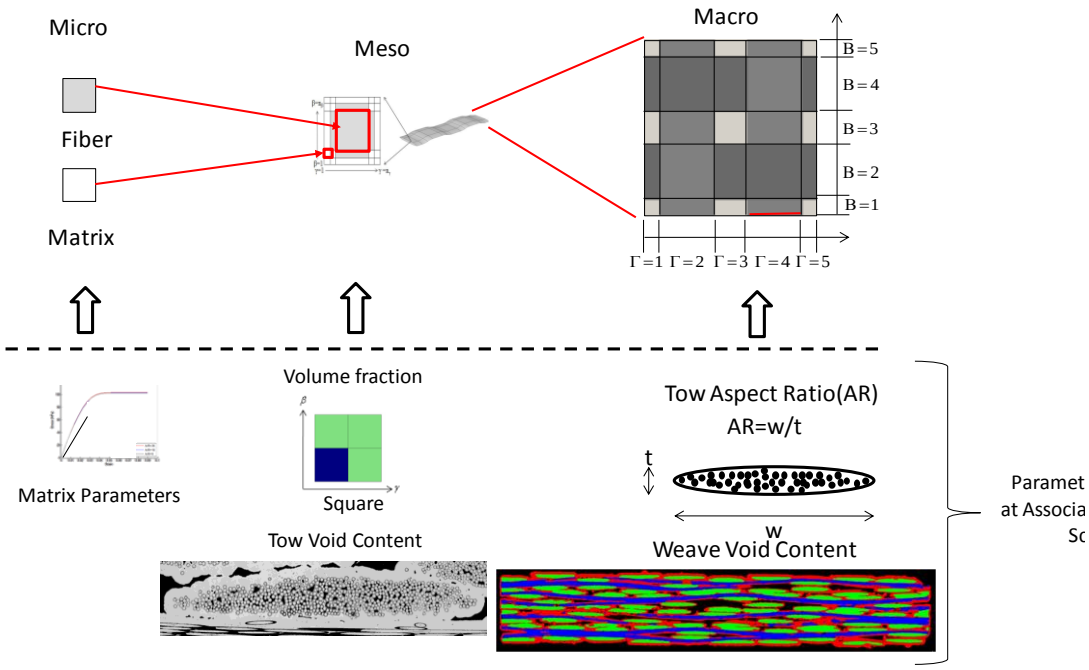

Fig. 6.2 Multiscale methodology with architectural effects being varied shown at three length scales considered. Actual micrographs are complements of P. Bonacuse, NASA GRC, 2010.

6.2.Void Modeling

Voids are accounted for in the RUC in one of three ways: 1) void content is neglected; 2) voids are assumed to be evenly distributed through the weave; or 3) voids are localized to critical areas determined from optical inspection (microscopy). Fig. 6.3 illustrates the three types of void modeling at the macroscale. The first figure shows no voids accounted for anywhere, the second figure depicts voids evenly distributed in the weave matrix (yellow, e.g., 12.7% void fraction), and the third figure shows high density (e.g., 85%) void regions in red and low density (e.g., 5%) void regions in blue. Note in both void idealization the total interweave void volume fraction is held constant at 12.7%. The voids are accounted for at a smaller length scale by analyzing a separate RUC

homogenizing those properties. This is done for two primary reasons. First, explicit modeling of voids in GMC will tend to "eliminate" an entire row and column due to the constant strain field assumptions within a subcell. Yet, by performing a separate analysis, this effect is dampened since void volume and shape merely change the resulting anisotropic "constituent" response. Secondly, this allows for a faster, more accurate representation of void shape and distribution then explicitly modeling voids at this length scale.

$$D = \{t/4, t/4, t/4, t/4\} \tag{6. 1}$$

$$H = \{\delta, w, \delta, w, \delta, w, \delta, w, \delta, w\}$$

$$L = \{\delta, w, \delta, w, \delta, w, \delta, w, \delta, w\}$$

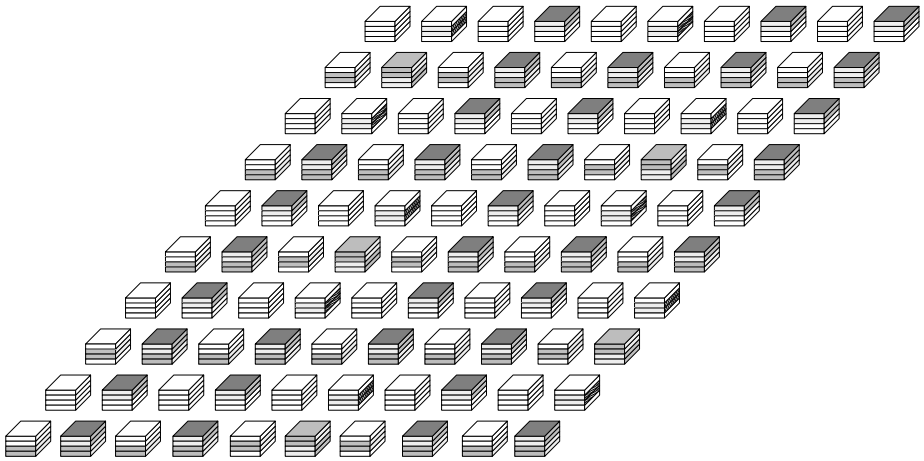

Fig. 6.3 Three Types of Void Distributions; white no voids, yellow and blue represent 5% voids, and red represents 85% void content

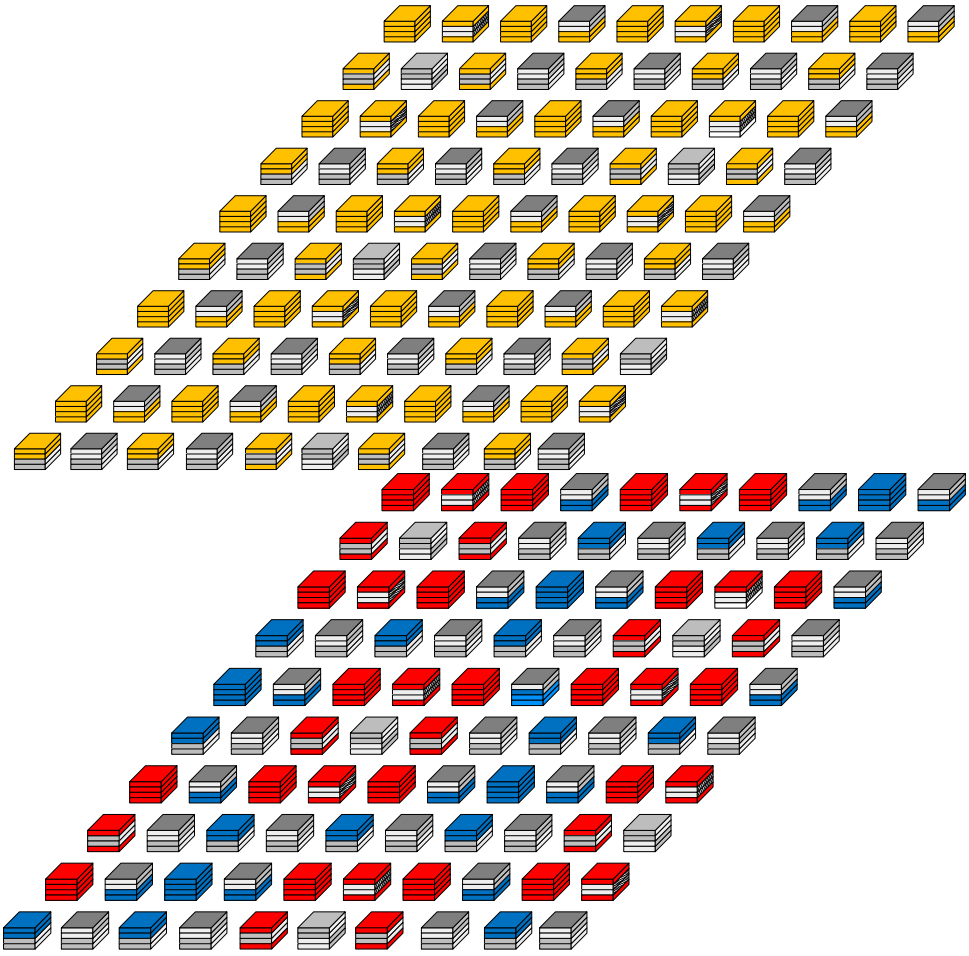

Fig. 6.3 (contd.) Three Types of Void Distributions; white no voids, yellow and blue represent 5% voids, and red represents 85% void content

6.3. Tow Repeating Unit Cell With Interface

The fiber tow bundles are modeled using a doubly periodic (continuously reinforced) 4x4 repeating unit cell consisting of three materials: fiber, fiber coating/interface, and matrix. Consequently the effective tow properties are influenced at each load step by all three constituents. In Fig. 6.4 , the black denotes the fiber, the hatched area represents the interface, and white represents the matrix. At this level there are also voids due to the CVI process. However, the voids at this level appear to be more evenly distributed than at the weave level and thus are represented by evenly distributing the void content in the tow areas

(see tow in Fig. 6.4). This is accomplished once again by calling a separate void analysis for each matrix subcell in the RUC, just as described in the weave RUC section. Consequently, the effective tow properties are being influence at each increment by all three constituents, matrix damage and intra-tow void volume fraction. For each fiber tow bundle, the orientation is carefully computed such that the undulation is properly accounted for and the failure criteria can be applied in the local coordinate system.

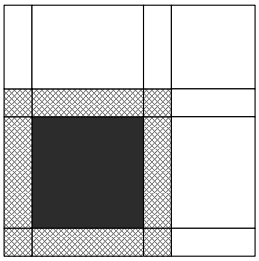

Fig. 6.4 Fiber Tow Bundle with Interface RUC

Voids are modeled through computation of a triply periodic (discontinuously reinforced) 2x2x2 RUC as shown in Fig. 6.5. The hatched subcell represents the void portion while the white represents the matrix. The relative size of the void cell is what determines the overall void content in both the fiber tow bundles and the weave. As mentioned previously, modeling of voids as a separate GMC analysis has many advantages. The overall RUC of the weave will remain constant regardless of the shape and distribution of the voids, i.e. no rediscretization is required. Consequently, the void location, quantity, and geometry can be quickly changed. Lastly, the strength and stiffness degradations and stress concentrations can be captured through GMC without reducing the accuracy of the analysis at the macroscale.

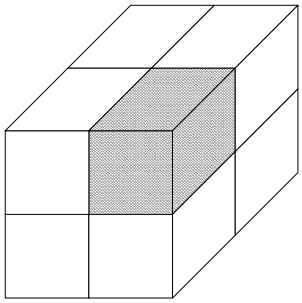

Fig. 6.5 3D Void RUC

6.4.Constitutive and Failure Modeling

6.4.1. Matrix Damage Modeling

The matrix material, assumed to be the same in both the weave and tow, is modeled through a scalar damage mechanics constitutive model driven by the magnitude of triaxiality, i.e. the first invariant of the stress/strain tensor. This constitutive model represents the cracks and brittle failure often seen in these CMCs. A scalar damage variable, ϕ, which varies between zero (no damage) and one (complete failure/damage), scales the elastic portion of the stiffness tensor and is employed directly in the stress strain relationship.

$$\sigma = (1-\phi) C\varepsilon \tag{6. 2}$$

To determine the magnitude of damage, a damage rule is defined as:

$$f = 3\varepsilon_H nK - \sigma_H = 0 \tag{6. 3}$$

In this potential, *n* represents the damaged normalized secant modulus and *K* represents the instantaneous tangent bulk modulus, see Fig. 6.6. This potential

uses a stress and strain measure as defined by the first invariant of the respective tensors. This is shown in the following equations.

$$\sigma_H = I_1(\sigma) = \frac{(\sigma_{11} + \sigma_{22} + \sigma_{33})}{3}$$
$$\varepsilon_H = I_1(\varepsilon) = \frac{(\varepsilon_{11} + \varepsilon_{22} + \varepsilon_{33})}{3} \quad (6.\ 4)$$

The damage rule in (6. 2) is only active once a critical stress criteria has been reach, i.e., it is only valid when $\sigma_H > \sigma_{dam}$. Equation (16) can be rewritten in incremental form with i+1 denoting the next increment ($\varepsilon^{i+1} = \varepsilon^i + \Delta\varepsilon^{i+1}$).

$$f = n3K^i \Delta\varepsilon_H{}^{i+1} - \Delta\sigma_H{}^{i+1} = 0 \quad (6.\ 5)$$

This can be converted to a strain based function by substituting the following relationship in for the stress increment:

$$\Delta\sigma_H{}^{i+1} = 3\left(K^{i+1}\Delta\varepsilon_H{}^{i+1} + \left(K^{i+1} - K^i\right)\varepsilon_H{}^{i+1}\right) \quad (6.\ 6)$$

Resulting in:

$$nK^0\Delta\varepsilon_H{}^{i+1} - \left(K^{i+1}\Delta\varepsilon_H{}^{i+1} + \left(K^{i+1} - K^i\right)\varepsilon_H{}^{i+1}\right) = 0 \quad (6.\ 7)$$

where K^0 represents the initial bulk modulus, see Fig. 6.6. The instantaneous tangent bulk modulus can be related back to the damage scalar through

$$K^{i+1} = \left(1 - \phi^{i+1}\right)K^0 \quad (6.\ 8)$$

:

Substitution of (6. 8) into (6. 7) and simplification yields a formulation for the damage scalar:

$$1-\phi^{i+1}=\lambda^{i+1}=K^{0}\frac{n\Delta\varepsilon_{H}^{\,i+1}+\lambda^{i}\varepsilon_{H}^{\,i+1}}{\left(\Delta\varepsilon_{H}^{\,i+1}+\varepsilon_{H}^{\,i+1}\right)} \tag{6. 9}$$

where the initial value, ϕ^{0}, is zero.

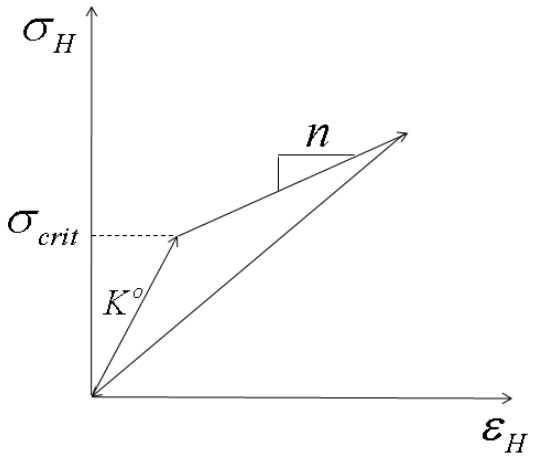

Fig. 6.6 Schematic showing bulk moduli change as function of triaxial strain.

6.4.2. Fiber Failure Modeling

The fiber is assumed to behave linearly elastic up to failure, with failure following the Hashin type failure criterion put forth in 1980, see Ref. 9. This criterion determines the catastrophic failure of the fiber based on the axial and shear strengths. When the failure criterion exceeds 1, the fiber stiffness matrix is degraded to a minimal value. A key assumption made in this analysis is that the compliant fiber interface will fail simultaneously with the fiber and does not present its own failure modes. The failure stress levels presented later are an in-situ failure stress considering the interface.

Table 6.1 iBN-Sylramic Fiber Properties

Name	iBN-Sylramic
Modulus	400 GPa
Poisson's Ratio	0.2
Axial Strength	2.2 GPa
Shear Strength	900 MPa

$$f = \frac{\sigma_{11}^{\ 2}}{\sigma_{axial}^{\ 2}} + \frac{1}{\tau_{axial}^{\ 2}}\left(\sigma_{13}^2 + \sigma_{12}^2\right) \qquad (6.\ 10)$$

6.5.Results

For this study, a five harness satin weave with a CVI-SiC matrix and iBN-Sylramic fiber (silicon carbide fiber coated with boron nitride) were chosen, due to the availability of experimental data for correlation. An approximate overall fiber volume fraction of 36% (which was held fixed for all cases examined) was determined along with a tow width of 10mm and total thickness of 2.5mm (i.e., eight plies), see actual micrograph inserts in Fig. 6.2 (compliments of P. Bonacuse, NASA GRC). The properties and necessary material parameters are listed in Tables 6.1 through 6.5, wherein the elastic properties were determined

Table 6.2 CVI-SiC Matrix Properties

Name	CVI-SiC
Modulus	420 GPa
Poisson's Ratio	0.2
σ_{dam}	180 MPa
n	0.04

Table 6.3 Boron Nitride Fiber Interface Properties

Name	Boron Nitride
Modulus	22 GPa
Poisson's Ratio	0.22

from either published values or discussions with colleagues while the strength and damage parameters were obtain from correlation with the macrolevel tensile response curve, shown in Fig. 6.7.

A typical response curve of an experimental, on-axis, tensile test is shown in Fig. 6.7, taken from Morscher (see Ref. 7 and 8), and is overlaid with a baseline correlation using the localized void model (see Fig. 6.3c). The simulated response shows good correlation with the experimental curve, approximately capturing the deviation from proportionality (often referred to as "first matrix cracking") and failure stress. In Fig. 6.8, the underlying mechanisms causing nonlinearity (which are subtle in some places), are denoted; the four primary events being: intra-tow matrix damage, inter-weave matrix damage (in the low stress and also in the high stress region) and fiber failure. The multiple damage initiation points are due to two reasons. First, different regions of the weave RUC

Table 6.4 5HS iBN-Sylramic/CVI-SIC Weave Architecture Properties

Type	5HS
Fiber Volume Fraction	36%
Tow Volume Fraction	78%
Tow Width	10mm
Tow Spacing	2.78mm
Thickness	2.5mm
Matrix	CVI-SiC

will initiate damage at different times. Secondly, different tow subcells within a given region initiate local damage at different time's thus providing variable effective tow properties. It is useful also to look at the instantaneous secant elastic modulus, which degrades due to matrix damage as shown in Fig. 6.9. It is easier to understand the degradation effects due to the matrix by directly looking at the stiffness effects. In a typical tensile response curve, there are four significant events that are useful for characterizing the material; these are: 1) initial modulus 2) point of nonlinearity (first matrix cracking) 3) post first matrix cracking (i.e., damaged) modulus and 4) fiber failure point. The subsequent parametric study will focus on the impact that material and architectural parameters have on these four significant measures.

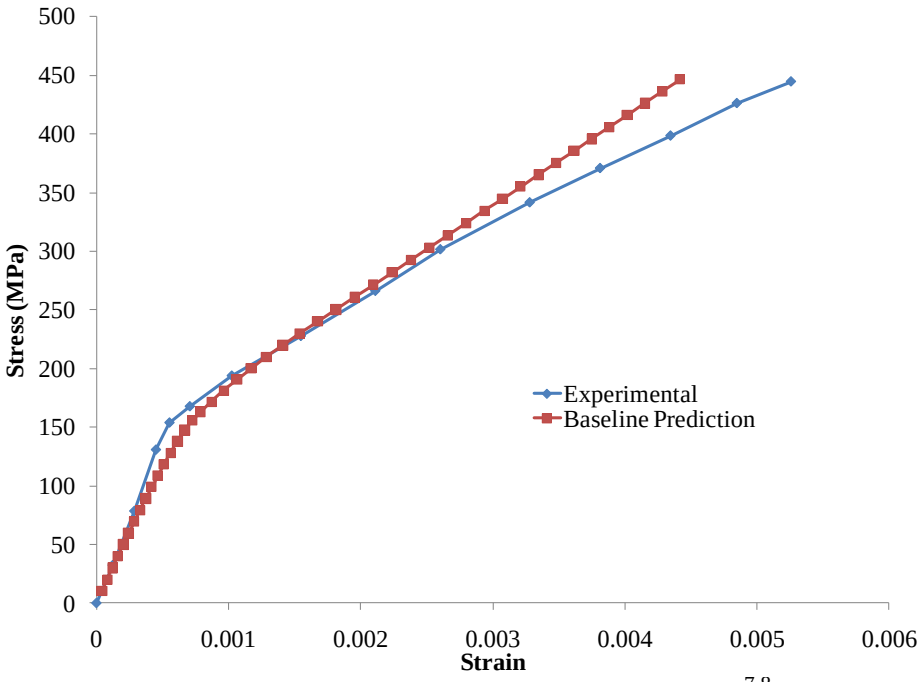

Fig. 6.7 Typical Experimental Response Curve[7,8]

Table 6.5 5HS iBN-Sylramic/CVI-SIC Tow Architecture Properties

Tow Fiber Volume Fraction	46%
Tow Packing Structure	Square
Fiber	IBN-Sylramic
Matrix	CVI-SiC
Interface	BN

Furthermore, it is critical to understand the underlying mechanisms governing these events. In the case of the initial modulus, it is clear that the individual constituents' stiffness matrices and the weave architecture are primary drivers, along with possible microcracking of the matrix constituent. The fact that some damage occurs before the first major point of nonlinearity, is substantiated by the experimental acoustic emission results in Ref. 7. Similarly, the model attributes this initial cracking to damage in the intra-tow matrix and to damage in the high void density region of the inter-weave matrix (known as the high stressed region). The second event (i.e., the first major point of nonlinearity) occurs at approximately 0.075% strain, for the CMC examined, is said to be "first matrix cracking". This point is taken to reflect a significant crack (or coalescence of microcracking) occurring in either the tow or weave matrix; thus enabling environmental attack of the composite. Correlating model results to that of the typical response (see Fig. 6.7), the model predicts that cracking occurs in both the tow and weave, at "first matrix cracking". Thirdly, the slope of the post first matrix cracking curve (damage modulus) is determined by the response of the tows in the loading direction, matrix material (i.e., the behavior after damage initiation) and corresponding constitutive model and weave architecture. Again,

the experimental acoustic emission results (of Ref. 7) are consistent with this in that they show some damage gradually occurring after first matrix cracking within this region of the response curve. This is most likely a combination of all previous damage growing as well as the onset of new damage in the high stressed regions. This damage progression continues with continuous local stress redistribution from matrix to tow/fiber until the final failure point is determined by reaching the failure strength of the fibers within the tow. Note, although not considered here, MSGMC can incorporate statistical fiber breakage by modeling multiple fibers within the Tow RUC. Further although both the axial and shear fiber failure strength values given in Table 6.1 were backed out from the composite level tensile curve, these parameters should be experimentally determined from either individual monofilament and/or tow testing. To the authors knowledge such tests have not be conducted to date, but will be critical tests that should be done in the future.

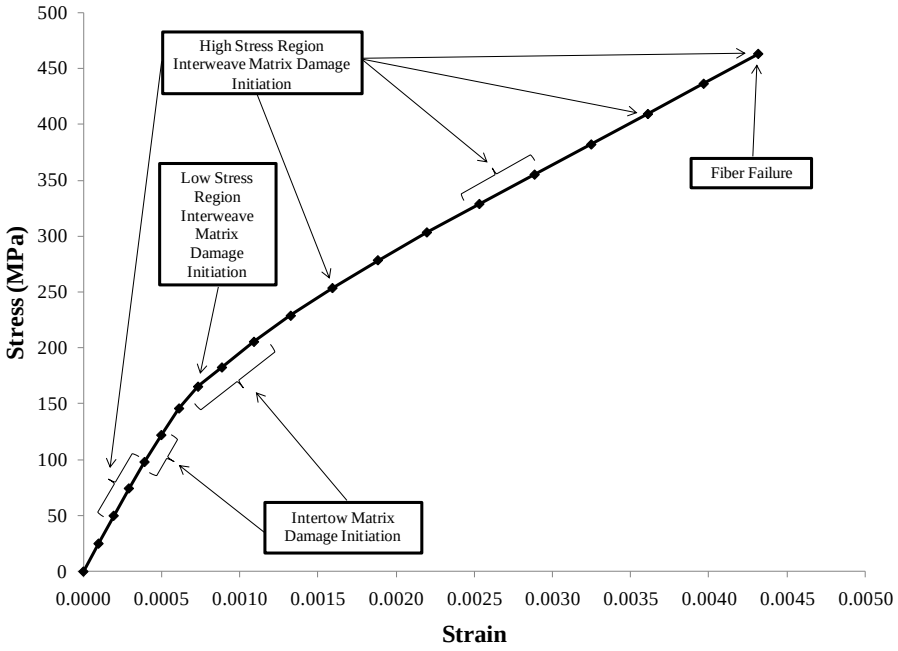

Fig. 6.8 Typical Simulated Response Curve

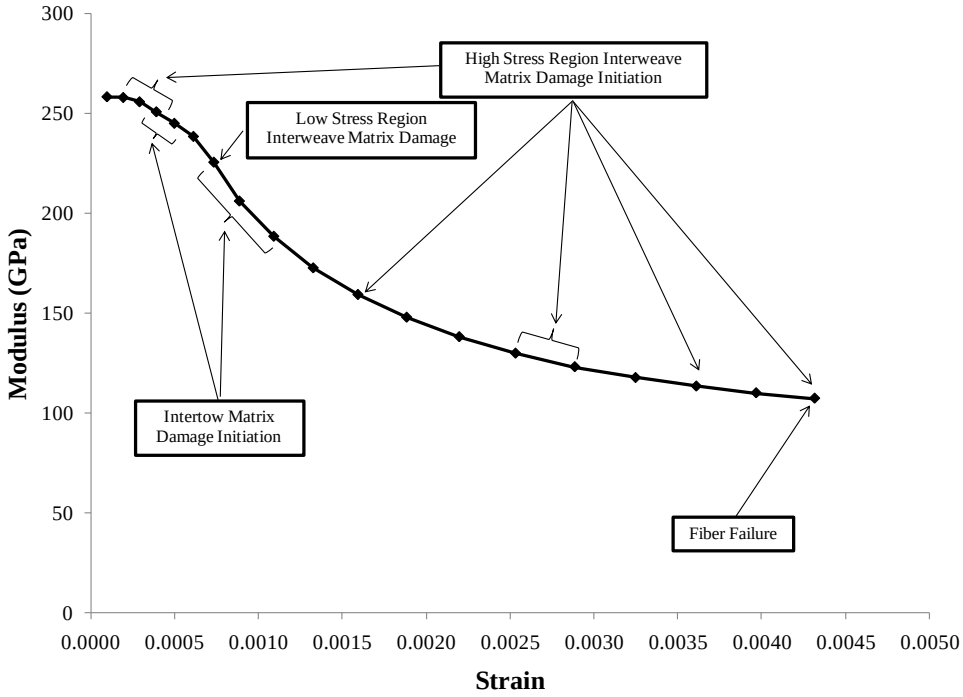

Fig. 6.9 Typical Simulated Secant Modulus

6.5.1. Effects of Material Properties

To understand the influence of constituent material variation on the overall macro response; three of the matrix material constitutive model parameters (i.e., the initial modulus, post first matrix cracking modulus, n, and critical cracking stress, σ_{dam}) were varied. Note, these properties were varied a significant amount from the baseline so that their effect could be clearly seen. For example, the initial modulus was increased by 50%, in another case n was increased by 200% and in a third case σ_{dam} was increased by 100%. Considering the results in Fig. 6.7, one would expect that changing the matrix modulus should correspond to changing the initial weave modulus and post first matrix cracking modulus. This is in agreement with the results shown in Fig. 6.10. In addition to the weave stiffness changing, the onset of "first matrix cracking" is also affected; resulting in a higher stress level (approximately 10%) and lower strain to failure (approximately 10%). Next changing only the parameter n from that of the baseline, one would expect the post first matrix cracking modulus to be primarily impacted, as verified in Fig. 6.10, with a corresponding change in failure stress (e.g., increased 10%), failure strain (e.g., decreased 12%), and post secondary modulus (e.g., increased 120%). Finally, increasing σ_{dam} caused the "first matrix cracking" onset to be delayed (approximately 110 MPa, or 94%) resulting in higher overall failure stresses (increase of 8%) and a lower failure strain level of 0.0031 (a 24% reduction). Note that the initial weave modulus and post first matrix cracking modulus are nearly unchanged, in this case.

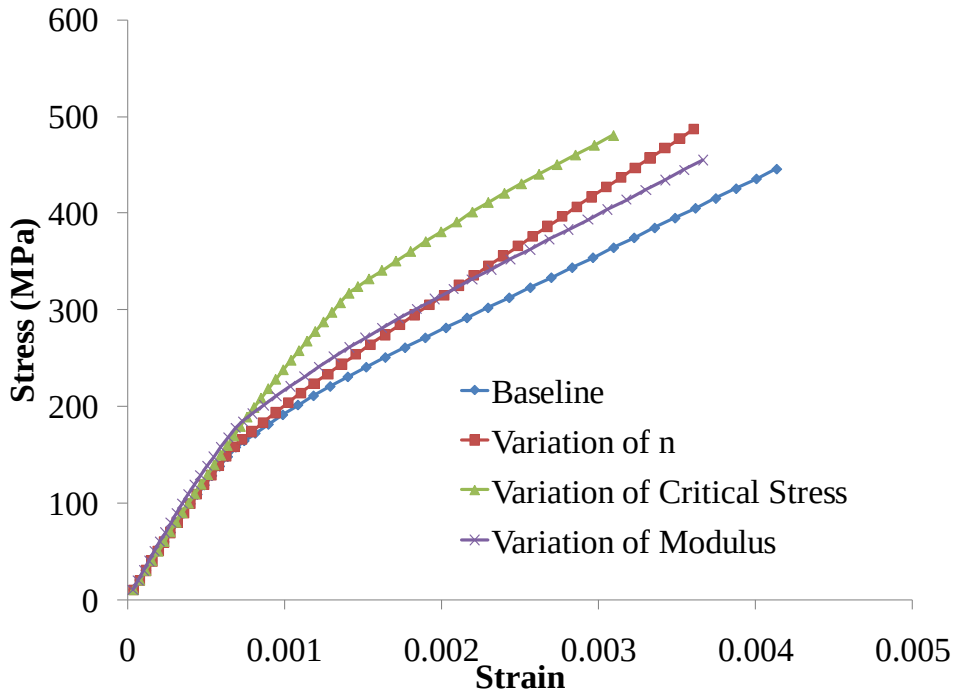

Fig. 6.10 Variation of Matrix Constituent Material Properties

6.5.1. Effects of Architecture

To study the effects of architectural variation on the macroscale response, a full factorial set of numerical simulations were conducted. The parameters varied are shown in Table 6.6 and depicted in Fig. 6.2. The three tow architectural parameters varied were: a) tow fiber volume fraction, b) tow aspect ratio, and c) tow void volume fraction. In addition, three weave void location cases were examined to illustrate the influence of void location due to manufacturing as well. Note in the present study void shape is not examined due to lack of knowledge of 3D variation. All other parameters in the analysis were kept constant. Additionally, other architectural effects exist that the authors did not investigate which could possibly have an effect. These include inter-ply nesting, fiber

Table 6.6 Varied Parameters and Ranges for 5HS iBN-Sylramic/CVI-SiC Study

Architectural Parameter	Relevant Length Scale	Values
Tow Fiber Volume Fraction (V_{tf})	Meso	0.46,0.48,0.50
Tow Void Volume Fraction	Meso	0.01,0.05,0.07
Tow Aspect Ratio (*AR*)	Macro	8,10,12
Weave Void Distribution	Macro	None, Even, Localized

packing structure, coating thickness, and fiber tow shifting to name a few. Future work will determine which of these parameters are the most significant. The tow fiber volume fraction and void volume fraction are both considered a mesoscale effect because their geometrical properties are involved in the mesoscale concentration matrix (Eq. (2)); whereas, the tow aspect ratio is considered a macroscale property because it is taken into account in the macroscale concentration matrices (Eqs. (5) and (11)). The tow volume was varied over a narrow range indicative of typical experimental variation: 0.46, 0.48, and 0.50. These three values were chosen based on common experimental values obtained for CMCs. Similarly, realistic tow aspect ratios were also chosen, i.e., 8, 10 and 12, where a value of 10 is typical for CMCs and three different fiber void volume fractions were used; 0.01, 0.05, and 0.07.

In Fig. 6.11 the effects of weave void distribution are examined; wherein three line plots (each corresponding to an assumed void distribution discussed earlier). Two cases, that is no void modeling and uniformly distributed voids, fail to capture the correct overall response. As the initial modulus is too stiff, “first matrix cracking” stress and failure stress levels are too high and the strain to

failure too large. This is a result of incorrect local failure modes and local stress distribution. Therefore one can concluded that to accurately capture the overall in-plane deformation and failure response the analysis must incorporate accurate localized void distributions. In addition it has been observed[8-10] that the out-of-plane moduli is significantly reduced as compared to that calculated when void shape is not accurately accounted for; only recently, has a sheet like network of voids been microscopically observed, Bonocuse et.al.[11,12],. Consquently, the influence of void shape is illustrated in Fig. 6.12, wherein a cubic, cylindrical and sheet like void shape is examined given the case of localized voids. The out-of-plane moduli is significantly influenced by the assumed void shape, in that E_z = 165, 172.5, and 88.8 GPa, when one considers cubic, cylindrical and flat (or sheet like) voids, respectively. However, the in-plane response (both deformation and failure) is unaffected by void shape as shown in Fig. 6.12, as one might expect.

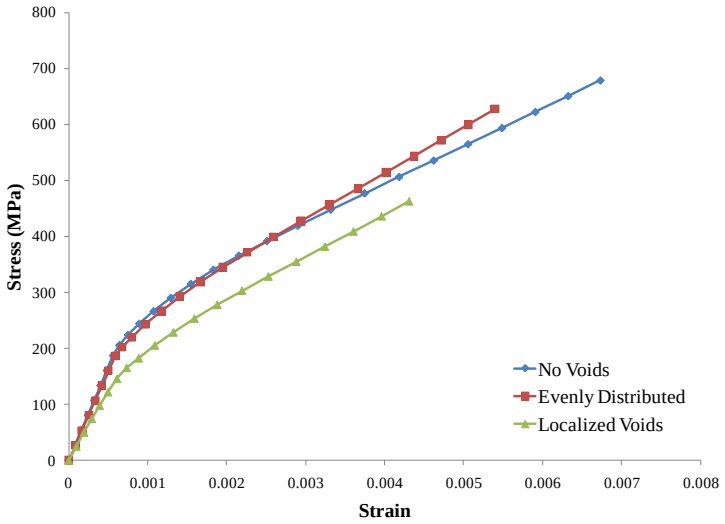

Fig. 6.11 Effects of Weave Void Distribution

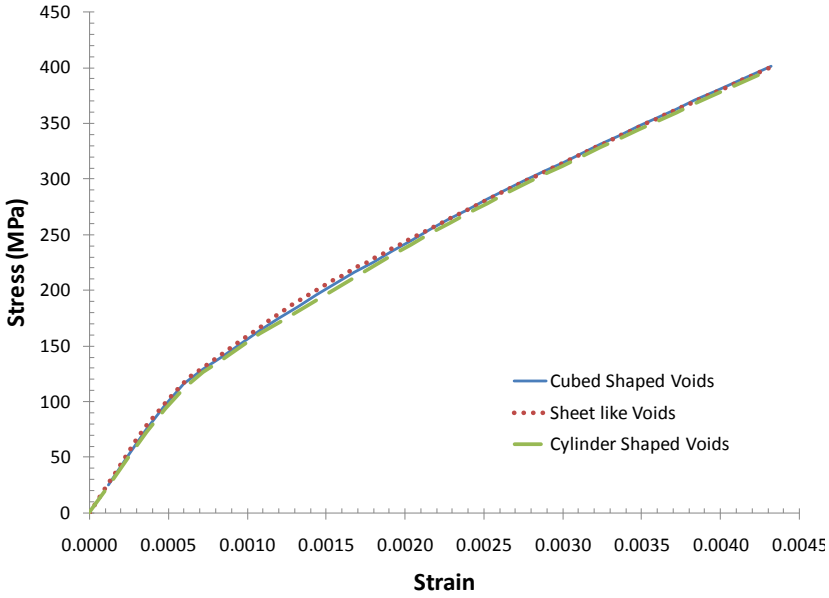

Fig. 6.12 Effect of void shape on tensile response, given localized void distribution.

The remaining parametric cases were all computed using the localized void model. However, it is important to note that the tow fiber volume fraction and weave void volume fraction are coupled and cannot be decoupled within the analysis, since when the fiber volume fraction within the tow increases, the tow spacing must increase in order to maintain continuity of the overall fiber volume fraction and thickness. This therefore creates a large volume domain for voids to fill, thus increasing the overall void content. Correspondingly, the effect of increasing void content and tow volume fraction are coupled together. The total variation in stress – strain response for all cases are shown in Fig. 6.13. Clearly, the overall response characteristic is very similar, irrespective of the value of the individual parameters, with the variation in the initial modulus being at most 22%, first matrix cracking approximately 16% and the ultimate tensile stress for all

practical purposes being identical. Furthermore, the post first matrix cracking modulus changes some 24% (i.e., from 72 GPa to 90 GPa) with a corresponding 16% change in final failure strain. The configuration providing the stiffest response is composed of a tow volume fraction of 46%, aspect ratio (AR) equal to 12 and tow void fraction of 1%, whereas the most compliant response is generated using a tow volume fraction of 50%, aspect ratio (AR) equal to 8 and tow void fraction of 7%.

In Fig. 6.14 through Fig. 6.16 the various responses are arranged so as to enable identification of parameter sensitivities. Fig. 6.14 shows the effect of tow void content on the overall response; where it can be seen that increasing the void content within the tow (thus lowering its effective stiffness) causes the macro response curve to be more compliant with generally an effect of increasing the strain to failure. Fig. 6.15 shows the effect of tow aspect ratio; where increasing the aspect ratio has the effect of stiffening the response curve and lowering the failure stress. Fig. 6.16 displays the influence of tow fiber volume fraction, which appears to be minimal at first glance. Although this trend is possible, as mentioned previously, it is strongly coupled with the overall weave void volume fraction and thus these two effects could be working in opposition to one another. Consequently, it is impossible to deduce from these graphs, the overall effect of tow fiber volume fraction.

Comparing all parameters, the weave void locations, tow void content, fiber volume fraction within a tow and tow aspect ratio, one can assess the severity of these effects. For example, it is clear from Fig. 6.11, that the location

(and shape) of voids at the macroscale is a critical driving parameter relative to failure. This far outweighs all other parameters. Similarly, the effect of inter-ply tow nesting could also be a critical/primary driving factor, yet this effect has been left for future work. Besides the weave void content (i.e., location and shape), the tow void content has the strongest effect on post first matrix cracking stiffness and the tow aspect ratio has the strongest effect on failure strain. The tow fiber volume fraction appears to have a minimal effect.

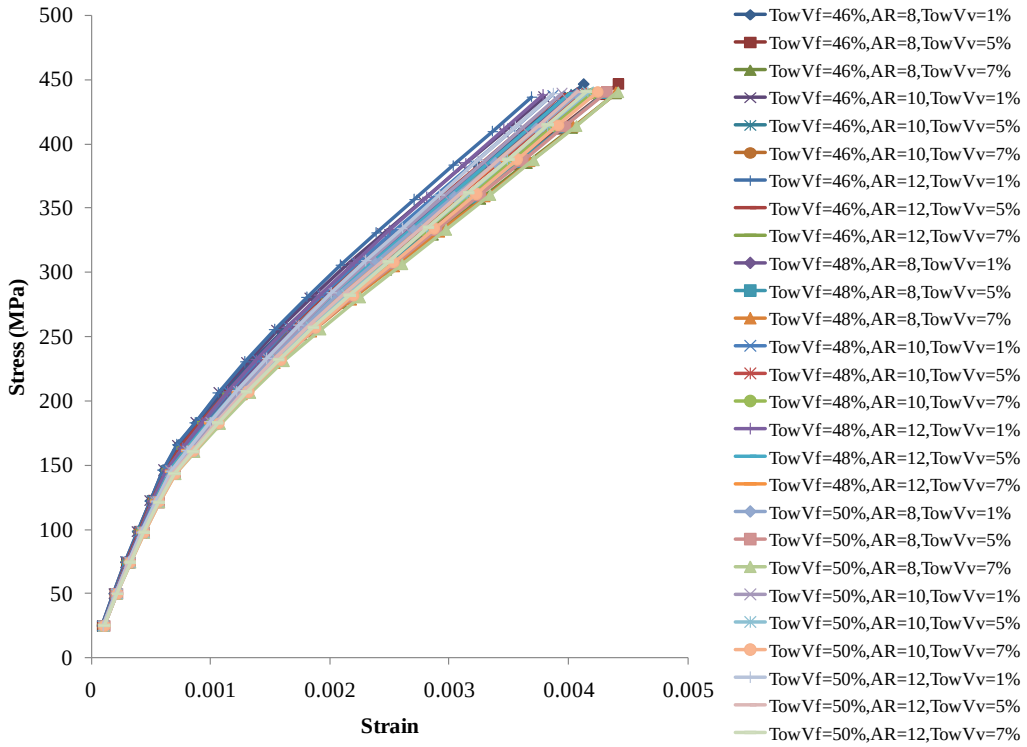

Fig. 6.13 All Simulated Cases

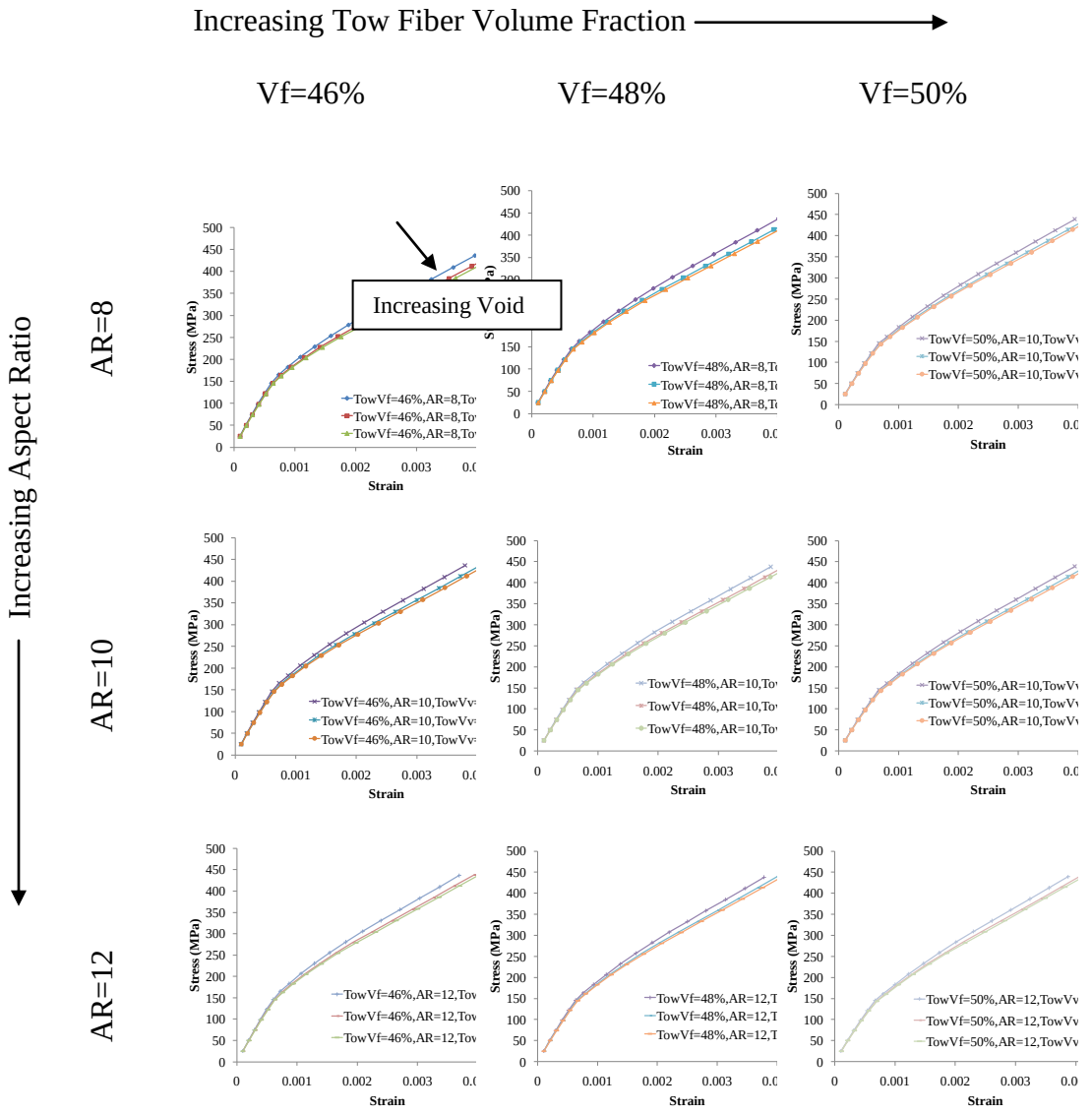

Fig. 6.14 Effects of Tow Void Content

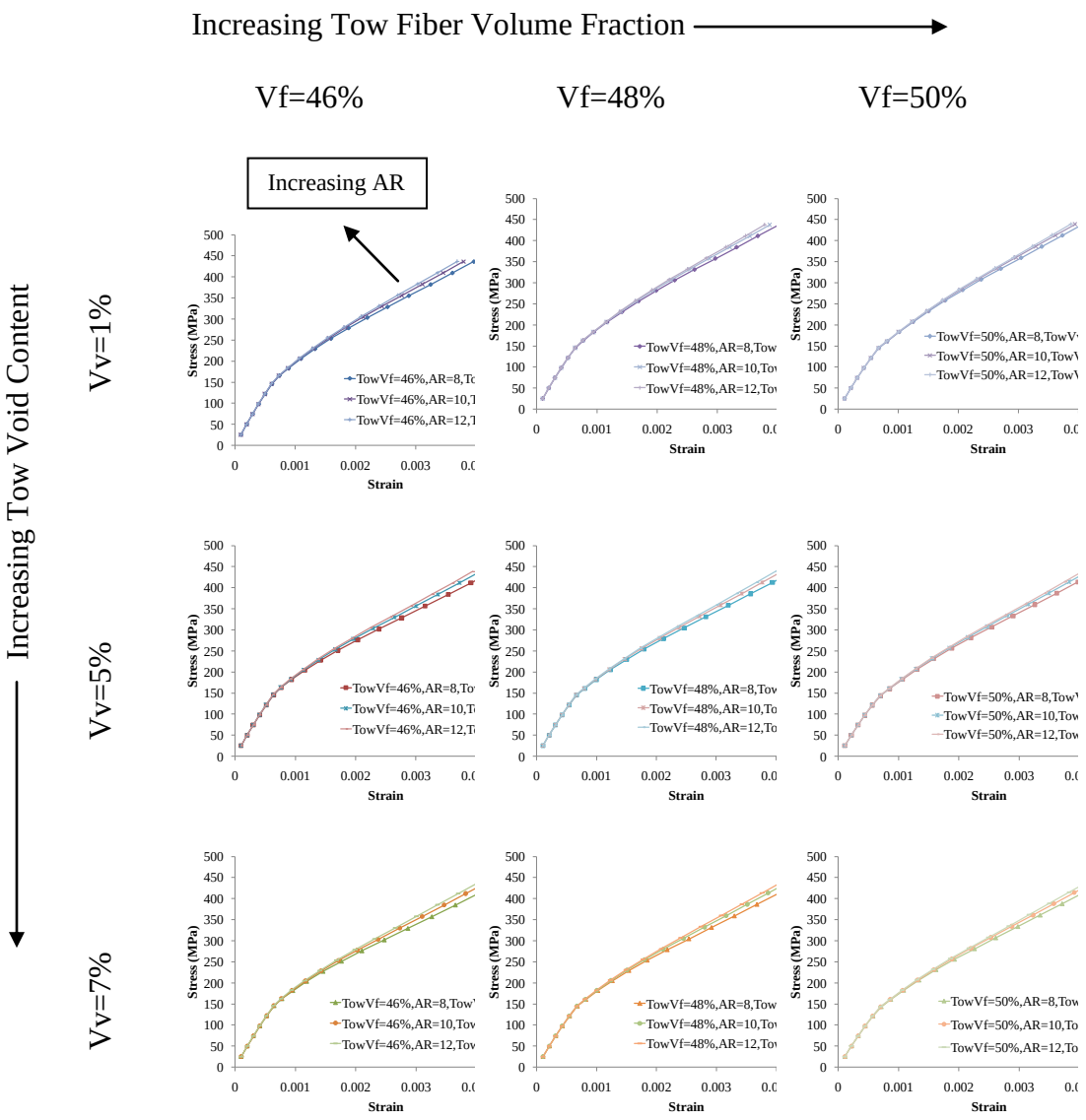

Fig. 6.15 Effects of Aspect Ratio

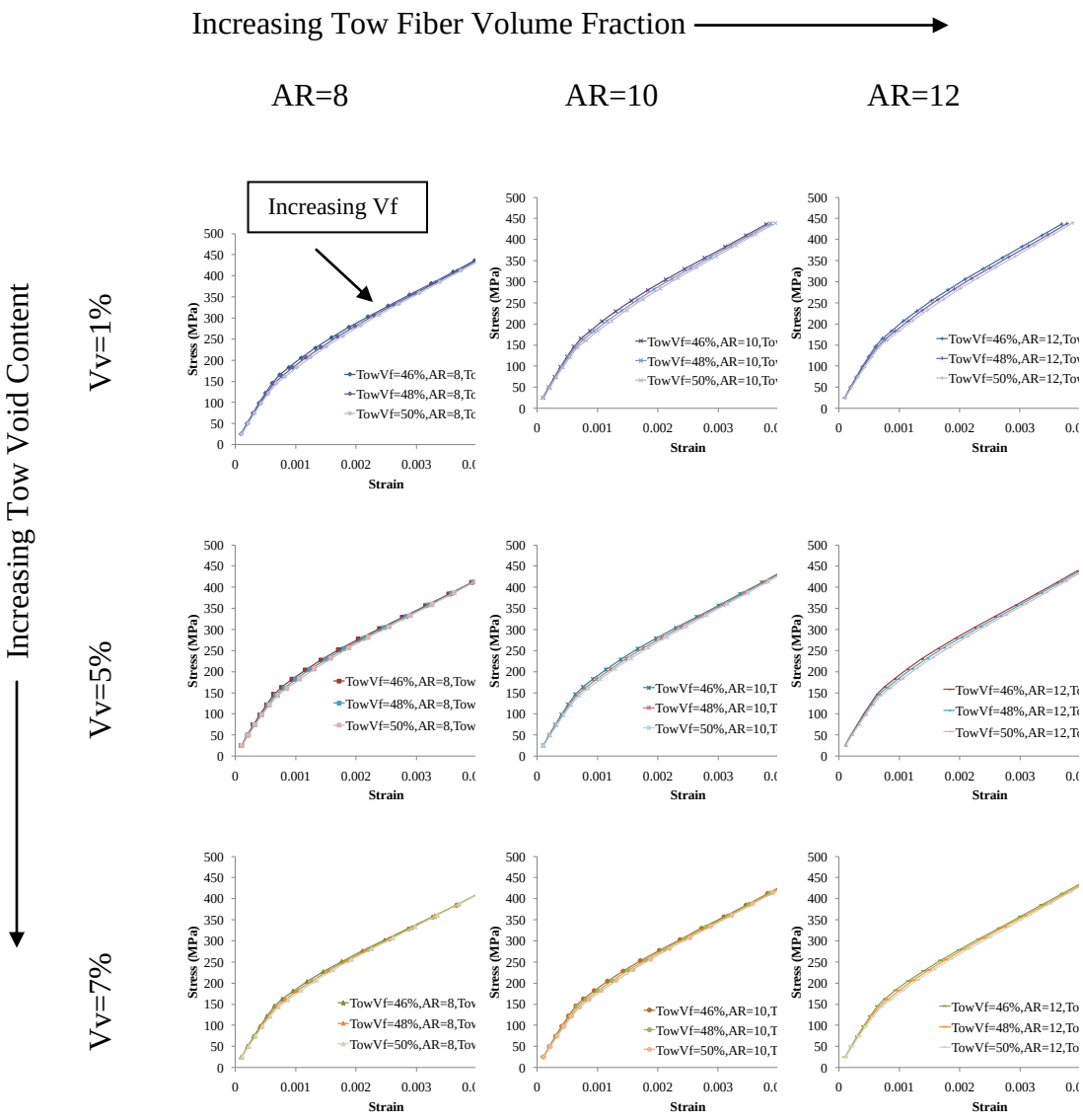

Fig. 6.16 Effects of Tow Volume Fraction

6.6. Future Work

Here the mechanical response of the ceramic matrix woven composites was predicted with a high accuracy. CMCs however are typically multifunctional materials that are used in thermo-mechanical loading as a heat barrier and load bearing structure. Modeling the thermal stresses, creep and high temperature

effects of CMCs is the next progressive step. In addition, implementation of MSGMC with an oxidation model to predict the degradation due to chemical effects will be useful as CMCs are a highly multifunctional material.

Chapter 7

7. Conclusion

7.1. Conclusion

This research in this dissertation can be summarized into two portions: multiscale modeling and analysis of complex composites. A novel micromechanics based multiscale modeling technique is reported that continuously bridges between all length scales and solves all governing equations simultaneously. This technique, known as MSGMC, is fully generalized for any multiple length scale periodic structure and fully capable with integrated with an elasto-plastic or damage mechanics based constitutive model. A specific formulation of MSGMC implementing a through thickness homogenization is formulated to allow for modeling of thin RUCs, such as woven and textile composites. Furthermore a reformulation to improve the computational efficiency is also provided. MSGMC was then used to analyze polymer matrix and ceramic matrix composites for triaxial and woven configurations. Results showed excellent correlation with experimental data and other theoretical methods.

REFERENCES

Abaqus Version, 6. (2007). *Abaqus/CAE and Abaqus/Standard.* Simulia World Headquarters, Providence.

Aboudi, J. (1995). Micromechanical analysis of thermo-inelastic multiphase short-fiber composites. *Composites Engineering* , 839-850.

Aggarwal, A., & Ramakrishna, S. (2001). Predicting the in-plane elastic constants of diamond braided composites. *Journal of Composite Materials* , 665-688.

Arnold, S., & Bednarcyk, B. (1999). Micromechanics Analysis Code with Generalized Method of Cells (MAC/GMC) User Guide. *NASA/TM-1999-109070* .

Barbero, E., Lonetti, P., & Sikkil, K. (2005). Finite element continuum damage modeling of plain weave reinforced composites. *Composites Part B: Engineering* , 137-147.

Beard, S., & Chang, F. (2002). Design of braided composite for energy absorption. *Journal of thermoplastic composite materials* , 3-13.

Bednarcyk, B. A. (2000). Modeling woven polymer matrix composites with MAC/GMC. *NASA/CR-2000-210370* .

Bednarcyk, B. A., Aboudi, J., & Arnold, S. M. (2006). The equivalence of the radial return and mendelson methods for integrating the classical plasticity equaitons. *NASA/TM-2006-214331* .

Blackketter, D.M., D.E. Walrath, & Hansen, A.C. (1993). Modeling Damage in a Plain Weave Fabric-Reinforced Composite Material. *Journal of Composites Technology and Research,* 15(2)136-142.

Byun, J. (2000). The analytical characterization of 2-D braided textile composites. *Composites Science and Technology* , 705-716.

Chapman, C. and Whitcomb, J. (1995). Effect of assumed tow architecture on predicted moduli and stresses in plain weave composites. *J. Compos. Mater.* 29(16):2134–2159.

Cox, B., & Flanagan, G. (1997). Handbook of analytical methods for textile composites. *NASA/CR-1997-4750* .

Dadkhah, M., Flintoff, J., Kniveton, T., & Cox, B. (1995). Simple models for triaxially braided composites. *Composites* , 561-577.

D'Amato. (2001). Finite element modeling of textile composites. *Composite Structures* , 467-475.

Dow, N.F. and Ramnath, V. (1987). Analysis of Woven Fabrics for Reinforced Composite Materials. *NASA-CR-178275*.

Ernst, G., Vogler, M., Huhne, C., & Rolfes, R. (2010). Multiscale progressive failure analysis of textile composites. *Composites Science and Technology*, 70(1):61-72.

Falzon, P., & Herszberg, I. (1998). Mechanical performance of 2-D braided carbon/epoxy composites. *Composites Science and Technology* , 253-265.

Halpin, J.C., Jerine, K., & J.M. Whitney (1971). The Laminate Analogy for 2 and 3 Dimensional Composite Materials. *Journal of Composite Materials January*, 5:36-49.

Ishikawa, T., & Chou, T.W. (1982). Elastic Behavior of Woven Hybrid Composites. *Journal of Composite Materials,* 16:2-19.

Ishikawa, T., & Chou, T.W. (1982). Stiffness and strength behaviour of woven fabric composites. *Journal Material Science,* 17:3211-3220.

Ishikawa, T., & Chou, T.W. (1983). Nonlinear Behavior of Woven Fabric Composites. *Journal of Composite Materials*, 17:399-413.

Ivanov, I. and Tabiei, A. (2001). Three-dimensional computational micro-mechanical model for woven fabric composites. *Compos. Struct.* 54(4):489–496.

Jortner, J. (1986). A Model for Nonlinear Stress-Strain Behavior of 2D Composites with Brittle Matrices and Wavy Yarns. *Advances in Composites Materials and Structures*. 135-146.

Karayaka, M. and Kurath, P. (1994). Deformation and failure behavior of woven composite laminates. *J. Eng. Mater. Technol.* 116:222–232.

Ko, F.K. and Pastore, C.M. (1985). Structure and Properties of an Integrated 3-D Fabric for Structure Composites. *Recent Advances in Composites in the United States and Japan, ASTM STP 865*. 428-439.

Ko, F.K. (1989). Three-Dimensional Fabrics for Composites. *Composite Materials Series, 3, Textile Structural Composites,* 129-171.

Kollgeal, M., & Sridharan, S. (2000). Strength prediction of plain woven fabrics. *Journal of Composite Materials* , 240-257.

Kriz, R.D. (1985). Influence of damage on mechanical properties of woven composites at low temperatures. *Journal of Composites Technology and Research,* 7:55-58.

Littell, J., Binienda, W., Goldberg, R., & Roberts, G. (2008). A modeling technique and representation of failure in the analysis of triaxial braided carbon fiber composites. *NASA/TM-2008-215245* .

Masters, J.E., Fedro, M.J., and Ifju, P.G. (1992). An Experimental and Analytical Characterization of Three Triaxially Braided Textile Composites. *Proceedings of the Third NASA Advanced Composites Technology Conference.* NASA CP 3178, 263-286.

Naik, N. K., & Sekhar, Y. C. (1998). Damage in laminated composites due to low velocity impact. *Journal of Reinforced Plastics and Composites* , 1232-1263.

Naik, N. K., Chandra Sekher, Y., Meduri, & Sailendra. (2000). Polyer matrix woven fabric composites subjected to low velocity impact: Part I-Damage initiation studies. *Journal of Reinforced Plastics and Composites* , 912-954.

Naik, N., & Ganesh, V. (1992). Prediction of on-axes elastic properties of plain weave fabric composites. *Composites Science and Technology* , 135-152.

Naik, N.K. and Shembekar, P.S. (1992). Elastic behavior of woven fabric composites: I lamina analysis. *J. Compos. Mater.* 26(15):2196–2225.

Naik, R.A. (1995). Failure Analysis of Woven and Braided Fabric Reinforced Composites. *Journal of Composite Materials*, 29:2334-236.

Naik, R.A., Ifju, P.G., & Masters, J.E. (1994). Effect of Fiber Architecture Parameters on Deformation Fields and Elastic Moduli of 2-D Braided Composites. *Journal of Composite Materials*, 28: 656-681.

Naik, N.K. and Ganesh, V.K. (1996). Failure behavior of plain weave fabric laminates under on-axis uniaxial tensile loading: II analytical predictions. *J. Compos. Mater.* 30(16):1779–1822.

Paley, M., & Aboudi, J. (1992). Micromechanical analysis of composites by the generalized cells model. *Mechanics of Materials* , 127-139.

Pindera, M., & Bednarcyk, B. (1990). An efficient implementation of the Generalized Method of Cells for unidirectional, multiphased composites with complex microstructures. *Composites Part B: Engineering* , 87-105.

Quek, S. C., Waas, A. M., Shahwan, W. K., & V., A. (2004). Compressive response and failure of braided textile composites: Part 2: Computations. *International Journal of Nonlinear Mechanics* , 649-663.

Quek, S. C., Waas, A., Shahwan, W. K., & Agaram, V. (2003). Analysis of 2D flat triaxial braided composites. *International Journal of Mechanical Sciences* , 1077-1096.

Quek, S. C., Waas, A., Shahwan, W. K., & Agaram, V. (2006). Failure mechanics of triaxially braided carbon composites under combined bending-compression loading. *Composites Science and Technology* , 2548-2556.

Quek, S. C., Waas, A., Shahwan, W. K., & V., A. (2003). Compressive response and failure of braided textile composites: Part 1: Experiments. *International Journal of Nonlinear Mechanics* , 635-648.

Smith, L., & Swanson, S. (1995). Micro-mechanics parameters controlling the strength of braided composites. *Composites Science and Technology* , 177-184.

Smith, L., & Swanson, S. (1996). Strength design with 2-D triaxial braid textile composites. *Composites Science and Technology* , 359-365.

Song, S., Waas, A. M., Shahwan, K. W., Faruque, O., & Xiao, X. (2007). Braided textile composites under compressive loads: Modeling the response, strength and degradation. *Composites Science and Technology* , 3059-3070.

Stanton, E.L. & Kipp, T.E. (1985). Nonlinear Mechanics of Two-Dimensions Carbon-Carbon Structures and Materials. *AIAA Journal*, 23(8):1278-1284.

Stat-ease Design Expert Software. (n.d.). Retrieved from http://www.statease.com/

Tabiei, A., Ivanov, I. (2004). Materially and geometrically non-linear woven composite micro-mechanical model with failure for finite element simulations, International Journal of Non-Linear Mechanics, 39(2) 175-188.

Tang, X., & Whitcomb, J. (2003). Progressive failure behaviors of 2D woven composites. *Journal of Composite Materials* , 1239-1258.

Tang, X., Whitcomb, J.D., Li, Yanmei, L., and Sue, H. (2005). Micromechanics modeling of moisture diffusion in woven composites. *Composites Science and Technology*, 65(6):817-826.

Tsai, K., Hwan, C., Chen, W., & Chiu, C. (2008). A parallelogram spring model for predicting the effective elastic properties of 2D braided composites. *Composite Structures* , 273-283.

Whitcomb, J.D., Kondagunta, G., and Woo, K. (1995). Boundary Effects in Woven Composites. *Journal of Composite Materials*, 29: 507-524.

Whitcomb, J.D. and Tang, X. (2001). Effective Moduli of Woven Composites. *Journal of Composite Materials*, 35: 2127-2144.

Wu, H.-Y., & Chang, F.-K. (1989). Transient dynamic analysis of laminated composite plates subjected to transverse impact. *Composite Structures* , 453-466.

Xue, P., Cao, J., & Chen, J. (2005). Integrated micro/macro-mechanical model of woven fabric composites under large deformation. *Composite Structures* , 69-80.

Yan, Y., & Van Hoa, S. (2002). Energy model of prediction of mechanical behavior of 2-D triaxially braided composites, Part 1: Model development. *Journal of Composite Materials* , 963-981.

Yan, Y., & Van Hoa, S. (2002). Energy model of prediction of mechanical behavior of 2-D triaxially braided composites, Part II: Parameter Analysis. *Journal of Composite Materials* , 1233-1253

APPENDIX A

TERMS OF MIXED STIFFNESS COMPLIANCE MATRIX

$$\Delta = C_{44}C_{23}^2 - 2C_{23}C_{24}C_{34} + C_{33}C_{24}^2 + C_{22}C_{34}^2 - C_{22}C_{33}C_{44}$$

$$\begin{aligned} R_{11} = \frac{1}{\Delta}(&-C_{12}^2C_{34}^2 + C_{33}C_{44}C_{12}^2 - 2C_{44}C_{12}C_{13}C_{23} + 2C_{12}C_{13}C_{24}C_{34} + \\ &2C_{12}C_{14}C_{23}C_{34} - 2C_{33}C_{12}C_{14}C_{24} - C_{13}^2C_{24}^2 + C_{22}C_{44}C_{13}^2 + \\ &2C_{13}C_{14}C_{23}C_{24} - 2C_{22}C_{13}C_{14}C_{34} + C_{11}C_{33}C_{34}^2 - C_{11}C_{22}C_{33}C_{44}) \end{aligned}$$

$$R_{12} = -\frac{C_{24}\left(C_{13}C_{34} - C_{14}C_{33}\right) + C_{23}\left(C_{14}C_{34} - C_{13}C_{44}\right) - C_{12}C_{34}^2 + C_{12}C_{33}C_{44}}{\Delta}$$

$$R_{13} = -\frac{C_{34}\left(C_{12}C_{24} - C_{14}C_{22}\right) + C_{23}\left(C_{14}C_{24} - C_{12}C_{44}\right) - C_{13}C_{24}^2 + C_{13}C_{22}C_{44}}{\Delta}$$

$$R_{14} = -\frac{C_{34}\left(C_{12}C_{23} - C_{13}C_{22}\right) + C_{24}\left(C_{13}C_{23} - C_{12}C_{33}\right) - C_{14}C_{23}^2 + C_{14}C_{22}C_{33}}{\Delta}$$

$$\begin{aligned} R_{15} = \frac{1}{\Delta}(&C_{15}C_{22}C_{34}^2 - C_{12}C_{25}C_{34}^2 - C_{13}C_{24}^2C_{35} + C_{15}C_{24}^2C_{33} - \\ &C_{14}C_{23}^2C_{45} + C_{15}C_{23}^2C_{44} + C_{13}C_{24}C_{25}C_{34} + C_{14}C_{23}C_{24}C_{35} + \\ &C_{14}C_{23}C_{25}C_{34} - C_{14}C_{24}C_{25}C_{33} - 2C_{15}C_{23}C_{24}C_{34} + \\ &C_{12}C_{24}C_{34}C_{35} + C_{13}C_{23}C_{24}C_{45} - C_{13}C_{23}C_{25}C_{44} - \\ &C_{14}C_{22}C_{34}C_{35} + C_{12}C_{23}C_{34}C_{45} - C_{12}C_{23}C_{35}C_{44} - \\ &C_{12}C_{24}C_{33}C_{45} + C_{12}C_{25}C_{33}C_{44} - C_{13}C_{22}C_{34}C_{45} + \\ &C_{13}C_{22}C_{35}C_{44} + C_{14}C_{22}C_{33}C_{45} - C_{15}C_{22}C_{33}C_{44}) \end{aligned}$$

$$\begin{aligned} R_{16} = \frac{1}{\Delta}(&C_{16}C_{22}C_{34}^2 - C_{12}C_{26}C_{34}^2 - C_{13}C_{24}^2C_{36} + C_{16}C_{24}^2C_{33} - \\ &C_{14}C_{23}^2C_{46} + C_{16}C_{23}^2C_{44} + C_{13}C_{24}C_{26}C_{34} + C_{14}C_{23}C_{24}C_{36} + \\ &C_{14}C_{23}C_{26}C_{34} - C_{14}C_{24}C_{26}C_{33} - 2C_{16}C_{23}C_{24}C_{34} + C_{12}C_{24}C_{34}C_{36} + \\ &C_{13}C_{23}C_{24}C_{46} - C_{13}C_{23}C_{26}C_{44} - C_{14}C_{22}C_{34}C_{36} + C_{12}C_{23}C_{34}C_{46} - \\ &C_{12}C_{23}C_{36}C_{44} - C_{12}C_{24}C_{33}C_{46} + C_{12}C_{26}C_{33}C_{44} - C_{13}C_{22}C_{34}C_{46} + \\ &C_{13}C_{22}C_{36}C_{44} + C_{14}C_{22}C_{33}C_{46} - C_{16}C_{22}C_{33}C_{44}) \end{aligned}$$

$$R_{21} = \frac{C_{24}\left(C_{13}C_{34} - C_{14}C_{33}\right) + C_{23}\left(C_{14}C_{34} - C_{13}C_{44}\right) - C_{12}C_{34}^2 + C_{12}C_{33}C_{44}}{\Delta}$$

$$R_{22} = -\frac{C_{33}C_{44} - C_{34}^2}{\Delta}$$

$$R_{23} = -\frac{C_{24}C_{34} - C_{23}C_{44}}{\Delta}$$

$$R_{24} = -\frac{C_{23}C_{34} - C_{24}C_{33}}{\Delta}$$

$$R_{25} = \frac{C_{24}\left(C_{34}C_{35} - C_{33}C_{45}\right) + C_{23}\left(C_{34}C_{45} - C_{35}C_{44}\right) - C_{25}C_{34}^2 + C_{25}C_{33}C_{44}}{\Delta}$$

$$R_{26} = \frac{C_{24}\left(C_{34}C_{36} - C_{33}C_{46}\right) + C_{23}\left(C_{34}C_{46} - C_{36}C_{44}\right) - C_{26}C_{34}^2 + C_{26}C_{33}C_{44}}{\Delta}$$

$$R_{31} = -R_{13}$$

$$R_{32} = R_{23}$$

$$R_{33} = -\frac{C_{22}C_{44} - C_{34}^2}{\Delta}$$

$$R_{34} = -\frac{C_{23}C_{24} - C_{22}C_{34}}{\Delta}$$

$$R_{35} = \frac{C_{34}\left(C_{24}C_{25} - C_{22}C_{45}\right) + C_{23}\left(C_{24}C_{45} - C_{25}C_{44}\right) - C_{35}C_{24}^2 + C_{22}C_{35}C_{44}}{\Delta}$$

$$R_{36} = \frac{C_{34}\left(C_{24}C_{26} - C_{22}C_{46}\right) + C_{23}\left(C_{24}C_{46} - C_{26}C_{44}\right) - C_{36}C_{24}^2 + C_{22}C_{36}C_{44}}{\Delta}$$

$$R_{41} = -R_{14}$$

$$R_{42} = R_{24}$$

$$R_{43} = R_{34}$$

$$R_{44} = -\frac{C_{22}C_{33} - C_{23}^2}{\Delta}$$

$$R_{45} = \frac{C_{34}\left(C_{23}C_{25} - C_{22}C_{35}\right) + C_{24}\left(C_{23}C_{35} - C_{25}C_{33}\right) - C_{45}C_{23}^2 + C_{22}C_{33}C_{45}}{\Delta}$$

$$R_{46} = \frac{C_{34}\left(C_{23}C_{26} - C_{22}C_{36}\right) + C_{24}\left(C_{23}C_{36} - C_{26}C_{33}\right) - C_{46}C_{23}^2 + C_{22}C_{33}C_{46}}{\Delta}$$

$$R_{51} = R_{15}$$

$$R_{52} = -R_{25}$$

$$R_{53} = -R_{35}$$

$$R_{54} = -R_{45}$$

$$\begin{aligned} R_{55} = \frac{1}{\Delta}(&-C_{23}^2C_{45}^2 + C_{44}C_{55}C_{23}^2 - 2C_{55}C_{23}C_{24}C_{34} + 2C_{23}C_{24}C_{35}C_{45} + \\ &2C_{23}C_{25}C_{34}C_{45} - 2C_{44}C_{23}C_{25}C_{35} - C_{24}^2C_{35}^2 + \\ &C_{33}C_{55}C_{24}^2 + 2C_{24}C_{25}C_{34}C_{35} - 2C_{22}C_{13}C_{14}C_{34} + \\ &C_{22}C_{44}C_{45}^2 - C_{22}C_{33}C_{44}C_{55}) \end{aligned}$$

$$\begin{aligned} R_{56} = \frac{1}{\Delta}(&C_{22}C_{56}C_{34}^2 - C_{24}^2C_{35}C_{36} - C_{25}C_{26}C_{34}^2 + C_{24}^2C_{33}C_{56} - \\ &C_{23}^2C_{45}C_{46} + C_{23}^2C_{44}C_{56} + C_{24}C_{25}C_{34}C_{36} + C_{24}C_{26}C_{34}C_{35} + \\ &C_{23}C_{24}C_{35}C_{46} + C_{23}C_{24}C_{36}C_{45} + C_{23}C_{25}C_{34}C_{46} - C_{23}C_{25}C_{36}C_{44} + \\ &C_{23}C_{26}C_{34}C_{45} - C_{23}C_{26}C_{35}C_{44} - C_{24}C_{25}C_{33}C_{46} - C_{24}C_{26}C_{33}C_{45} + \\ &C_{25}C_{26}C_{33}C_{44} - C_{22}C_{34}C_{35}C_{46} - C_{22}C_{34}C_{36}C_{45} + C_{22}C_{35}C_{36}C_{44} - \\ &2C_{23}C_{24}C_{34}C_{56} + C_{22}C_{33}C_{45}C_{46} - C_{22}C_{33}C_{44}C_{56}) \end{aligned}$$

$$R_{61} = R_{16}$$

$$R_{62} = -R_{26}$$

$$R_{63} = -R_{36}$$

$$R_{64} = -R_{46}$$

$$R_{65} = R_{56}$$

$$R_{66} = \frac{1}{\Delta}(-C_{23}^2 C_{46}^2 + C_{44} C_{66} C_{23}^2 - 2C_{66} C_{23} C_{24} C_{34} + 2C_{23} C_{24} C_{36} C_{46} + 2C_{23} C_{26} C_{34} C_{46} - 2C_{44} C_{23} C_{26} C_{36} - C_{24}^2 C_{36}^2 + C_{33} C_{66} C_{24}^2 + 2C_{24} C_{26} C_{34} C_{36} - 2C_{22} C_{13} C_{14} C_{34} + C_{22} C_{44} C_{46}^2 - C_{22} C_{33} C_{44} C_{66})$$

$$Q = -\begin{bmatrix} R_{11} & 0 & 0 & 0 & R_{15} & R_{16} \\ R_{21} & -1 & 0 & 0 & R_{25} & R_{26} \\ R_{31} & 0 & -1 & 0 & R_{35} & R_{36} \\ R_{41} & 0 & 0 & -1 & R_{45} & R_{46} \\ R_{51} & 0 & 0 & 0 & R_{55} & R_{56} \\ R_{61} & 0 & 0 & 0 & R_{65} & R_{66} \end{bmatrix}$$

APPENDIX B

PLAIN WEAVE PARAMETRIC STUDY GRAPHS

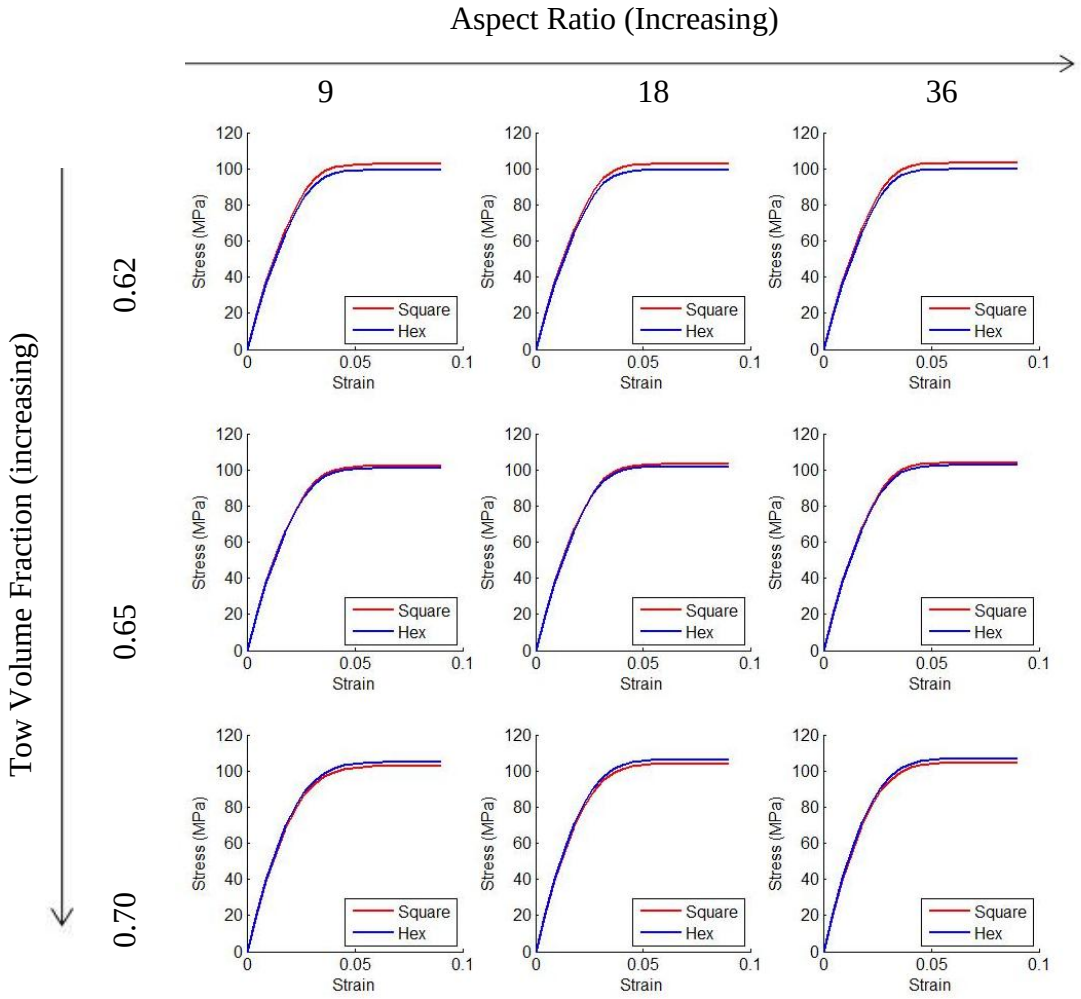

Figure 1 Fiber Packing Effects on Shear Response for a 5HS Weave.

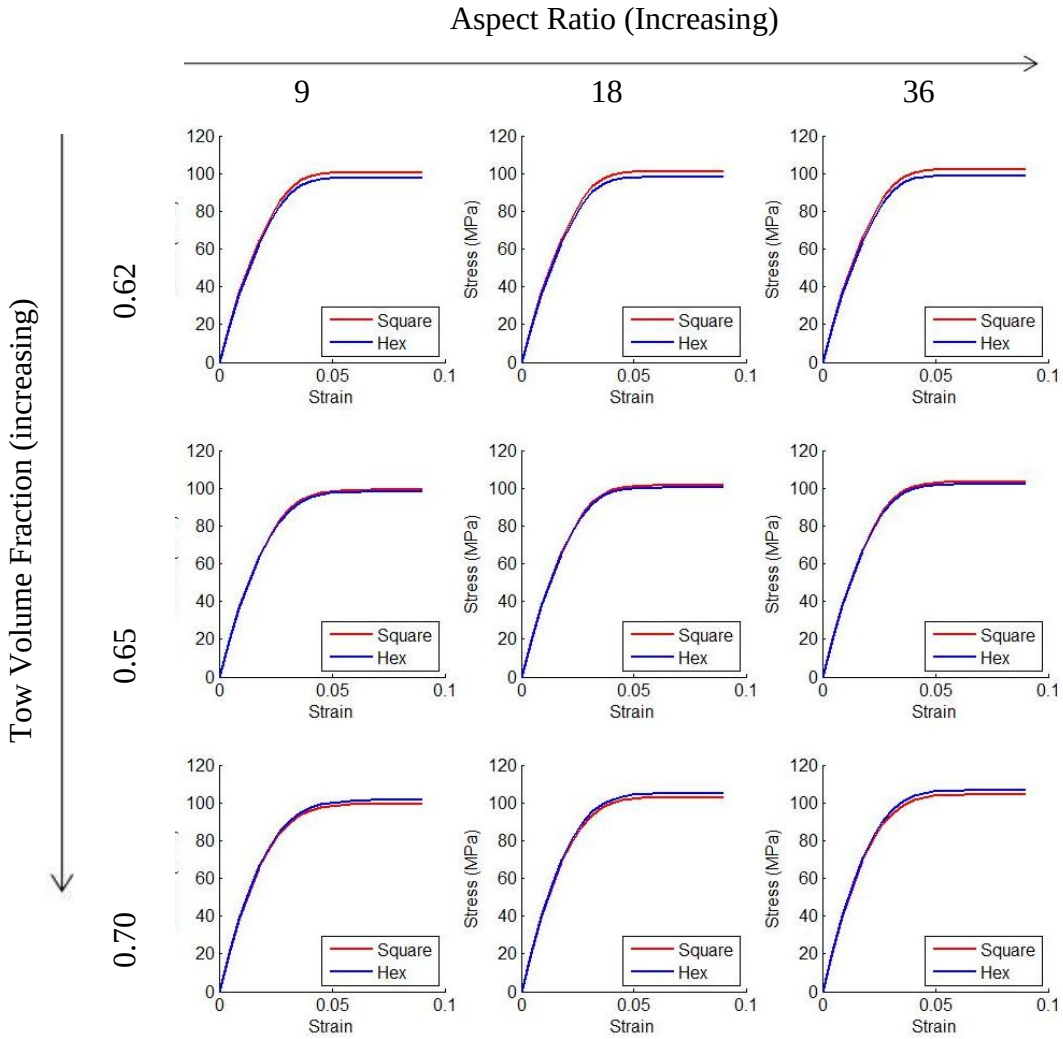

Figure 2 Fiber Packing Effects on Shear Response for a Plain Weave.

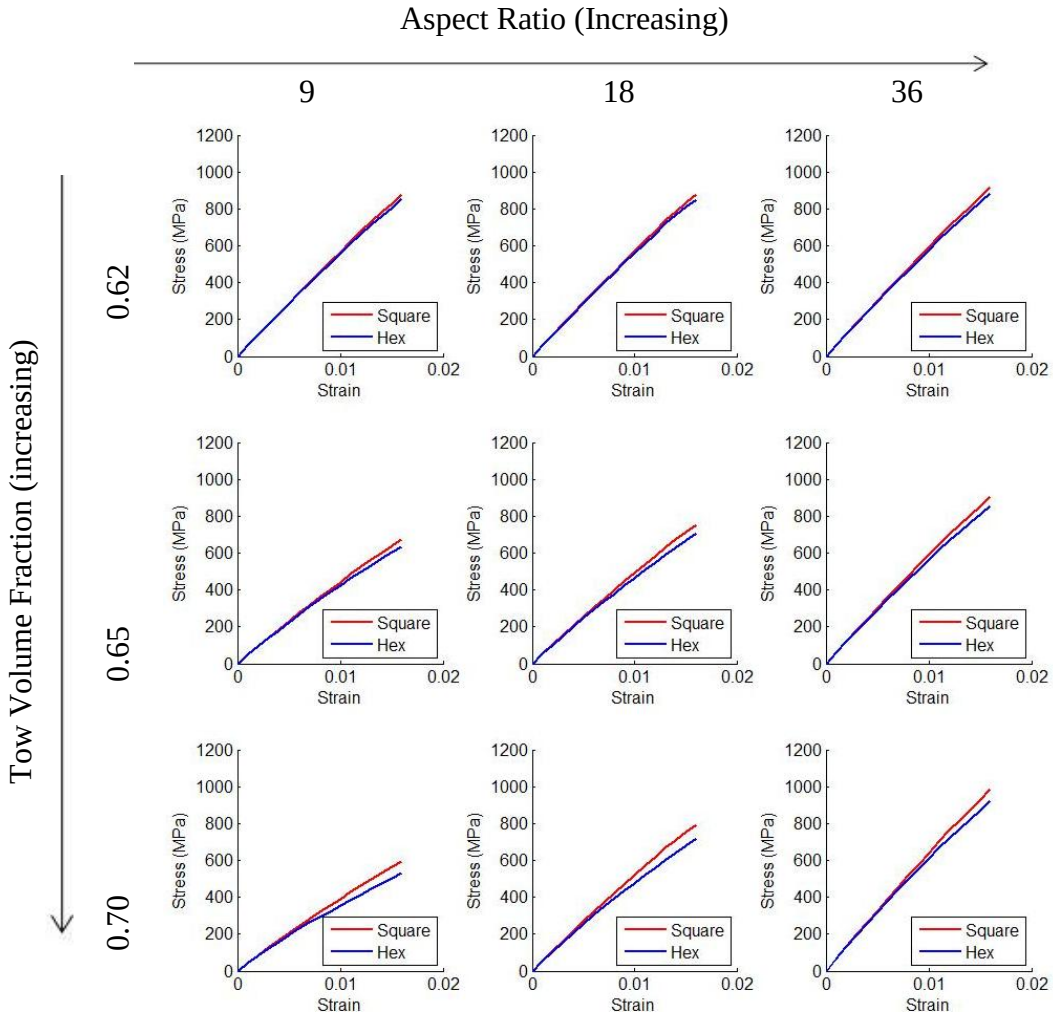

Figure 3 Fiber Packing Effects on Tensile Response for a Plain Weave.

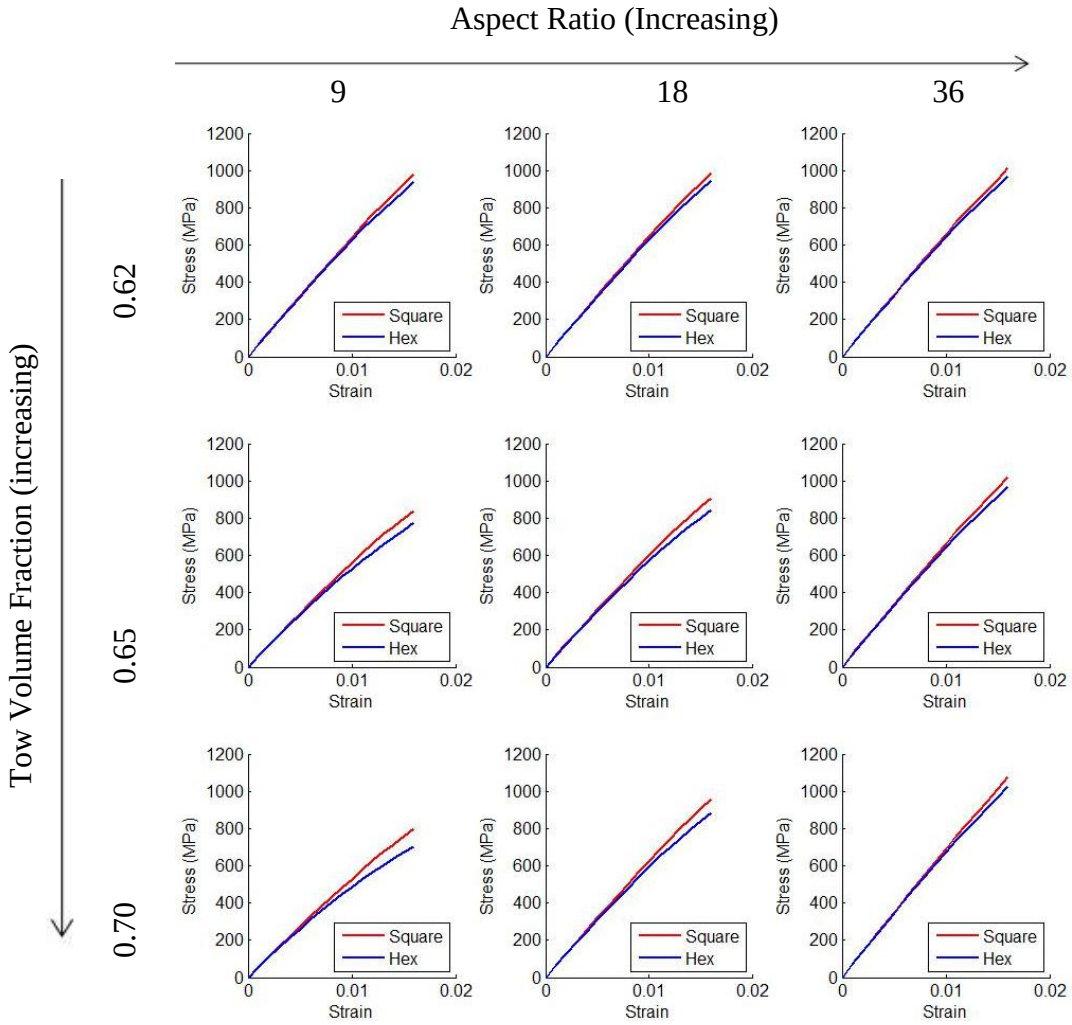

Figure 4 Fiber Packing Effects on Tensile Response for a 5HS Weave.

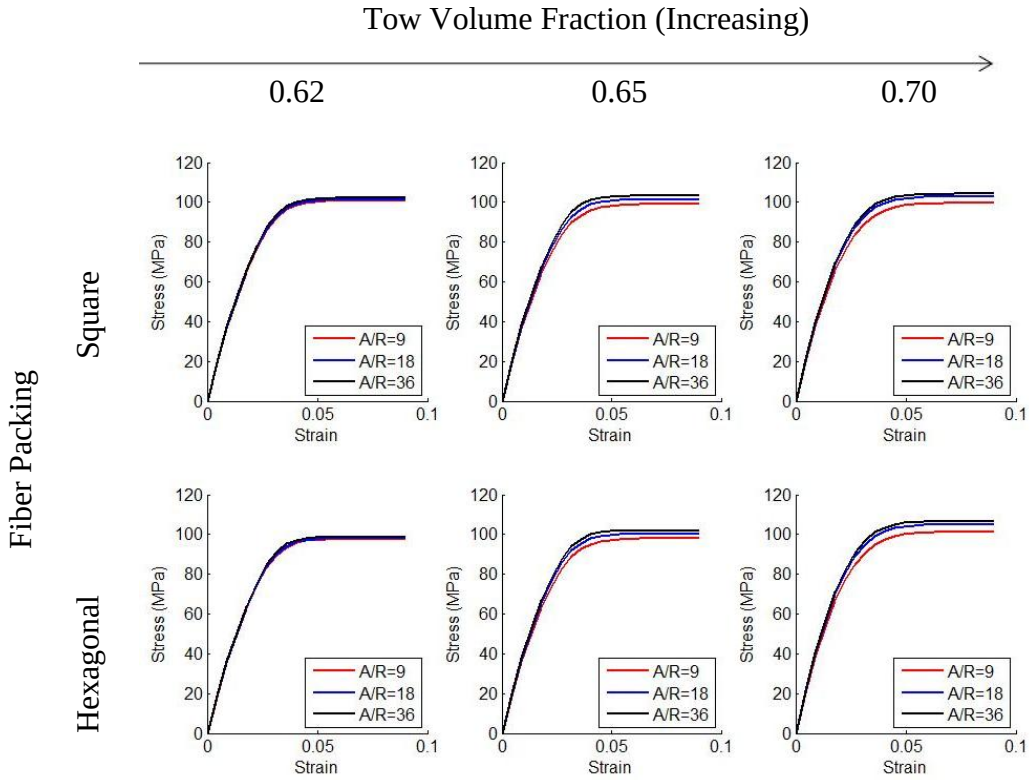

Figure 5 Tow Aspect Ratio Effects on Shear Response for a Plain Weave.

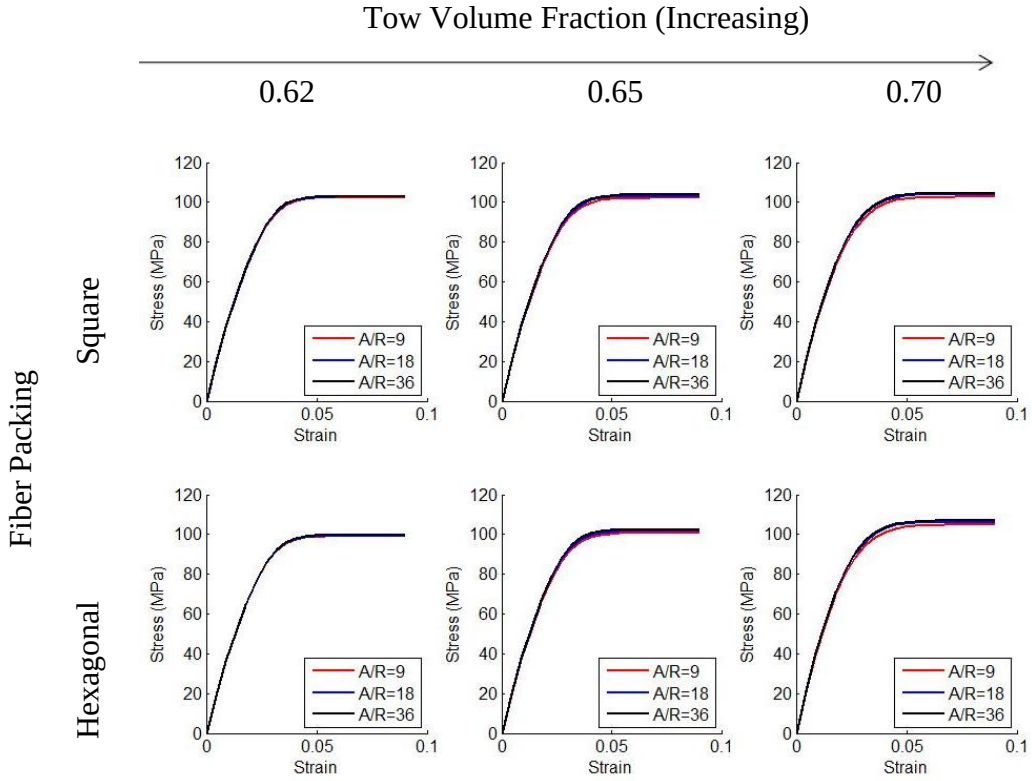

Figure 6 Tow Aspect Ratio Effects on Shear Response for a 5HS Weave.

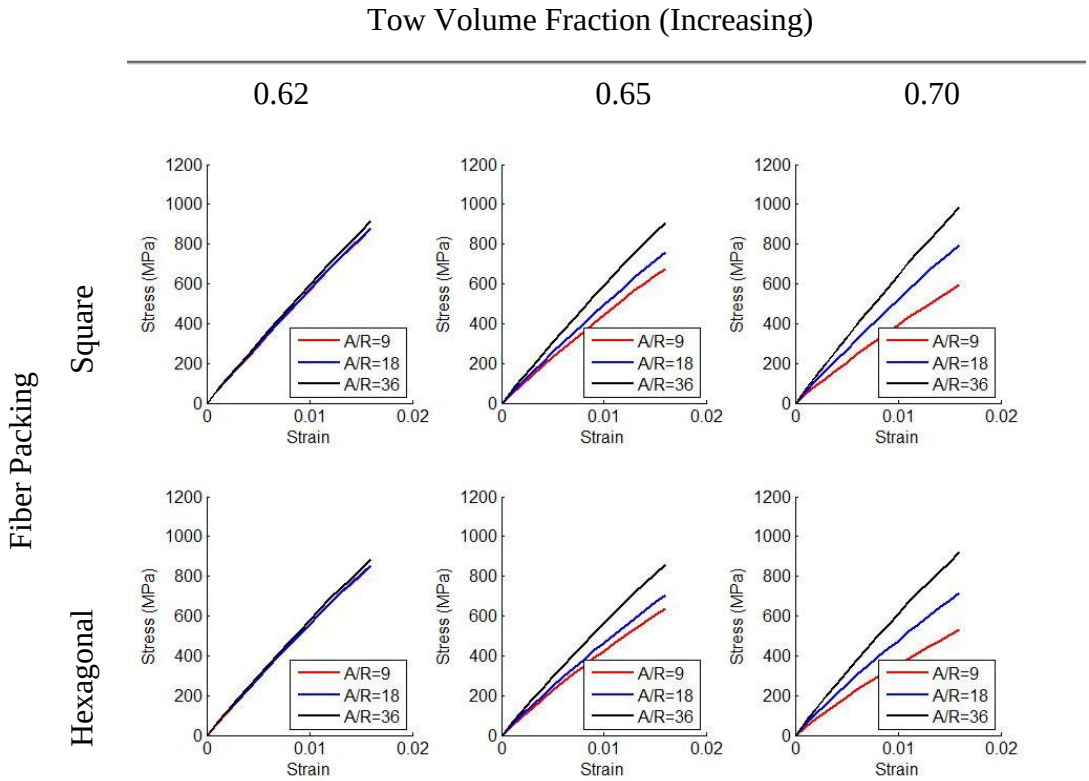

Figure 7 Tow Aspect Ratio Effects on Tensile Response for a Plain Weave.

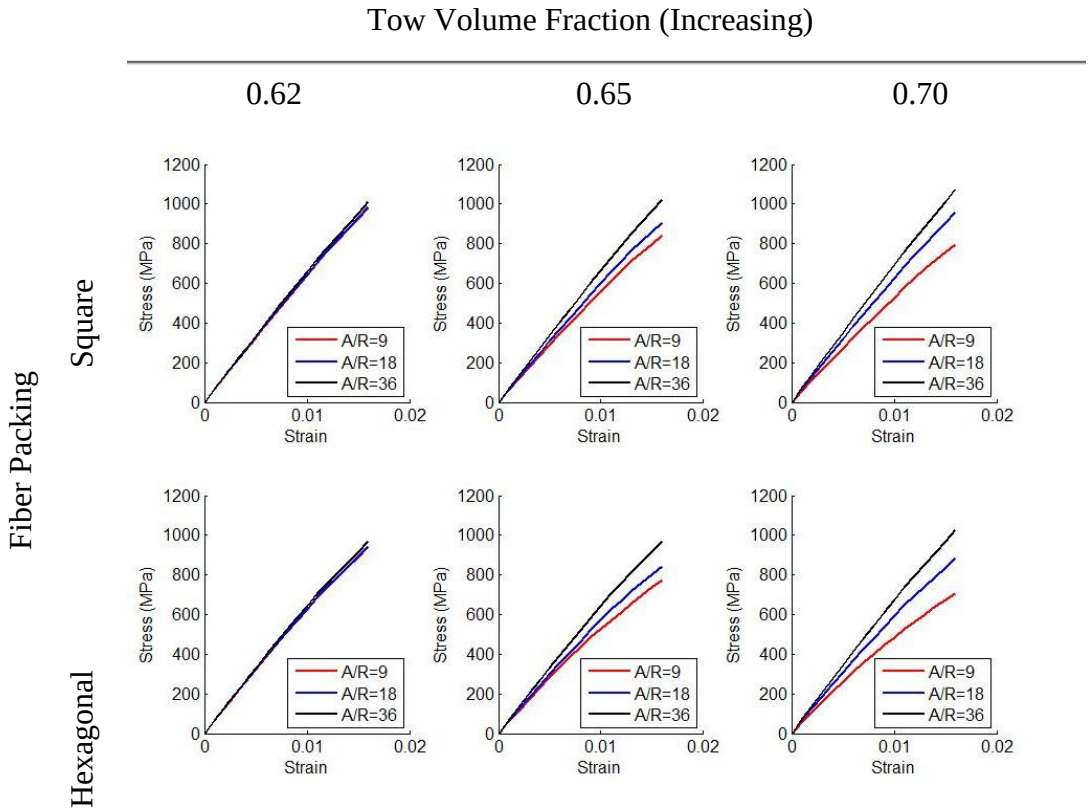

Figure 8 Tow Aspect Ratio Effects on Tensile Response for a 5HS Weave.

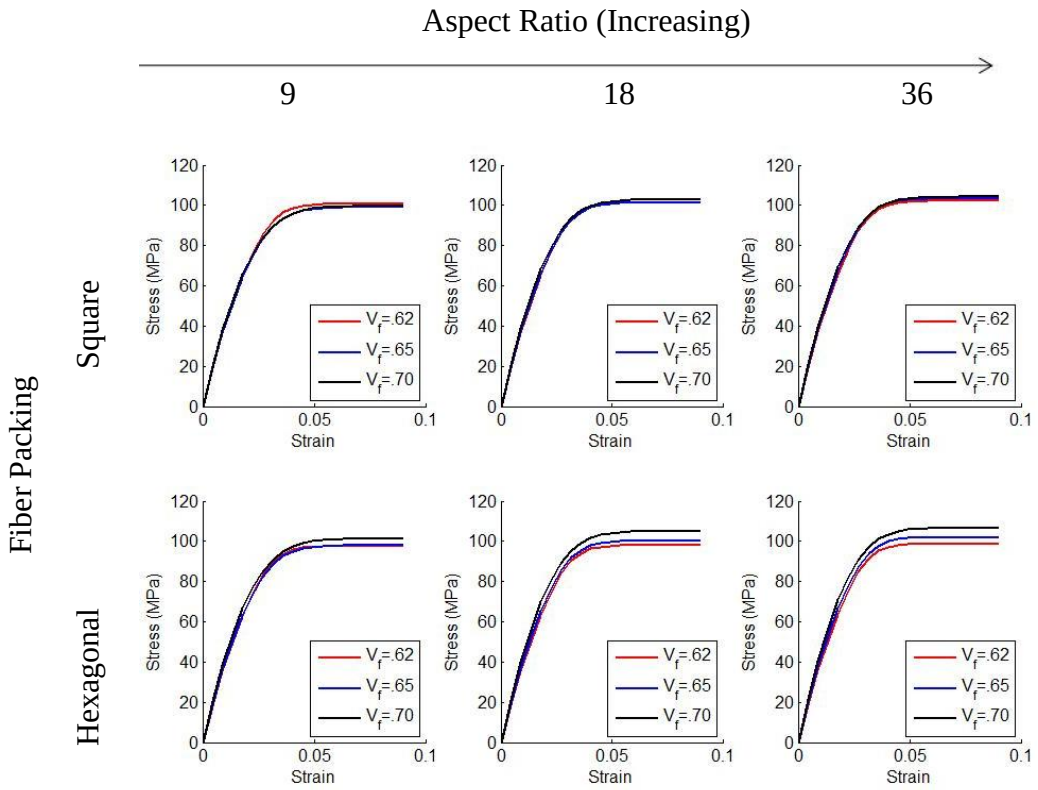

Figure 9 Tow Volume Fraction Effects on Shear Response for a Plain Weave.

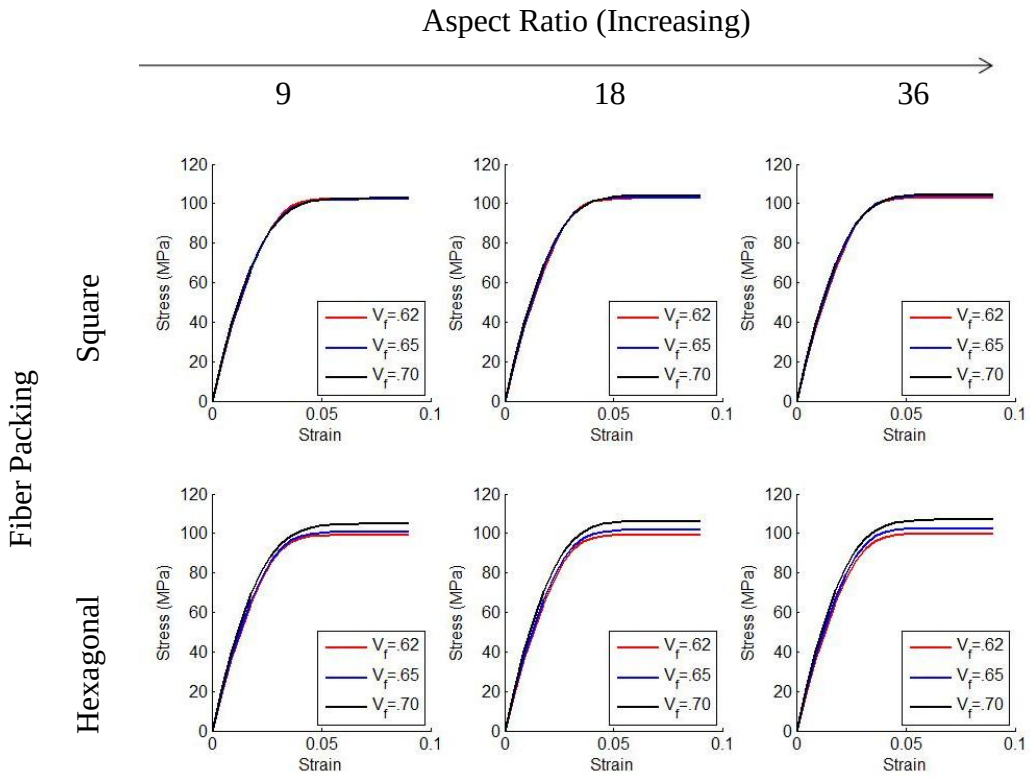

Figure 10 Tow Volume Fraction Effects on Shear Response for a 5HS Weave.

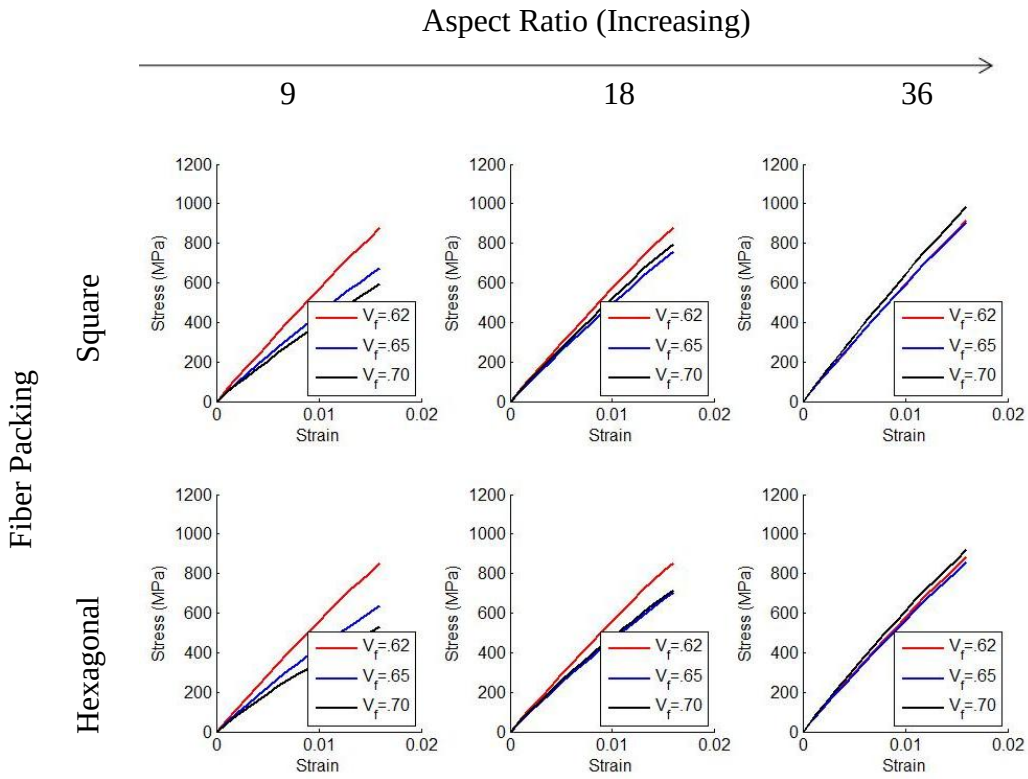

Figure 11 Tow Volume Fraction Effects on Tensile Response for a Plain Weave.

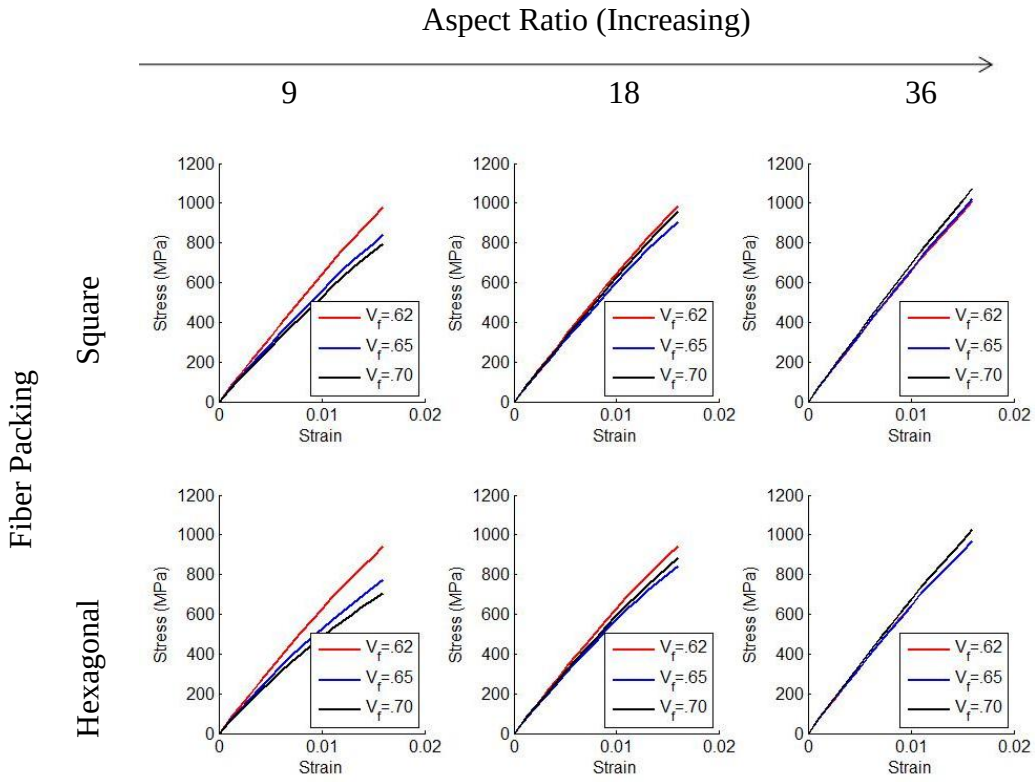

Figure 12 Tow Volume Fraction Effects on Tensile Response for a 5HS Weave.